UNIVERSITÀ DI PARMA

UNIVERSITÀ DEGLI STUDI DI PARMA

DOTTORATO DI RICERCA IN
INGEGNERIA INDUSTRIALE

CICLO XXXVII

Linearization and Modal Problems in Multibody System Dynamics for Modern Wind Turbines

Coordinatore:
Chiar.mo Prof. Gianni Royer-Carfagni

Tutore:
Chiar.mo Prof. Alessandro Tasora

Dottorando: Chao Peng

Anni Accademici 01/2022 - 12/2024

Abstract

Wind energy, as a primary source of renewable energy, plays a crucial role in achieving global carbon neutrality goals. To enhance cost-efficiency, modern wind turbines are being scaled to larger sizes. However, this trend introduces significant challenges related to aeroelastic instability, which is increasingly evident in turbines with slender blades. The eigenvalue analysis method, based on linear aeroelastic models, is widely used to investigate the modal dynamics of wind turbines. While custom simulation tools have been developed to predict aeroelastic stability, discrepancies in aeroelastic damping ratios across different tools persist. Additionally, field validation using full-scale wind turbines under normal operational conditions remains either insufficient or lacking.

This study investigates the problem of aeroelastic stability assessment in modern wind turbines using the eigenvalue approach. A linearization and modal analysis framework is developed within the context of multibody system dynamics, with a particular focus on its application to the modal dynamics of wind turbines. A comprehensive verification and validation procedure is proposed to demonstrate the effectiveness of the developed method.

The slender blades of wind turbines are discretized using a generic tapered Timoshenko beam element, combined with the corotational formulation to capture geometric nonlinearities during large deflections. Rotor aerodynamics are computed using the classical blade element momentum method. The equations of motion for the wind turbine are derived using Newton-Euler equations, with mechanical joints modeled as algebraic constraints based on quaternion parametrization. Analytical linearization of the inertial, elastic, viscous, and algebraic terms is performed in the local reference frames at the rotor's rotating center, while numerical differentiation is used to linearize the steady aerodynamic forces in the quasi-static equilibrium configuration. The various terms are assembled in consistent coordinate systems, yielding a set of linearized differential-algebraic equations. Multi-blade coordinate transformations are applied to both generalized coordinates and Lagrange multipliers, resulting in linear time-invariant systems that are suitable for eigenvalue analysis. An efficient sparse-preserving Krylov-Schur eigenvalue solver is employed to solve the eigenvalue problem, enabling the subsequent investigation of the wind turbine's modal dynamics.

Aeroelastic damping predictions are verified through numerical simulations using a series of virtual models, which are generated by scaling the blade torsional stiffness. A strong correlation between the damping ratio and the blade edgewise vibration level is observed in the numerical experiments. Field validation is performed on two prototype wind turbines, where the unstable wind speed range observed in the blade edgewise vibration closely aligns with the region of predicted negative damping. The verification and validation analyses confirm the applicability of the developed linearization and modal analysis framework for assessing the aeroelastic stability of wind turbines in engineering practice.

A unified analytical expression for the tangent stiffness matrix of holonomic constraints is derived for the first time. Numerical examples highlight the importance of this matrix in ensuring proper convergence of static equilibrium analysis and in achieving accurate eigenvalue results for multibody systems with free-motion joints under stressed equilibrium conditions.

As a complementary effort, a modal reduction procedure is developed for rotating subsystems comprising rigid bodies, finite elements, and mechanical joints, within the context of multibody system dynamics. The accuracy and effectiveness of this procedure are verified through a series of academic numerical examples.

This work establishes an effective framework for linearization and modal analysis in multibody system dynamics, advancing the aeroelastic stability assessment of wind turbines and providing a foundation for future engineering applications and research.

Keywords: multibody system dynamics; linearization; wind turbine aeroelasticity; aeroelastic stability; eigenvalue analysis; modal reduction.

Contents

Nomenclature

Multibody system dynamics

DOF Degree Of Freedom

DAE Differential Algebraic Equation

ODE Ordinary Differential Equation

MCS Minimal Coordinate Set

RCS Redundant Coordinate Set

SEP Standard Eigenvalue Problem

QEP Quadratic Eigenvalue Problem

GEP Generalized Eigenvalue Problem

FFRF Floating Frame of Reference Formulation

CRF CoRotational Formulation

GEBT Geometricially Exact Beam Theory

ANCF Absolute Nodal Coordinate Formulation

HHT Hilber-Hughes-Taylor integrator

CMS Component Mode Synthesis

FPM Fully Populated Matrix

FEM Finite Element Method

LTI Linear Time-Invariant

Wind turbines

BEM Blade Element Momentum

LCOE Levelized Cost Of Electricity

MBC Multi-Blade Coordinate

NWP Normal Wind Profile

SIV Stall Induced Vibration

VIV Vortex Induced Vibration

Symbols

t	Time
k	Step index in the time integration scheme
$\boldsymbol{f}$	Force vector
$\boldsymbol{m}$	Moment vector
$\boldsymbol{q}$	Generalized coordinate vector
$\dot{\boldsymbol{q}}$	Generalized velocity vector
$\ddot{\boldsymbol{q}}$	Generalized acceleration vector
$\boldsymbol{r}$	Position vector
$\boldsymbol{R}$	Rotation matrix
$\boldsymbol{\rho}$	Quaternion
s	Scalar part of quaternion $\boldsymbol{\rho}$
$\boldsymbol{v}$	Vectorial part of quaternion $\boldsymbol{\rho}$
$\boldsymbol{\phi}$	Rotation pseudovector
ϕ	Rotation angle
$\boldsymbol{n}$	Rotation axis as a unit-length vector
$\delta\boldsymbol{\theta}$	Virtual rotation vector
$\boldsymbol{\omega}$	Angular velocity vector
$\boldsymbol{M}$	Mass matrix
$\boldsymbol{D}$	Damping matrix

$\boldsymbol{K}$ Stiffness matrix

$\boldsymbol{c}$ Constraint vector

$\boldsymbol{C_q}$ Jacobian matrix of constraints

$\boldsymbol{\gamma}$ Lagrange multipliers

ν Lumped mass

$\boldsymbol{s}$ Mass center offset

$\boldsymbol{J}$ Mass moment of inertia tensor

$\boldsymbol{z}$ Multi-blade coordinates

$\boldsymbol{T}$ MBC transformation matrix

$\boldsymbol{I}$ Identity matrix

$\jmath$ Imaginary unit

λ Eigenvalue

$\boldsymbol{\Phi}$ Eigenvector corresponding to generalized coordinates

$\boldsymbol{\xi}$ Eigenvector corresponding to Lagrange multipliers

Operators

$\widetilde{\boldsymbol{\phi}}$ Skew symmetric matrix of the vector $\boldsymbol{\phi} \in \mathbb{R}^3$

$\text{axial}\,(\boldsymbol{\Phi})$ The axial vector of the skew symmetric matrix $\boldsymbol{\Phi}$

$\exp(\boldsymbol{X})$ The exponential of matrix $\boldsymbol{X}$

$\log(\boldsymbol{X})$ The logarithm of matrix $\boldsymbol{X}$

$\text{vert}\,(\boldsymbol{X})$ Concatenate the matrix $\boldsymbol{X}$ in the vertical direction

$\text{diag}\,(\boldsymbol{X})$ Concatenate the matrix $\boldsymbol{X}$ in the diagonal direction

$\boldsymbol{X}^{-1}$ The inverse of matrix $\boldsymbol{X}$

$\boldsymbol{X}^{+}$ The pseudo-inverse of matrix $\boldsymbol{X}$

$\boldsymbol{X}^{T}$ The transpose of matrix $\boldsymbol{X}$

$\dot{\square}$ Time derivative

$\ddot{\square}$ Second time derivative

$\boldsymbol{\rho}^{*}$ Conjugate of quaternion $\boldsymbol{\rho}$

Preface

This thesis is submitted in partial fulfillment of the requirements for the degree of PhD in Industrial Engineering. The research was conducted at the Department of Engineering for Industrial Systems and Technologies, University of Parma, from January 2022 to December 2024. The PhD program was funded by a scholarship from the PON REACT-EU program, specifically under PON DM 1061/2021.

Modern wind turbines, as the largest rotating machines ever developed by humankind, face critical challenges related to aeroelastic instability. The eigenvalue approach has been widely used to investigate the modal dynamics and predict the aeroelastic stability of these turbines. Despite the widespread use of this method within the wind energy community, inconsistencies in stability predictions persist across various studies. This challenge has hindered the design process in engineering practice, and it has motivated me to explore this issue in greater depth. The primary goal of this thesis is to develop an effective linearization and modal analysis framework within the context of multibody system dynamics, with a particular focus on aeroelastic stability assessment for modern wind turbines.

The thesis is structured into six chapters:

Chapter 1 begins with an overview of the wind energy market, followed by a comprehensive literature review on the modal dynamics of wind turbines and the key challenges associated with aeroelastic stability. The chapter then defines the overall objectives of the thesis and presents a brief outline of its structure.

Chapter 2 presents the foundational theory of flexible multibody system dynamics. It covers essential topics, including rotation parametrization, kinetic descriptions, algebraic constraints and their corresponding Jacobian matrices, and the theory of differential-algebraic equations. The chapter then explores the modeling approach for flexible structures, with particular emphasis on the development of a generic Timoshenko beam element integrated with the corotational formulation. This formulation is crucial for accurately modeling slender wind turbine blades. Additionally, the chapter introduces key computational methods, including the time integrator, static equilibrium solver, and eigenvalue solver. Serving as a condensed textbook on multibody system dynamics, this chapter establishes the theoretical foundation for the subsequent discussions. It also presents the essential background theory for the smooth dynamics in the open-source multibody system

dynamics library CHRONO.

Chapter 3 introduces the core concepts of linearization and modal analysis within the context of flexible multibody system dynamics, with a specific focus on multi-bladed wind turbines. The chapter presents the scheme for aerodynamic linearization using numerical differentiation, followed by a detailed derivation of the analytical linearization of structural dynamics. A traditional multi-blade coordinate transformation is applied to the linearized differential-algebraic equations, yielding a linear time-invariant system suitable for eigenvalue analysis. A comprehensive interpretation of the modal dynamics of wind turbines is also presented.

Chapter 4 begins with an investigation into the eigenvalues of a multi-bladed rotor's free rotation mode. These eigenvalues are not necessarily zero and may even be real-valued, leading to the counterintuitive conclusion that a free-rotating multi-bladed rotor might fail to maintain stable rotation in a vacuum. The chapter further delves into the aeroelastic stability of wind turbines and presents a comprehensive verification and validation procedure, demonstrating the applicability of the developed linearization and modal analysis framework for assessing the aeroelastic stability of wind turbines.

Chapter 5 presents a modal reduction procedure based on the corotational concept. This method is designed for subsystems composed of rigid bodies, finite elements, and algebraic constraints. The chapter includes detailed derivations of the modal reduction transformation, motion decomposition, tangent system matrices, and a scheme to update the floating frame of reference. Numerical examples are provided to demonstrate the accuracy and effectiveness of the proposed method.

Chapter 6 summarizes the key findings and contributions of this research, along with recommendations for future research directions.

This research has been conducted in close collaboration with Goldwind, a leading wind turbine manufacturer. Goldwind provided significant support, including additional funding, wind turbine numerical models, computational resources, measurement data, and access to testing environments for algorithm development and code implementation. Additionally, Goldwind hosted me at their Beijing office to facilitate the research process. I extend my heartfelt gratitude to Goldwind for their invaluable support.

Some of the results presented in this thesis have been published in the following references: [178, 209, 208, 207].

Chapter 1

Introduction

1.1 Wind Energy

To mitigate the adverse effects of global climate change and rising temperatures, the Paris Agreement was established and has been ratified by numerous countries around the world. In Europe, the European Climate Law has set an intermediate goal to reduce net greenhouse gas emissions by at least 55 % by 2030, relative to 1990 levels [76]. Meanwhile, the Chinese government has pledged that China's carbon dioxide emissions will peak around 2030.

Renewable energy policies have significantly accelerated the growth of wind power in recent years. According to the report of Global Wind Energy Council, the global cumulative installed wind power capacity surpassed the 1 TW milestone in 2023. To meet global climate and energy targets, global annual installations over the remainder of this decade are projected to exceed 320 GW on average, with the European Union expected to contribute approximately 33 GW annually [103].

To further promote the deployment of wind energy in the future, it is crucial to reduce the levelized cost of energy (LCOE) and enhance cost-efficiency. A practical strategy in the wind industry to achieve these goals is the adoption of larger wind turbines [241]. As illustrated in Figure 1.1, the average power rating of installed turbines in Europe has progressively increased from 2014 to 2023. In 2023, the average power rating of newly installed onshore turbines in Europe reached 4.5 MW, while the rating for offshore turbines rose to 9.7 MW [285]. Moreover, with the average power rating of both onshore and offshore turbines ordered in 2023 having further increased, the power ratings are expected to continue rising in the coming years.

In recent years, leading original equipment manufacturers (OEMs) around the world have endeavored to develop more powerful wind turbines with longer blades. The Haliade-X wind turbine, developed by GE Vernova, received its full type certification for operations up to 14.7 MW at the end of 2022 [275]. Subsequently, in 2023, it was commercially deployed at Dogger Bank, the world's largest offshore

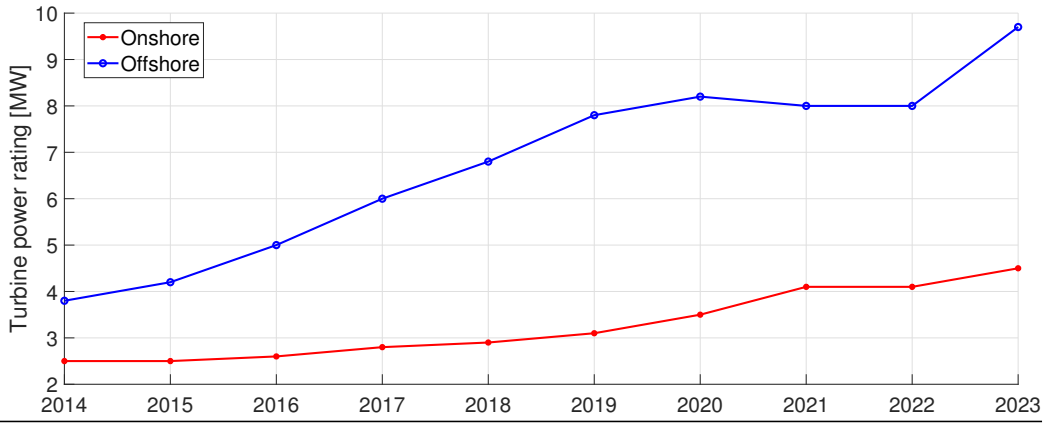

	2014	2015	2016	2017	2018	2019	2020	2021	2022	2023
Onshore	2.5	2.5	2.6	2.8	2.9	3.1	3.5	4.1	4.1	4.5
Offshore	3.8	4.2	5.0	6.0	6.8	7.8	8.2	8.0	8.0	9.7

Figure 1.1: Average power rating of installed turbines in Europe, 2014-2023. Source: WindEurope [285].

wind farm, where 277 turbines with a power capacity of 13 MW and a blade length of 107 m were installed [78]. In 2024, the first of 60 Siemens Gamesa SG 14-222 DD wind turbines, equipped with 108 m blades and capable of generating up to 15 MW of power in 'Power Boost' mode, was deployed at the Moray West offshore wind farm [71]. Vestas developed the V236-15.0 MW offshore wind turbine, featuring 115.5 m blades. The turbine received its full type certification at the end of 2023 and was subsequently ready for the conditional order for the Empire Wind 1 project [56]. Mingyang Smart Energy has installed a prototype of the MySE 18.X-20 MW turbine, which provides flexible power ratings ranging from 18.X MW to 20 MW and features rotor diameters between 260 and 292 meters [186]. In October 2024, Dongfang Electric rolled out a 26 MW offshore wind turbine, marking a significant advancement in turbine capacity [288]. Several other OEMs have either announced conceptual models of large turbines or developed prototype turbines to compete in the race for the most powerful wind turbines. Table 1.1 presents a list of the major large offshore wind turbines, while Figure 1.2 displays two examples of offshore wind turbine prototypes.

The numerical models and algorithms employed in simulation tools for the design of large wind turbines must be continually revised to account for the challenges posed by size up-scaling, which often pushes beyond the limits of basic assumptions [272]. In this context, reference wind turbine (RWT) models are essential for validating the various tools utilized within the wind energy community, as they provide standardized, openly accessible model data.

As part of International Energy Agency (IEA) Wind TCP Task 55, the National Renewable Energy Laboratory (NREL) and the Technical University of Denmark (DTU) have collaboratively developed a new reference wind turbine model. This

Table 1.1: A list of the major large offshore wind turbines.

Manufacturer	Model	Power [MW]	Rotor diameter [m]	Blade length [m]
Dongfang Electric	-	26.0	310+	-
Mingyang	MySE 22MW	22.0	310+	-
Mingyang	MySE 18.X-20 MW	18.X-20.0	260-292	-
Dongfang Electric	DEW-18 MW-260	18.0	260	126
Goldwind	GWH252-16MW	16.0	252	123
Vestas	V236-15.0 MW	15.0	236	115.5
Siemens Gamesa	SG 14-222 DD	15.0	222	108
GE Vernova	Haliade-X 14MW	14.7	220	107

(a) MySE 18.X-20 MW

(b) GWH252-16MW

Figure 1.2: Two examples of offshore wind turbine prototypes.

state-of-the-art model, with a power rating of 22 MW, features a rotor diameter of 284 meters and a blade length of 137.8 meters [292].

1.2 Modal dynamics of wind turbines

International standards provide comprehensive guidelines for the design of modern wind turbines [139, 141, 142], which are extensively utilized in the design and certification processes within the wind energy industry. The design of modern wind turbines is primarily driven by considerations of power performance and production cost under various constraints on structural integrity. These constraints comprise ultimate strength, fatigue strength, buckling, and the clearance between the tower and blades, among other factors.

Modern wind turbines are characterized by long slender blades mounted on tall towers. Severe vibrations can generate significant fatigue loads on these expensive components; thus, it is essential to mitigate vibration risks during the design phase. This can be achieved through careful system design, the implementation of advanced control strategies, or the incorporation of dedicated vibration dampers. Given the intense competitiveness of the market, commercial wind turbines are increasingly pushed toward the limits of aeroelastic stability. Consequently, instability phenomena may emerge in production wind turbines. A clear understanding of the modal dynamics of wind turbines, along with accurate predictions of aeroelastic stability, is crucial for conducting root cause analyses and developing technical solutions to address instability issues. Ultimately, aeroelastic stability has become a critical concern in the design of modern wind turbines.

1.2.1 Numerical methods

The challenge of aeroelastic instability in the wind energy sector can date back to stall-regulated wind turbines of the previous century. The first experimental case of blade edgewise instability was observed in the mid-1990s on stall-regulated turbines with rotor diameters ranging from 35 to 40 meters [116]. This finding prompted systematic research into blade edgewise stability, which subsequently expanded to include the broader study of wind turbine modal dynamics [3].

Wind turbine systems are inherently time-variant due to rotor rotation. Performing a straightforward modal analysis at a series of azimuthal positions can produce results lacking physical significance [225]. Therefore, careful consideration is essential to ensure a meaningful modal analysis. For isotropic multi-bladed rotors, when the generalized coordinates of the rotating blades are expressed in their respective rotating frames, the system equations of motion can be transformed into a consistent inertial frame using the multi-blade coordinate (MBC) transformation, also referred to as the Coleman transformation. This approach yields a linear time-invariant (LTI) system [112, 118, 29].

Hansen [112] investigated the modal dynamics by applying an eigenvalue approach in conjunction with the MBC transformation to eliminate the time-varying terms in the equations of motion. The study revealed that blade motion out of the

rotor plane in the forward whirling mode is greater than in the backward whirling mode, providing an explanation for the observed rotor edgewise backward whirling mode on the Bonus 600 kW stall-regulated wind turbine. Additionally, the distinct damping levels between the rotor edgewise backward and forward whirling modes indicate that modal analysis based on an isolated blade may be misleading for aeroelastic stability assessments. However, the classical flutter limits predicted for an isolated blade and a full wind turbine showed no significant discrepancies, which could be attributed to the specific turbine model used in the study [117].

Various approaches have been utilized in aeroelastic stability analysis, including the eigenvalue method in combination with the MBC transformation [229, 30, 29], Floquet analysis [31, 246, 113], and time-domain nonlinear dynamic simulation [157, 212, 8].

Hansen [118] presented a comprehensive review of aeroelastic stability analysis and delivered a systematic interpretation of the modal dynamics of three-bladed wind turbines. The study identified two critical aeroelastic instability phenomena: stall-induced vibrations in stall-regulated turbines and classical flutter in pitch-regulated turbines. As an outcome of the collaborative project "Aeroelastic Stability and Control of Large Wind Turbines" (STABCON), a summary of design guidelines for passive instability suppression was presented [115]. These guidelines serve as a practical reference for troubleshooting aeroelastic instabilities.

Due to the severe blade stall-induced edgewise vibrations observed in stall-regulated wind turbines, the wind energy industry transitioned to a new technical route: pitch-regulated, variable-speed wind turbines, beginning in the first decade of this century. This shift effectively eliminated the risk of blade edgewise aeroelastic instability during normal operations. Nevertheless, scientific research on aeroelastic stability analysis continues to advance.

Hansen [120] developed a linearization framework based on a geometrically nonlinear corotational finite element formulation integrated with the Blade Element Momentum (BEM) method. The study presented an analytical linearization of aerodynamics, incorporating a linearized unsteady aerodynamic model derived from the Beddoes-Leishman type dynamic stall model [119]. Additionally, the influence of blade backward sweep design on the classical flutter limit was investigated.

The MBC transformation method provides several advantages, including algorithmic simplicity, computational efficiency, and a clear interpretation of modal dynamics. Consequently, it has become a widely used technique for aeroelastic stability analysis of multi-bladed wind turbines. However, the MBC transformation is limited to isotropic rotors, where all blades have identical structural configurations and aerodynamic states with respect to the rotor center. Furthermore, it is only applicable to rotors with more than two blades [113].

However, three-bladed wind turbine rotors can never achieve perfect isotropy. Factors such as gravitational forces on the blades, wind shear, wind inflow angles,

yaw misalignment, mass imbalances, pitch errors among the blades, and other effects disrupt rotor isotropy. To address these challenges, Floquet analysis can be employed for modal and stability analyses. This method constructs a Lyapunov-Floquet transformation matrix based on the dynamic response obtained through time integration over one period for arbitrary periodic time-variant systems. Eigenvalue analysis is then performed to extract the principal eigenvalues, along with an infinite number of branch eigenvalues corresponding to integer multiples of the rotor's rotational frequency.

Floquet analysis, as a more general approach, is capable of handling anisotropic wind turbine rotors. However, its computational cost is high due to the time integration required, particularly for large-scale systems. As an alternative, Hill's method can be used to reduce computational costs. In Hill's method, the system matrix in the state-space representation is expanded into a Fourier series, thereby avoiding the need for numerical integration. However, this approach requires truncation of the Fourier series to discard higher-order harmonic terms, which may lead to a reduction in accuracy.

Floquet analysis has been extensively applied in the stability analysis of rotorcraft [12, 15]. The modal dynamics of wind turbines with anisotropic rotors have been investigated and compared using the MBC transformation, Floquet analysis, and Hill's method [245]. It has been demonstrated that the MBC transformation is a special case of Lyapunov–Floquet transformations for isotropic rotors [247].

An efficient implicit Floquet analysis has been utilized to study the effects of wind shear on the aeroelastic modal damping of a Siemens 2.3 MW pitch-regulated wind turbine with three 45-meter blades [248, 249]. The results indicate that, for the less damped modes, the impact on modal frequencies and damping values is minimal and falls within the uncertainty range of numerical predictions. However, for larger rotors, the increased structural flexibility may amplify these effects, raising concerns about whether wind shear—and by extension, other anisotropic factors—might significantly influence modal damping in modern wind turbines with slender blades exceeding 100 meters in length. Further investigation is required to clarify these effects for current turbine designs.

The concept of two-bladed wind turbines is appealing from a manufacturing cost perspective, as it requires one less blade compared to three-bladed designs. The modal dynamics of two-bladed rotors have been analyzed using Hill's method, which reveals the presence of additional higher-order harmonic terms in the system matrix. This leads to more complex modal coupling and a greater number of resonance frequencies compared to three-bladed turbines [113].

The concept of multi-rotor wind turbines offers the potential to achieve the same power capacity using shorter blades, thereby enhancing the aeroelastic stability of the blades. The MBC transformation for a single multi-bladed rotor has been extended to a tri-rotor wind turbine, resulting in a linearized aeroelastic model suitable for eigenvalue analysis. The modal dynamics of the tri-rotor wind turbine

have been investigated [81], revealing that additional modal coupling occurs between the rotors. This coupling introduces complexities that must be carefully addressed during the conceptual design phase.

Further insights into the modal dynamics of wind turbines have been obtained through investigations into the effects of blade bending-twist coupling [255] and unsteady aerodynamic phenomena, such as dynamic wake and dynamic stall [40, 41]. A comprehensive sensitivity study has identified key modeling parameters that influence aeroelastic stability. Among these, the shear center position aligned parallel to the chord exhibits the highest sensitivity in relation to blade edgewise modal damping [274].

1.2.2 Code-to-code verification

Custom tools have been developed for linearization and modal analysis of multi-bladed wind turbines. Among these, the commercial software Bladed [69] by DNV, the open-source code OpenFAST [194] by NREL, and HAWCStab2 [70] by DTU are widely utilized in the wind energy community. These tools rely on blade element momentum (BEM) theory as the basis for aerodynamic computations, augmented by dynamic wake and dynamic stall models to account for unsteady aerodynamic effects. In Bladed and OpenFAST, aerodynamic forces are linearized using numerical differentiation, while HAWCStab2 employs an analytical derivation to achieve greater accuracy. Multibody system dynamics formulations have been employed in all three codes. In Bladed, the floating frame of reference formulation (FFRF) is used for modeling slender blades. To accurately capture geometric nonlinearity, the blade is typically divided into multiple segments, with each segment represented as a modal superelement. HAWCStab2, on the other hand, applies a corotational formulation to account for large blade deflections and associated geometric nonlinearities. OpenFAST [149, 150] provides two distinct options: a modal superelement representation and geometrically exact beam theory (GEBT). The multi-blade coordinate (MBC) transformation is implemented in all three tools to generate a linear time-invariant (LTI) system. Eigenvalue analysis is then performed to determine modal frequencies, damping ratios, and modal shapes.

Significant nonlinearities in wind turbine dynamics arise from large blade deflections under heavy aerodynamic loads, periodic rotation in three-dimensional space, and unsteady aerodynamic effects. To develop a linear model, some nonlinear terms are simplified or neglected during the linearization process. However, the implementation details of aeroelastic coupling modeling can significantly influence the resulting linear model and, consequently, the predicted modal dynamics. A code-to-code comparison is therefore valuable for verifying linear models and subsequent stability analyses.

As part of the "AdVanced Aerodynamic Tools for lArge Rotors" (AVATAR) project, various numerical models for predicting aeroelastic stability were compared.

Tools such as Bladed, HAWCStab2, BLADEMODE, and GAST were employed to perform stability analyses of the AVATAR reference wind turbine through eigenvalue analyses based on linearized models. Additionally, a periodic autoregressive with exogenous input (PARX) model [37, 224, 223] was identified from time-series data of the system dynamic response simulated using Cp-Lambda. Floquet analysis was subsequently conducted to extract modal frequencies and damping ratios. The comparison showed strong agreement in modal frequency predictions across the tools. While the overall trends in modal damping ratios were consistent, notable discrepancies in their absolute values were observed [63].

A recent comparison of the aeroelastic codes Bladed, HAWCStab2, and OpenFAST was conducted using the IEA 22 MW reference turbine. The steady-state results and time-domain statistics showed overall good agreement across the codes. However, in the linear stability analysis, while the modal frequency predictions were consistent, evident deviations were observed in the aeroelastic damping ratios, particularly for critical modes in the torsional and edgewise directions [55].

Another aeroelastic stability comparison between HAWCStab2 and OpenFAST was performed using a land-based version of the IEA 15 MW turbine model with quasi-steady aerodynamics. While strong agreement was observed in the modal frequency predictions, a noticeable discrepancy in the rotor aeroelastic damping ratios was identified. This discrepancy was attributed to the absence of the tower torsional degree of freedom (DOF) in OpenFAST [34].

The blade edgewise stability was analyzed using HAWC2/HAWCStab2, Bladed, Simpack, and alaska/Wind, and the results were compared [273]. A dynamic mode decomposition (DMD) postprocessing methodology was applied to nonlinear time-domain simulations to extract the modal damping ratios, enabling a direct comparison between stability predictions from linear stability analysis and nonlinear time-domain simulations. The results demonstrated similar trends in modal damping ratios across the operating range, though noticeable discrepancies were observed in the absolute values. A parameter sensitivity analysis was conducted to evaluate the influence of torsional stiffness, edgewise stiffness, principal axis orientation, and the positions of the center of gravity and the shear center along the chord on edgewise stability. The analysis revealed that uncertainty in torsional stiffness had the highest impact on the damping ratio of the critical edgewise mode.

It is evident that modal frequency predictions from various aeroelastic codes generally show good agreement when the model DOFs, modeling parameters, and geometric nonlinearities in blade large deflections are appropriately accounted for. In contrast, achieving consistent quantitative values for aeroelastic damping ratios remains a significant challenge, particularly for the less damped edgewise modes.

1.2.3 Code-to-measurement validation

It is difficult to reproduce blade aeroelastic instability in scaled experimental blades and wind turbines because of the conflicts in the scaling similarity principles for aerodynamics and structural dynamics. However, experimental validation on full-size wind turbines is feasible under careful and controlled testing conditions.

A field validation of the stability limit was conducted on the SWT-7.0-154 prototype wind turbine [151]. The experiment was carried out at low free wind speeds, with the blades fixed at a fine pitch and the generator operating at zero power production. The rotor speed was gradually increased until it exceeded the estimated stability limit by approximately 7 %. The Siemens Wind Power (SWP) in-house aeroelastic code, BHawC, was utilized to perform time-domain dynamic simulations and predict the stability limit. Two phenomena were identified from the spectrum of the blade edgewise moment in both simulations and experiments: a resonance of the blade first edgewise mode at the critical rotor speed and a flutter-like edgewise instability associated with the blade second edgewise mode above the critical rotor speed. The predicted stability limit was found to be within 5 % of the experimentally observed value.

Additional test data was collected on a second SWT-7.0-154 prototype turbine on December 5, 2018 [278]. The aeroelastic damping ratios of the blade first and second edgewise modes were identified using logarithmic decrement damping fits applied to band-pass filtered signals of the measured edgewise moments. A modal analysis of the isolated blade was performed in HAWCStab2 to compute the aeroelastic damping ratios of the first and second edgewise modes across various rotor speeds. The aeroelastic damping ratios were plotted as functions of rotor speed for the results obtained from both numerical analysis and experimental identification. Excellent agreement on the crossing points was observed.

Based on the findings from the two field experiments [151, 278], it was concluded that the critical rotor speed for blade edgewise instability can be accurately predicted through time-domain nonlinear simulations and eigenvalue-based stability analyses.

1.3 Key challenges in aeroelastic stability

With the continuous increase in blade length and flexibility, aeroelastic instability has become one of the primary design constraints for modern wind turbines. The key challenges in the engineering practice of pitch-regulated, variable-speed wind turbines can be classified as follows [116, 272]:

1. Resonance;

2. Blade edgewise instability in normal operational conditions;

3. Blade stall-induced vibrations (SIV) in standstill conditions;

4. Blade and tower vortex-induced vibrations (VIV);

5. Classical flutter.

1.3.1 Resonance

Resonance is a primary challenge in the field of aeroelastic stability. It can be readily identified using a Campbell diagram, which plots the aeroelastic modal frequencies across the operating wind speed range alongside the harmonic excitation frequencies determined by the rotor speed. Potential resonances are indicated by the intersection points between these excitation frequencies and modal frequencies [43]. Large wind turbines are particularly vulnerable to resonance due to their increased structural flexibility, which leads to a denser distribution of modal frequencies on the Campbell diagram and, consequently, a greater risk of resonance.

For three-bladed rotor turbines, particular attention must be given to harmonic excitation frequencies resolved in the ground-fixed frame, including 1P, 3P, 6P, 9P (where nP $= n/$rev), and higher orders. The primary source of periodic excitation arises from aerodynamic forces induced by turbulence. Other significant sources of disturbances include gravitational forces acting on the blades, tower shadow effects, wind shear, wind inflow inclination, yaw misalignment, rotor mass imbalance, and aerodynamic imbalances among the blades. In wind farms, rotor wakes from upstream turbines can further influence the aerodynamics of downstream turbines, introducing additional periodic excitations.

Pitch angles influence resonance by altering the aeroelastic modal characteristics. Low turbulence intensity allows a longer time period for resonance to develop, as the rotor speed remains relatively stable. In contrast, high turbulence intensity reduces the likelihood of strong resonance by causing more rapid fluctuations in rotor speed [267].

In general, resonance with rotor flapwise modes is not a major concern due to their high damping. However, resonant points at the cut-in rotor speed and the rated rotor speed should be avoided, as rotor speed tends to remain stable under generator torque and pitch regulation. For operating points between these speeds, resonance may be acceptable, as the rotor speed typically passes through the resonant point quickly in turbulent wind inflow. If resonance generates excessive fatigue loads, a control algorithm can be implemented to accelerate the passage through the resonant point.

Resonance between 1P, 3P and the tower first side–side mode, as well as between 6P and the tower second side–side mode, should be avoided at stable rotor speeds due to the low damping of the tower side–side modes. Similarly, resonance between 3P and the rotor first edgewise modes, as well as between 6P and the

rotor second edgewise modes, should also be avoided in constant rotor speed operating conditions. The assessment should account for backward whirling, forward whirling, and collective modes. When resonance involving rotor collective modes is unavoidable during the system design phase, rotor vibrations can be mitigated by introducing a drivetrain damper through generator torque regulation. However, mitigating resonance associated with rotor backward and forward whirling modes poses greater challenges, as it is significantly more difficult to resolve using control strategies.

A real case of resonant vibration between 3P and the rotor edgewise backward whirling mode on a 4.8 MW commercial turbine was studied [268]. The investigation highlighted the critical importance of an accurate aeroelastic model for reproducing resonance in numerical simulations. In particular, precise modeling of the yaw system's torsional stiffness was shown to be essential. Increasing the yaw stiffness can reduce blade resonant vibrations by suppressing the whirling motion of the rotor center. To ensure sufficient accuracy in numerical simulations, it is recommended to include the flexibility of drivetrain bending and torsion, mainframe nodding, and foundation fore-aft and side–side bending in the simulation model.

1.3.2 Blade edgewise instability in normal operations

Blade edgewise instability in normal operational conditions was a major design constraint for stall-regulated wind turbines around the turn of the century [229, 118]. This issue was effectively addressed by transitioning to pitch-regulated, variable-speed turbines. However, based on the author's experience in the wind industry, the risk of blade edgewise instability re-emerges as blade lengths approach 100 m or more. Both the blade first and second edgewise modes become relevant for aeroelastic instability, particularly at wind speeds above rated, where the rotor speed remains relatively constant. As it occurs in normal power production, blade edgewise instability poses a considerable threat to the structural integrity of modern wind turbines.

As discussed in Section 1.2.1, blade edgewise stability can be analyzed using the eigenvalue approach based on linearized aeroelastic coupling models. However, as noted in Section 1.2.2, damping ratios obtained from different aeroelastic stability analysis tools often show inconsistencies. While the stability limit predicted by these tools has been validated through field experiments, as outlined in Section 1.2.3, the observed blade edgewise instability occurred under fixed pitch and zero power production conditions at low wind speeds. This phenomenon, referred to as flutter-like instability, involves aerodynamic loads and blade deflections that are expected to differ significantly from those associated with blade edgewise instability in normal operational conditions. Given the substantial uncertainties in predicting aeroelastic damping ratios of blade edgewise modes using the eigenvalue

approach, time-domain nonlinear dynamic simulations are regarded as a more reliable alternative. However, this method is computationally expensive and therefore not suitable for extensive iterations within automatic optimization frameworks.

When the blade first or second edgewise mode exhibits negative damping, several strategies can be employed to mitigate blade edgewise vibrations. These strategies include increasing the blade torsional stiffness, adjusting the flapwise-to-edgewise stiffness ratio to add more out-of-plane motion, tuning the shear center position, incorporating a presweep design, or reducing the rotor speed [115, 274].

1.3.3 Stall induced vibration in standstill

In storm conditions, grid faults may deactivate the pitch and yaw systems of wind turbines. Similarly, when turbines are erected but awaiting commissioning, or are parked for maintenance, they are unable to respond to varying wind conditions. In such scenarios, when the wind inflow comes from skewed directions, the blades may experience moderate stall, characterized by an angle of attack (AOA) within the range $\alpha \in [15\,^\circ, 40\,^\circ]$. Negative aerodynamic damping arises due to the negative slope ($\partial C_L/\partial\alpha$) of the airfoil $C_L - \alpha$ curve, where C_L is the lift coefficient [281, 280]. This negative damping causes rapid growth in blade oscillations at the first edgewise mode, a phenomenon known as stall-induced vibration (SIV) in standstill. Standstill conditions can be categorized into two cases: parked, where the rotor is locked, and idling, where the rotor is free to rotate very slowly. Blade SIV can lead to significant fatigue damage within a short period and may also challenge the ultimate strength of the blades at very high wind speeds.

The risk of blade SIV across a yaw misalignment range of $[-180\,^\circ, 180\,^\circ]$ can be evaluated using eigenvalue analyses [30, 215, 253, 187] or time-domain dynamic simulations [228, 171, 8]. The most critical yaw misalignment angle is approximately 30°, where the wind comes from the right front direction relative to the rotor [281].

The dynamic stall effect provides additional damping that can help mitigate blade SIV and is therefore crucial for a reliable assessment of SIV. However, different dynamic stall models can produce significantly different amplitudes of SIV [8]. Proper implementation of a dynamic stall model is essential for achieving accurate dynamic simulations of blade SIV. Despite its importance, evident discrepancies between experimental results and simulations have been observed across various dynamic stall models, with none of them demonstrating consistently better agreement than the others [130].

When the flow around an airfoil is fully separated, significant uncertainties arise in aeroelastic engineering modeling. For instance, airfoil polars beyond stall points are often inaccurate, and unsteady aerodynamic models remain poorly calibrated due to insufficient experimental data [253]. Consequently, the load amplitude of

blade SIV cannot be quantitatively determined solely through numerical simulations using current engineering models. In engineering practice, system design modifications may provide more practical solutions for mitigating the risk of blade SIV. Examples include using a backup power supply to temporarily activate the yaw system and move the turbine out of dangerous yaw misalignment angles, or installing fishnets on the blades to alter airfoil characteristics and suppress negative aerodynamic damping.

1.3.4 Vortex induced vibration

When fluid flows around a cylindrical structure, vortex shedding occurs at a characteristic frequency, generating periodic excitation on the structure. If this shedding frequency approaches the natural frequency of the structure, resonance may develop due to the interaction between fluid-induced excitation and the structural mode, leading to substantial vibrations. This phenomenon, known as vortex-induced vibration (VIV), can affect wind turbine blades and towers, and therefore must be carefully addressed.

In standstill conditions, when the wind comes from a yaw misalignment angle of approximately $\pm 90°$, vortices may shed from the blade tip toward the root at specific inclination angles—defined as the relative angle between the freestream velocity and the blade pitch axis—leading to blade vortex-induced vibrations (VIV) [122]. Blade VIV is a highly three-dimensional fluid-structure interaction (FSI) phenomenon, which renders standard engineering models such as BEM theory not applicable. To accurately capture this complex behavior, high-fidelity FSI simulations are required [122, 134, 132, 100, 133, 99], whether for a rigid or flexible isolated blade or in the context of a full rotor system [213].

The freestream wind speed and the inflow inclination angle are two critical parameters governing the onset of blade VIV in standstill conditions [134]. Additionally, the blade AOA must be near $\pm 90°$, which corresponds to a yaw misalignment angle of approximately $\pm 90°$ for feather-pitched blades [133]. The amplitude of blade VIV is confined to limit cycles due to aerodynamic nonlinearities [100]. Moreover, these vibrations can potentially be mitigated through the use of trailing-edge flaps [134] or specialized tip geometry designs [132].

Tower VIV can occur during the installation phase, particularly when the tower is erected without the rotor-nacelle assembly or when the rotor has not yet been bolted to the mainshaft [277, 276]. VIV can also arise in full wind turbines with tall tubular towers. The risk of blade VIV is significantly lower compared to tower VIV, as the former requires strict conditions, such as specific yaw misalignment and inflow inclination angles, to be satisfied. In contrast, tower VIV can be triggered by appropriate wind speeds, with wind direction playing a much less critical role.

A semi-empirical engineering framework for VIV analysis, based on modal parameters, has been proposed to facilitate a quick assessment of blade and tower

VIV [180]. However, several key parameters within the framework may require calibration to ensure accurate predictions. Mitigation strategies designed for suppressing blade SIV, such as backup power supply or fishnets, can also be effectively applied for blade VIV. For tower VIV, helical strakes have been identified as a highly efficient and cost-effective solution [156].

1.3.5 Classical flutter

The blade flutter mode, primarily characterized by coupled flapwise and torsional deflections, can exhibit significant negative damping at high rotor speeds, resulting in intense torsional vibrations within a short time frame. Classical flutter is widely recognized as a critical aeroelastic instability in pitch-regulated wind turbines [118] and has been the subject of extensive research over the years.

Classical flutter limits can be evaluated using two primary methods: the eigenvalue approach [111, 117, 168, 169, 118, 220, 203, 121, 98, 299, 153, 79, 54] and time-domain dynamic simulations [214, 212, 295, 53, 105, 164]. Accurate prediction of classical flutter requires incorporating the effects of unsteady shed vorticity and trailed vorticity in the aerodynamic models [168, 118, 212]. In the time-domain approach, a runaway scenario is commonly simulated by allowing the turbine rotor to rotate freely without generator torque, while the three blades are stuck at fixed pitch angles. To avoid excessively rapid rotor acceleration, the wind speed is gradually increased from a low initial value [212, 105].

As reported in the literature [229, 118, 293], there are no recorded cases of classical flutter occurring in operational wind turbines. Additionally, based on the author's experience in the wind energy industry, classical flutter has not yet been a major concern in the design of commercial blades and wind turbines as of December 2024. Classical flutter usually occurs at rotor speeds above rated. In modern wind turbines, when the rotor speed goes above the first threshold beyond the rated value, the control system initiates blade pitching toward feather to stop the turbine. If the rotor speed continues to increase and reaches a second, higher threshold, the safety system is triggered to shut the turbine down completely. The probability of modern wind turbines experiencing simultaneous failures of all three pitch systems and a converter disconnection from the grid is extremely low. Consequently, this fault combination is not considered in standard design load cases [139, 141, 142]. The hypothetical runaway simulation scenario is therefore beyond the scope of all plausible operational conditions during the lifetime of a wind turbine. Given this, the wind energy community may need to reconsider the assessment procedures for classical flutter in modern wind turbines.

1.4 Objectives

Blade edgewise instability in normal operational conditions has been a critical concern in the design and analysis of modern wind turbines. As highlighted in Section 1.3.2, the eigenvalue approach, widely regarded as an efficient and quantitative assessment method, has not yet been consistently verified and validated in terms of key indicators, such as aeroelastic damping ratios. To address this research gap, the following global objectives are established for this thesis:

1. Develop an analytical linearization framework for three-bladed wind turbines, leveraging multibody system dynamics theory. This framework will facilitate a comprehensive investigation of the modal dynamics of wind turbines using the eigenvalue approach.

2. Propose a verification and validation procedure to ensure the accuracy and reliability of the developed linearization and modal analysis framework, with a focus on its application to the aeroelastic stability analysis of modern wind turbines.

3. As a complementary endeavor, develop a modal reduction procedure tailored for rotating subsystems composed of rigid bodies, finite elements, and mechanical joints within the context of multibody system dynamics.

1.5 Outline

In addition to the introductory content presented in **Chapter 1**, a brief outline of the remaining chapters is provided below to guide the reader through the thesis:

Chapter 2 — Flexible multibody system dynamics

An overall presentation of multibody system dynamics theory is provided as the foundation for subsequent developments. Finite rotations in three-dimensional space are parameterized using quaternions, enabling a robust representation of rotational motion. A generic formulation of algebraic constraints for various types of mechanical joints is established based on quaternion parametrization, accompanied by the derivation of the corresponding Jacobian matrix. A general linearized formulation in the form of Differential-Algebraic Equations (DAEs) is presented for flexible multibody dynamic systems, highlighting the presence of various terms within the system matrices. An advanced Timoshenko beam element model with generic cross-sectional properties, specifically tailored for wind turbine blade modeling, is developed within the framework of the corotational formulation. The Hilber-Hughes-Taylor (HHT) time integration scheme is introduced with particular attention to the incremental update of rotation. Additionally, a static equilibrium

solver accommodating rheonomic constraints is developed to efficiently determine the aeroelastic equilibrium state of rotating rotor systems. Finally, a sparsity-preserving Krylov-Schur eigenvalue solver is implemented to enable modal analysis for large-scale multibody dynamic systems.

Chapter 3 — Linearization

A linearization and modal analysis framework is developed based on the multibody system dynamics theory presented in Chapter 2. A unified analytical expression for the tangent stiffness matrix of holonomic constraints is derived based on the Jacobian matrix parameterized by quaternions, improving the accuracy of eigenvalue analyses for multibody systems with mechanical joints in stressed equilibrium configurations. Steady aerodynamic forces are linearized through numerical differentiation techniques. An analytical framework for the linearization of the structural dynamics of multi-bladed rotor systems is established, resulting in linearized DAEs formulated in an auxiliary mixed basis with respect to the rotor's rotating center. The derivation of the system mass, stiffness, and damping matrices is presented in detail. Finally, the modal analysis in the multi-blade coordinate is conducted using the developed eigenvalue solver, accompanied by a comprehensive interpretation of the modal dynamics of three-bladed wind turbines.

Chapter 4 — Stability analysis

The stability analysis of multi-bladed rotors and wind turbines is conducted. A comprehensive verification and validation framework for the aeroelastic stability assessment of modern wind turbines is proposed. First, the eigenvalues corresponding to a rotor's free rotation mode are examined. The influence of the geometric stiffness matrix, the inertial stiffness matrix, and the tangent stiffness matrix of constraints on the eigenvalues is thoroughly analyzed. Second, the aeroelastic coupling model developed in this study is verified by comparing structural deflections and steady-state aerodynamic predictions against results obtained from the commercial tool Bladed under quasi-static equilibrium conditions. The proposed aeroelastic stability assessment framework is further verified using a series of virtual wind turbine numerical models and validated against measurement data from two prototype wind turbines.

Chapter 5 — Modal reduction

A modal reduction procedure is developed for rotating subsystems composed of rigid bodies, finite elements, and mechanical joints. The modal reduction is carried out using the mode acceleration method, offering greater flexibility in the selection of boundary conditions. The gross motion of the elastic subsystems is decomposed

into rigid-body motion, represented by a floating frame of reference, and elastic deformations, expressed in the local basis of the floating frame. A projection method is derived to facilitate this decomposition efficiently. Analytical expressions for the tangent stiffness and inertial matrices are derived, incorporating geometric nonlinear terms to enhance numerical robustness and accuracy, particularly for large deflections. A procedure for updating the floating frame of reference is also presented. Several numerical experiments are conducted to validate the capacity and accuracy of the developed modal reduction method.

Chapter 6 — Final remarks

A summary of the comprehensive study is presented, highlighting the key findings. Additionally, recommendations for future research are discussed with the potential to further enhance the proposed methodologies.

Chapter 2

Flexible multibody system dynamics

This chapter provides a brief introduction to flexible multibody system dynamics. To prevent potential confusion in the numerous equations that follow, the notation used throughout this thesis is presented first. The chapter then discusses rotation parametrization using quaternions, followed by a concise overview of three-dimensional kinematics. Constraint equations are introduced to model the mechanical joints commonly employed in the assembly of multibody systems. The Jacobian matrix of holonomic constraints is formulated using quaternion parametrization. The generic form of the linearized index-3 Differential-Algebraic Equations (DAEs), based on a Redundant Coordinate Set (RCS), is then presented to illustrate the composition of the system matrices. Special attention is given to the selection of generalized coordinates for rotational degrees of freedom (DOFs). A brief review of beam element modeling and the associated formulations relevant to wind turbine blades is also provided, followed by a detailed description of the corotational Timoshenko beam element model used in this study. Finally, various solvers are introduced, including the time integration scheme, the static equilibrium solver, and the eigenvalue solver. Although not exhaustive, the topics covered in this chapter are closely related to the subsequent discussions on the linearization and modal problems of multi-bladed rotor systems.

2.1 Notation

First, the concepts of time derivative, variation and difference are emphasized:

- $\boldsymbol{q}$, $\dot{\boldsymbol{q}}$, $\ddot{\boldsymbol{q}}$ are the vectors of generalized coordinates (including position and orientation), generalized velocities, and generalized accelerations of the system, respectively. In general, the relationships between them can be expressed as time derivatives: $\dot{\boldsymbol{q}} = \dfrac{\mathrm{d}\boldsymbol{q}}{\mathrm{d}t}$ and $\ddot{\boldsymbol{q}} = \dfrac{\mathrm{d}^2\boldsymbol{q}}{\mathrm{d}t^2}$.

- $\delta(\cdot)$ is the variation of a variable, which is in the sense of infinitesimal increment. For example, $\delta\boldsymbol{q}$, $\delta\dot{\boldsymbol{q}}$, $\delta\ddot{\boldsymbol{q}}$ are the variations of generalized coordinates, velocities and accelerations, respectively. The variation operation is often used in the linearization of equations of motion.

- $\Delta(\cdot)$ is the finite difference of a variable, which is the discretization form of variation, and hence is in the sense of finite increment in time or space. For example, if discretized in time, $\Delta^t\boldsymbol{q} = \boldsymbol{q}^{k+1} - \boldsymbol{q}^k$, $\Delta^t\dot{\boldsymbol{q}} = \dot{\boldsymbol{q}}^{k+1} - \dot{\boldsymbol{q}}^k$, $\Delta^t\ddot{\boldsymbol{q}} = \ddot{\boldsymbol{q}}^{k+1} - \ddot{\boldsymbol{q}}^k$ are the finite increments of generalized coordinates, velocities and accelerations between two time steps k and $k+1$, respectively. Here, k is the time step index, and t^k is the time instant corresponding to the step index k. If the time step size is fixed as h, we have $t^k = kh$. In the Newton–Raphson iteration, we use $\Delta^{\mathrm{NR}}(\cdot)$ to denote the finite increment between two iterative steps n and $n+1$ at time instant t^k, for instance, $\Delta^{\mathrm{NR}}\boldsymbol{q} = \boldsymbol{q}_{n+1}^k - \boldsymbol{q}_n^k$. It is worth noting that, the computation of the difference of finite rotation needs special attention, depending on the choice of rotation parametrization.

To avoid potential confusion in the complex formulas in multibody system dynamics, it is essential to declare the generic notations used in this thesis. The most important and commonly used notations are introduced below.

The position of a point in three–dimensional space can be denoted with $\boldsymbol{r} \in \mathbb{R}^3$. It is often required to resolve the relative position or its time derivatives (e.g., translational velocity, translational acceleration) of one point B with respect to another point A within a reference frame C. The relative position vector describes a translation which brings the point A to another point B. This can be expressed using the subscript as below

$$\boldsymbol{r}_{\mathrm{FROM.TO}_{(\mathrm{BASIS})}}$$

where 'FROM' is the starting point A of the relative position vector $\boldsymbol{r}$, 'TO' is the end point B, and 'BASIS' is a specific reference frame C in which $\boldsymbol{r}$ is resolved.

As shown in Figure 2.1, the relative position vector from point A to point B resolved in the basis of frame C is denoted as $\boldsymbol{r}_{A.B_{(C)}}$.

If the reference frame is the inertial frame W, the 'BASIS' frame can be omitted, leading to a simpler notation $\boldsymbol{r}_{A.B}$. Moreover, if the vector starts from the origin of the inertial frame W, the 'FROM' frame can be omitted altogether, resulting in the simplest notation $\boldsymbol{r}_B$.

The orientation of a frame in three–dimensional space can be expressed using the rotation matrix $\boldsymbol{R} \in \mathsf{SO}(3)$. The relative orientation of 'LOCAL' frame B with respect to 'PARENT' frame A can be denoted using the subscript as below

$$\boldsymbol{R}_{\mathrm{LOCAL}_{(\mathrm{PARENT})}}$$

As shown in Figure 2.2, the rotation matrix $\boldsymbol{R}_{B_{(A)}}$ can be interpreted a rotation process which rotates 'PARENT' frame A to 'LOCAL' frame B. If the rotation

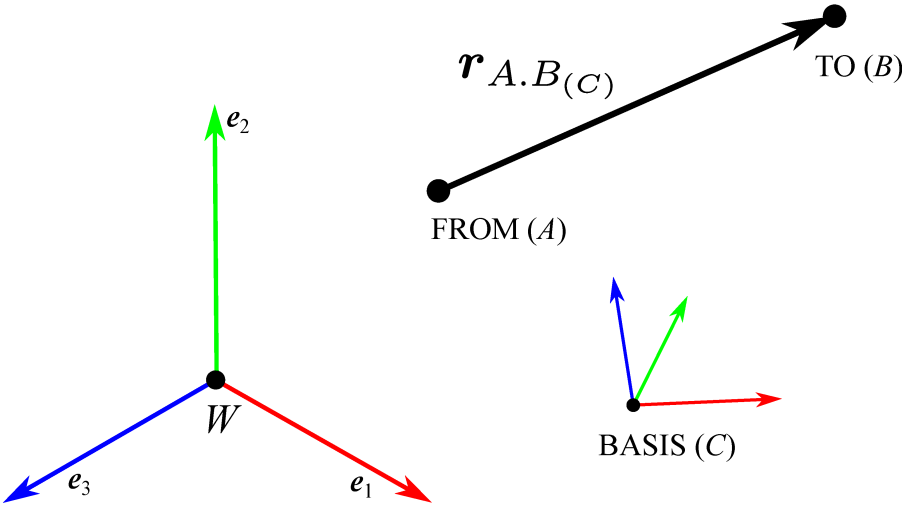

Figure 2.1: Notation of position vector $\boldsymbol{r}_{A.B_{(C)}}$.

starts from the inertial frame W, the 'PARENT' frame can be omitted, resulting in a simplified notation $\boldsymbol{R}_B$.

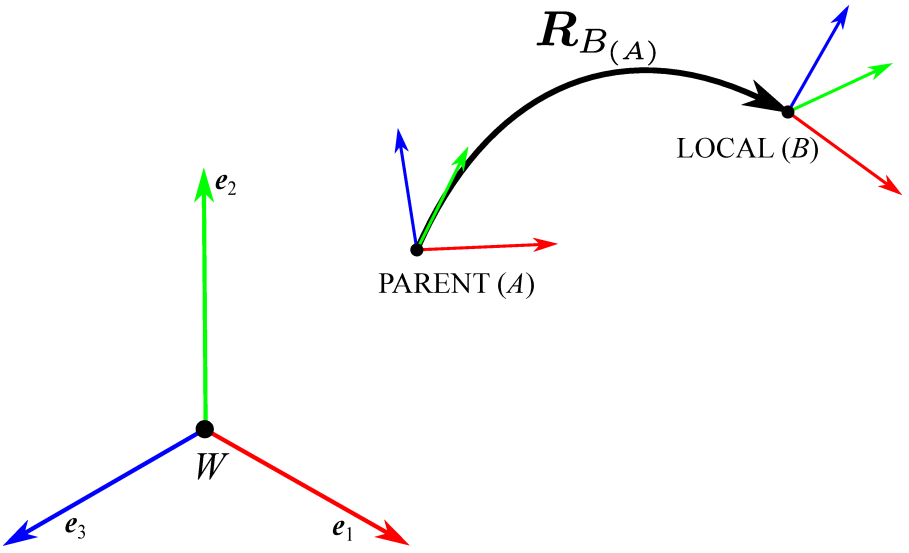

Figure 2.2: Notation of rotation matrix $\boldsymbol{R}_{B_{(A)}}$.

For some rotational vectors, e.g., virtual rotation vectors, angular velocities and their time derivatives, we use the subscript 'l' or 'a' as shorthand symbols for the 'BASIS' frame, where 'l' means the vector is measured in the *local* basis of its associated reference frame, and 'a' represents the measurement in the *absolute* basis of the inertial frame W.

The configuration of a frame A, that is composed of its origin's position vector

$\boldsymbol{r}_A$ and its orientation described by the rotation matrix $\boldsymbol{R}_A$, can be denoted as $\{\boldsymbol{r}_A, \boldsymbol{R}_A\}$.

Some examples are provided below to illustrate the notations:

$\boldsymbol{r}_{A.B_{(C)}}$	Position vector of B with respect to A, in C basis
$\boldsymbol{r}_{A.B}$	Position vector of B with respect to A, in W basis, shorthand for $\boldsymbol{r}_{A.B_{(W)}}$
$\boldsymbol{r}_B$	Position vector of B with respect to the inertial frame W, in W basis, shorthand for $\boldsymbol{r}_{W.B_{(W)}}$ or $\boldsymbol{r}_{W.B}$
$\boldsymbol{R}_{B_{(A)}}$	Rotation matrix of frame B with respect to frame A
$\boldsymbol{R}_B$	Rotation matrix of frame B with respect to the inertial frame W, shorthand for $\boldsymbol{R}_{B_{(W)}}$
$\delta\boldsymbol{\theta}_{a_B}$	Virtual rotation vector of frame B with respect to the inertial frame W, in *absolute* basis, shorthand for $\delta\boldsymbol{\theta}_{W.B_{(W)}}$ or $\delta\boldsymbol{\theta}_{W.B}$
$\delta\boldsymbol{\theta}_{l_B}$	Virtual rotation vector of frame B with respect to the inertial frame W, in *local* basis of frame B, shorthand for $\delta\boldsymbol{\theta}_{W.B_{(B)}}$
$\boldsymbol{\omega}_{a_B}$	Angular velocity of frame B with respect to the inertial frame W, in *absolute* basis, shorthand for $\boldsymbol{\omega}_{W.B_{(W)}}$ or $\boldsymbol{\omega}_{W.B}$
$\boldsymbol{\omega}_{l_B}$	Angular velocity of frame B with respect to the inertial frame W, in *local* basis of frame B, shorthand for $\boldsymbol{\omega}_{W.B_{(B)}}$

2.2 Properties of skew–symmetric matrix

Throughout this thesis, several useful properties of skew–symmetric matrices are extensively used in the derivations. For convenience, these properties are listed below.

Assuming two arbitrary vectors $\boldsymbol{a}, \boldsymbol{b} \in \mathbb{R}^3$ and a rotation tensor $\boldsymbol{R} \in \mathsf{SO}(3)$, one has the following properties

$$\widetilde{\boldsymbol{a}}^T = -\widetilde{\boldsymbol{a}} \tag{2.1a}$$

$$\widetilde{\boldsymbol{a}+\boldsymbol{b}} = \widetilde{\boldsymbol{a}} + \widetilde{\boldsymbol{b}} \tag{2.1b}$$

$$\widetilde{\boldsymbol{a}}\boldsymbol{b} = -\widetilde{\boldsymbol{b}}\boldsymbol{a} \tag{2.1c}$$

$$\widetilde{\widetilde{\boldsymbol{a}}\boldsymbol{b}} = \widetilde{\boldsymbol{a}}\widetilde{\boldsymbol{b}} - \widetilde{\boldsymbol{b}}\widetilde{\boldsymbol{a}} \tag{2.1d}$$

$$\widetilde{\boldsymbol{R}\boldsymbol{a}} = \boldsymbol{R}\widetilde{\boldsymbol{a}}\boldsymbol{R}^T \tag{2.1e}$$

$$\dot{\widetilde{\boldsymbol{a}}} = \widetilde{\dot{\boldsymbol{a}}} \tag{2.1f}$$

$$\delta\widetilde{\boldsymbol{a}} = \widetilde{\delta\boldsymbol{a}} \tag{2.1g}$$

For a unit–length vector $\boldsymbol{n} \in \mathbb{R}^3$, the following properties hold

$$\boldsymbol{n}\boldsymbol{n}^T = \boldsymbol{I} + \tilde{\boldsymbol{n}}\tilde{\boldsymbol{n}} \tag{2.2a}$$
$$\tilde{\boldsymbol{n}}\tilde{\boldsymbol{n}}\tilde{\boldsymbol{n}} = -\tilde{\boldsymbol{n}} \tag{2.2b}$$
$$\tilde{\boldsymbol{n}}\dot{\tilde{\boldsymbol{n}}}\tilde{\boldsymbol{n}} = \boldsymbol{0} \tag{2.2c}$$

2.3 Rotation

In three–dimensional space, the orientation of frame A with respect to the inertial frame W can be expressed using a rotation matrix $\boldsymbol{R}_A \in \mathbb{R}^{3\times3}$. The three columns of the rotation matrix $\boldsymbol{R}_A$ are the unit–length vectors of the frame axes: $\boldsymbol{R}_A = [\boldsymbol{e}_{1A}, \boldsymbol{e}_{2A}, \boldsymbol{e}_{3A}]$. The rotation matrix $\boldsymbol{R}_A$ describes a finite rotation of magnitude ϕ about a unit–length axis $\boldsymbol{n} \in \mathbb{R}^3$, which is denoted as a rotation pseudovector $\boldsymbol{\phi} = \phi\boldsymbol{n}$, as illustrated in Figure 2.3.

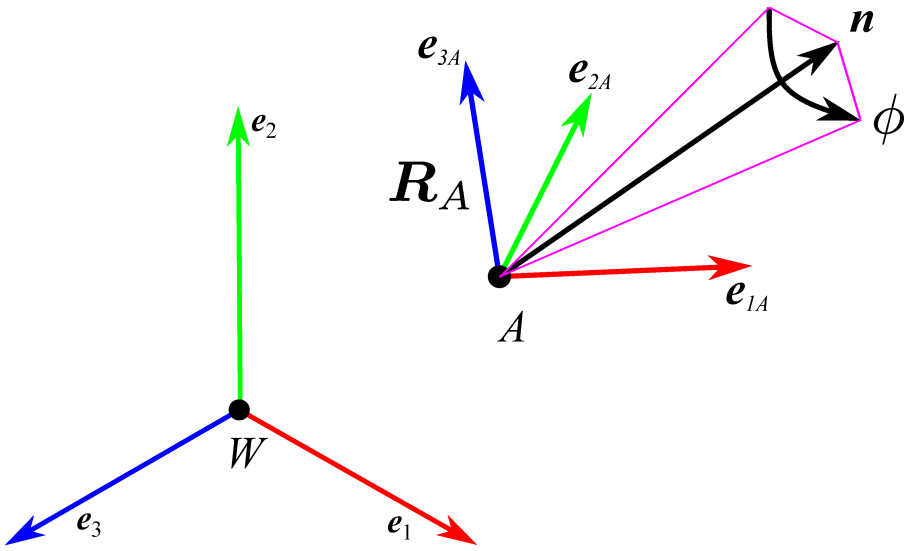

Figure 2.3: The orientation of frame A in three–dimensional space expressed with the rotation matrix $\boldsymbol{R}_A$.

2.3.1 Tangent operators

The rotation matrix can be computed using the rotation pseudovector via the following *Rodrigues' rotation formula*

$$\boldsymbol{R}(\boldsymbol{\phi}) = \boldsymbol{I} + \sin\phi\tilde{\boldsymbol{n}} + (1 - \cos\phi)\,\tilde{\boldsymbol{n}}\tilde{\boldsymbol{n}} \tag{2.3}$$

Remembering (2.1a), the transpose of the rotation matrix is read as

$$\boldsymbol{R}^T = \boldsymbol{I} - \sin\phi\widetilde{\boldsymbol{n}} + (1-\cos\phi)\,\widetilde{\boldsymbol{n}}\widetilde{\boldsymbol{n}} \tag{2.4}$$

There is an interesting property $\boldsymbol{R}\boldsymbol{\phi} = \boldsymbol{R}^T\boldsymbol{\phi} = \boldsymbol{\phi}$, that means $\boldsymbol{\phi}$ is the eigenvector of the rotation matrices $\boldsymbol{R}$ and $\boldsymbol{R}^T$.

Applying time derivative on (2.3), yields

$$\dot{\boldsymbol{R}} = (\cos\phi)\dot{\phi}\widetilde{\boldsymbol{n}} + (\sin\phi)\dot{\widetilde{\boldsymbol{n}}} + (\sin\phi)\dot{\phi}\widetilde{\boldsymbol{n}}\widetilde{\boldsymbol{n}} + (1-\cos\phi)\left(\dot{\widetilde{\boldsymbol{n}}}\widetilde{\boldsymbol{n}} + \widetilde{\boldsymbol{n}}\dot{\widetilde{\boldsymbol{n}}}\right) \tag{2.5}$$

The angular velocities of the frame A in the absolute and local basis of the inertial frame W are defined in the form of skew–symmetric matrix, respectively, as

$$\widetilde{\boldsymbol{\omega}}_a := \dot{\boldsymbol{R}}\boldsymbol{R}^T \qquad \Rightarrow \qquad \dot{\boldsymbol{R}} = \widetilde{\boldsymbol{\omega}}_a\boldsymbol{R} \tag{2.6a}$$

$$\widetilde{\boldsymbol{\omega}}_l := \boldsymbol{R}^T\dot{\boldsymbol{R}} \qquad \Rightarrow \qquad \dot{\boldsymbol{R}} = \boldsymbol{R}\widetilde{\boldsymbol{\omega}}_l \tag{2.6b}$$

By comparing the equalities in (2.6) and employing the property (2.1e), it can be easily verified that

$$\boldsymbol{\omega}_a = \boldsymbol{R}\boldsymbol{\omega}_l \tag{2.7}$$

Substituting (2.4) and (2.5) into (2.6a), and remembering the properties (2.2b), (2.2c), one obtains

$$\widetilde{\boldsymbol{\omega}}_a = \dot{\phi}\widetilde{\boldsymbol{n}} + \sin\phi\dot{\widetilde{\boldsymbol{n}}} + (1-\cos\phi)\,\widetilde{\widetilde{\boldsymbol{n}}\dot{\boldsymbol{n}}} \tag{2.8}$$

Extracting the axial vector from the skew–symmetric matrix in (2.8), the angular velocity in the absolute basis can be expressed using the rotation angle-axis as

$$\boldsymbol{\omega}_a = \dot{\phi}\boldsymbol{n} + \sin\phi\dot{\boldsymbol{n}} + (1-\cos\phi)\,\widetilde{\boldsymbol{n}}\dot{\boldsymbol{n}} \tag{2.9}$$

Remembering (2.4) and (2.9), the angular velocity in the local basis can be derived as

$$\begin{aligned}\boldsymbol{\omega}_l &= \boldsymbol{R}^T\boldsymbol{\omega}_a \\ &= \dot{\phi}\boldsymbol{n} + \sin\phi\dot{\boldsymbol{n}} - (1-\cos\phi)\,\widetilde{\boldsymbol{n}}\dot{\boldsymbol{n}}\end{aligned} \tag{2.10}$$

Applying time derivative on the rotation pseudovector $\boldsymbol{\phi}$, one obtains

$$\dot{\boldsymbol{\phi}} = \dot{\phi}\boldsymbol{n} + \phi\dot{\boldsymbol{n}} \tag{2.11}$$

Recalling $\boldsymbol{n}$ is a unit–length vector, the properties $\boldsymbol{n}^T\boldsymbol{n} = 1$ and $\boldsymbol{n}^T\dot{\boldsymbol{n}} = 0$ can be easily verified. Employing (2.11) in conjunction with the two properties, the time derivatives of ϕ and $\boldsymbol{n}$ can be expressed as

$$\dot{\phi} = \boldsymbol{n}^T\dot{\boldsymbol{\phi}} \tag{2.12a}$$

$$\dot{\boldsymbol{n}} = \frac{1}{\phi}\left(\boldsymbol{I} - \boldsymbol{n}\boldsymbol{n}^T\right)\dot{\boldsymbol{\phi}} \tag{2.12b}$$

Substituting (2.12a) and (2.12b) into (2.9) and (2.10), and remembering the property (2.2a), the angular velocities can be expressed using the rotation pseudovector as

$$\boldsymbol{\omega}_a = \boldsymbol{G}_a(\boldsymbol{\phi})\,\dot{\boldsymbol{\phi}} \tag{2.13a}$$

$$\boldsymbol{\omega}_l = \boldsymbol{G}_l(\boldsymbol{\phi})\,\dot{\boldsymbol{\phi}} \tag{2.13b}$$

where the two tangent operators are

$$\boldsymbol{G}_a(\boldsymbol{\phi}) = \boldsymbol{I} + \frac{1-\cos\phi}{\phi^2}\widetilde{\boldsymbol{\phi}} + \frac{\phi-\sin\phi}{\phi^3}\widetilde{\boldsymbol{\phi}}\widetilde{\boldsymbol{\phi}} \tag{2.14a}$$

$$\boldsymbol{G}_l(\boldsymbol{\phi}) = \boldsymbol{I} - \frac{1-\cos\phi}{\phi^2}\widetilde{\boldsymbol{\phi}} + \frac{\phi-\sin\phi}{\phi^3}\widetilde{\boldsymbol{\phi}}\widetilde{\boldsymbol{\phi}} \tag{2.14b}$$

Due to the independence between ϕ and $\boldsymbol{n}$, in general we cannot integrate the angular velocities $\boldsymbol{\omega}_a$, $\boldsymbol{\omega}_l$ in (2.9) and (2.10) to obtain consecutive three–dimensional finite rotations. The angular velocities $\boldsymbol{\omega}_a$, $\boldsymbol{\omega}_l$ are nonholonomic vectors [11].

Similar to the definitions of angular velocities in (2.6a) and (2.6b), virtual rotation vectors in the absolute and local basis are introduced as

$$\widetilde{\delta\boldsymbol{\theta}}_a := \delta\boldsymbol{R}\boldsymbol{R}^T \qquad \Rightarrow \qquad \delta\boldsymbol{R} = \widetilde{\delta\boldsymbol{\theta}}_a\boldsymbol{R} \tag{2.15a}$$

$$\widetilde{\delta\boldsymbol{\theta}}_l := \boldsymbol{R}^T\delta\boldsymbol{R} \qquad \Rightarrow \qquad \delta\boldsymbol{R} = \boldsymbol{R}\widetilde{\delta\boldsymbol{\theta}}_l \tag{2.15b}$$

By comparing the equalities in (2.15) and employing the property (2.1e), it can be easily verified that

$$\delta\boldsymbol{\theta}_a = \boldsymbol{R}\delta\boldsymbol{\theta}_l \tag{2.16}$$

In general, $\delta\boldsymbol{\theta}$ is not the variation of a Euclidean vector $\boldsymbol{\theta}$. Similar to angular velocity $\boldsymbol{\omega}$, there is no way to obtain a finite $\boldsymbol{\theta}$ by directly integrating the vector $\delta\boldsymbol{\theta}$. The vector $\delta\boldsymbol{\theta}$ is also nonholonomic.

Thanks to the similarity between the computations of time derivative and variation, one can deduce

$$\delta\boldsymbol{\theta}_a = \boldsymbol{G}_a(\boldsymbol{\phi})\,\delta\boldsymbol{\phi} \tag{2.17a}$$

$$\delta\boldsymbol{\theta}_l = \boldsymbol{G}_l(\boldsymbol{\phi})\,\delta\boldsymbol{\phi} \tag{2.17b}$$

The tangent operators $\boldsymbol{G}_a(\boldsymbol{\phi})$ and $\boldsymbol{G}_l(\boldsymbol{\phi})$ are functions of the rotation pseudovector $\boldsymbol{\phi}$ of the investigated frame A in Figure 2.3. $\boldsymbol{\phi}$ can be arbitrarily large, which may result in the matrices $\boldsymbol{G}_a(\boldsymbol{\phi})$, $\boldsymbol{G}_l(\boldsymbol{\phi})$ differing significantly from the identity matrix.

Note, differently from $\boldsymbol{\omega}_a$, $\boldsymbol{\omega}_l$ and $\delta\boldsymbol{\theta}_a$, $\delta\boldsymbol{\theta}_l$, we do not have the distinction for the rotation pseudovector in the absolute basis $\boldsymbol{\phi}_a$ or in the local basis $\boldsymbol{\phi}_l$ because

we do not distinguish the absolute rotation matrix $\boldsymbol{R}_a$ or the local rotation matrix $\boldsymbol{R}_l$ for a frame.

If the rotation pseudovector $\boldsymbol{\phi}$ is small, the tangent operators can be linearized with a first-order approximation as

$$\boldsymbol{G}_a(\boldsymbol{\phi}) \approx \boldsymbol{I} + \frac{1}{2}\widetilde{\boldsymbol{\phi}} \tag{2.18a}$$

$$\boldsymbol{G}_l(\boldsymbol{\phi}) \approx \boldsymbol{I} - \frac{1}{2}\widetilde{\boldsymbol{\phi}} \tag{2.18b}$$

2.3.2 Rotation parametrization via quaternions

Quaternions are often used for the parametrization of finite rotations because they do not exhibit numerical singularities. Although the definitions and various properties of quaternions have been comprehensively introduced in the literature (e.g., [21, 131, 160]), several relevant properties used in the thesis are revisited in this section.

The four components of a unit quaternion $\boldsymbol{\rho} = [\rho_0, \rho_1, \rho_2, \rho_3]^T$ can be interpreted as the elements of *Euler parameters* [11]

$$\begin{aligned} \rho_0 &= \cos(\phi/2) & \rho_1 &= n_x \sin(\phi/2) \\ \rho_2 &= n_y \sin(\phi/2) & \rho_3 &= n_z \sin(\phi/2) \end{aligned} \tag{2.19}$$

which describe a finite rotation about the spinning axis $\boldsymbol{n} = [n_x, n_y, n_z]^T$ by the angle ϕ. The vector $\boldsymbol{\phi} = \phi\boldsymbol{n}$ is the corresponding rotation pseudovector.

From (2.19), it is easy to see that the norm of a unit quaternion is equal to one

$$\|\boldsymbol{\rho}\| = \sqrt{\rho_0^2 + \rho_1^2 + \rho_2^2 + \rho_3^2} = 1 \tag{2.20}$$

A unit quaternion can also be denoted as $\boldsymbol{\rho} = (s, \boldsymbol{v})$, where $s = \rho_0$ is the scalar part, and $\boldsymbol{v} = [\rho_1, \rho_2, \rho_3]^T$ is the vectorial part. The rotation pseudovector $\boldsymbol{\phi}$ can be computed from the quaternion $\boldsymbol{\rho}$ as

$$\boldsymbol{\phi} = 2\frac{\boldsymbol{v}}{\|\boldsymbol{v}\|}\tan^{-1}\left(\frac{\|\boldsymbol{v}\|}{s}\right) \tag{2.21}$$

The addition and multiplication for two quaternions can be expressed in a compact form

$$\boldsymbol{\rho}_a \pm \boldsymbol{\rho}_b = (s_a \pm s_b, \boldsymbol{v}_a \pm \boldsymbol{v}_b) \tag{2.22a}$$

$$\boldsymbol{\rho}_a\boldsymbol{\rho}_b = (s_a s_b - \boldsymbol{v}_a \cdot \boldsymbol{v}_b, s_a\boldsymbol{v}_b + s_b\boldsymbol{v}_a + \boldsymbol{v}_a \times \boldsymbol{v}_b) \tag{2.22b}$$

where $(\cdot)$ is the dot product of two vectors, and $(\times)$ is the cross product of two vectors.

The variation of the identity quaternion $\boldsymbol{\rho}_I = [1, 0, 0, 0]^T$ is equal to the zero quaternion $\boldsymbol{\rho}_0 = [0, 0, 0, 0]^T$, leading to

$$\begin{aligned} \delta\boldsymbol{\rho}_I = \delta\left(\boldsymbol{\rho}\boldsymbol{\rho}^*\right) = \delta\left(\boldsymbol{\rho}^*\boldsymbol{\rho}\right) = \boldsymbol{\rho}_0 \\ \Rightarrow \delta\boldsymbol{\rho}\boldsymbol{\rho}^* + \boldsymbol{\rho}\delta\boldsymbol{\rho}^* = \delta\boldsymbol{\rho}^*\boldsymbol{\rho} + \boldsymbol{\rho}^*\delta\boldsymbol{\rho} = \boldsymbol{\rho}_0 \end{aligned} \tag{2.23}$$

where $\boldsymbol{\rho}^*$ denotes quaternion conjugate.

The unit quaternion $\boldsymbol{\rho}$ can be used to operate a rotation transformation of a vector $\boldsymbol{x}$ in the three–dimensional space via expanding $\boldsymbol{x}$ to a pure quaternion $\boldsymbol{\rho}_\odot = (0, \boldsymbol{x})$

$$(0, \boldsymbol{x}_a) = \boldsymbol{\rho}\,(0, \boldsymbol{x}_l)\,\boldsymbol{\rho}^* \tag{2.24}$$

where $\boldsymbol{x}_l$, $\boldsymbol{x}_a$ are the vectors expressed in the local and inertial frames, respectively.

Alternatively, the rotation transformation (2.24) can be performed via a rotation matrix

$$\boldsymbol{x}_a = \boldsymbol{R}\boldsymbol{x}_l \tag{2.25}$$

where the rotation matrix $\boldsymbol{R}$ can be computed from its corresponding quaternion $\boldsymbol{\rho}$ as

$$\boldsymbol{R}(\boldsymbol{\rho}) = \begin{bmatrix} \rho_0^2 + \rho_1^2 - \rho_2^2 - \rho_3^2 & 2(\rho_1\rho_2 - \rho_3\rho_0) & 2(\rho_1\rho_3 + \rho_2\rho_0) \\ 2(\rho_1\rho_2 + \rho_3\rho_0) & \rho_0^2 - \rho_1^2 + \rho_2^2 - \rho_3^2 & 2(-\rho_1\rho_0 + \rho_2\rho_3) \\ 2(\rho_1\rho_3 - \rho_2\rho_0) & 2(\rho_1\rho_0 + \rho_2\rho_3) & \rho_0^2 - \rho_1^2 - \rho_2^2 + \rho_3^2 \end{bmatrix} \tag{2.26}$$

The rotation matrix $\boldsymbol{R}(\boldsymbol{\rho})$ can be also recast as a product of two auxiliary matrices $\boldsymbol{F}(\boldsymbol{q})_\oplus$ and $\boldsymbol{F}(\boldsymbol{q})_\ominus$ as

$$\boldsymbol{R}(\boldsymbol{\rho}) = \boldsymbol{F}(\boldsymbol{\rho})_\oplus \boldsymbol{F}(\boldsymbol{\rho})_\ominus{}^T \tag{2.27a}$$

$$\boldsymbol{F}(\boldsymbol{\rho})_\oplus = \begin{bmatrix} +\rho_1 & +\rho_0 & -\rho_3 & +\rho_2 \\ +\rho_2 & +\rho_3 & +\rho_0 & -\rho_1 \\ +\rho_3 & -\rho_2 & +\rho_1 & +\rho_0 \end{bmatrix} \tag{2.27b}$$

$$\boldsymbol{F}(\boldsymbol{\rho})_\ominus = \begin{bmatrix} +\rho_1 & +\rho_0 & +\rho_3 & -\rho_2 \\ +\rho_2 & -\rho_3 & +\rho_0 & +\rho_1 \\ +\rho_3 & +\rho_2 & -\rho_1 & +\rho_0 \end{bmatrix} \tag{2.27c}$$

These two auxiliary matrices have the following properties, that hold only for the unit quaternion $\boldsymbol{\rho}$

$$\boldsymbol{F}(\boldsymbol{\rho})_\oplus \boldsymbol{F}(\boldsymbol{\rho})_\oplus{}^T = \boldsymbol{F}(\boldsymbol{\rho})_\ominus \boldsymbol{F}(\boldsymbol{\rho})_\ominus{}^T = \boldsymbol{I} \tag{2.28a}$$

$$\boldsymbol{F}(\boldsymbol{\rho})_\oplus{}^T \boldsymbol{F}(\boldsymbol{\rho})_\oplus = \boldsymbol{F}(\boldsymbol{\rho})_\ominus{}^T \boldsymbol{F}(\boldsymbol{\rho})_\ominus = (\boldsymbol{I} - \boldsymbol{\rho}^*\boldsymbol{\rho}^{*T}) \tag{2.28b}$$

Applying variation on (2.24) and employing the chain rule, yields

$$(0, \delta \boldsymbol{x}_a) = \delta \boldsymbol{\rho}(0, \boldsymbol{x}_l)\boldsymbol{\rho}^* + \boldsymbol{\rho}(0, \boldsymbol{x}_l)\delta\boldsymbol{\rho}^* + \boldsymbol{\rho}(0, \delta\boldsymbol{x}_l)\boldsymbol{\rho}^* \tag{2.29}$$

Applying variation on (2.25) and remembering the equality (2.15b), yields

$$\delta \boldsymbol{x}_a = \delta \boldsymbol{R}\boldsymbol{x}_l + \boldsymbol{R}\delta\boldsymbol{x}_l = \boldsymbol{R}\widetilde{\delta\boldsymbol{\theta}}_l\boldsymbol{x}_l + \boldsymbol{R}\delta\boldsymbol{x}_l \tag{2.30}$$

Expanding (2.30) to the notation of pure quaternions, and remembering the equivalent rotation transformation via the quaternion in (2.24) and the rotation matrix in (2.25), one obtains

$$(0, \delta \boldsymbol{x}_a) = \boldsymbol{\rho}\left(0, \widetilde{\delta\boldsymbol{\theta}}_l\boldsymbol{x}_l\right)\boldsymbol{\rho}^* + \boldsymbol{\rho}\,(0, \delta\boldsymbol{x}_l)\,\boldsymbol{\rho}^* \tag{2.31}$$

By comparing (2.31) and (2.29), one obtains

$$\boldsymbol{\rho}\left(0, \widetilde{\delta\boldsymbol{\theta}}_l\boldsymbol{x}_l\right)\boldsymbol{\rho}^* = \delta\boldsymbol{\rho}\,(0, \boldsymbol{x}_l)\,\boldsymbol{\rho}^* + \boldsymbol{\rho}\,(0, \boldsymbol{x}_l)\,\delta\boldsymbol{\rho}^* \tag{2.32}$$

By left and right multiplying $\boldsymbol{\rho}^*$ and $\boldsymbol{\rho}$ on (2.32), respectively, and making use of the property (2.23), one obtains

$$\left(0, \widetilde{\delta\boldsymbol{\theta}}_l\boldsymbol{x}_l\right) = \boldsymbol{\rho}^*\delta\boldsymbol{\rho}\,(0, \boldsymbol{x}_l) - (0, \boldsymbol{x}_l)\,\boldsymbol{\rho}^*\delta\boldsymbol{\rho} \tag{2.33}$$

Observing that the sum of $\boldsymbol{\rho}^*\delta\boldsymbol{\rho}$ and its conjugate is $\boldsymbol{\rho}_0$ from (2.23), one deduces that $\boldsymbol{\rho}^*\delta\boldsymbol{\rho}$ is a pure quaternion and hence can be denoted as $\boldsymbol{\rho}^*\delta\boldsymbol{\rho} = (0, \boldsymbol{v}_\diamondsuit)$. Given the multiplication property (2.22b), after removing the zero real part, (2.33) can be simplified as

$$\widetilde{\delta\boldsymbol{\theta}}_l\boldsymbol{x}_l = 2\widetilde{\boldsymbol{v}_\diamondsuit}\boldsymbol{x}_l \tag{2.34}$$

The equality (2.34) holds for any arbitrary vector $\boldsymbol{x}_l$, resulting in the concise equation $\delta\boldsymbol{\theta}_l = 2\boldsymbol{v}_\diamondsuit$. By expanding it to pure quaternions and considering the quaternion-based rotation transformation (2.24), one obtains the transformation relation between the variation of a rotation quaternion $\delta\boldsymbol{\rho}$ and its corresponding virtual rotation vector $\delta\boldsymbol{\theta}_l$

$$\delta\boldsymbol{\rho} = \frac{1}{2}\boldsymbol{\rho}\,(0, \delta\boldsymbol{\theta}_l) \tag{2.35a}$$

$$\delta\boldsymbol{\rho} = \frac{1}{2}\,(0, \delta\boldsymbol{\theta}_a)\,\boldsymbol{\rho} \tag{2.35b}$$

As an alternative, by using matrix algebra, and remembering (2.27) and (2.28), (2.35) can be recast as

$$\delta\boldsymbol{\rho} = \frac{1}{2}\boldsymbol{F}(\boldsymbol{\rho}^*)_\oplus{}^T\delta\boldsymbol{\theta}_l \tag{2.36a}$$

$$\delta\boldsymbol{\rho} = \frac{1}{2}\boldsymbol{F}(\boldsymbol{\rho}^*)_\ominus{}^T\delta\boldsymbol{\theta}_a \tag{2.36b}$$

2.4 Kinematics

The kinematic description in three–dimensional space is essential for multibody system dynamics. In this section, the expressions of the position, orientation, velocity and acceleration of an arbitrary frame are presented.

2.4.1 Position and orientation

Assuming a rigid body in three–dimensional space, as depicted in Figure 2.4, the absolute position of the origin of an arbitrary frame A attached to the rigid body can be decomposed into two parts: the position vector from W to F, and from F to A

$$\boldsymbol{r}_A = \boldsymbol{r}_F + \boldsymbol{r}_{F.A} = \boldsymbol{r}_F + \boldsymbol{R}_F \boldsymbol{r}_{F.A_{(F)}} \tag{2.37}$$

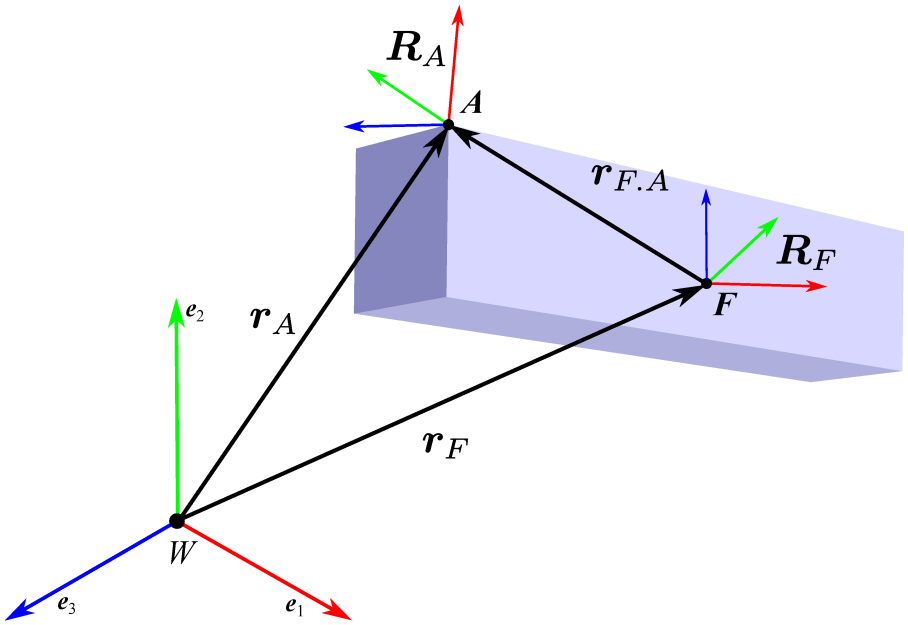

Figure 2.4: Position and orientation of frame A with respect to the reference frame F. The configurations of frame A and F are $\{\boldsymbol{r}_A, \boldsymbol{R}_A\}$ and $\{\boldsymbol{r}_F, \boldsymbol{R}_F\}$, respectively.

The orientation of frame A can also be split into two rotations: the rotation of the reference frame F and its relative rotation with respect to F

$$\boldsymbol{R}_A = \boldsymbol{R}_F \boldsymbol{R}_{A_{(F)}} \tag{2.38}$$

2.4.2 Velocity

Applying time derivative on (2.37), and employing the equality in (2.6b), the translational velocity of frame A can be expressed as

$$\dot{\boldsymbol{r}}_A = \dot{\boldsymbol{r}}_F + \boldsymbol{R}_F \widetilde{\boldsymbol{\omega}}_{l_F} \boldsymbol{r}_{F.A_{(F)}} + \boldsymbol{R}_F \dot{\boldsymbol{r}}_{F.A_{(F)}} \tag{2.39}$$

Applying time derivative on (2.38), and employing the equality (2.6b) in conjunction with the properties (2.1a) and (2.1b), the relative angular velocity of frame A with respect to frame F resolved in the local basis of frame A is expressed as

$$\boldsymbol{\omega}_{l_{A_{(F)}}} = \boldsymbol{\omega}_{F.A_{(A)}} = \boldsymbol{\omega}_{l_A} - \boldsymbol{R}_A^T \boldsymbol{R}_F \boldsymbol{\omega}_{l_F} \tag{2.40}$$

By left-multiplying $\boldsymbol{R}_A$ to transform (2.40) into the absolute basis, the relative angular velocity of frame A with respect to frame F expressed in the inertial frame W is read as

$$\boldsymbol{\omega}_{a_{A_{(F)}}} = \boldsymbol{\omega}_{F.A} = \boldsymbol{\omega}_{a_A} - \boldsymbol{\omega}_{a_F} \tag{2.41}$$

2.4.3 Acceleration

By performing time derivative on (2.39), the translational acceleration of frame A can be calculated as

$$\ddot{\boldsymbol{r}}_A = \ddot{\boldsymbol{r}}_F + \boldsymbol{R}_F \widetilde{\dot{\boldsymbol{\omega}}}_{l_F} \boldsymbol{r}_{F.A_{(F)}} + \boldsymbol{R}_F \widetilde{\boldsymbol{\omega}}_{l_F} \widetilde{\boldsymbol{\omega}}_{l_F} \boldsymbol{r}_{F.A_{(F)}} + 2\boldsymbol{R}_F \widetilde{\boldsymbol{\omega}}_{l_F} \dot{\boldsymbol{r}}_{F.A_{(F)}} + \boldsymbol{R}_F \ddot{\boldsymbol{r}}_{F.A_{(F)}} \tag{2.42}$$

Applying time derivative on (2.41), the relative angular acceleration of frame A with respect to frame F expressed in the inertial frame W is

$$\dot{\boldsymbol{\omega}}_{a_{A_{(F)}}} = \dot{\boldsymbol{\omega}}_{F.A} = \dot{\boldsymbol{\omega}}_{a_A} - \dot{\boldsymbol{\omega}}_{a_F} \tag{2.43}$$

By left-multiplying $\boldsymbol{R}_A^T$ to rotate back (2.43), the relative angular acceleration of frame A with respect to frame F resolved in the local basis of frame A is expressed as

$$\dot{\boldsymbol{\omega}}_{l_{A_{(F)}}} = \dot{\boldsymbol{\omega}}_{F.A_{(A)}} = \dot{\boldsymbol{\omega}}_{l_A} - \boldsymbol{R}_A^T \boldsymbol{R}_F \dot{\boldsymbol{\omega}}_{l_F} \tag{2.44}$$

2.5 Jacobian matrix of constraints

Constraint equations are commonly used to establish joints between bodies in a system through a set of algebraic equations involving generalized coordinates (positions, orientations) $\boldsymbol{q}$, generalized velocities $\dot{\boldsymbol{q}} \in \mathbb{R}^{n_q}$, and time t. If a constraint is independent of generalized velocities $\dot{\boldsymbol{q}}$, it is termed *holonomic*, which is the most frequently encountered scenario in practice; otherwise, it is called *nonholonomic*.

In this work, we discuss only the first case. The holonomic constraint equations can generally be expressed as follows:

$$\boldsymbol{c}(\boldsymbol{q}, t) = \boldsymbol{0} \tag{2.45}$$

The vector of holonomic constraints is linearized as

$$\delta \boldsymbol{c}\,(\boldsymbol{q}, t) = \boldsymbol{C_q} \delta \boldsymbol{q} + \boldsymbol{C}_t \delta t \tag{2.46}$$

by introducing the following symbols

$$\boldsymbol{C_q} := \frac{\partial \boldsymbol{c}\,(\boldsymbol{q}, t)}{\partial \boldsymbol{q}} \quad \in \mathbb{R}^{n_c \times n_q} \tag{2.47a}$$

$$\boldsymbol{C}_t := \frac{\partial \boldsymbol{c}\,(\boldsymbol{q}, t)}{\partial t} \quad \in \mathbb{R}^{n_c} \tag{2.47b}$$

where $\boldsymbol{C_q}$ is the *Jacobian matrix of constraints*.

If the holonomic constraint is not explicitly dependent on time, we call it *scleronomic*; otherwise, it is referred to as *rheonomic*. Rheonomic constraints are typically used to model the driving function of an actuator as demanded by an external controller. This approach simplifies the problem by neglecting the complex internal coupling dynamics between the mechanical, electrical, and control components of the actuator. Rheonomic constraints are also employed in the path planning problem in robotics.

In this section, the formulations of the Jacobian matrices for both scleronomic and rheonomic constraints are presented.

2.5.1 Scleronomic constraints

Suppose a holonomic-scleronomic constraint is used to connect two rigid bodies, whose reference frames are B_1 and B_2, respectively. In this case, the constraint equations depend solely on the system configuration, i.e., $\boldsymbol{c}\,(\boldsymbol{q}) = 0$, thereby eliminating any dependence on time. As depicted in Figure 2.5, two auxiliary joint frames F_1 and F_2, attached to the respective bodies, are introduced. Body 1 is considered the *driven* body, while body 2 is referred to the *main* body since it is the one with respect to which the constraint equations are expressed. The configurations of the two bodies' reference frames $\{\boldsymbol{r}_{B_1}, \boldsymbol{R}_{B_1}\}$ and $\{\boldsymbol{r}_{B_2}, \boldsymbol{R}_{B_2}\}$ are functions of system's generalized coordinates $\boldsymbol{q}$. The two joint frames F_1, F_2 are initially defined by the body-relative positions and orientations, namely $\boldsymbol{r}_{B_1.F_{1(B_1)}}$, $\boldsymbol{R}_{F_{1(B_1)}}$, $\boldsymbol{r}_{B_2.F_{2(B_2)}}$, $\boldsymbol{R}_{F_{2(B_2)}}$, which are constant geometric properties.

The constraint equations can be expressed in an arbitrary frame. Since in engineering practice the reaction forces and moments are typically described or measured in the local basis of the joint, we choose to use the basis of the main frame F_2 so that the reaction forces and moments are consistent with the intuitive understanding.

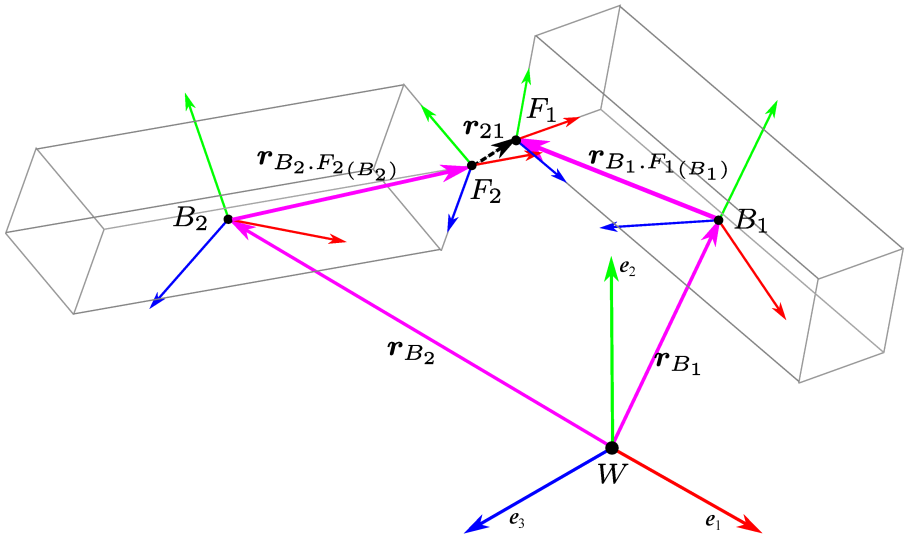

Figure 2.5: The main frame F_2 and the driven frame F_1 for a holonomic-scleronomic constraint. In this figure, the constraint equations are not exactly satisfied, as indicated by a small clearance $\boldsymbol{r}_{21}$, illustrating the constraint violation.

Translational scleronomic constraints

In order to constrain the relative displacement between the two frames, the positions of the origins of F_1 and F_2 should be made coincident, which can be done by imposing the condition

$$\boldsymbol{c}\left(\boldsymbol{q}\right) = \boldsymbol{r}_{F_2.F_{1\left(F_2\right)}} = \boldsymbol{R}_{F_2}^T\left(\boldsymbol{r}_{F_1} - \boldsymbol{r}_{F_2}\right) = \boldsymbol{0}_{3\times 1} \tag{2.48}$$

Using the point transformation (2.37) to expand the terms, one obtains

$$\boldsymbol{c}\left(\boldsymbol{q}\right) = \boldsymbol{R}_{F_2}^T\left(\boldsymbol{r}_{B_1} + \boldsymbol{R}_{B_1}\boldsymbol{r}_{B_1.F_{1\left(B_1\right)}} - \boldsymbol{r}_{B_2} - \boldsymbol{R}_{B_2}\boldsymbol{r}_{B_2.F_{2\left(B_2\right)}}\right) = \boldsymbol{0}_{3\times 1} \tag{2.49}$$

Performing variation on (2.49) and grouping the terms into four variation blocks – $\delta\boldsymbol{r}_{B_1}$, $\delta\boldsymbol{\theta}_{l_{B_1}}$, $\delta\boldsymbol{r}_{B_2}$, $\delta\boldsymbol{\theta}_{l_{B_2}}$ – within the vector of variations for the generalized coordinates $\delta\boldsymbol{q}$, yields

$$\begin{aligned}\delta\boldsymbol{c}\left(\boldsymbol{q}\right) =& \boldsymbol{R}_{F_2}^T\boldsymbol{R}_{B_2}\widetilde{\boldsymbol{r}_{21}}_{\left(B_2\right)}\delta\boldsymbol{\theta}_{l_{B_2}} + \\ & \boldsymbol{R}_{F_2}^T\left(\delta\boldsymbol{r}_{B_1} - \boldsymbol{R}_{B_1}\widetilde{\boldsymbol{r}}_{B_1.F_{1\left(B_1\right)}}\delta\boldsymbol{\theta}_{l_{B_1}} - \delta\boldsymbol{r}_{B_2} + \boldsymbol{R}_{B_2}\widetilde{\boldsymbol{r}}_{B_2.F_{2\left(B_2\right)}}\delta\boldsymbol{\theta}_{l_{B_2}}\right)\end{aligned} \tag{2.50}$$

where the equalities (2.1a), (2.1c) and (2.15b) are employed in conjunction with the assumptions $\delta\boldsymbol{r}_{B_1.F_{1\left(B_1\right)}} = \boldsymbol{0}$, $\delta\boldsymbol{R}_{F_{1\left(B_1\right)}} = \boldsymbol{0}$, $\delta\boldsymbol{r}_{B_2.F_{2\left(B_2\right)}} = \boldsymbol{0}$, $\delta\boldsymbol{R}_{F_{2\left(B_2\right)}} = \boldsymbol{0}$. Moreover, for the sake of notation compactness, we grouped the vector from F_2 to F_1 expressed in the basis of frame B_2 into:

$$\boldsymbol{r}_{21_{\left(B_2\right)}} = \boldsymbol{R}_{B_2}^T\boldsymbol{r}_{F_2.F_1} = \boldsymbol{R}_{B_2}^T\left(\boldsymbol{r}_{B_1} + \boldsymbol{R}_{B_1}\boldsymbol{r}_{B_1.F_{1\left(B_1\right)}} - \boldsymbol{r}_{B_2} - \boldsymbol{R}_{B_2}\boldsymbol{r}_{B_2.F_{2\left(B_2\right)}}\right) \tag{2.51}$$

Finally, recalling the Equation (2.46), one can group the terms in (2.50) and write the four blocks in the sparse Jacobian matrix $\boldsymbol{C_q}$ for the translational constraints as

$$\boldsymbol{C_q}(\boldsymbol{q}) = \left[\begin{array}{c|c|c|c} \boldsymbol{R}_{F_2}^T & -\boldsymbol{R}_{F_2}^T \boldsymbol{R}_{B_1} \widetilde{\boldsymbol{r}}_{B_1.F_1(B_1)} & -\boldsymbol{R}_{F_2}^T & \boldsymbol{R}_{F_2}^T \boldsymbol{R}_{B_2} \widetilde{\boldsymbol{r}}_{B_2.F_2(B_2)} + \boldsymbol{R}_{F_2}^T \boldsymbol{R}_{B_2} \widetilde{\boldsymbol{r}\mathbf{21}}_{(B_2)} \end{array} \right] \tag{2.52}$$

Rotational scleronomic constraints

Remembering the implicit constraint of the unit quaternion (2.20), only its imaginary part of $\boldsymbol{\rho}$ is required to formulate the constraint equation $\boldsymbol{c}(\boldsymbol{q})$ for the three rotational *Degrees Of Freedom* (DOFs). It should be noted that while the unit norm of the quaternion could be explicitly enforced by a constraint, it is typically guaranteed by appropriate integration schemes - for instance in integrators based on Lie group theory (Lie group integrators) the quaternion is updated through an exponential mapping [259].

To constrain the relative rotation between two frames F_1 and F_2, the constraint equation is given as

$$\boldsymbol{c}(\boldsymbol{q}) = \mathrm{Im}\left(\boldsymbol{\rho}_{F_1(F_2)}\right) = \mathbf{0}_{3\times 1} \tag{2.53}$$

where $\mathrm{Im}(\cdot)$ is the operator to extract the imaginary vectorial part of a quaternion.

Unlike using the four components of the quaternion $\boldsymbol{\rho}_{F_1(F_2)}$ to define the rotational constraint equation, which complicates the mathematical formulation of the Jacobian matrix [264], the constraint equation (2.53) could simplify the mathematical derivations and result in a more concise expression of the Jacobian matrix.

Recalling the formula (A.2) (see Appendix A.1 for specific notation and definitions), the variation of the constraint equation (2.53) is differentiated as

$$\delta\boldsymbol{c}(\boldsymbol{q}) = \mathrm{Im}\left(\delta\boldsymbol{\rho}_{F_1(F_2)}\right) = \boldsymbol{P}\left(\boldsymbol{\rho}_{F_1(F_2)}\right) \delta\boldsymbol{\theta}_{l_{F_1(F_2)}} \tag{2.54}$$

The relative virtual rotation vector $\delta\boldsymbol{\theta}_{l_{F_1(F_2)}}$ of the driven frame F_1 with respect to the main frame F_2 can be calculated through deriving the variation of the corresponding rotation matrix $\delta\boldsymbol{R}_{F_1(F_2)}$. The relative rotation matrix can be expanded as $\boldsymbol{R}_{F_1(F_2)} = \boldsymbol{R}_{F_2(B_2)}^T \boldsymbol{R}_{B_2}^T \boldsymbol{R}_{B_1} \boldsymbol{R}_{F_1(B_1)}$. Its variation is calculated as

$$\delta\boldsymbol{R}_{F_1(F_2)} = \boldsymbol{R}_{F_2(B_2)}^T \left(-\widetilde{\delta\boldsymbol{\theta}}_{l_{B_2}} \boldsymbol{R}_{B_2}^T \boldsymbol{R}_{B_1} + \boldsymbol{R}_{B_2}^T \boldsymbol{R}_{B_1} \widetilde{\delta\boldsymbol{\theta}}_{l_{B_1}}\right) \boldsymbol{R}_{F_1(B_1)} \tag{2.55}$$

Substituting (2.55) into $\widetilde{\delta\boldsymbol{\theta}}_{l_{F_1(F_2)}} = \boldsymbol{R}_{F_1(F_2)}^T \delta\boldsymbol{R}_{F_1(F_2)}$, after some calculations and extracting the spinning vectors of the skew–symmetric matrices, one obtains

$$\delta\boldsymbol{\theta}_{l_{F_1(F_2)}} = \boldsymbol{R}_{F_1}^T \left(\boldsymbol{R}_{B_1} \delta\boldsymbol{\theta}_{l_{B_1}} - \boldsymbol{R}_{B_2} \delta\boldsymbol{\theta}_{l_{B_2}}\right) \tag{2.56}$$

Substituting (2.56) into (2.54), the variation of the constraint equation of rotational DOFs is obtained as

$$\delta \boldsymbol{c}\left(\boldsymbol{q}\right) = \boldsymbol{P}\left(\boldsymbol{\rho}_{F_1(F_2)}\right) \boldsymbol{R}_{F_1}^T \left(\boldsymbol{R}_{B_1} \delta \boldsymbol{\theta}_{l_{B_1}} - \boldsymbol{R}_{B_2} \delta \boldsymbol{\theta}_{l_{B_2}}\right) \tag{2.57}$$

Remembering the equality (A.4), the above relation (2.57) can be recast with respect to the main frame F_2 as

$$\delta \boldsymbol{c}\left(\boldsymbol{q}\right) = \boldsymbol{P}\left(\boldsymbol{\rho}_{F_1(F_2)}\right)^T \boldsymbol{R}_{F_2}^T \left(\boldsymbol{R}_{B_1} \delta \boldsymbol{\theta}_{l_{B_1}} - \boldsymbol{R}_{B_2} \delta \boldsymbol{\theta}_{l_{B_2}}\right) \tag{2.58}$$

Eventually, the Jacobian matrix of constraints $\boldsymbol{C_q}$ for the rotational DOFs becomes

$$\boldsymbol{C_q}\left(\boldsymbol{q}\right) = \left[\begin{array}{c|c|c|c} \boldsymbol{0} & \boldsymbol{P}\left(\boldsymbol{\rho}_{F_1(F_2)}\right)^T \boldsymbol{R}_{F_2}^T \boldsymbol{R}_{B_1} & \boldsymbol{0} & -\boldsymbol{P}\left(\boldsymbol{\rho}_{F_1(F_2)}\right)^T \boldsymbol{R}_{F_2}^T \boldsymbol{R}_{B_2} \end{array}\right] \tag{2.59}$$

Complete Jacobian of scleronomic constraints

The complete expression of the Jacobian matrix of constraints $\boldsymbol{C_q}$ is obtained by combining (2.52) and (2.59)

$$\begin{aligned} &\boldsymbol{C_q}\left(\boldsymbol{q}\right) \\ &= \left[\begin{array}{c|c|c|c} \boldsymbol{R}_{F_2}^T & -\boldsymbol{R}_{F_2}^T \boldsymbol{R}_{B_1} \widetilde{\boldsymbol{r}}_{B_1.F_1(B_1)} & -\boldsymbol{R}_{F_2}^T & \boldsymbol{R}_{F_2}^T \boldsymbol{R}_{B_2} \widetilde{\boldsymbol{r}}_{B_2.F_2(B_2)} + \boldsymbol{R}_{F_2}^T \boldsymbol{R}_{B_2} \widetilde{\boldsymbol{r}\mathit{21}}_{(B_2)} \\ \hline \boldsymbol{0} & \boldsymbol{P}\left(\boldsymbol{\rho}_{F_1(F_2)}\right)^T \boldsymbol{R}_{F_2}^T \boldsymbol{R}_{B_1} & \boldsymbol{0} & -\boldsymbol{P}\left(\boldsymbol{\rho}_{F_1(F_2)}\right)^T \boldsymbol{R}_{F_2}^T \boldsymbol{R}_{B_2} \end{array}\right] \end{aligned} \tag{2.60}$$

For simplicity, we can rewrite (2.60) to emphasize its six rows: the first three correspond to the translational constraints, and the last three correspond to the rotational constraints:

$$\boldsymbol{C_q}\left(\boldsymbol{q}\right) = \begin{bmatrix} \boldsymbol{C}_{\boldsymbol{q}_x} \\ \boldsymbol{C}_{\boldsymbol{q}_y} \\ \boldsymbol{C}_{\boldsymbol{q}_z} \\ \boldsymbol{C}_{\boldsymbol{q}_{Rx}} \\ \boldsymbol{C}_{\boldsymbol{q}_{Ry}} \\ \boldsymbol{C}_{\boldsymbol{q}_{Rz}} \end{bmatrix} \tag{2.61}$$

While the above general expression constrains all six DOFs between the two frames F_1 and F_2, it is straightforward to represent other types of joints by suppressing the corresponding rows according to the free DOFs, as shown in Table 2.1. The '$\times$' symbol indicates that the corresponding rows are active and thus constrain the associated DOFs, while the '$\circ$' symbol denotes that the associated DOFs are free. For example, the Jacobian matrix for a revolute joint along the x axis will have only five rows out of six, since the row corresponding to $\boldsymbol{C}_{\boldsymbol{q}_{Rx}}$ will be suppressed.

Table 2.1: Some common joints inherited from the lock constraint.
'×': constrained; '○': free.

	$\boldsymbol{C}_{\boldsymbol{q}_x}$	$\boldsymbol{C}_{\boldsymbol{q}_y}$	$\boldsymbol{C}_{\boldsymbol{q}_z}$	$\boldsymbol{C}_{\boldsymbol{q}_{Rx}}$	$\boldsymbol{C}_{\boldsymbol{q}_{Ry}}$	$\boldsymbol{C}_{\boldsymbol{q}_{Rz}}$
Fix	×	×	×	×	×	×
Coaxial	○	×	×	○	×	×
Prismatic	○	×	×	×	×	×
Revolute	×	×	×	○	×	×
Orthogonal	○	○	○	×	○	○
Parallel	○	○	○	○	×	×
Plane	×	○	○	○	×	×
Spherical	×	×	×	○	○	○
Distance along X	×	○	○	○	○	○

2.5.2 Rheonomic constraints

In rheonomic constraints, the relative motion of the driven frame F_1 with respect to the main frame F_2 is explicitly dependent on time, expressed as $C(\boldsymbol{q}, t) = 0$. This scenario is commonly encountered in the modeling of linear or rotational actuators that receive a motion set-point from a controller.

Translational rheonomic constraints

The constraint equation of the rheonomic translational constraints can be expressed as

$$\begin{aligned}\boldsymbol{c}\left(\boldsymbol{q}, t\right) &= \boldsymbol{r}_{F_2.F_{1\left(F_2\right)}} - \boldsymbol{r}_t \\ &= \boldsymbol{R}_{F_2}^T \left(\boldsymbol{r}_{B_1} + \boldsymbol{R}_{B_1}\boldsymbol{r}_{B_1.F_{1\left(B_1\right)}} - \boldsymbol{r}_{B_2} - \boldsymbol{R}_{B_2}\boldsymbol{r}_{B_2.F_{2\left(B_2\right)}}\right) - \boldsymbol{r}_t \\ &= \boldsymbol{0}_{3\times 1}\end{aligned} \tag{2.62}$$

where $\boldsymbol{r}_t$ is the position vector representing the relative translational motion of the driven frame F_1 with respect to the main frame F_2, as specified by end users as a function of time.

According to the definitions in (2.47a) and (2.47b), the two Jacobian matrices can be expressed as

$$\boldsymbol{C}_{\boldsymbol{q}} = \frac{\partial}{\partial \boldsymbol{q}}\left(\boldsymbol{R}_{F_2}^T \left(\boldsymbol{r}_{B_1} + \boldsymbol{R}_{B_1}\boldsymbol{r}_{B_1.F_{1\left(B_1\right)}} - \boldsymbol{r}_{B_2} - \boldsymbol{R}_{B_2}\boldsymbol{r}_{B_2.F_{2\left(B_2\right)}}\right)\right) \tag{2.63a}$$

$$\boldsymbol{C}_t = -\frac{\partial \boldsymbol{r}_t}{\partial t} \tag{2.63b}$$

The rheonomic term $\boldsymbol{r}_t$ does not affect the computation of $\boldsymbol{C}_{\boldsymbol{q}}$, thus the Jacobian matrix of translational rheonomic constraints is the same as (2.52).

Rotational rheonomic constraints

The constraint equation of the rheonomic rotational constraints is given as

$$\boldsymbol{c}\left(\boldsymbol{q},t\right)=-\mathrm{Im}\left(\boldsymbol{\rho}_{t}\boldsymbol{\rho}_{F_{2}(F_{1})}\right)=\mathbf{0}_{3\times1} \tag{2.64}$$

where $\boldsymbol{\rho}_t$ is the quaternion representing the relative rotational motion of the driven frame F_1 with respect to the main frame F_2, as specified by end users as a function of time. If the constraint is satisfied, there should be $\boldsymbol{\rho}_{F_1}=\boldsymbol{\rho}_{F_2}\boldsymbol{\rho}_t$.

By introducing a shadow frame $F_1^{\Diamond}$ as $\boldsymbol{\rho}_{F_1^{\Diamond}}=\boldsymbol{\rho}_{F_1}\boldsymbol{\rho}_t^{*}$, and remembering the equalities $\boldsymbol{\rho}_{F_{2}(F_{1})}=\boldsymbol{\rho}_{F_1}^{*}\boldsymbol{\rho}_{F_2}$ and $\boldsymbol{\rho}_{F_{2}(F_{1})}^{*}=\boldsymbol{\rho}_{F_{1}(F_{2})}$, the constraint equation (2.64) can be rewritten as

$$\boldsymbol{c}\left(\boldsymbol{q},t\right)=\mathrm{Im}\left(\boldsymbol{\rho}_{F_{1}^{\Diamond}(F_{2})}\right)=\mathbf{0}_{3\times1} \tag{2.65}$$

The shadow frame $F_1^{\Diamond}$ is rotated back from the driven frame F_1 by the given rotation $\boldsymbol{\rho}_t$ to arrive at the same orientation as the main frame F_2. If the constraint is satisfied, the shadow frame $F_1^{\Diamond}$ is coincident with the main frame F_2.

Similarly as the derivation from (2.53) to the results of (2.57) and (2.58), the variation of (2.65) is computed as

$$\delta\boldsymbol{c}(\boldsymbol{q},t)=\boldsymbol{P}\left(\boldsymbol{\rho}_{F_{1}^{\Diamond}(F_{2})}\right)\boldsymbol{R}_{F_{1}^{\Diamond}}^{T}\left(\boldsymbol{R}_{B_{1}}\delta\boldsymbol{\theta}_{l_{B_{1}}}-\boldsymbol{R}_{B_{2}}\delta\boldsymbol{\theta}_{l_{B_{2}}}\right) \tag{2.66}$$

$$=\boldsymbol{P}\left(\boldsymbol{\rho}_{F_{1}^{\Diamond}(F_{2})}\right)^{T}\boldsymbol{R}_{F_{2}}^{T}\left(\boldsymbol{R}_{B_{1}}\delta\boldsymbol{\theta}_{l_{B_{1}}}-\boldsymbol{R}_{B_{2}}\delta\boldsymbol{\theta}_{l_{B_{2}}}\right) \tag{2.67}$$

where the rheonomic term $\boldsymbol{C}_t=\dfrac{\partial}{\partial t}\left(\mathrm{Im}\left(\boldsymbol{\rho}_{F_{1}^{\Diamond}(F_{2})}\right)\right)$ does not affect $\boldsymbol{C}_{\boldsymbol{q}}$ and is not shown.

Complete Jacobian of rheonomic constraints

The complete expression of the Jacobian matrix of rheonomic constraints $\boldsymbol{C}_{\boldsymbol{q}}\left(\boldsymbol{q},t\right)$ is obtained by replacing the blocks corresponding to the rotational DOFs in (2.60) with (2.67):

$$\boldsymbol{C}_{\boldsymbol{q}}\left(\boldsymbol{q},t\right)$$
$$=\left[\begin{array}{c|c|c|c}\boldsymbol{R}_{F_2}^{T} & -\boldsymbol{R}_{F_2}^{T}\boldsymbol{R}_{B_1}\widetilde{\boldsymbol{r}}_{B_1.F_1(B_1)} & -\boldsymbol{R}_{F_2}^{T} & \boldsymbol{R}_{F_2}^{T}\boldsymbol{R}_{B_2}\widetilde{\boldsymbol{r}}_{B_2.F_2(B_2)}+\boldsymbol{R}_{F_2}^{T}\boldsymbol{R}_{B_2}\widetilde{\boldsymbol{r}_{21}}_{(B_2)}\\ \hline \mathbf{0} & \boldsymbol{P}\left(\boldsymbol{\rho}_{F_{1}^{\Diamond}(F_{2})}\right)^{T}\boldsymbol{R}_{F_2}^{T}\boldsymbol{R}_{B_1} & \mathbf{0} & -\boldsymbol{P}\left(\boldsymbol{\rho}_{F_{1}^{\Diamond}(F_{2})}\right)^{T}\boldsymbol{R}_{F_2}^{T}\boldsymbol{R}_{B_2}\end{array}\right] \tag{2.68}$$

2.6 Differential-algebraic equations

In our formulation, we assume that translational coordinates are described in the absolute frame (the inertial frame W), while rotational coordinates are expressed

in the *local* frame of the object; we call it a *mixed-basis* formalism. This choice, though somewhat arbitrary, is motivated by the simpler form of the rotational equations [259].

The equations of motion for a rigid body can be established using the *Newton-Euler* formulation, as it offers advantages in terms of easier mathematical derivation and higher computational efficiency. For a rigid body with mass ν and mass moment of inertia $\boldsymbol{J}_l$, subjected to an external force $\boldsymbol{f}_a$ and moment $\boldsymbol{m}_l$, and considering the offset of the mass center $\boldsymbol{s}_l$ with respect to its own reference frame characterized by the configuration $\{\boldsymbol{r}_a, \boldsymbol{R}\}$, the Newton-Euler equations of motion are expressed as

$$\begin{bmatrix} \nu \boldsymbol{I} & \nu \boldsymbol{R} \widetilde{\boldsymbol{s}}_l^T \\ \nu \widetilde{\boldsymbol{s}}_l \boldsymbol{R}^T & \boldsymbol{J}_l \end{bmatrix} \begin{pmatrix} \ddot{\boldsymbol{r}}_a \\ \dot{\boldsymbol{\omega}}_l \end{pmatrix} = \begin{pmatrix} \boldsymbol{f}_a - \nu \boldsymbol{R} \widetilde{\boldsymbol{\omega}}_l \widetilde{\boldsymbol{\omega}}_l \boldsymbol{s}_l \\ \boldsymbol{m}_l - \widetilde{\boldsymbol{\omega}}_l \boldsymbol{J}_l \boldsymbol{\omega}_l \end{pmatrix} \tag{2.69}$$

where $\ddot{\boldsymbol{r}}_a$ is the absolute translational acceleration, and $\dot{\boldsymbol{\omega}}_l$, $\boldsymbol{\omega}_l$ are the local angular acceleration and angular velocity, respectively.

Mechanical joints are commonly employed to connect rigid bodies and flexible elements in multibody systems, leading to the presence of redundant coordinates at the connection points. When the number of joints in the system is limited, particularly in systems with a tree-like topology, the equations of motion can be represented as *Ordinary Differential Equations* (ODEs) by carefully selecting the independent coordinates.

However, as the complexity of the system increases with the addition of more bodies and joints, especially when closed loops are involved, it becomes challenging to identify the independent coordinates, often not even unique [237]. To address this issue, the Lagrange multiplier method has been developed and widely adopted in the field of multibody system dynamics. The fundamental idea is to initially formulate the ODEs for all rigid bodies and flexible elements as if they were completely uncoupled. Subsequently, constraint equations are introduced to define the relationships between redundant coordinates, resulting in a set of *Differential-Algebraic Equations* (DAEs).

The DAEs of a holonomic constrained dynamic system can be expressed as

$$\begin{cases} \boldsymbol{M}(\boldsymbol{q})\, \ddot{\boldsymbol{q}} + \boldsymbol{C}_{\boldsymbol{q}}(\boldsymbol{q}, t)^T \boldsymbol{\gamma} = \boldsymbol{f}(\boldsymbol{q}, \dot{\boldsymbol{q}}, t) & \text{(2.70a)} \\ \boldsymbol{c}(\boldsymbol{q}, t) = \boldsymbol{0} & \text{(2.70b)} \end{cases}$$

where $\ddot{\boldsymbol{q}} = \left[\ddot{\boldsymbol{r}}_a^T, \dot{\boldsymbol{\omega}}_l^T\right]^T$ represents the acceleration coordinates, $\boldsymbol{M}(\boldsymbol{q})$ is the mass matrix. The term $\boldsymbol{\gamma}$ corresponds to the Lagrange multipliers, while $\boldsymbol{C}_{\boldsymbol{q}}^T \boldsymbol{\gamma}$ represents the reaction forces and moments at the joints.

The vector $\boldsymbol{f}$ consists of applied external forces $\boldsymbol{f}_a(\boldsymbol{q}, \dot{\boldsymbol{q}}, t)$, internal elastic forces $\boldsymbol{f}_e(\boldsymbol{q})$, viscous damping forces $\boldsymbol{f}_d(\dot{\boldsymbol{q}})$, and quadratic velocity terms $\boldsymbol{f}_v(\boldsymbol{q}, \dot{\boldsymbol{q}})$. Consequently, $\boldsymbol{f}$ can be expressed as $\boldsymbol{f}(\boldsymbol{q}, \dot{\boldsymbol{q}}, t) = \boldsymbol{f}_a(\boldsymbol{q}, \dot{\boldsymbol{q}}, t) + \boldsymbol{f}_e(\boldsymbol{q}) + \boldsymbol{f}_d(\dot{\boldsymbol{q}}) + \boldsymbol{f}_v(\boldsymbol{q}, \dot{\boldsymbol{q}})$.

The term $\boldsymbol{M}(\boldsymbol{q})\, \ddot{\boldsymbol{q}}$ is the linear component of the inertial forces. The quadratic velocity terms $\boldsymbol{f}_v$, which are nonlinear functions of the generalized coordinates $\boldsymbol{q}$

and the generalized velocities $\dot{\boldsymbol{q}}$, constitute the nonlinear component of the inertial forces. Thus, the complete expression for the inertial forces is given by $\boldsymbol{f}_i = \boldsymbol{M}(\boldsymbol{q})\,\ddot{\boldsymbol{q}} - \boldsymbol{f}_v$.

It is important to emphasize that, in this work, we assume there are no redundant constraints within the system. Consequently, the Jacobian matrix of the constraints $\boldsymbol{C}_{\boldsymbol{q}}$ in (2.70) is assumed to be of *full row rank*.

2.6.1 DAEs theory

The algebraic equations (2.70b) enforce the kinematic constraints at the configuration level. Applying time derivative to (2.70b), yields the corresponding constraint equations at the velocity level

$$\dot{\boldsymbol{c}}(\boldsymbol{q},t) = \boldsymbol{C}_{\boldsymbol{q}}(\boldsymbol{q},t)\,\dot{\boldsymbol{q}} + \boldsymbol{C}_t(\boldsymbol{q},t) = \boldsymbol{0} \tag{2.71}$$

The constraint equations at the acceleration level are derived by applying an additional time derivative to (2.71):

$$\ddot{\boldsymbol{c}}(\boldsymbol{q},t) = \boldsymbol{C}_{\boldsymbol{q}}(\boldsymbol{q},t)\,\ddot{\boldsymbol{q}} + \frac{\partial\left(\boldsymbol{C}_{\boldsymbol{q}}(\boldsymbol{q},t)\,\dot{\boldsymbol{q}}\right)}{\partial \boldsymbol{q}}\dot{\boldsymbol{q}} + 2\boldsymbol{C}_{\boldsymbol{q}t}(\boldsymbol{q},t)\,\dot{\boldsymbol{q}} + \boldsymbol{C}_{tt}(\boldsymbol{q},t) = \boldsymbol{0} \tag{2.72}$$

where

$$\boldsymbol{C}_{\boldsymbol{q}t} := \frac{\partial^2 \boldsymbol{c}(\boldsymbol{q},t)}{\partial \boldsymbol{q}\partial t} \quad \in \mathbb{R}^{n_c \times n_q} \tag{2.73a}$$

$$\boldsymbol{C}_{tt} := \frac{\partial^2 \boldsymbol{c}(\boldsymbol{q},t)}{\partial t^2} \quad \in \mathbb{R}^{n_c} \tag{2.73b}$$

The *differential index*, or simply the *index*, of DAEs refers to the minimum number of differentiations required on the constraint equations (2.70b) to obtain ODEs [173, 211]. Substituting (2.70a) into (2.72), it is evident that an additional time derivative is necessary to yield pure ODEs involving variables of both $\boldsymbol{q}$ and $\boldsymbol{\gamma}$, establishing that the index of the DAEs from (2.70) is three. The index can be interpreted as a measure of the complexity in solving the DAEs, i.e., a higher index indicates greater difficulty. In practical applications, employing the naive approach of repeatedly differentiating the DAEs to convert them into ODEs is not feasible. This is because performing time integration on the constraints at the third derivative level can result in a *drift-off* phenomenon in the configuration-level kinematic constraints due to the accumulation of numerical errors during the time evolution.

There are various methods available to deal with the algebraic constraint equations in index-3 DAEs. One approach is to reduce the index by incorporating derivatives of the constraint equations from (2.71) and/or (2.72) into (2.70), though

this comes at the expense of relaxing the satisfaction of the differential equations [86, 83, 23]. Baumgarte [22] developed a method that replaces the original configuration-level kinematic constraint equations (2.70b) with a linear combination of the configuration-, velocity-, and acceleration-level constraint equations, thereby transforming the system into pure ODEs, as shown below:

$$\begin{cases} \boldsymbol{M}(\boldsymbol{q})\,\ddot{\boldsymbol{q}} + \boldsymbol{C}_{\boldsymbol{q}}(\boldsymbol{q},t)^T\boldsymbol{\gamma} = \boldsymbol{f}(\boldsymbol{q},\dot{\boldsymbol{q}},t) & \text{(2.74a)} \\ \ddot{\boldsymbol{c}}(\boldsymbol{q},t) + 2\alpha_c\dot{\boldsymbol{c}}(\boldsymbol{q},t) + \beta_c\boldsymbol{c}(\boldsymbol{q},t) = \boldsymbol{0} & \text{(2.74b)} \end{cases}$$

where α_c and β_c are adjustable parameters.

The second equation (2.74b) behaves like a spring-damper mechanism, where α_c determines the damping level, and β_c defines the stiffness of the mechanism. In Baumgarte's formulation, the algebraic constraint equations (2.70b) are not strictly enforced, but rather satisfied approximately. If the values of α_c and β_c are too small, they may be insufficient to correct constraint drifts, potentially leading to divergent solutions. As β_c increases, the solution of the constraints approaches the true solution, but the problem (2.74b) also becomes stiffer, exhibiting greater challenges in numerical integration. For instance, a smaller time step size may be required to achieve a stable solution. This also explains that the algebraic constraint equations in (2.70b) can be regarded as infinite-stiffness or zero-inertia mechanical systems that respond instantaneously to external excitations. There is no standardized method for optimally tuning the α_c and β_c parameters for all problems, which has limited the broader application of Baumgarte's method.

Borri et al. [33] developed an embedded projection method that reduces arbitrary-index DAEs to index-1 ODEs plus additional algebraic equations by introducing an unconstrained, modified state variable. However, the complexity of this approach can lead to increased computational cost. Masarati [184, 183] proposed a method that projects motion onto the constraint manifold for both position and velocity based on Gauss' principle of least constraint, where the constraints are not explicitly enforced. Zhou et al. [297, 298] employed QR factorization of the Jacobian matrix of constraints to project motion onto the subspace locally tangent to the constraint manifold, developing a true continuation algorithm to track the evolution of the subspace of independent coordinates. Subsequently, Masarati et al. [185] extended the subspace evolution method to systems with redundant constraints and discussed the singularity detection. Nada [193] introduced a new constraint stabilization method based on fuzzy control algorithms.

Index reduction methods and constraint stabilization techniques for solving high-index DAEs have been extensively discussed in the literature. For a more comprehensive overview of these methods, readers are referred to review papers by Laulusa and Bauchau [159, 19].

When the number of constraints is significantly smaller than the number of physical coordinates, i.e., $n_c \ll n_q$, as is often the case in flexible structures, the benefits of index reduction methods and constraint stabilization techniques become

less pronounced. This is because, in such situations, the reduction in problem size becomes negligible, while the computational complexity increases rapidly. This is particularly relevant in the dynamic simulations of wind turbines.

An alternative approach is to directly integrate the index-3 DAEs, ensuring that both the differential and algebraic equations are satisfied in a monolithic manner through the development of custom time integration schemes. Bottasso et al. [35] proposed a simple left- and right-scaling transformation for index-3 DAEs and demonstrated that the error propagation and condition number of the iteration matrix are both $\mathcal{O}(h^0)$, meaning that the behavior of the numerical integration of index-3 DAEs is comparable to that of regular ODEs. Subsequently, Bottasso et al.[36] extended this scaling preconditioning method to the Newmark family of integration schemes, and provided a thorough theoretical analysis of the perturbation problem to consolidate the preconditioning strategy. Moreover, Bauchau et al. [17] expanded the scaling approach to include the augmented Lagrange term and showed that this extension is essential when the factorization of the iteration matrix is performed without pivoting, which is crucial for the efficient solution of large-scale sparse linear equations.

2.6.2 General linearization of DAEs

The terms in (2.70) can be linearized around an equilibrium configuration using a Taylor series expansion and preserving the linear terms

$$\boldsymbol{M}\left(\boldsymbol{q}\right)\ddot{\boldsymbol{q}} = \boldsymbol{M}(\boldsymbol{q}_0)\left(\ddot{\boldsymbol{q}}_0 + \delta\ddot{\boldsymbol{q}}\right) + \frac{\partial\left(\boldsymbol{M}\ddot{\boldsymbol{q}}_0\right)}{\partial\boldsymbol{q}}\delta\boldsymbol{q} \tag{2.75a}$$

$$\boldsymbol{C}_{\boldsymbol{q}}\left(\boldsymbol{q},t\right)^T\boldsymbol{\gamma} = \boldsymbol{C}_{\boldsymbol{q}}(\boldsymbol{q}_0,t_0)^T\left(\boldsymbol{\gamma}_0 + \delta\boldsymbol{\gamma}\right) + \frac{\partial\left(\boldsymbol{C}_{\boldsymbol{q}}^T\boldsymbol{\gamma}_0\right)}{\partial\boldsymbol{q}}\delta\boldsymbol{q} \tag{2.75b}$$

$$\boldsymbol{f}\left(\boldsymbol{q},\dot{\boldsymbol{q}},t\right) = \boldsymbol{f}_0 + \left(\frac{\partial\boldsymbol{f}_a}{\partial\dot{\boldsymbol{q}}} + \frac{\partial\boldsymbol{f}_d}{\partial\dot{\boldsymbol{q}}} + \frac{\partial\boldsymbol{f}_v}{\partial\dot{\boldsymbol{q}}}\right)\delta\dot{\boldsymbol{q}} + \left(\frac{\partial\boldsymbol{f}_a}{\partial\boldsymbol{q}} + \frac{\partial\boldsymbol{f}_e}{\partial\boldsymbol{q}} + \frac{\partial\boldsymbol{f}_v}{\partial\boldsymbol{q}}\right)\delta\boldsymbol{q} \tag{2.75c}$$

$$\boldsymbol{c}\left(\boldsymbol{q},t\right) = \boldsymbol{c}_0 + \boldsymbol{C}_{\boldsymbol{q}}(\boldsymbol{q}_0,t_0)\delta\boldsymbol{q} \tag{2.75d}$$

where the subscript '0' indicates that the quantity is evaluated in the equilibrium configuration.

By substituting (2.75) into (2.70), removing the equilibrium terms, and preserving only the infinitesimal perturbation terms, the linearized DAEs are obtained as

$$\begin{cases} \boldsymbol{M}\left(\boldsymbol{q}_0\right)\delta\ddot{\boldsymbol{q}} + \boldsymbol{D}\left(\boldsymbol{q}_0,\dot{\boldsymbol{q}}_0\right)\delta\dot{\boldsymbol{q}} + \boldsymbol{K}\left(\boldsymbol{q}_0,\dot{\boldsymbol{q}}_0,\ddot{\boldsymbol{q}}_0,\boldsymbol{\gamma}_0\right)\delta\boldsymbol{q} + \boldsymbol{C}_{\boldsymbol{q}}\left(\boldsymbol{q}_0,t_0\right)^T\delta\boldsymbol{\gamma} = \boldsymbol{0} & (2.76a) \\ \boldsymbol{C}_{\boldsymbol{q}}\left(\boldsymbol{q}_0,t_0\right)\delta\boldsymbol{q} = \boldsymbol{0} & (2.76b) \end{cases}$$

where two tangent matrices are introduced

$$\begin{aligned}\boldsymbol{D}\left(\boldsymbol{q}_0, \dot{\boldsymbol{q}}_0\right) &= -\frac{\partial \boldsymbol{f}_a}{\partial \dot{\boldsymbol{q}}} - \frac{\partial \boldsymbol{f}_d}{\partial \dot{\boldsymbol{q}}} - \frac{\partial \boldsymbol{f}_v}{\partial \dot{\boldsymbol{q}}} \\ &= \boldsymbol{D}_a + \boldsymbol{D}_m + \boldsymbol{D}_i \end{aligned} \tag{2.77}$$

$$\begin{aligned}\boldsymbol{K}\left(\boldsymbol{q}_0, \dot{\boldsymbol{q}}_0, \ddot{\boldsymbol{q}}_0, \boldsymbol{\gamma}_0\right) &= -\frac{\partial \boldsymbol{f}_a}{\partial \boldsymbol{q}} - \frac{\partial \boldsymbol{f}_e}{\partial \boldsymbol{q}} + \frac{\partial\left(\boldsymbol{M}\ddot{\boldsymbol{q}}_0 - \boldsymbol{f}_v\right)}{\partial \boldsymbol{q}} + \frac{\partial\left(\boldsymbol{C}_{\boldsymbol{q}}^T \boldsymbol{\gamma}_0\right)}{\partial \boldsymbol{q}} \\ &= \boldsymbol{K}_a + \boldsymbol{K}_e + \boldsymbol{K}_i + \boldsymbol{K}_c \end{aligned} \tag{2.78}$$

The tangent damping matrix, $\boldsymbol{D}$, is composed of three components: the damping matrix of external forces, $\boldsymbol{D}_a = -\partial \boldsymbol{f}_a / \partial \dot{\boldsymbol{q}}$; the structural damping matrix, $\boldsymbol{D}_m = -\partial \boldsymbol{f}_d / \partial \dot{\boldsymbol{q}}$, which arises from the structural damping properties; and the inertial damping matrix, $\boldsymbol{D}_i = -\partial \boldsymbol{f}_v / \partial \dot{\boldsymbol{q}}$, linearized from the quadratic velocity terms $\boldsymbol{f}_v$.

In the modal analysis of wind turbines, the aerodynamic damping matrix, $\boldsymbol{D}_a$, provides significant damping in the blade flapwise direction and may introduce negative damping in the blade edgewise direction. The structural damping matrix, $\boldsymbol{D}_m$, is a crucial source for compensating potential negative aerodynamic damping. The inertial damping matrix, $\boldsymbol{D}_i$, includes the well–known gyroscopic damping matrix. Although it does not inject or dissipate energy from the blades, it changes their motion direction and ultimately influences the aeroelastic damping.

The tangent stiffness matrix, $\boldsymbol{K}$, is composed of several components: the stiffness matrix of external forces, $\boldsymbol{K}_a = -\partial \boldsymbol{f}_a / \partial \boldsymbol{q}$; the structural stiffness matrix, $\boldsymbol{K}_e = -\partial \boldsymbol{f}_e / \partial \boldsymbol{q}$; the inertial stiffness matrix, $\boldsymbol{K}_i = \partial\left(\boldsymbol{M}\ddot{\boldsymbol{q}}_0 - \boldsymbol{f}_v\right) / \partial \boldsymbol{q}$, which includes the gyroscopic stiffness matrix; and the tangent stiffness matrix of constraints, $\boldsymbol{K}_c = \partial\left(\boldsymbol{C}_{\boldsymbol{q}}^T \boldsymbol{\gamma}_0\right) / \partial \boldsymbol{q}$, which arises due to the orientation change of the reaction forces and moments at the joints. The structural stiffness matrix, $\boldsymbol{K}_e$, can be further divided into two components: $\boldsymbol{K}_e = \boldsymbol{K}_m + \boldsymbol{K}_g$, where $\boldsymbol{K}_m$ is the material stiffness matrix and $\boldsymbol{K}_g$ is the geometric stiffness matrix induced by the internal forces of the finite elements.

2.6.3 Generalized coordinates for rotation

To formulate the eigenvalue problem [178] and the discretization form of the time integration scheme [196] from the linearized DAEs in (2.76), the generalized coordinates of displacement $\delta \boldsymbol{q}$, velocity $\delta \dot{\boldsymbol{q}}$ and acceleration $\delta \ddot{\boldsymbol{q}}$ are assumed to hold the time derivative relations. While this is straightforward for translations, it is more complex for rotations.

One can choose the variation of the rotation pseudovector and its derivatives $\delta \boldsymbol{\phi}$, $\delta \dot{\boldsymbol{\phi}}$, $\delta \ddot{\boldsymbol{\phi}}$, or the virtual rotation vector and its derivatives $\delta \boldsymbol{\theta}_l$, $\delta \dot{\boldsymbol{\theta}}_l$, $\delta \ddot{\boldsymbol{\theta}}_l$ to satisfy the rigorous time derivative relations. However, both approaches lack physical

meaning, particularly for the rotational velocity and acceleration, which can complicate the development of the time integration scheme. Another option is to use the quaternion and its derivatives $\delta\boldsymbol{\rho}$, $\delta\dot{\boldsymbol{\rho}}$, $\delta\ddot{\boldsymbol{\rho}}$. This approach results in the system matrices $\boldsymbol{M}$, $\boldsymbol{D}$, $\boldsymbol{K}$ for rotational DOFs having blocks of size 4×4 rather than the conventional 3×3, leading to larger system matrices. Additionally, this method requires an extra constraint equation for each node or rigid body to enforce the unit length of quaternion. Consequently, even when no link is present in the system, algebraic constraint equations arise, and the final equations of motion take the form of index–3 DAEs, making the solution process more cumbersome.

In this study, the update of finite rotation in the time integration is carried out using a finite increment of the rotation pseudovector $\boldsymbol{\phi}_\Delta$ based on the rotation $\boldsymbol{\phi}^k$ converged at the previous time instant t^k. Here, k denotes the time step index, t^k represents the time instant corresponding to the step index k, and Δ signifies the finite differential of a quantity.

If the incremental rotation is computed in the local basis, we denote the local finite increment of the rotation pseudovector as $\boldsymbol{\phi}_{l_\Delta}$, which brings the rotation from step k to step $k+1$

$$\boldsymbol{R}\left(\boldsymbol{\phi}^{k+1}\right) = \boldsymbol{R}\left(\boldsymbol{\phi}^{k}\right)\boldsymbol{R}\left(\boldsymbol{\phi}_{l_\Delta}\right) \tag{2.79}$$

In the incremental rotation update scheme, the previous configuration at time instant t^k is assumed to be fixed, so $\boldsymbol{R}\left(\boldsymbol{\phi}^{k}\right)$ is considered constant. Applying variation to (2.79), and employing $\delta\boldsymbol{R} = \boldsymbol{R}\widetilde{\delta\boldsymbol{\theta}}_l$ and the relation (2.17b), yields

$$\begin{aligned}
\delta\boldsymbol{R}\left(\boldsymbol{\phi}^{k+1}\right) &= \delta\boldsymbol{R}\left(\boldsymbol{\phi}^{k}\right)\boldsymbol{R}\left(\boldsymbol{\phi}_{l_\Delta}\right) + \boldsymbol{R}\left(\boldsymbol{\phi}^{k}\right)\delta\boldsymbol{R}\left(\boldsymbol{\phi}_{l_\Delta}\right) \\
\Rightarrow \boldsymbol{R}\left(\boldsymbol{\phi}^{k+1}\right)\widetilde{\delta\boldsymbol{\theta}}_l^{k+1} &= \boldsymbol{R}\left(\boldsymbol{\phi}^{k}\right)\boldsymbol{R}\left(\boldsymbol{\phi}_{l_\Delta}\right)\widetilde{\delta\boldsymbol{\theta}}_{l_\Delta} \\
\Rightarrow \delta\boldsymbol{\theta}_l^{k+1} &= \delta\boldsymbol{\theta}_{l_\Delta} = \boldsymbol{G}_l\left(\boldsymbol{\phi}_{l_\Delta}\right)\delta\boldsymbol{\phi}_{l_\Delta} \\
\Rightarrow \delta\boldsymbol{\theta}_l^{k+1} &= \delta\boldsymbol{\theta}_{l_\Delta} = \delta\boldsymbol{\phi}_{l_\Delta}, \quad \forall\boldsymbol{\phi}_{l_\Delta} \to \boldsymbol{0}
\end{aligned} \tag{2.80}$$

where the below limitation is used

$$\lim_{\boldsymbol{\phi}_{l_\Delta}\to\boldsymbol{0}} \boldsymbol{G}_l\left(\boldsymbol{\phi}_{l_\Delta}\right) = \boldsymbol{I} \tag{2.81}$$

From (2.80), we can observe that for an infinitesimal increment of rotation in the local basis $\boldsymbol{\phi}_{l_\Delta} \to \boldsymbol{0}$, the virtual rotation vector at the next time step $\delta\boldsymbol{\theta}_l^{k+1}$, the virtual rotation vector associated with the rotation increment $\delta\boldsymbol{\theta}_{l_\Delta}$, and the variation of the rotation increment $\delta\boldsymbol{\phi}_{l_\Delta}$ are strictly equal to each other.

Replacing variation with time derivative in (2.80), yields

$$\begin{aligned}
\dot{\boldsymbol{R}}\left(\boldsymbol{\phi}^{k+1}\right) &= \cancel{\dot{\boldsymbol{R}}\left(\boldsymbol{\phi}^{k}\right)}\boldsymbol{R}\left(\boldsymbol{\phi}_{l_\Delta}\right) + \boldsymbol{R}\left(\boldsymbol{\phi}^{k}\right)\dot{\boldsymbol{R}}\left(\boldsymbol{\phi}_{l_\Delta}\right) \\
\Rightarrow \boldsymbol{R}\left(\boldsymbol{\phi}^{k+1}\right)\widetilde{\boldsymbol{\omega}}_l^{k+1} &= \boldsymbol{R}\left(\boldsymbol{\phi}^{k}\right)\boldsymbol{R}\left(\boldsymbol{\phi}_{l_\Delta}\right)\widetilde{\boldsymbol{\omega}}_{l_\Delta} \\
\Rightarrow \boldsymbol{\omega}_l^{k+1} &= \boldsymbol{\omega}_{l_\Delta} = \boldsymbol{G}_l\left(\boldsymbol{\phi}_{l_\Delta}\right)\dot{\boldsymbol{\phi}}_{l_\Delta} \\
\Rightarrow \boldsymbol{\omega}_l^{k+1} &= \boldsymbol{\omega}_{l_\Delta} \approx \dot{\boldsymbol{\phi}}_{l_\Delta}, \quad \forall \boldsymbol{\phi}_{l_\Delta} \approx \boldsymbol{0}
\end{aligned} \tag{2.82}$$

where $\boldsymbol{\omega}_{l_\Delta}$ is the local angular velocity vector associated with the rotation increment $\boldsymbol{\phi}_{l_\Delta}$. For a small rotation increment $\boldsymbol{\phi}_{l_\Delta} \approx \boldsymbol{0}$, the tangent operator can be approximated as identity matrix: $\boldsymbol{G}_l\left(\boldsymbol{\phi}_{l_\Delta} \approx \boldsymbol{0}\right) \approx \boldsymbol{I}$.

Note that $\boldsymbol{\omega}_{l_\Delta}$ should not be confused with the increment of the local angular velocity vector: $\Delta\boldsymbol{\omega}_l = \boldsymbol{\omega}_l^{k+1} - \boldsymbol{\omega}_l^k \neq \boldsymbol{\omega}_{l_\Delta}$. $\boldsymbol{\omega}_{l_\Delta} = \boldsymbol{\omega}_l^{k+1}$ is not an increment, but $\Delta\boldsymbol{\omega}_l$ is.

Similarly, $\dot{\boldsymbol{\phi}}_{l_\Delta} = \dfrac{\mathrm{d}}{\mathrm{d}t}\left(\boldsymbol{\phi}_{l_\Delta}\right)$ should not be confused with the increment of the time derivative of the rotation pseudovector: $\Delta\dot{\boldsymbol{\phi}} = \dot{\boldsymbol{\phi}}^{k+1} - \dot{\boldsymbol{\phi}}^k \neq \dot{\boldsymbol{\phi}}_{l_\Delta}$.

Applying time derivative to (2.82), the relations for the rotational acceleration can be readily derived as:

$$\dot{\boldsymbol{\omega}}_l^{k+1} = \dot{\boldsymbol{\omega}}_{l_\Delta} \approx \ddot{\boldsymbol{\phi}}_{l_\Delta}, \quad \forall \boldsymbol{\phi}_{l_\Delta} \approx \boldsymbol{0} \tag{2.83}$$

According to (2.80), (2.82) and (2.83), in the local incremental rotation update scheme, for convenience in the variation derivation and to ensure the clear physical interpretation of the generalized velocity of rotation, in the derivation process for linearizing the DAEs, the variations (infinitesimal increments) of rotation, rotational velocity and rotational acceleration are chosen as $\delta\boldsymbol{\theta}_l, \delta\boldsymbol{\omega}_l, \delta\dot{\boldsymbol{\omega}}_l$, respectively. In the time integration scheme, the finite increments of rotation, rotational velocity and rotational acceleration are discretized as $\boldsymbol{\phi}_{l_\Delta}, \Delta\boldsymbol{\omega}_l, \Delta\dot{\boldsymbol{\omega}}_l$, respectively.

The full picture of the utilized generalized coordinates is summarized as follows:

- The generalized coordinates for positions and rotations, the generalized velocities and the generalized accelerations of a multibody system are stored in vectors $\boldsymbol{q}$, $\dot{\boldsymbol{q}}$ and $\ddot{\boldsymbol{q}}$, respectively, as below [1]

$$\boldsymbol{q} = \left[\boldsymbol{r}_1^T, \boldsymbol{\rho}_1^T, \boldsymbol{r}_2^T, \boldsymbol{\rho}_2^T, \ldots, \boldsymbol{r}_n^T, \boldsymbol{\rho}_n^T\right]^T \in \mathbb{R}^{(3+4)n} \tag{2.84a}$$

$$\dot{\boldsymbol{q}} = \left[\dot{\boldsymbol{r}}_1^T, \boldsymbol{\omega}_{l_1}^T, \dot{\boldsymbol{r}}_2^T, \boldsymbol{\omega}_{l_2}^T, \ldots, \dot{\boldsymbol{r}}_n^T, \boldsymbol{\omega}_{l_n}^T\right]^T \in \mathbb{R}^{(3+3)n} \tag{2.84b}$$

$$\ddot{\boldsymbol{q}} = \left[\ddot{\boldsymbol{r}}_1^T, \dot{\boldsymbol{\omega}}_{l_1}^T, \ddot{\boldsymbol{r}}_2^T, \dot{\boldsymbol{\omega}}_{l_2}^T, \ldots, \ddot{\boldsymbol{r}}_n^T, \dot{\boldsymbol{\omega}}_{l_n}^T\right]^T \in \mathbb{R}^{(3+3)n} \tag{2.84c}$$

[1] For simplicity, we keep using the notations $\boldsymbol{q}$, $\dot{\boldsymbol{q}}$, and $\ddot{\boldsymbol{q}}$, while noting that they no longer represent one another's time derivatives. In detail, $\dot{\boldsymbol{q}} \neq \dfrac{\mathrm{d}\boldsymbol{q}}{\mathrm{d}t}$ and $\ddot{\boldsymbol{q}} \neq \dfrac{\mathrm{d}^2\boldsymbol{q}}{\mathrm{d}t^2}$.

- In the linearization process, the variations of generalized coordinates, generalized velocities and generalized accelerations are chosen as

$$\delta \boldsymbol{q} = \left[\delta \boldsymbol{r}_1^T, \delta \boldsymbol{\theta}_{l_1}^T, \delta \boldsymbol{r}_2^T, \delta \boldsymbol{\theta}_{l_2}^T, \ldots, \delta \boldsymbol{r}_n^T, \delta \boldsymbol{\theta}_{l_n}^T\right]^T \in \mathbb{R}^{(3+3)n} \tag{2.85a}$$

$$\delta \dot{\boldsymbol{q}} = \left[\delta \dot{\boldsymbol{r}}_1^T, \delta \boldsymbol{\omega}_{l_1}^T, \delta \dot{\boldsymbol{r}}_2^T, \delta \boldsymbol{\omega}_{l_2}^T, \ldots, \delta \dot{\boldsymbol{r}}_n^T, \delta \boldsymbol{\omega}_{l_n}^T\right]^T \in \mathbb{R}^{(3+3)n} \tag{2.85b}$$

$$\delta \ddot{\boldsymbol{q}} = \left[\delta \ddot{\boldsymbol{r}}_1^T, \delta \dot{\boldsymbol{\omega}}_{l_1}^T, \delta \ddot{\boldsymbol{r}}_2^T, \delta \dot{\boldsymbol{\omega}}_{l_2}^T, \ldots, \delta \ddot{\boldsymbol{r}}_n^T, \delta \dot{\boldsymbol{\omega}}_{l_n}^T\right]^T \in \mathbb{R}^{(3+3)n} \tag{2.85c}$$

- In the time integration scheme, the finite increments of generalized coordinates, generalized velocities and generalized accelerations are discretized as

$$\Delta \boldsymbol{q} = \left[\Delta \boldsymbol{r}_1^T, \boldsymbol{\phi}_{l_{\Delta 1}}^T, \Delta \boldsymbol{r}_2^T, \boldsymbol{\phi}_{l_{\Delta 2}}^T, \ldots, \Delta \boldsymbol{r}_n^T, \boldsymbol{\phi}_{l_{\Delta n}}^T\right]^T \in \mathbb{R}^{(3+3)n} \tag{2.86a}$$

$$\Delta \dot{\boldsymbol{q}} = \left[\Delta \dot{\boldsymbol{r}}_1^T, \Delta \boldsymbol{\omega}_{l_1}^T, \Delta \dot{\boldsymbol{r}}_2^T, \Delta \boldsymbol{\omega}_{l_2}^T, \ldots, \Delta \dot{\boldsymbol{r}}_n^T, \Delta \boldsymbol{\omega}_{l_n}^T\right]^T \in \mathbb{R}^{(3+3)n} \tag{2.86b}$$

$$\Delta \ddot{\boldsymbol{q}} = \left[\Delta \ddot{\boldsymbol{r}}_1^T, \Delta \dot{\boldsymbol{\omega}}_{l_1}^T, \Delta \ddot{\boldsymbol{r}}_2^T, \Delta \dot{\boldsymbol{\omega}}_{l_2}^T, \ldots, \Delta \ddot{\boldsymbol{r}}_n^T, \Delta \dot{\boldsymbol{\omega}}_{l_n}^T\right]^T \in \mathbb{R}^{(3+3)n} \tag{2.86c}$$

Since the angular velocity $\boldsymbol{\omega}_l$ cannot be directly integrated [11], a linear approximation must be assumed in the time integration as a compromise:

$$\boldsymbol{\phi}_{l_\Delta} \approx \boldsymbol{\omega}_l h \tag{2.87}$$

where h is the time step size.

The numerical error introduced by (2.87) increases with both the time step size h and the angular velocity $\boldsymbol{\omega}_l$, which restricts its applicability to dynamic systems operating at high rotational speeds.

2.7 Flexible structures

When the flexibility of components significantly influences the overall dynamics of multibody systems – such as when component deflections are non-negligible or the natural frequencies of the components are close to the bandwidth of external excitation – it is essential to account for these deflections during motion to accurately capture the dynamic response. This is commonly done by discretizing the components into finite elements.

In the engineering practice of flexible multibody system dynamics, the computational cost of long–term dynamic simulations often restricts the number of a system's DOFs , typically to the order of 10^2 to 10^3. When the physical DOFs of the system significantly exceed this range, modal reduction techniques are generally employed to reduce the number of DOFs. On contrary, if the physical DOFs fall within this range, it may be feasible to conduct the dynamics simulation directly.

2.7.1 Beam element models and formulations

In this section, a brief overview of beam element models and formulations aimed at wind turbine blades is presented. The main challenges and potential research directions are also highlighted.

Beam element models in structural mechanics

Modern wind turbine blades are long slender structures made of composite materials, most commonly glass fiber– or carbon fiber–reinforced polyester, to achieve a high stiffness–to–mass ratio [292]. The cross–sections are designed as aerodynamic airfoils to generate lift from wind inflow. These designs incorporate continuous and smooth distributions of chord, thickness and pretwist to achieve optimal angles of attack along the spanwise and include appropriate prebend out of the rotational plane to increase blade–to–tower clearance. Additionally, a slight presweep may be included to enhance aeroelastic stability. Ultimately, these designs, which involve composite materials and irregular airfoil geometries, result in complex inhomogeneous and anisotropic characteristics of the cross–sections and complicated three–dimensional bending–twist coupling of the blades.

It is straightforward to discretize wind turbine blades into beam elements to obtain an effective compromise between computational accuracy and efficiency. The Euler–Bernoulli beam element is the simplest discretization of blades, assuming that cross–sections remain rigid and perpendicular to the centerline after bending while neglecting the rotational inertia of the cross–sections. Incorporating the rotational inertia of cross-sections leads to the development of the Rayleigh beam element model. Furthermore, accounting for the shear distortion of cross–sections results in the Timoshenko beam element [107], which has been the mainstream beam element model used in the wind energy community, for instance, in *Bladed* [69], *HAWC2* [158], and *QBlade* [182].

By introducing polynomial functions to interpolate the displacement field along the reference line of a beam element, and by considering the internal force equilibrium equations and compatibility conditions at the two end nodes, the shape function matrix of classic three–dimensional Timoshenko beam elements can be derived [26]. This matrix can be further generalized by incorporating the intersecting coupling in the bending and shearing directions in the constitutive relation [172, 252]. This approach involves the use of the 6×6 *Fully Populated Matrix* (FPM) of cross–sectional stiffness properties. It is also possible to derive the exact shape functions for Timoshenko beam elements with tapered cross–sections [270]. However, in engineering practice, it is more common to approximate tapered cross–sections as uniform cross–sections by averaging their mass and stiffness properties [69, 5].

Several novel Timoshenko beam elements have been developed for application

in wind turbine blades. Kim et al. [154] extended the shape functions to arbitrary–order polynomials and derived the element stiffness and mass matrices based on pre–calculated anisotropic beam properties. Krenk and Couturier [155] developed a complementary–energy formulation for an inhomogeneous anisotropic beam element in which the element stiffness matrix is derived by employing equilibrium internal–force distributions without the need for polynomial shape functions. The proposed equilibrium–based beam element demonstrated superior accuracy in recovering cross–sectional internal forces when integrated with the in–house aeroelastic tool *BHawC* [234, 58].

The geometric stiffness term in beam element models for wind turbine blades, induced by heavy aerodynamic loading and centrifugal forces, is critically important for accurate simulation. A unified formulation of the Timoshenko geometric stiffness matrix has been derived via considering higher–order terms in the strain tensor [230], which results in larger displacement under high axial loads.

In principal, the reference line of a beam element can be aligned with arbitrary locations in the cross–sections, as long as the reference line is consistently specified along the blade spanwise and proper formulations are employed to account for the offsets of elastic centers, shear centers, mass centers and aerodynamic centers. In Bladed, the reference line is placed at the elastic centers, whereas in HAWC2, the half–chord points are chosen. OpenFAST, on the other hand, does not restrict the choice of the reference line. However, through comparisons between the beam element model, the three–dimensional shell element model, and experimental measurements on a blade test rig, Couturier et al. [57] proposed using the locus of the cross–sectional elastic energy centers as the reference line, yielding more accurate results than the traditional beam element model which employs the elastic centers as the reference line.

The blade structural damping is a critical factor in compensating for the little aeroelastic damping of the blade edgewise modes. An anisotropic stiffness–proportional damping model has been proposed to offer more flexibility in the parameter setting of the blade structural damping [114].

The cross–sectional mass and stiffness properties are required as input for the development of beam elements. Various cross–sectional analysis tools can be employed to compute these properties, including *VABS* [290], *BECAS* [32] and *ANBA4* [190, 300]. Typically, these tools account for the warping effect, as it can significantly influence the bending–twist coupling in the closed thin–walled beams [291, 32, 190]. However, in the implementation of Timoshenko beam elements within mainstream aeroelastic simulation tools used in the wind energy community, the warping effect is commonly neglected due to the rigid cross–section assumption [69, 158, 194, 182].

For very large modern wind turbines, obtaining consistent results from various aeroelastic tools remains a challenging task [105, 221, 55]. Despite numerous aspects related to aerodynamics and structural dynamics that can influence aeroelastic results, this inconsistency suggests that the structural model of long slender

blades requires further improvement. To this end, it is possible to update the beam element model using invertible neural networks to improve the agreement in numerical simulations [200].

Beam formulations in multibody dynamics

Wind turbine blades experience large out–of–plane deflections and free rotations under heavy aerodynamic loading during normal operation conditions, resulting in significant geometric nonlinearity from the perspective of flexible multibody system dynamics [96]. In the design phase of wind turbines, it is required to run thousands of load cases to account for all possible combinations throughout the turbine's lifetime [139]. Considering the design iterations involving aerodynamics, structures and controllers, extensive long–term dynamics simulations are necessary in the engineering practice of wind industry. It is essential that these computational tasks are finished with minimal intervention from engineers. Therefore, the computational efficiency and numerical robustness are of crucial importance for selecting the appropriate formulation to develop the equations of motion.

Since the 1980s, modal–based approaches have been extensively employed to formulate the equations of motion of blades in wind turbine aeroelastic simulation tools. Representative examples include *Flex5* [304, 42], various old versions of Bladed v3.x and FAST v7.x., and the ElastoDyn module in OpenFAST [194]. In the modal–based approach, modal shapes are employed as shape functions to interpolate the elastic deformations of blades. This method provides sufficient accuracy for short blades, even when blade torsional DOFs are neglected.

As blades get longer to reduce the levelized cost of electricity (LCOE), blade deflections go beyond the linear assumption region. Consequently, it becomes essential to divide the blade into multiple segments to accurately capture geometrical nonlinearities [97]. Concurrently, the *Floating Frame of Reference Formulation* (FFRF) is utilized to formulate the equations of motion involving large rotations [237]. In the FFRF, the rigid-body motion of the continuum is represented by the floating frame of reference, while the elastic deformations of the blade segments are described relative to the reference frame. The FFRF has been employed in both Bladed [69] and HAWC2 [158].

The greater the number of segments into which the blade is divided, the higher the accuracy achieved by the FFRF. In the extreme case where the number of segments equals the number of beam elements used for blade discretization, the FFRF becomes equivalent to the *CoRotational Formulation* (CRF). A key difference between FFRF and CRF is that, in FFRF, one floating frame of reference is shared by multiple elements, whereas, in CRF, each element has its own independent reference frame. An important motivation for developing CRF is to reuse the various existing small–strain elements that have been extensively developed in *Finite Element Method* (FEM) codes and apply them in the analysis of flexible

multibody system dynamics [80]. In the CRF, the motion of the continuum is also assumed to consist of rigid–body motion and pure elastic deformation. The rigid–body motion is represented by the shadow configuration. Rankin, Nour-Omid and coworkers [218, 201] developed projectors to achieve this motion decomposition, leading to the element–independent corotational formulation. Crisfield and coworkers [61, 62, 60] developed the consistent and unified CRF for solids, shells and beams. Felippa and Haugen [80] presented a unified theoretical framework for the CRF, in which they derived the element internal force and the consistent tangent stiffness matrix. They also discussed three variants of consistent CRF achieved through selective simplifications and highlighted several remaining open topics in the CRF domain. The proposed CRF [80] was applied to the analysis of rotating systems and demonstrated good accuracy [262]. Battini and Pacoste [10] introduced the warping effect into the corotational beam element by adding a seventh DOF at each node and applied this to buckling analysis. Wang et al. [279] discretized the mass distribution of beam elements into three lumped masses to obtain accurate inertial terms in the CRF. Moon et al. [137, 138] implemented a corotational anisotropic tapered beam element for the simulation of wind turbine blades, introducing an additional warping DOF at each node. The CRF has been utilized in the in–house aeroelastic tool BHawC [234] at Siemens Gamesa, as well as in the aeroelastic stability analysis tool *HAWCStab2* [70].

In both FFRF and CRF, the displacements and rotations of beam structure cross–sections are described relative to their respective reference frames, based on the small–strain linear assumption used in FEM. It is well known that three–dimensional finite rotations exhibit significant geometric nonlinearities and, therefore, can not be interpolated linearly. To address this issue, the *Geometrically Exact Beam Theory* (GEBT) describes the kinematics of cross–sections in an exact way, without any assumptions on the amplitude of rotations and cross–sectional strains. This approach leads to a general formulation but at the cost of increased complexity.

GEBT, also known as Simo–Reissner beam theory, was initially proposed by Reissner [219] and later extended by Simo [242, 243, 244] to address three–dimensional problems. Hodges and his coworkers [65, 126, 127] decomposed the three–dimensional problem into a linear, two–dimensional cross–sectional analysis and a geometrically exact nonlinear, one–dimensional beam analysis, applying this approach to the modeling of wind turbine blades [125]. The most significant challenge in the development of GEBT is the description and interpolation of finite rotations. Jelenić and Crisfield [144, 145] proposed an interpolation of current local rotations in a corotational manner to preserve the objectivity of strain measures. The kinematics of beam element cross-sections can be described on the special Euclidean group $SE(3)$, with an exponential mapping employed to interpolate and update the rotations [250, 233]. Additionally, the motion formalism can be employed to treat displacement and rotation fields in a unified manner, resulting in simpler

equations of motion with lower-order algebraic nonlinearities [109, 20]. Classic polynomials can be utilized as shape functions to interpolate displacement, rotation, and gradients along the beam element. Alternatively, using Lagrangian interpolants with node locations at the Gauss–Lobatto–Legendre points as shape functions results in the so-called Legendre spectral finite elements, which provide higher efficiency [147, 284, 283]. Furthermore, the isogeometric analysis (IGA) computational approach performs the interpolation based on non-uniform rational B-splines (NURBS) functions, thereby eliminating the discretization errors within finite element tools when geometries are imported from computer-aided design (CAD) models. As a result, this approach has gained increasing research interest [233, 261]. Warping and Wagner effects, which can be modeled by introducing additional DOFs to describe the corresponding deformations, are crucial for accurately modeling thin–walled rods under large bending–twist coupling deformations. Several scholars [48, 181, 233] have incorporated warping and Wagner effects with GEBT. However, it has been found that GEBT with warping effects cannot accurately capture the trailing edge local buckling phenomenon of wind turbine blades in case of significant local buckling when compared to results from a shell–element model [77]. GEBT has been used by various researchers to investigate the aeroelasticity of wind turbines [282, 179, 235, 174] and helicopters [128, 16, 240]. GEBT has also been implemented in aeroelastic simulation tools for wind turbines, such as the BeamDyn module in OpenFAST [194], Cp–Lambda [39], and hGAST [205].

Significant geometric nonlinearity is inherent in the three–dimensional finite rotation, introducing numerous challenges in rotation parametrization, interpolation, update, and the associated time integration scheme. These challenges are present in FFRF, CRF, and GEBT. The continuum mechanics based *Absolute Nodal Coordinate Formulation* (ANCF) completely bypasses the use of rotational DOFs, instead introducing the global position vector gradients as nodal coordinates. A characteristic feature and advantage of the ANCF beam element is its constant generalized mass matrix and the fact that the quadratic velocity term is identically zero. However, the generalized stiffness matrix incorporates significant nonlinearities due to large deformations and displacements, such as the geometric stiffening effect. Since ANCF does not include rotational coordinates, it is not straightforward to establish joint constraints between ANCF finite element nodes and other rigid bodies or classical element nodes with six rotational DOFs. This difficulty also applies to the imposition of concentrated moments at ANCF element nodes. The polar decomposition can be used to consistently establish algebraic constraints between position vector gradients and rotational coordinates, effectively addressing the setup of joint constraints and the imposition of concentrated moments [232]. As a continuum mechanics approach, ANCF is subject to Poisson locking, which leads to an overestimation of structural rigidity and failure to converge to the correct solution for thick beams. Selective reduced integration can be applied to eliminate the Poisson locking effect [92, 191]. By introducing additional DOFs to describe

cross–sectional shear, stretch, and deformations, the warping effect can be accurately modeled using ANCF beam elements [167, 258]. Bayoumy et al. [1, 25, 24] developed a structural dynamics model for wind turbine blades using ANCF thin plate elements and addressed slope discontinuities through the implementation of an intermediate coordinate system. In contrast, Nada [192] employed ANCF shell elements as an alternative approach. Sugiyama et al. [256] proposed an ANCF beam element with initially curved configurations. Yu et al. [289] introduced a variant of the ANCF beam element with variable cross-sections by incorporating higher–order nodal coordinates. For a comprehensive review of ANCF, readers are referred to [93, 202, 238]. It is noteworthy that, to date, there is no available ANCF beam element designed for aeroelastic dynamic simulations of wind turbine blades that feature initially curved and twisted configurations, variable irregular cross–sections, and inhomogeneous anisotropic material properties.

Both GEBT and ANCF describe the kinematics of beam cross–sections in the inertial frame and can accurately represent the finite rotation and deformation of beam elements. However, ANCF is inherently less accurate than GEBT due to differences in kinematic descriptions and is also more computationally intensive [231, 18]. Since both FFRF and CRF employ the small–strain linear assumption within finite elements, their accuracy is generally lower than that of GEBT and ANCF. Consequently, the order of numerical accuracy is typically as follows: GEBT > ANCF > CRF > FFRF. However, this ranking can be substantially influenced by the specific details of model assumptions and algorithm implementation.

Finally, a summary of the various beam element models and formulations employed in mainstream aeroelastic simulation tools within the wind energy community is provided in Table 2.2.

Future research

The location of the reference line at the cross-sections of beam elements affects the computational results of blade deflections [57], which could contribute to discrepancies among various aeroelastic simulation tools [221, 55].

The observation of local buckling at the trailing edge and macroscopic cross–sectional deformations — known as the ‘breathing effect’ — suggests that the warping and Wagner effects of cross–sections could be relevant for accurately calculating the large bending–twist coupling deflections of modern slender wind turbine blades.

Given its higher numerical accuracy and efficiency compared to ANCF, GEBT is the preferred formulation for highly accurate simulations.

A detailed three–dimensional shell element model of wind turbine blades could provide a reliable reference for verifying the deflection solutions of developed beam element models. Additionally, blade deflection measurements from test rigs and operating wind turbines can be employed to validate these beam element models.

Table 2.2: Overview of beam models and formulations used in aeroelastic simulation tools for wind turbine analysis.

Tool	Beam model	Formulation	Developer
Bladed	Timoshenko	FFRF, multi-segment	DNV
HAWC2	Timoshenko	FFRF, multi-segment	DTU[1]
HAWCStab2	Timoshenko	CRF	DTU[1]
QBlade	Timoshenko	CRF	TU Berlin[2]
BHawC	Timoshenko	CRF	Siemens Gamesa
Flex5	Modal element	FFRF	DTU[1]
OpenFAST (ElastoDyn)	Modal element	FFRF	NREL[3]
OpenFAST (BeamDyn)	Simo–Reissner	GEBT	NREL[3]
Cp-Lambda	Simo–Reissner	GEBT	Polimi[4]
hGAST	Simo–Reissner	GEBT	NTUA[5]

[1]DTU: Technical University of Denmark
[2]TU Berlin: Technical University of Berlin
[3]NREL: National Renewable Energy Laboratory
[4]Polimi: Polytechnic University of Milan
[5]NTUA: National Technical University of Athens

In summary, a high–precision GEBT–based tapered beam element that incorporates warping and Wagner effects, supports arbitrary cross–sections, accommodates inhomogeneous anisotropic material properties, and can handle initially curved and twisted configurations is necessary for achieving higher accuracy. Verification against high–fidelity shell element models and validation against measurements from test rigs and operating wind turbines are also required.

2.7.2 Corotational Timoshenko beam element

Although the brief review of beam element models and formulations in Section 2.7.1 suggests that GEBT provides the highest accuracy, we have chosen to use CRF to formulate the equations of motion for wind turbine blades and towers. This decision is based on a trade–off between numerical accuracy, computational efficiency, and robustness.

In this section, we revisit the corotational Timoshenko beam element to lay the foundation for the subsequent discussions in this thesis.

Timoshenko beam element

The classic Timoshenko beam element is directly incorporated with the CRF to model wind turbine blades; therefore, it is first recalled here.

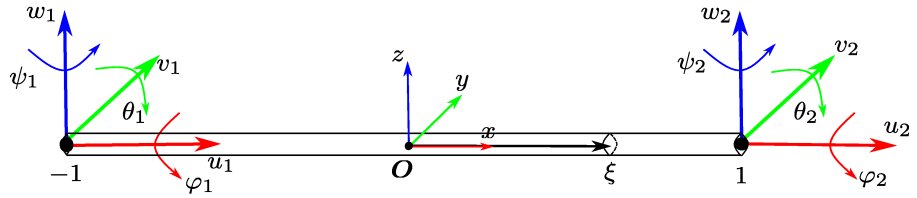

Figure 2.6: The displacement field of a 2–node three–dimensional Timoshenko beam element with length L. The dimensionless abscissa is defined as $\xi = 2x/L \in [-1, 1]$.

Considering a 2–node three–dimensional Timoshenko beam element illustrated in Figure 2.6, the nodal displacement vector $\boldsymbol{e}$ expressed in the element local coordinate system $Oxyz$ is denoted as

$$\boldsymbol{e} = \begin{bmatrix} u_1 & v_1 & w_1 & \varphi_1 & \theta_1 & \psi_1 & u_2 & v_2 & w_2 & \varphi_2 & \theta_2 & \psi_2 \end{bmatrix}^T \tag{2.88}$$

where $u_i, v_i, w_i, \varphi_i, \theta_i, \psi_i$ for $i = 1, 2$ are the displacements and rotations of the two nodes of the element.

In Timoshenko beam theory, the slope of the transverse displacement can be decomposed into two components [216]

$$\frac{\partial v}{\partial x} = \psi + \gamma_y \tag{2.89a}$$

$$\frac{\partial w}{\partial x} = -\theta + \gamma_z \tag{2.89b}$$

where θ, ψ are the pure rotation angles under bending moments about the y and z axes, respectively; γ_y, γ_z represent the shear strains under transverse forces along the y and z axes, respectively.

By introducing the generalized strain vector

$$\boldsymbol{\varepsilon} = \begin{bmatrix} \dfrac{\partial u}{\partial x} & \gamma_y & \gamma_z & \dfrac{\partial \varphi}{\partial x} & \dfrac{\partial \theta}{\partial x} & \dfrac{\partial \psi}{\partial x} \end{bmatrix}^T \tag{2.90}$$

and the vector of cross–sectional internal forces and moments

$$\boldsymbol{f}_{\text{sec}} = \begin{bmatrix} F_x & F_y & F_z & M_x & -M_y & -M_z \end{bmatrix}^T \tag{2.91}$$

the cross–sectional constitutive relation can be expressed as

$$\boldsymbol{f}_{\text{sec}} = \boldsymbol{K}_{\text{sec}} \boldsymbol{\varepsilon} \tag{2.92}$$

where $\boldsymbol{K}_{\text{sec}}$ is the cross–sectional stiffness matrix, which can be computed using cross–sectional analysis tools, for instance, BECAS [32] and VABS [290].

In general, $\boldsymbol{K}_{\text{sec}}$ is a 6×6 fully populated matrix (FPM) for anisotropic and inhomogeneous cross–sections of arbitrary geometry. As a standard implementation, the off–diagonal terms in $\boldsymbol{K}_{\text{sec}}$ are neglected, resulting in a diagonal stiffness matrix

$$\boldsymbol{K}_{\text{sec}} = \begin{bmatrix} EA & & & & & \\ & GA_y^s & & & & \\ & & GA_z^s & & & \\ & & & GI_p & & \\ & & & & EI_{yy} & \\ & & & & & EI_{zz} \end{bmatrix} \tag{2.93}$$

where EA represents the axial stiffness, GA_y^s, GA_z^s denote the shear stiffness along the y and z axes, respectively, GI_p is the torsional stiffness, and EI_{yy}, EI_{zz} are the bending stiffness about the y and z axes, respectively.

Shape functions The shape functions of the three–dimensional Timoshenko beam element are thoroughly introduced in Bazoune (2003) [26]. Since the cross–sectional stiffness matrix in (2.93) already includes integration over the cross–section, it is necessary to avoid duplicate integration which can be achieved by setting the transverse dimensionless abscissas $\eta = y/L$ and $\zeta = z/L$ in the formula (46) of Bazoune (2003) [26] to zero. Additionally, considering the definition of the axial dimensionless abscissa $\xi = 2x/L$ used here, as depicted in Figure 2.6, the displacements of a cross–section at position ξ can be interpolated using

$$u(\xi) = \frac{1}{2}(1-\xi)\,u_1 + \frac{1}{2}(1+\xi)\,u_2 \tag{2.94a}$$

$$\begin{aligned} v(\xi) = &-\frac{(\xi-1)\left(-\xi^2-\xi+2\Phi_y+2\right)}{4\left(\Phi_y+1\right)}v_1 - \frac{L\left(\xi^2-1\right)\left(\Phi_y-\xi+1\right)}{8\left(\Phi_y+1\right)}\psi_1 \\ &+\frac{(\xi+1)\left(-\xi^2+\xi+2\Phi_y+2\right)}{4\left(\Phi_y+1\right)}v_2 + \frac{L\left(\xi^2-1\right)\left(\Phi_y+\xi+1\right)}{8\left(\Phi_y+1\right)}\psi_2 \end{aligned} \tag{2.94b}$$

$$\begin{aligned} w(\xi) = &-\frac{(\xi-1)\left(-\xi^2-\xi+2\Phi_z+2\right)}{4\left(\Phi_z+1\right)}w_1 + \frac{L\left(\xi^2-1\right)\left(\Phi_z-\xi+1\right)}{8\left(\Phi_z+1\right)}\theta_1 \\ &+\frac{(\xi+1)\left(-\xi^2+\xi+2\Phi_z+2\right)}{4\left(\Phi_z+1\right)}w_2 - \frac{L\left(\xi^2-1\right)\left(\Phi_z+\xi+1\right)}{8\left(\Phi_z+1\right)}\theta_2 \end{aligned} \tag{2.94c}$$

where the two shear deformation parameters are given as

$$\Phi_y = \frac{12EI_{zz}}{GA_z^s L^2} \qquad\qquad \Phi_z = \frac{12EI_{yy}}{GA_y^s L^2} \tag{2.95}$$

The torsional angle φ at position ξ employs the same linear interpolation as the axial displacement

$$\varphi(\xi) = \frac{1}{2}(1-\xi)\,\varphi_1 + \frac{1}{2}(1+\xi)\,\varphi_2 \tag{2.96}$$

The rotational angles θ and ψ at position ξ can be interpolated using

$$\begin{aligned}\theta(\xi) = &-\frac{1}{2L}\left(3\xi^2-3\right)a_z w_1 + \left(\frac{1}{4}\left(3\xi^2-2\xi-1\right)a_z + \frac{1}{2}(-\xi+1)\,b_z\right)\theta_1 \\ &+ \frac{1}{2L}\left(3\xi^2-3\right)a_z w_2 + \left(\frac{1}{4}\left(3\xi^2+2\xi-1\right)a_z + \frac{1}{2}(\xi+1)\,b_z\right)\theta_2 \end{aligned} \tag{2.97a}$$

$$\begin{aligned}\psi(\xi) = &\frac{1}{2L}\left(3\xi^2-3\right)a_y v_1 + \left(\frac{1}{4}\left(3\xi^2-2\xi-1\right)a_y + \frac{1}{2}(-\xi+1)\,b_y\right)\psi_1 \\ &- \frac{1}{2L}\left(3\xi^2-3\right)a_y v_2 + \left(\frac{1}{4}\left(3\xi^2+2\xi-1\right)a_y + \frac{1}{2}(\xi+1)\,b_y\right)\psi_2 \end{aligned} \tag{2.97b}$$

where the four parameters are

$$a_y = \frac{1}{1+\Phi_y}, \qquad b_y = \frac{\Phi_y}{1+\Phi_y}, \qquad a_z = \frac{1}{1+\Phi_z}, \qquad b_z = \frac{\Phi_z}{1+\Phi_z} \tag{2.98}$$

By grouping the corresponding terms in equations (2.94), (2.96) and (2.97) according to the displacement vector $\boldsymbol{e}$, the cross–sectional displacements and rotations $\boldsymbol{u}(\xi) = [u, v, w, \varphi, \theta, \psi]^T$ can be written in the matrix form

$$\boldsymbol{u}(\xi) = \boldsymbol{N}(\xi)\boldsymbol{e} \tag{2.99}$$

where $\boldsymbol{N}(\xi)$ is the shape function matrix of size 6×12.

The shear strains γ_y and γ_z at position ξ can be interpolated using

$$\gamma_y(\xi) = -\frac{1}{L}b_y v_1 - \frac{1}{2}b_y\psi_1 + \frac{1}{L}b_y v_2 - \frac{1}{2}b_y\psi_2 \tag{2.100a}$$

$$\gamma_z(\xi) = -\frac{1}{L}b_z w_1 + \frac{1}{2}b_z\theta_1 + \frac{1}{L}b_z w_2 + \frac{1}{2}b_z\theta_2 \tag{2.100b}$$

From the equations in (2.100), it is observed that the shear strains γ_y and γ_z at position ξ are independent of the abscissa ξ, and thus remain constant along the beam element.This implies that the internal shear forces at an intermediate node, calculated from two adjacent beam elements with different cross–sections, may not be equal. Consequently, a smoothing algorithm is required in the post–processing phase to achieve an appropriate shear force distribution along the blade.

Applying derivative with respect to the axial coordinate x to equations (2.94a), (2.96) and (2.97), yields the axial strain $\epsilon_x = \partial u/\partial x$, the torsional rate $\kappa_x = \partial\varphi/\partial x$, and the curvatures $\kappa_y = \partial\theta/\partial y$ and $\kappa_z = \partial\psi/\partial z$, respectively. Additionally,

considering equations (2.100) and grouping the corresponding terms according to the displacement vector $\boldsymbol{e}$, the generalized strain vector $\boldsymbol{\varepsilon} = [\epsilon_x, \gamma_y, \gamma_z, \kappa_x, \kappa_y, \kappa_z]^T$ can be expressed as

$$\boldsymbol{\varepsilon}(\xi) = \boldsymbol{B}(\xi)\boldsymbol{e} \tag{2.101}$$

where $\boldsymbol{B}(\xi)$ is the strain–displacement relation matrix of size 6×12.

Element mass, stiffness and damping matrices The element consistent mass matrix $\boldsymbol{M}_{\text{ele}}$ of the classic Timoshenko beam element can be obtained by integration over the beam length

$$\boldsymbol{M}_{\text{ele}} = \int_{-1}^{1} \boldsymbol{N}(\xi)^T \boldsymbol{M}_{\text{sec}} \boldsymbol{N}(\xi) \mathrm{d}\xi \tag{2.102}$$

where $\boldsymbol{M}_{\text{sec}}$ is the cross–sectional mass matrix of size 6×6.

$\boldsymbol{M}_{\text{sec}}$ can also be computed using BECAS or VABS and can be expressed in the element local coordinate system $Oxyz$ as

$$\boldsymbol{M}_{\text{sec}} = \begin{bmatrix} \nu & 0 & 0 & 0 & \nu z_m & -\nu y_m \\ & \nu & 0 & -\nu z_m & 0 & 0 \\ & & \nu & \nu y_m & 0 & 0 \\ & & & J_{xx} & 0 & 0 \\ & \text{sym} & & & J_{yy} & -J_{yz} \\ & & & & & J_{zz} \end{bmatrix} \tag{2.103}$$

where ν is the mass per unit length of the cross–section, y_m and z_m represent the mass center offsets relative to the reference line of the beam element. J_{xx} is the polar moment of inertia per unit length, J_{yy} and J_{zz} are the mass moments of inertia per unit length about the y and z axes, respectively, and J_{yz} is the product mass moment of inertia per unit length.

When the element size is sufficiently fine to capture the significant modes that contribute to the dynamic response of the structure, the lumped mass approximation provides adequate accuracy and is simpler to implement. Consequently, it is preferred in our implementation.

The standard element stiffness matrix $\boldsymbol{K}_{\text{std}}$ of the classic Timoshenko beam element can be obtained by integration over the beam length

$$\boldsymbol{K}_{\text{std}} = \int_{-1}^{1} \boldsymbol{B}(\xi)^T \boldsymbol{K}_{\text{sec}} \boldsymbol{B}(\xi) \mathrm{d}\xi \tag{2.104}$$

The damping properties of wind turbine blades in the axial, flapwise, edgewise, and torsion directions can be different. Inspired by Hansen (2001) [114], a stiffness–proportional anisotropic damping model is utilized in this work. By introducing a

damping coefficient matrix $\boldsymbol{\beta}_{\text{dmp}} = \text{diag}\{\beta_a, \beta_y, \beta_z, \beta_t, \beta_z, \beta_y\}$, the cross–sectional damping matrix is constructed as

$$\boldsymbol{D}_{\text{sec}} = \boldsymbol{\beta}_{\text{dmp}}^T \boldsymbol{K}_{\text{sec}} \boldsymbol{\beta}_{\text{dmp}} \tag{2.105}$$

The coefficients β_a, β_y, β_z and β_t are used to tune the damping effects in the axial, bending about the z axis, bending about the y axis and torsional directions, respectively.

The element damping matrix $\boldsymbol{D}_{\text{std}}$ of the Timoshenko beam element can be obtained by integration over the beam length

$$\boldsymbol{D}_{\text{std}} = \int_{-1}^{1} \boldsymbol{B}(\xi)^T \boldsymbol{D}_{\text{sec}} \boldsymbol{B}(\xi) \text{d}\xi \tag{2.106}$$

The mass–proportional damping term is not included for wind turbine blades as it can damp the rigid–body motion of large rotations.

For a tapered beam element with different cross–sectional mass and stiffness properties at each end, it is equivalent to a beam element with constant cross-sectional properties, calculated as the mean values of the properties at the two ends.

In this study, the integrals required to compute the element mass, stiffness, and damping matrices from (2.102), (2.104) and (2.106) are evaluated analytically. The closed-form expressions are derived using MATLAB Symbolic Toolbox [143]. Due to their complexity, these expressions are not presented here for the sake of brevity.

Correction for shear center offsets The cross–section of wind turbine blades is irregular, as illustrated in Figure 2.7. The elastic center, mass center, shear center, aerodynamic center, and pitch axis do not coincide. The coordinates of the elastic center O_e are initialized with respect to the pitch axis coordinate system O_pyz. In our implementation of the beam element for wind turbine blades, the reference line is defined as the straight line connecting the elastic centers. The coordinate systems of the shear center O_syz, mass center O_myz, and aerodynamic center O_ayz, are defined relative to the elastic center coordinate system O_eyz.

To address the shear center offsets at the two end nodes of a beam element, a transformation matrix $\boldsymbol{T}_s$ is introduced [5]

$$\boldsymbol{T}_s = \begin{bmatrix} \boldsymbol{T}_{ax}\boldsymbol{T}_{s1} & 0 \\ 0 & \boldsymbol{T}_{ax}\boldsymbol{T}_{s2} \end{bmatrix} \tag{2.107}$$

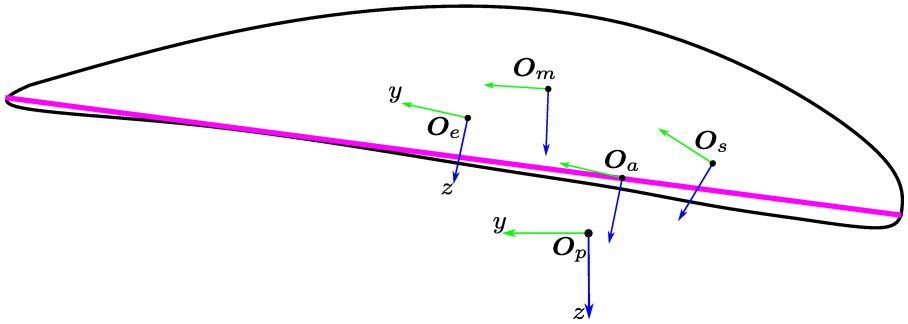

Figure 2.7: An airfoil cross–section of wind turbine blades.

where the sub matrices are given as

$$\boldsymbol{T}_{ax} = \begin{bmatrix} 1 & & & & & \\ & 1 & & & & \\ & & 1 & & & \\ & & & c_1 & & \\ & & & c_2 & 1 & \\ & & & c_3 & & 1 \end{bmatrix}, \quad \boldsymbol{T}_{si} = \begin{bmatrix} 1 & & & & & \\ & 1 & & -z_{si} & & \\ & & 1 & y_{si} & & \\ & & & 1 & & \\ & & & & 1 & \\ & & & & & 1 \end{bmatrix} \quad \text{for} \quad i = 1, 2 \tag{2.108}$$

with y_{si} and z_{si} being the shear center coordinates in the elastic center coordinate system O_eyz, and the three coefficients, c_1, c_2, c_3, being calculated as

$$\begin{aligned} c_1 = \frac{L_{s,yz}}{L}, \quad c_2 = \frac{(y_{s1} - y_{s2})\, L_{s,yz}}{L L_{s,y}}, \quad c_3 = \frac{z_{s1} - z_{s2}}{L_{s,y}}, \\ L_{s,y} = \sqrt{L^2 + (y_{s1} - y_{s2})^2}, \quad L_{s,yz} = \sqrt{L_{s,y}^2 + (z_{s1} - z_{s2})^2} \end{aligned} \tag{2.109}$$

The transformation matrix $\boldsymbol{T}_s$ is applied to the standard element stiffness matrix $\boldsymbol{K}_{\text{std}}$ in (2.104) and the element damping matrix $\boldsymbol{D}_{\text{std}}$ in (2.106), resulting in the final element stiffness and damping matrices, respectively

$$\boldsymbol{K}_{\text{ele}} = \boldsymbol{T}_s^T \boldsymbol{K}_{\text{std}} \boldsymbol{T}_s \tag{2.110}$$

$$\boldsymbol{D}_{\text{ele}} = \boldsymbol{T}_s^T \boldsymbol{D}_{\text{std}} \boldsymbol{T}_s \tag{2.111}$$

FPM stiffness property If the cross–sectional stiffness matrix $\boldsymbol{K}_{\text{sec}}$ is evaluated at the elastic center along the principal axis and expressed in the FPM form, it

becomes [32]

$$\boldsymbol{K}_{\text{sec}} = \begin{bmatrix} EA & 0 & 0 & 0 & 0 & 0 \\ & GA_y^s & k_{vw} & k_{v\varphi} & 0 & 0 \\ & & GA_z^s & k_{w\varphi} & 0 & 0 \\ & & & GI_p & 0 & 0 \\ & \text{sym} & & & EI_{yy} & 0 \\ & & & & & EI_{zz} \end{bmatrix} \tag{2.112}$$

where the coupling terms between shear and torsion, k_{vw}, $k_{v\varphi}$ and $k_{w\varphi}$, are present.

The cross-sectional FPM stiffness matrix $\boldsymbol{K}_{\text{sec}}$ in (2.112) must be incorporated into Equation (2.104) to compute the element stiffness matrix $\boldsymbol{K}_{\text{std}}$.

Considering equations (2.92) and (2.112), and remembering the relationship between the bending moment and the shear force $F = \mathrm{d}M/\mathrm{d}x$, the shear forces in the y and z axes can be expressed, respectively, as

$$F_y = \frac{\mathrm{d}M_z}{\mathrm{d}x} = GA_y^s\gamma_y + k_{vw}\gamma_z + k_{v\varphi}\kappa_x \tag{2.113a}$$

$$F_z = -\frac{\mathrm{d}M_y}{\mathrm{d}x} = k_{vw}\gamma_y + GA_z^s\gamma_z + k_{w\varphi}\kappa_x \tag{2.113b}$$

Equation (2.113a) differs from Equation (18) in Bazoune (2003) [26], rendering the interpolation relations in (2.94b) and (2.94c) invalid. Therefore, the shape function matrix $\boldsymbol{N}$ and the strain–displacement relation matrix $\boldsymbol{B}$ must be updated, as proposed in [252]. The closed–form expression of the element stiffness matrix, $\boldsymbol{K}$, computed with the cross–sectional FPM stiffness matrix, is exceedingly complex. Alternatively, it can be evaluated using numerical integration methods, such as Gauss-Legendre quadrature (see Appendix A.2). In our implementation, four Gauss-Legendre quadrature points are used to ensure sufficient accuracy.

Corotational formulation

In this section, we revisit a simplified version of the corotational formulation, which is easy to implement and provides a good trade–off between numerical accuracy, computational efficiency, and robustness.

The concept of the CRF for a beam element is illustrated in Figure 2.8. In the CRF, the gross motion of the beam element is decomposed into two components: the rigid–body motion represented by the reference frame F, and the small–strain elastic deformation described in the local basis of frame F. The reference frame F brings the continuum from the initial configuration $\mathcal{C}_0$ to the intermediate *shadow* configuration $\mathcal{C}_S$. The elastic deformation is measured at the deformed configuration $\mathcal{C}_D$ with respect to the shadow configuration $\mathcal{C}_S$.

The reference frame F is placed at the midpoint of the beam element's reference line AB. The X axis is defined as the vector from node A to node B, while the Y

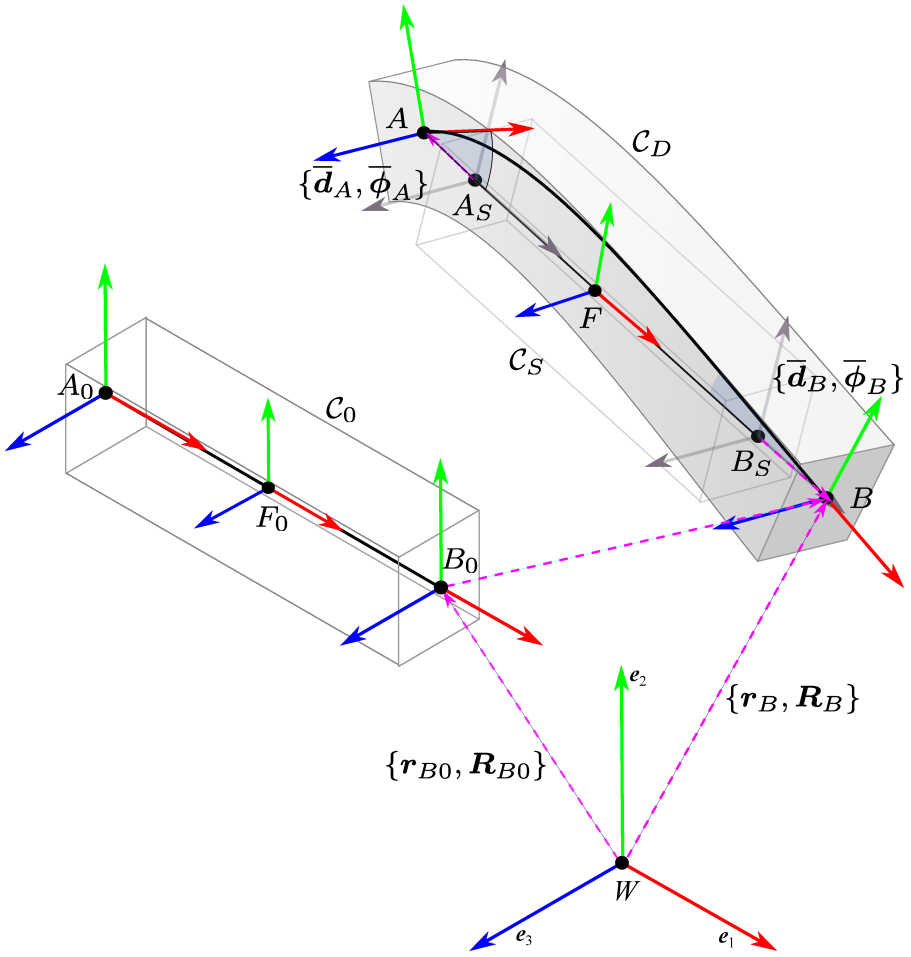

Figure 2.8: A scheme of the corotational formulation for a beam element.

axis is determined as the average direction of the Y axes of the two nodal frames A and B.

$$\boldsymbol{x}_F = \boldsymbol{r}_B - \boldsymbol{r}_A \tag{2.114a}$$

$$\boldsymbol{y}_F = \boldsymbol{R}_A \boldsymbol{R}_{A_0}^T \boldsymbol{y}_I + \boldsymbol{R}_B \boldsymbol{R}_{B_0}^T \boldsymbol{y}_I \tag{2.114b}$$

where $\boldsymbol{R}_{A_0}$ and $\boldsymbol{R}_{B_0}$ are the rotation matrices of the two nodal frames A and B in the initial configuration $\mathcal{C}_0$, respectively. The vector $\boldsymbol{y}_I = [0, 1, 0]^T$ represents the unit vector along the Y axis.

In case of curved beams or bending deflections, the mean Y axis does not lie in the plane orthogonal to the X axis. Consequently, the Gram–Schmidt orthogonalization is employed to determine the proper Y axis and the remaining Z axis, ultimately resulting in the rotation matrix of the reference frame F after normalizing to unit length: $\boldsymbol{R}_F = [\boldsymbol{x}_F, \boldsymbol{y}_F, \boldsymbol{z}_F]$. Whenever the beam element moves, the reference frame F is updated accordingly.

Local displacements The local position vectors of nodes A and B in the reference frame F remain constant in both the initial configuration $\mathcal{C}_0$ and the shadow configuration $\mathcal{C}_S$. This implies that

$$\boldsymbol{R}_F^T\left(\boldsymbol{r}_{A_S}-\boldsymbol{r}_F\right)=\boldsymbol{R}_{F_0}^T\left(\boldsymbol{r}_{A_0}-\boldsymbol{r}_{F_0}\right) \tag{2.115a}$$

$$\boldsymbol{R}_F^T\left(\boldsymbol{r}_{B_S}-\boldsymbol{r}_F\right)=\boldsymbol{R}_{F_0}^T\left(\boldsymbol{r}_{B_0}-\boldsymbol{r}_{F_0}\right) \tag{2.115b}$$

The elastic displacements of nodes A and B in the reference frame F can be computed as

$$\overline{\boldsymbol{d}}_A=\boldsymbol{R}_F^T\left(\boldsymbol{r}_A-\boldsymbol{r}_{A_S}\right)=\boldsymbol{R}_F^T\left(\boldsymbol{r}_A-\boldsymbol{r}_F\right)-\boldsymbol{R}_{F_0}^T\left(\boldsymbol{r}_{A_0}-\boldsymbol{r}_{F_0}\right) \tag{2.116a}$$

$$\overline{\boldsymbol{d}}_B=\boldsymbol{R}_F^T\left(\boldsymbol{r}_B-\boldsymbol{r}_{B_S}\right)=\boldsymbol{R}_F^T\left(\boldsymbol{r}_B-\boldsymbol{r}_F\right)-\boldsymbol{R}_{F_0}^T\left(\boldsymbol{r}_{B_0}-\boldsymbol{r}_{F_0}\right) \tag{2.116b}$$

which can be further simplified as

$$\overline{\boldsymbol{d}}_A=\boldsymbol{R}_F^T\boldsymbol{r}_A-\boldsymbol{R}_{F_0}^T\boldsymbol{r}_{A_0} \tag{2.117a}$$

$$\overline{\boldsymbol{d}}_B=\boldsymbol{R}_F^T\boldsymbol{r}_B-\boldsymbol{R}_{F_0}^T\boldsymbol{r}_{B_0} \tag{2.117b}$$

since the movement of the reference frame F does not contribute to the internal elastic forces.

The computation of rotational displacements is more complex. Considering node B as an example, the incremental rotation from frame B_S to frame B, parameterized using the quaternion $\boldsymbol{\rho}_{a_\Delta}$, can be computed as

$$\boldsymbol{\rho}_{a_\Delta}=\boldsymbol{\rho}_B\boldsymbol{\rho}_{B_S}^* \tag{2.118}$$

where the subscript 'a' indicates that the incremental rotation is conducted around fixed axes in the inertial frame W.

The relative rotation of frame B_S with respect to frame F remains constant in the initial configuration $\mathcal{C}_0$ and the shadow configuration $\mathcal{C}_S$. Therefore, we have $\boldsymbol{\rho}_F^*\boldsymbol{\rho}_{B_S}=\boldsymbol{\rho}_{F_0}^*\boldsymbol{\rho}_{B_0}$, leading to

$$\boldsymbol{\rho}_{B_S}^*=\boldsymbol{\rho}_{B_0}^*\boldsymbol{\rho}_{F_0}\boldsymbol{\rho}_F^* \tag{2.119}$$

Substituting (2.119) into (2.118), and introducing the rotation pseudovector $\boldsymbol{\phi}_{a_\Delta}$ to describe the incremental rotation: $\boldsymbol{\rho}_{a_\Delta}=\left(0,\frac{1}{2}\boldsymbol{\phi}_{a_\Delta}\right)$, we obtain

$$\left(0,\frac{1}{2}\boldsymbol{\phi}_{a_\Delta}\right)=\boldsymbol{\rho}_B\boldsymbol{\rho}_{B_0}^*\boldsymbol{\rho}_{F_0}\boldsymbol{\rho}_F^* \tag{2.120}$$

Let $\overline{\boldsymbol{\phi}}_B$ represent the incremental rotation pseudovector expressed in the local basis of the reference frame F. Using quaternion to perform the transformation, we obtain

$$\left(0,\boldsymbol{\phi}_{a_\Delta}\right)=\boldsymbol{\rho}_F\left(0,\overline{\boldsymbol{\phi}}_B\right)\boldsymbol{\rho}_F^* \tag{2.121}$$

From (2.120) and (2.121), we can easily derive

$$\left(0, \frac{1}{2}\overline{\boldsymbol{\phi}}_B\right) = \boldsymbol{\rho}_F^* \boldsymbol{\rho}_B \boldsymbol{\rho}_{B_0}^* \boldsymbol{\rho}_{F_0} = \boldsymbol{\rho}_{l_\Delta} \tag{2.122}$$

where $\boldsymbol{\rho}_{l_\Delta}$ is introduced to represent the incremental rotation expressed in the local frame F.

As follows, the local incremental rotation pseudovector $\overline{\boldsymbol{\phi}}_B$ can be computed from quaternion $\boldsymbol{\rho}_{l_\Delta}$ using formula (2.21). The local incremental rotation pseudovector $\overline{\boldsymbol{\phi}}_A$ for node A can be obtained using the same procedure.

The local elastic displacement vector of the beam element is then obtained

$$\overline{\boldsymbol{d}} = \begin{bmatrix} \overline{\boldsymbol{d}}_A^T & \overline{\boldsymbol{\phi}}_A^T & \overline{\boldsymbol{d}}_A^T & \overline{\boldsymbol{\phi}}_B^T \end{bmatrix}^T \tag{2.123}$$

Assuming the beam element strain is small, the local elastic displacement vector $\overline{\boldsymbol{d}}$ is identical to the nodal displacement vector $\boldsymbol{e}$ in (2.88).

Corotational transformation The local internal elastic forces of the beam element can be computed as $\overline{\boldsymbol{f}}_e = -\boldsymbol{K}_{\text{ele}}\overline{\boldsymbol{d}}$. Since we place the internal elastic forces on the right–hand side of the equations of motion in (2.70a), a minus sign is introduced in front of $\overline{\boldsymbol{f}}_e$.

It is essential to transform the local internal forces to the global reference frame. This means that the translational components are expressed in the reference frame F, while the rotational components are expressed in the inertial frame W. This transformation can be achieved using projectors [80, 263]. In this work, a significant simplification is implemented by introducing the following corotational transformation matrix

$$\boldsymbol{R}_\Diamond = \begin{bmatrix} \boldsymbol{R}_F & & & \\ & \boldsymbol{R}_A^T\boldsymbol{R}_F & & \\ & & \boldsymbol{R}_F & \\ & & & \boldsymbol{R}_B^T\boldsymbol{R}_F \end{bmatrix} \tag{2.124}$$

The global internal elastic forces are then computed as

$$\boldsymbol{f}_e = -\boldsymbol{R}_\Diamond \overline{\boldsymbol{f}}_e = -\boldsymbol{R}_\Diamond \boldsymbol{K}_{\text{ele}} \overline{\boldsymbol{d}} \tag{2.125}$$

The tangent mass, damping and stiffness matrices are computed respectively as

$$\boldsymbol{M} = \boldsymbol{R}_\Diamond \boldsymbol{M}_{\text{ele}} \boldsymbol{R}_\Diamond^T \tag{2.126a}$$

$$\boldsymbol{D}_m = \boldsymbol{R}_\Diamond \boldsymbol{D}_{\text{ele}} \boldsymbol{R}_\Diamond^T \tag{2.126b}$$

$$\boldsymbol{K}_m = \boldsymbol{R}_\Diamond \boldsymbol{K}_{\text{ele}} \boldsymbol{R}_\Diamond^T \tag{2.126c}$$

where $\boldsymbol{M}_{\text{ele}}$, $\boldsymbol{D}_{\text{ele}}$ and $\boldsymbol{K}_{\text{ele}}$ are the beam element mass, damping and stiffness matrices computed from equations (2.102), (2.111) and (2.110), respectively.

Assuming that the mass and inertia of a beam element are concentrated at its two end nodes, the tangent mass matrix can be explicitly formulated. For instance, for one of the element nodes, it can be expressed as

$$\boldsymbol{M} = \begin{bmatrix} \nu \boldsymbol{I} & \nu \boldsymbol{R} \widetilde{\boldsymbol{s}}_l^T \\ \nu \widetilde{\boldsymbol{s}}_l \boldsymbol{R}^T & \boldsymbol{J}_l \end{bmatrix} \tag{2.127}$$

where ν is the lumped mass, $\boldsymbol{R}$ represents the rotation matrix of the nodal frame. $\boldsymbol{s}_l = [0, y_m, z_m]^T$ is the offset vector of the cross–sectional mass center in the nodal frame. $\boldsymbol{J}_l$ is the inertia tensor lumped at the beam node and evaluated in the nodal frame.

Under centrifugal forces and aerodynamic loads along the blade, the intense internal stress results in significant geometric stiffening. This greatly affects blade deflections, especially those out of the rotor plane. In contrast, the internal stress introduces a geometric softening effect on wind turbine towers under gravitational forces, consequently reducing their ultimate buckling loads. The geometric stiffening or softening effect is essential for accurate simulations. By introducing higher–order terms in the strain tensor, the geometric stiffness matrix of the Timoshenko beam element has been derived [230]. However, for simplicity, we utilize the geometric stiffness matrix of the Euler–Bernoulli plane beam element [216] and extend it to the three–dimensional form, denoted as $\boldsymbol{K}_{g_{\text{std}}}$. The same correction for shear center offsets and corotational transformation are applied to obtain the tangent geometric stiffness matrix as below

$$\boldsymbol{K}_g = \boldsymbol{R}_\diamondsuit \boldsymbol{T}_s^T \boldsymbol{K}_{g_{\text{std}}} \boldsymbol{T}_s \boldsymbol{R}_\diamondsuit^T \tag{2.128}$$

The global internal damping forces can be computed as

$$\boldsymbol{f}_d = -\boldsymbol{D}_m \dot{\boldsymbol{q}} \tag{2.129}$$

where $\dot{\boldsymbol{q}}$ is the generalized velocity given as (2.84b).

Based on the lumped mass assumption, the quadratic velocity terms at one node, composed of the centrifugal forces and gyroscopic torques, can be computed as

$$\boldsymbol{f}_v = \begin{pmatrix} -\nu \boldsymbol{R} \widetilde{\boldsymbol{\omega}}_l \widetilde{\boldsymbol{\omega}}_l \boldsymbol{s}_l \\ -\widetilde{\boldsymbol{\omega}}_l \boldsymbol{J}_l \boldsymbol{\omega}_l \end{pmatrix} \tag{2.130}$$

By considering the expressions of the tangent mass matrix (2.126a) or (2.127), the generalized acceleration (2.84c), the internal elastic forces (2.125), the internal damping forces (2.129) and the quadratic velocity terms (2.130), the equations of motion of a beam structure can be expressed in the form of (2.70).

Inertial damping and stiffness matrices The inertial damping and stiffness matrices can be relevant to the numerical convergence of the time integration for those systems operating at high rotational speeds. In the modal analysis of rotor dynamics, they are also required, particularly the inertial damping matrix as it can affect the stability assessment significantly.

By considering the expressions in (2.127), (2.84c) and (2.130), the complete inertial forces lumped at one node can be computed as

$$\boldsymbol{f}_i = \boldsymbol{M}\left(\boldsymbol{q}\right)\ddot{\boldsymbol{q}} - \boldsymbol{f}_v = \begin{pmatrix} \nu\ddot{\boldsymbol{r}} + \nu\boldsymbol{R}\widetilde{\boldsymbol{s}}_l^T\dot{\boldsymbol{\omega}}_l + \nu\boldsymbol{R}\widetilde{\boldsymbol{\omega}}_l\widetilde{\boldsymbol{\omega}}_l\boldsymbol{s}_l \\ \nu\widetilde{\boldsymbol{s}}_l\boldsymbol{R}^T\ddot{\boldsymbol{r}} + \boldsymbol{J}_l\dot{\boldsymbol{\omega}}_l + \widetilde{\boldsymbol{\omega}}_l\boldsymbol{J}_l\boldsymbol{\omega}_l \end{pmatrix} \tag{2.131}$$

Applying variations to (2.131), and using the algebra properties in (2.1), and also recalling the equation (2.15b), the inertial forces $\boldsymbol{f}_i$ can be linearized as

$$\delta\boldsymbol{f}_i = \boldsymbol{M}\begin{pmatrix}\delta\ddot{\boldsymbol{r}} \\ \delta\dot{\boldsymbol{\omega}}_l\end{pmatrix} + \boldsymbol{D}_i\begin{pmatrix}\delta\dot{\boldsymbol{r}} \\ \delta\boldsymbol{\omega}_l\end{pmatrix} + \boldsymbol{K}_i\begin{pmatrix}\delta\boldsymbol{r} \\ \delta\boldsymbol{\theta}_l\end{pmatrix} \tag{2.132}$$

where the inertial damping matrix is expressed as

$$\boldsymbol{D}_i = \begin{bmatrix}\boldsymbol{0} & -\nu\boldsymbol{R}\left(\widetilde{\boldsymbol{\omega}}_l\widetilde{\boldsymbol{s}}_l + \widetilde{\widetilde{\boldsymbol{\omega}}_l\boldsymbol{s}_l}\right) \\ \boldsymbol{0} & \widetilde{\boldsymbol{\omega}}_l\boldsymbol{J}_l - \widetilde{\boldsymbol{J}_l\boldsymbol{\omega}_l}\end{bmatrix} \tag{2.133}$$

and the inertial stiffness matrix is expressed as

$$\boldsymbol{K}_i = \begin{bmatrix}\boldsymbol{0} & -\nu\boldsymbol{R}\left(\widetilde{\widetilde{\boldsymbol{\omega}}_l\boldsymbol{s}_l} + \widetilde{\widetilde{\boldsymbol{\omega}}_l\widetilde{\boldsymbol{\omega}}_l\boldsymbol{s}_l}\right) \\ \boldsymbol{0} & \nu\widetilde{\boldsymbol{s}}_l\widetilde{\boldsymbol{R}^T\ddot{\boldsymbol{r}}}\end{bmatrix} \tag{2.134}$$

The inertial stiffness matrix can be split into two components by separating the inertial forces $\boldsymbol{M}\left(\boldsymbol{q}\right)\ddot{\boldsymbol{q}}$ and $\boldsymbol{f}_v$

$$\boldsymbol{K}_i = \boldsymbol{K}_{i,1} + \boldsymbol{K}_{i,2} \tag{2.135}$$

where

$$\boldsymbol{K}_{i,1} = -\frac{\partial\boldsymbol{f}_v}{\partial\boldsymbol{q}} = \begin{bmatrix}\boldsymbol{0} & -\nu\boldsymbol{R}\widetilde{\widetilde{\boldsymbol{\omega}}_l\widetilde{\boldsymbol{\omega}}_l\boldsymbol{s}_l} \\ \boldsymbol{0} & \boldsymbol{0}\end{bmatrix} \tag{2.136a}$$

$$\boldsymbol{K}_{i,2} = \frac{\partial\left(\boldsymbol{M}\left(\boldsymbol{q}\right)\ddot{\boldsymbol{q}}\right)}{\partial\boldsymbol{q}} = \begin{bmatrix}\boldsymbol{0} & -\nu\boldsymbol{R}\widetilde{\widetilde{\boldsymbol{\omega}}_l\boldsymbol{s}_l} \\ \boldsymbol{0} & \nu\widetilde{\boldsymbol{s}}_l\widetilde{\boldsymbol{R}^T\ddot{\boldsymbol{r}}}\end{bmatrix} \tag{2.136b}$$

It is worth noting that the inertial damping and stiffness matrices in (2.133) and (2.134) represent generic expressions. In the special case where the mass center

is aligned with the axis of rotation, resulting in $\boldsymbol{s}_l = \boldsymbol{0}$, these matrices reduce to simpler expressions as follows

$$\boldsymbol{D}_i = \begin{bmatrix} \boldsymbol{0} & \boldsymbol{0} \\ \boldsymbol{0} & \widetilde{\boldsymbol{\omega}}_l \boldsymbol{J}_l - \widetilde{\boldsymbol{J}_l \boldsymbol{\omega}_l} \end{bmatrix} \tag{2.137a}$$

$$\boldsymbol{K}_i = \begin{bmatrix} \boldsymbol{0} & \boldsymbol{0} \\ \boldsymbol{0} & \boldsymbol{0} \end{bmatrix} \tag{2.137b}$$

where the inertial stiffness matrix $\boldsymbol{K}_i$ becomes zero, while the inertial damping matrix $\boldsymbol{D}_i$, consisting solely of gyroscopic terms, can be called the gyroscopic damping matrix and remains nonzero.

2.8 Time integrator

The DAEs of flexible multibody systems are of index–3, making them challenging to integrate. The *Minimal Coordinate Set* (MCS) approach can be employed to eliminate the algebraic constraint equations [185, 298]. Alternatively, the *Redundant Coordinate Set* (RCS) approach has been developed, providing an additional advantage of straightforwardly extracting reaction forces at the joints. In our work, we choose to use the RCS approach.

This section provides a concise introduction to the Hilber-Hughes-Taylor (HHT) integration scheme, as proposed by Negrut [196].

The HHT integrator calculates the discretized position and velocity using two parameters β and γ, as below

$$\begin{cases} \boldsymbol{q}^{k+1} = \boldsymbol{q}^k + h\dot{\boldsymbol{q}}^k + \dfrac{h^2}{2}\left[(1-2\beta)\,\ddot{\boldsymbol{q}}^k + 2\beta\ddot{\boldsymbol{q}}^{k+1}\right] & \text{(2.138a)} \\ \dot{\boldsymbol{q}}^{k+1} = \dot{\boldsymbol{q}}^k + h\left[(1-\gamma)\,\ddot{\boldsymbol{q}}^k + \gamma\ddot{\boldsymbol{q}}^{k+1}\right] & \text{(2.138b)} \\ t^{k+1} = t^k + h & \text{(2.138c)} \end{cases}$$

where the parameters are given as

$$\gamma = \frac{1-2\alpha}{2} \qquad \beta = \frac{(1-\alpha)^2}{4} \tag{2.139}$$

with a user input parameter $\alpha \in [-\dfrac{1}{3}, 0]$ to control the numerical damping of the time integration.

In Equations (2.138a) and (2.138b), the position $\boldsymbol{q}^{k+1}$ and the velocity $\dot{\boldsymbol{q}}^{k+1}$ are functions of the acceleration $\ddot{\boldsymbol{q}}^{k+1}$.

The DAEs in (2.70) can be discretized as

$$\begin{cases} (\boldsymbol{M}\ddot{\boldsymbol{q}})^{k+1} + (1+\alpha)\left(\boldsymbol{C}_{\boldsymbol{q}}^T\boldsymbol{\gamma} - \boldsymbol{f}\right)^{k+1} - \alpha\left(\boldsymbol{C}_{\boldsymbol{q}}^T\boldsymbol{\gamma} - \boldsymbol{f}\right)^{k} = \boldsymbol{0} & \text{(2.140a)} \\ \boldsymbol{c}^{k+1} = \boldsymbol{0} & \text{(2.140b)} \end{cases}$$

The residual vector of the equations in (2.140), denoted as $\boldsymbol{G} = \left[\boldsymbol{G}_{\boldsymbol{f}}^T, \boldsymbol{G}_{\boldsymbol{c}}^T\right]^T$, is computed as

$$\boldsymbol{G}_{\boldsymbol{f}} = \frac{1}{1+\alpha}\left(\boldsymbol{M}\ddot{\boldsymbol{q}}\right)^{k+1} + \left(\boldsymbol{C}_{\boldsymbol{q}}^T\boldsymbol{\gamma} - \boldsymbol{f}\right)^{k+1} - \frac{\alpha}{1+\alpha}\left(\boldsymbol{C}_{\boldsymbol{q}}^T\boldsymbol{\gamma} - \boldsymbol{f}\right)^{k} \tag{2.141a}$$

$$\boldsymbol{G}_{\boldsymbol{c}} = \boldsymbol{c}^{k+1} \tag{2.141b}$$

where $\boldsymbol{G}_{\boldsymbol{f}}$ is the residual of force equilibrium equations of the system, and $\boldsymbol{G}_{\boldsymbol{c}}$ is the residual of constraint equations.

To satisfy $\boldsymbol{G} = \boldsymbol{0}$, the Newton–Raphson iteration is commonly used to solve for the proper updated acceleration and Lagrange multipliers $\ddot{\boldsymbol{q}}^{k+1}, \boldsymbol{\gamma}^{k+1}$:

$$\begin{bmatrix} \dfrac{\partial \boldsymbol{G}_{\boldsymbol{f}}}{\partial \ddot{\boldsymbol{q}}} & \dfrac{\partial \boldsymbol{G}_{\boldsymbol{f}}}{\partial \boldsymbol{\gamma}} \\ \dfrac{\partial \boldsymbol{G}_{\boldsymbol{c}}}{\partial \ddot{\boldsymbol{q}}} & \dfrac{\partial \boldsymbol{G}_{\boldsymbol{c}}}{\partial \boldsymbol{\gamma}} \end{bmatrix}_n^{k+1} \begin{pmatrix} \Delta^{\mathrm{NR}}\ddot{\boldsymbol{q}}^{k+1} \\ \Delta^{\mathrm{NR}}\boldsymbol{\gamma}^{k+1} \end{pmatrix} + \boldsymbol{G}\left(\boldsymbol{q}_n^{k+1}, \dot{\boldsymbol{q}}_n^{k+1}, \ddot{\boldsymbol{q}}_n^{k+1}, \boldsymbol{\gamma}_n^{k+1}\right) = \boldsymbol{0} \tag{2.142}$$

where $\Delta^{\mathrm{NR}}\ddot{\boldsymbol{q}}^{k+1} = \ddot{\boldsymbol{q}}_{n+1}^{k+1} - \ddot{\boldsymbol{q}}_n^{k+1}, \Delta^{\mathrm{NR}}\boldsymbol{\gamma}^{k+1} = \boldsymbol{\gamma}_{n+1}^{k+1} - \boldsymbol{\gamma}_n^{k+1}$ are the increments of accelerations and Lagrange multipliers in the Newton iteration steps.

The Jacobian matrix is then introduced as

$$\boldsymbol{J}_{\mathrm{NR}} = \begin{bmatrix} \dfrac{\partial \boldsymbol{G}_{\boldsymbol{f}}}{\partial \ddot{\boldsymbol{q}}} & \dfrac{\partial \boldsymbol{G}_{\boldsymbol{f}}}{\partial \boldsymbol{\gamma}} \\ \dfrac{\partial \boldsymbol{G}_{\boldsymbol{c}}}{\partial \ddot{\boldsymbol{q}}} & \dfrac{\partial \boldsymbol{G}_{\boldsymbol{c}}}{\partial \boldsymbol{\gamma}} \end{bmatrix}_n^{k+1} \tag{2.143}$$

The top left block of the Jacobian matrix (2.143) can be expanded as

$$\left[\frac{\partial \boldsymbol{G}_{\boldsymbol{f}}}{\partial \ddot{\boldsymbol{q}}}\right]_n^{k+1} = \frac{\partial \boldsymbol{G}_{\boldsymbol{f},n}^{k+1}}{\partial \ddot{\boldsymbol{q}}_n^{k+1}} + \frac{\partial \boldsymbol{G}_{\boldsymbol{f},n}^{k+1}}{\partial \dot{\boldsymbol{q}}_n^{k+1}}\frac{\partial \dot{\boldsymbol{q}}_n^{k+1}}{\partial \ddot{\boldsymbol{q}}_n^{k+1}} + \frac{\partial \boldsymbol{G}_{\boldsymbol{f},n}^{k+1}}{\partial \boldsymbol{q}_n^{k+1}}\frac{\partial \boldsymbol{q}_n^{k+1}}{\partial \ddot{\boldsymbol{q}}_n^{k+1}} \tag{2.144}$$

Recalling the expression in (2.141a) and the notations in (2.77), (2.78), we can derive

$$\frac{\partial \boldsymbol{G}_{\boldsymbol{f},n}^{k+1}}{\partial \ddot{\boldsymbol{q}}_n^{k+1}} = \frac{1}{1+\alpha}\boldsymbol{M}_n^{k+1} \tag{2.145a}$$

$$\frac{\partial \boldsymbol{G}_{\boldsymbol{f},n}^{k+1}}{\partial \dot{\boldsymbol{q}}_n^{k+1}} = -\frac{\partial \boldsymbol{f}_n^{k+1}}{\partial \dot{\boldsymbol{q}}_n^{k+1}} = \left(\boldsymbol{D}_a + \boldsymbol{D}_m + \boldsymbol{D}_i\right)_n^{k+1} \tag{2.145b}$$

$$\begin{aligned} \frac{\partial \boldsymbol{G}_{\boldsymbol{f},n}^{k+1}}{\partial \boldsymbol{q}_n^{k+1}} &= -\frac{\partial \boldsymbol{f}_n^{k+1}}{\partial \boldsymbol{q}_n^{k+1}} + \frac{1}{1+\alpha}\frac{\partial \left(\boldsymbol{M}\ddot{\boldsymbol{q}}\right)_n^{k+1}}{\partial \boldsymbol{q}_n^{k+1}} + \frac{\partial \left(\boldsymbol{C}_{\boldsymbol{q}}^T\boldsymbol{\gamma}\right)_n^{k+1}}{\partial \boldsymbol{q}_n^{k+1}} \\ &= \left(\boldsymbol{K}_a + \boldsymbol{K}_m + \boldsymbol{K}_g + \boldsymbol{K}_c + \boldsymbol{K}_{i,1} + \frac{1}{1+\alpha}\boldsymbol{K}_{i,2}\right)_n^{k+1} \end{aligned} \tag{2.145c}$$

Employing (2.138a) and (2.138b), we can obtain

$$\frac{\partial \dot{\boldsymbol{q}}_n^{k+1}}{\partial \ddot{\boldsymbol{q}}_n^{k+1}} = \gamma h \boldsymbol{I}, \quad \frac{\partial \boldsymbol{q}_n^{k+1}}{\partial \ddot{\boldsymbol{q}}_n^{k+1}} = \beta h^2 \boldsymbol{I} \tag{2.146}$$

Substituting (2.145a),(2.145b),(2.145c) and (2.146) into (2.144), and introducing a notation $\boldsymbol{H}$, yields

$$\begin{aligned} \boldsymbol{H} \coloneqq \left[\frac{\partial \boldsymbol{G_f}}{\partial \ddot{\boldsymbol{q}}}\right]_n^{k+1} &= \frac{1}{1+\alpha}\boldsymbol{M}_n^{k+1} + \gamma h \left(\boldsymbol{D}_a + \boldsymbol{D}_m + \boldsymbol{D}_i\right)_n^{k+1} \\ &\quad + \beta h^2 \left(\boldsymbol{K}_a + \boldsymbol{K}_m + \boldsymbol{K}_g + \boldsymbol{K}_c + \boldsymbol{K}_{i,1} + \frac{1}{1+\alpha}\boldsymbol{K}_{i,2}\right)_n^{k+1} \end{aligned} \tag{2.147}$$

Since in many applications $\boldsymbol{K}_c$ and $\boldsymbol{K}_i$ are very small if compared to $\boldsymbol{K}_m$, they can be neglected in the code implementation to obtain a better computational performance at the risk of lower convergence speed.

The other three blocks of the Jacobian matrix (2.143) can be computed as

$$\left[\frac{\partial \boldsymbol{G_f}}{\partial \boldsymbol{\gamma}}\right]_n^{k+1} = \boldsymbol{C}_{\boldsymbol{q},n}^{T,s+1} \tag{2.148a}$$

$$\left[\frac{\partial \boldsymbol{G_c}}{\partial \ddot{\boldsymbol{q}}}\right]_n^{k+1} = \frac{\partial \boldsymbol{G}_{\boldsymbol{c},n}^{k+1}}{\partial \boldsymbol{q}_n^{k+1}} \frac{\partial \boldsymbol{q}_n^{k+1}}{\partial \ddot{\boldsymbol{q}}_n^{k+1}} = \beta h^2 \boldsymbol{C}_{\boldsymbol{q},n}^{k+1} \tag{2.148b}$$

$$\left[\frac{\partial \boldsymbol{G_c}}{\partial \boldsymbol{\gamma}}\right]_n^{k+1} = \boldsymbol{0} \tag{2.148c}$$

In the end, the linear equations in (2.142) can be recast as

$$\begin{bmatrix} \boldsymbol{H} & \boldsymbol{C}_{\boldsymbol{q}}^T \\ \boldsymbol{C}_{\boldsymbol{q}} & \boldsymbol{0} \end{bmatrix}_n^{k+1} \begin{pmatrix} \Delta^{\mathrm{NR}} \ddot{\boldsymbol{q}}^{k+1} \\ \Delta^{\mathrm{NR}} \boldsymbol{\gamma}^{k+1} \end{pmatrix} = \begin{pmatrix} -\boldsymbol{G}_{f,n}^{k+1} \\ -\dfrac{1}{\beta h^2} \boldsymbol{G}_{c,n}^{k+1} \end{pmatrix} \tag{2.149}$$

The Jacobian matrix $\boldsymbol{J}_{\mathrm{NR}}$ is finally computed as

$$\boldsymbol{J}_{\mathrm{NR}} = \begin{bmatrix} \boldsymbol{H} & \boldsymbol{C}_{\boldsymbol{q}}^T \\ \boldsymbol{C}_{\boldsymbol{q}} & \boldsymbol{0} \end{bmatrix}_n^{k+1} \tag{2.150}$$

To enhance the symmetry and conditioning of the Jacobian matrix $\boldsymbol{J}_{\mathrm{NR}}$, the second row in (2.149) is scaled by a factor of $\frac{1}{\beta h^2}$. This adjustment is motivated by two key considerations: (1) it ensures that the position kinematic constraint equations are appropriately scaled, and (2) it brings the unknowns $\ddot{\boldsymbol{q}}$ and $\boldsymbol{\gamma}$ to the same kinematic level, as suggested by Negrut [196]. This straightforward scaling approach has

been implemented in the open-source multibody dynamics library CHRONO [260], and is capable to provide stable solutions across numerous engineering applications. Nonetheless, there are opportunities for further improvement of the scaling procedure [35, 36, 17].

Since finite rotations are parameterized using quaternions, the additive operation between a quaternion and a rotation pseudovector in (2.138a) is invalid. To this end, an exponential mapping is used to perform the rotation incremental update. The corresponding quaternion, $\boldsymbol{\rho}_{l_\Delta}$, for a rotation pseudovector, $\boldsymbol{\phi}_{l_\Delta}$, representing a rotation increment in the local basis, can be computed as follows

$$\boldsymbol{\rho}_{l_\Delta} = \exp\left(0, \frac{1}{2}\boldsymbol{\phi}_{l_\Delta}\right) = \left(\cos\left(\frac{1}{2}\|\boldsymbol{\phi}_{l_\Delta}\|\right), \frac{\boldsymbol{\phi}_{l_\Delta}}{\|\boldsymbol{\phi}_{l_\Delta}\|}\sin\left(\frac{1}{2}\|\boldsymbol{\phi}_{l_\Delta}\|\right)\right) \tag{2.151}$$

The rotation incremental update is computed as a *product* between two quaternions

$$\boldsymbol{\rho}^{k+1} = \boldsymbol{\rho}^k \boldsymbol{\rho}_{l_\Delta} = \boldsymbol{\rho}^k \exp\left(0, \frac{1}{2}\boldsymbol{\phi}_{l_\Delta}\right) \tag{2.152}$$

Finally, the incremental update in Equation (2.138a) is computed as

$$\boldsymbol{q}^{k+1} = \begin{pmatrix} \boldsymbol{r}_1^k + \Delta\boldsymbol{r}_1 \\ \boldsymbol{\rho}_1^k \exp\left(0, \frac{1}{2}\boldsymbol{\phi}_{l_{\Delta 1}}\right) \\ \boldsymbol{r}_2^k + \Delta\boldsymbol{r}_2 \\ \boldsymbol{\rho}_2^k \exp\left(0, \frac{1}{2}\boldsymbol{\phi}_{l_{\Delta 2}}\right) \\ \vdots \\ \boldsymbol{r}_n^k + \Delta\boldsymbol{r}_n \\ \boldsymbol{\rho}_n^k \exp\left(0, \frac{1}{2}\boldsymbol{\phi}_{l_{\Delta n}}\right) \end{pmatrix} \tag{2.153}$$

2.9 Static equilibrium solver

The static equilibrium configuration refers to the status of a system where the kinetic energy is zero or constant, and the potential energy is at a minimum. This configuration is of practical value in engineering applications. During time integration, initializing the dynamics model with the static equilibrium configuration can reduce or even eliminate initial impulses. In modal and stability analyses, the static equilibrium configuration is often selected as the system's working point for analysis.

There are various methods to solve for the static equilibrium configuration. Often, a potential energy function is introduced and minimized to determine the static equilibrium configuration [6, 85, 106, 146]. Alternatively, time integration

can be used to find the static equilibrium configuration of a wind turbine [194], but this approach has several drawbacks: high computational cost, difficulty in converging to a stable state due to extremely low or even negative damping in the blade edgewise direction, and periodic excitations such as gravitational forces, wind shear effects, and wind inflow angle after rotor inclination.

In this work, we transform the problem into a static one by moving the inertial and damping forces to the right–hand side, followed by a Newton–Raphson iteration to solve for the static equilibrium configuration. This scheme involves only Newton–Raphson iteration steps and does not require time–stepping.

Here, we consider solving for the static equilibrium configuration of a general flexible multibody system that may involve rheonomic constraints. It is assumed that the generalized velocity $\dot{\boldsymbol{q}}_0$ and the generalized acceleration $\ddot{\boldsymbol{q}}_0$ are derived from these rheonomic constraints and are properly updated at each step of the Newton–Raphson iteration.

In the static equilibrium solver, the generalized coordinates and Lagrange multipliers are discretized as follows

$$\begin{cases} \boldsymbol{q}_{n+1} = \boldsymbol{q}_n + \Delta^{\mathrm{NR}}\boldsymbol{q} & \text{(2.154a)} \\ \boldsymbol{\gamma}_{n+1} = \boldsymbol{\gamma}_n + \Delta^{\mathrm{NR}}\boldsymbol{\gamma} & \text{(2.154b)} \end{cases}$$

The residual vector of the DAEs (2.70) is computed as

$$\boldsymbol{G_f} = \boldsymbol{M}\ddot{\boldsymbol{q}} + \boldsymbol{C}_{\boldsymbol{q}}^{T}\boldsymbol{\gamma} - \boldsymbol{f} \quad \text{(2.155a)}$$

$$\boldsymbol{G_c} = \boldsymbol{c} \quad \text{(2.155b)}$$

To satisfy $\boldsymbol{G} = \boldsymbol{0}$, the Newton-Raphson iteration method is employed. This involves solving a set of linear equations to determine the increments of the generalized coordinates $\Delta^{\mathrm{NR}}\boldsymbol{q}$ and the increments of the Lagrange multipliers $\Delta^{\mathrm{NR}}\boldsymbol{\gamma}$

$$\begin{bmatrix} \dfrac{\partial \boldsymbol{G_f}}{\partial \boldsymbol{q}} & \dfrac{\partial \boldsymbol{G_f}}{\partial \boldsymbol{\gamma}} \\ \dfrac{\partial \boldsymbol{G_c}}{\partial \boldsymbol{q}} & \dfrac{\partial \boldsymbol{G_c}}{\partial \boldsymbol{\gamma}} \end{bmatrix}_n \begin{pmatrix} \Delta^{\mathrm{NR}}\boldsymbol{q} \\ \Delta^{\mathrm{NR}}\boldsymbol{\gamma} \end{pmatrix} + \boldsymbol{G}\left(\boldsymbol{q}_n, \dot{\boldsymbol{q}}_0, \ddot{\boldsymbol{q}}_0, \boldsymbol{\gamma}_n\right) = \boldsymbol{0} \quad \text{(2.156)}$$

where the sub–block Jacobian matrices can be computed as

$$\left[\frac{\partial \boldsymbol{G_f}}{\partial \boldsymbol{q}}\right]_n = \frac{\partial}{\partial \boldsymbol{q}_n}\left(\boldsymbol{M}\ddot{\boldsymbol{q}} - \boldsymbol{f} + \boldsymbol{C}_{\boldsymbol{q}}^T\boldsymbol{\gamma}\right)_n$$
$$= \left(\boldsymbol{K}_a + \boldsymbol{K}_m + \boldsymbol{K}_g + \boldsymbol{K}_c + \boldsymbol{K}_i\right)_n \tag{2.157a}$$
$$\left[\frac{\partial \boldsymbol{G_f}}{\partial \boldsymbol{\gamma}}\right]_n = \boldsymbol{C}_{\boldsymbol{q},n}^T \tag{2.157b}$$
$$\left[\frac{\partial \boldsymbol{G_c}}{\partial \boldsymbol{q}}\right]_n = \boldsymbol{C}_{\boldsymbol{q},n} \tag{2.157c}$$
$$\left[\frac{\partial \boldsymbol{G_c}}{\partial \boldsymbol{\gamma}}\right]_n = \boldsymbol{0} \tag{2.157d}$$

The Jacobian matrix in (2.156) is then expressed as

$$\boldsymbol{J}_{\mathrm{NR}} = \begin{bmatrix} \dfrac{\partial \boldsymbol{G_f}}{\partial \boldsymbol{q}} & \dfrac{\partial \boldsymbol{G_f}}{\partial \boldsymbol{\gamma}} \\ \dfrac{\partial \boldsymbol{G_c}}{\partial \boldsymbol{q}} & \dfrac{\partial \boldsymbol{G_c}}{\partial \boldsymbol{\gamma}} \end{bmatrix}_n = \begin{bmatrix} \boldsymbol{H} & \boldsymbol{C}_{\boldsymbol{q}}^T \\ \boldsymbol{C}_{\boldsymbol{q}} & \boldsymbol{0} \end{bmatrix}_n \tag{2.158}$$

where the left-top sub-block matrix is given as

$$\boldsymbol{H} = \boldsymbol{K}_a + \boldsymbol{K}_m + \boldsymbol{K}_g + \boldsymbol{K}_c + \boldsymbol{K}_i \tag{2.159}$$

The matrix $\boldsymbol{H}$ is the tangent stiffness matrix of the system. The matrix $\boldsymbol{K}_c$ is relevant for the static equilibrium problem for those systems with rotational DOFs of rigid body motion, such as a pendulum.

The residual terms in (2.156) are computed as

$$\boldsymbol{G}_{\boldsymbol{f},n} = \left(\boldsymbol{M}\ddot{\boldsymbol{q}}_0 - \boldsymbol{f}_v\right)_n + \left(\boldsymbol{D}_m\dot{\boldsymbol{q}}_0\right)_n + \left(\boldsymbol{C}_{\boldsymbol{q}}^T\boldsymbol{\gamma}\right)_n - \boldsymbol{f}_{a,n} - \boldsymbol{f}_{e,0} \tag{2.160a}$$
$$\boldsymbol{G}_{\boldsymbol{c},n} = \boldsymbol{c}_n \tag{2.160b}$$

where $\left(\boldsymbol{M}\ddot{\boldsymbol{q}}_0 - \boldsymbol{f}_v\right)_n$ represents the total inertial forces under the given velocities $\dot{\boldsymbol{q}}_0$ and accelerations $\ddot{\boldsymbol{q}}_0$. $\left(\boldsymbol{D}_m\dot{\boldsymbol{q}}_0\right)_n$ denotes the structural damping forces, while $\left(\boldsymbol{C}_{\boldsymbol{q}}^T\boldsymbol{\gamma}\right)_n$ accounts for the reaction forces and moments at the joints. $\boldsymbol{f}_{a,n}$ represents the applied external forces, for example, the aerodynamic loads on wind turbine blades. $\boldsymbol{f}_{e,0}$ denotes the initial elastic forces if the system includes prestress in the initial configuration. Finally, $\boldsymbol{c}_n$ is the residual of the constraints.

The linear equations in (2.156) are finally recast as

$$\begin{bmatrix} \boldsymbol{H} & \boldsymbol{C}_{\boldsymbol{q}}^T \\ \boldsymbol{C}_{\boldsymbol{q}} & \boldsymbol{0} \end{bmatrix}_n \begin{pmatrix} \Delta^{\mathrm{NR}}\boldsymbol{q} \\ \Delta^{\mathrm{NR}}\boldsymbol{\gamma} \end{pmatrix} = \begin{pmatrix} -\boldsymbol{G}_{\boldsymbol{f},n} \\ -\boldsymbol{G}_{\boldsymbol{c},n} \end{pmatrix} \tag{2.161}$$

The same exponential mapping used in (2.153) is applied to perform the incremental update for rotations in (2.154a) .

2.10 Eigenvalue solver

The eigenvalue problem, formulated based on the linearized equations of motion at specified equilibrium configurations, allows for an eigenvalue analysis that yields the eigenvalues and eigenvectors of the mechanical system. In the standpoint of mathematics, the eigenvalue analysis projects the nonlinear coupled dynamic system into a new space spanned by linear-independent bases. From the perspective of mechanical system dynamics, the modal frequencies, damping ratios, and modal shapes extracted from the eigenvalues and eigenvectors provide crucial insights into the system's intrinsic dynamic characteristics at the operating conditions of interest [246]. Understanding these modal dynamics is instrumental in optimizing system design, interpreting dynamic responses under specific circumstances, preventing potential resonances during operation, diagnosing the root causes of weird vibrations, and addressing various other aspects in engineering practice. Damping ratios, in particular, serve as effective indicators for assessing system stability, for instance the aeroelastic stability of helicopter blades, wind turbine rotors and other slender structures [117, 129, 7, 206].

For large-scale dynamic systems, component mode synthesis, also referred to as modal reduction techniques, provides a practical solution for reducing the problem size by transforming physical coordinates into a significantly smaller set of generalized modal coordinates, thereby greatly reducing computational effort [286, 46, 251]. In the context of controller design, it is often necessary to develop an equivalent linear state-space representation with a reduced number of state variables to facilitate appropriate parameter tuning. This requirement necessitates the application of advanced modal reduction techniques, which depend on solving the eigenvalue problem [222].

Motivated by the aforementioned applications, here we discuss the numerical challenges associated with the computation of eigenvalues and eigenvectors in flexible multibody systems under the most general conditions. Specifically, we assume that the system may exhibit singular modes (also referred to as rigid body or free-free modes), account for the potential presence of damping (resulting in complex-valued eigenpairs), allow for an arbitrary number of components and constraints, and consider the system's size to be arbitrarily large. This latter consideration, in particular, imposes constraints on the choice of the solver, which must maintain the sparsity of matrices to ensure acceptable computational efficiency and should be capable of extracting only a small subset of eigenvalues, such as the lowest ones or those clustered around a specific frequency of interest.

The computation of eigenvalues has been extensively studied within the context of Finite Element Analysis (FEA) in the literature and has subsequently been extended to the field of multibody systems. An additional challenge in addressing the eigenvalue problem for multibody systems, as opposed to conventional FEA, is the pervasive presence of constraints, which are often formulated through algebraic

equations and Lagrange multipliers. To address this, an orthogonal complement can be employed to eliminate constraints, thereby reducing the generalized coordinates to the minimal necessary set, as discussed in [152] and [294]. Similar to the index-reduction techniques outlined in Section 2.6.1, this classical method allows for the application of conventional eigenvalue solvers commonly used in FEA. However, it also presents certain limitations, which will be discussed in subsequent paragraphs.

Alternatively, one may solve the eigenvalue problem while retaining the constraints, leading to larger but sparser matrices, as demonstrated in [95] and [206]. Although this approach increases the matrix size, it offers two key advantages: it simplifies the formulation of the eigenvalue problem and, more importantly, preserves the sparsity of the matrices, enabling the design of a solver that can efficiently exploit this beneficial characteristic.

The Implicit Restarted Arnoldi Method (IRAM) [161] has been widely employed for solving eigenvalue problems across numerous applications. Implemented in ARPACK, a well-known Fortran77 library, it is capable of handling generalized eigenvalue problems for sparse matrices. Although it satisfies many of our requirements, we experienced that ARPACK's implementation sometimes encounters difficulties with numerical convergence in certain challenging scenarios, prompting us to explore the more recent Krylov-Schur method.

The Krylov-Schur method, as presented in [254], offers enhanced robustness and faster convergence compared to earlier Krylov subspace methods, such as IRAM and Lanczos, due to its more efficient and reliable restarting strategy. For these reasons, the Krylov-Schur method is the default eigenvalue solver used in the `eigs` function in MATLAB, ensuring robustness and computational efficiency. Other well-known libraries, such as SLEPc [123] and TRILINOS [124], have also adopted the Krylov-Schur method. However, these libraries are primarily designed for high-performance computing tasks and involve complex build processes. Alternatively, there are lightweight options like the SPECTRA C++ library [217], which includes an implementation of the Krylov-Schur method. However, it does not support generalized eigenvalue problems for asymmetric sparse matrices. The absence of a reliable, fully-featured, and lightweight open-source library for the Krylov-Schur method led us to develop our own C++ version.

In the following paragraphs, we provide a comprehensive review of the different formulations used to establish the eigenvalue problem, considering cases both with and without constraints, as well as with and without damping. We then discuss various computational aspects related to the implementation of the sparsity-preserving Krylov-Schur solver.

2.10.1 An alternative linearization form: Null-space transformation

The generic form of the linearized DAEs in (2.76) requires the introduction of constraints, which are represented by the Jacobian matrix of constraints $\boldsymbol{C_q}$ and the Lagrange multipliers $\delta\boldsymbol{\gamma}$. To obtain a minimal coordinate representation, a QR decomposition of matrix $\boldsymbol{C_q}(\boldsymbol{q},t)$ can be performed, yielding the null space matrix $\boldsymbol{\Xi}(\boldsymbol{q},t) \in \mathbb{R}^{n_q \times (n_q - n_c)}$, which satisfies $\boldsymbol{C_q}\boldsymbol{\Xi} = \boldsymbol{0}$. This allows for the introduction of a reduced set of independent coordinates $\boldsymbol{y} \in \mathbb{R}^{n_q - n_c}$, such that the generalized velocities can be expressed as $\dot{\boldsymbol{q}} = \boldsymbol{\Xi}\dot{\boldsymbol{y}}$. As a result, the DAEs in (2.70) can be reformulated as a system of ODEs

$$\boldsymbol{\Xi}^T \boldsymbol{M}(\boldsymbol{q})\,\boldsymbol{\Xi}\ddot{\boldsymbol{y}} + \boldsymbol{\Xi}^T \boldsymbol{M}(\boldsymbol{q})\,\dot{\boldsymbol{\Xi}}\dot{\boldsymbol{y}} = \boldsymbol{\Xi}^T \boldsymbol{f}(\boldsymbol{q},\dot{\boldsymbol{q}},t) \tag{2.162}$$

which can be linearized to yield an alternative formulation to (2.76):

$$\boldsymbol{M}_Y(\boldsymbol{q}_0)\,\delta\ddot{\boldsymbol{y}} + \boldsymbol{D}_Y(\boldsymbol{q}_0,\dot{\boldsymbol{q}}_0)\,\delta\dot{\boldsymbol{y}} + \boldsymbol{K}_Y(\boldsymbol{q}_0,\dot{\boldsymbol{q}}_0,\ddot{\boldsymbol{q}}_0)\,\delta\boldsymbol{y} = \boldsymbol{0} \tag{2.163}$$

with

$$\boldsymbol{M}_Y(\boldsymbol{q}_0) = \boldsymbol{\Xi}^T \boldsymbol{M}(\boldsymbol{q}_0)\,\boldsymbol{\Xi} \tag{2.164}$$

$$\boldsymbol{D}_Y(\boldsymbol{q}_0,\dot{\boldsymbol{q}}_0) = -\boldsymbol{\Xi}^T \frac{\partial \boldsymbol{f}(\boldsymbol{q}_0,\dot{\boldsymbol{q}}_0,t_0)}{\partial \dot{\boldsymbol{y}}} + \boldsymbol{\Xi}^T \boldsymbol{M}(\boldsymbol{q}_0)\,\frac{\partial \dot{\boldsymbol{\Xi}}\dot{\boldsymbol{y}}}{\partial \dot{\boldsymbol{y}}} \tag{2.165}$$

$$\begin{aligned}\boldsymbol{K}_Y(\boldsymbol{q}_0,\dot{\boldsymbol{q}}_0,\ddot{\boldsymbol{q}}_0) = &\left(\frac{\partial \boldsymbol{\Xi}^T}{\partial \boldsymbol{y}}\boldsymbol{M}(\boldsymbol{q}_0)\,\boldsymbol{\Xi} + \boldsymbol{\Xi}^T \frac{\partial \boldsymbol{M}(\boldsymbol{q}_0)}{\partial \boldsymbol{y}}\boldsymbol{\Xi} + \boldsymbol{\Xi}^T \boldsymbol{M}(\boldsymbol{q}_0)\,\frac{\partial \boldsymbol{\Xi}}{\partial \boldsymbol{y}}\right)\ddot{\boldsymbol{y}}_0 \\ &+ \left(\frac{\partial \boldsymbol{\Xi}^T}{\partial \boldsymbol{y}}\boldsymbol{M}(\boldsymbol{q}_0)\,\dot{\boldsymbol{\Xi}} + \boldsymbol{\Xi}^T \frac{\partial \boldsymbol{M}(\boldsymbol{q}_0)}{\partial \boldsymbol{y}}\dot{\boldsymbol{\Xi}}\right)\dot{\boldsymbol{y}}_0 \\ &- \frac{\partial \boldsymbol{\Xi}^T}{\partial \boldsymbol{y}}\boldsymbol{f}(\boldsymbol{q}_0,\dot{\boldsymbol{q}}_0,t_0) - \boldsymbol{\Xi}^T \frac{\partial \boldsymbol{f}(\boldsymbol{q}_0,\dot{\boldsymbol{q}}_0,t_0)}{\partial \boldsymbol{y}}\end{aligned} \tag{2.166}$$

However, we note that the expressions for $\boldsymbol{D}_Y$ and $\boldsymbol{K}_Y$ are substantially more complex[2] than those for $\boldsymbol{D}$ and $\boldsymbol{K}$ in (2.77) and (2.78). For instance, the formulation in (2.166) requires the evaluation of $\dot{\boldsymbol{\Xi}}$ and $\partial\boldsymbol{\Xi}^T/\partial\boldsymbol{y}$, although $\dot{\boldsymbol{\Xi}}$ can be computed exactly from the time derivative of the Jacobian matrix of constraints, as demonstrated in [298, 185]. Another challenge associated with the formulation in (2.163) is that the multiplications by $\boldsymbol{\Xi}$ and $\boldsymbol{\Xi}^T$ can disrupt the sparsity of the

[2]Under simplifying assumptions, where the effects of $\dot{\boldsymbol{\Xi}}$ and $\partial\boldsymbol{\Xi}^T/\partial\boldsymbol{y}$ are negligible, the reduced matrices can be approximated as $\boldsymbol{D}_Y \approx \boldsymbol{\Xi}^T\boldsymbol{D}\boldsymbol{\Xi}$, $\boldsymbol{K}_Y \approx \boldsymbol{\Xi}^T\boldsymbol{K}\boldsymbol{\Xi}$. However, this simplification is only valid when the constraints do not undergo significant directional changes. For example, in the case of an oscillating pendulum, such an approximation would erroneously predict a zero natural frequency.

original system matrices, $\boldsymbol{M}$, $\boldsymbol{D}$, and $\boldsymbol{K}$. This increases memory requirements and floating-point computational costs, leading to a substantial decline in performance for large-scale problems. Therefore, in this work, we prefer to formulate the eigenvalue problem based on the linearized form in (2.76), accepting the necessity of handling constraints during the iterative eigenvalue solution process.

2.10.2 Formulations for eigenvalue problems

In this section, we discuss the formulations of eigenvalue problems for two distinct types of systems: undamped and damped. This distinction is made because, in many applications, only the modal frequencies and modal shapes are of interest, with damping effects being negligible or irrelevant.

Undamped Case

We begin with the simplest case: an unconstrained and undamped system. The linearized equations of motion are expressed as

$$\boldsymbol{M}\delta\ddot{\boldsymbol{q}} + \boldsymbol{K}\delta\boldsymbol{q} = \boldsymbol{0} \tag{2.167}$$

Assuming a homogeneous solution of the form $\delta\boldsymbol{q} = \boldsymbol{\Phi}_i e^{\jmath\omega_i t}$, where $\jmath = \sqrt{-1}$ denotes the imaginary unit, the characteristic equation is formulated as

$$\left(-\omega_i^2\boldsymbol{M} + \boldsymbol{K}\right)\boldsymbol{\Phi}_i = \boldsymbol{0} \tag{2.168}$$

The *Standard Eigenvalue Problem* (SEP) is then established as

$$\left(\boldsymbol{M}^{-1}\boldsymbol{K} - \lambda_i\boldsymbol{I}\right)\boldsymbol{\Phi}_i = \boldsymbol{0} \tag{2.169a}$$

$$\Rightarrow \left(\boldsymbol{C} - \lambda_i\boldsymbol{I}\right)\boldsymbol{\Phi}_i = \boldsymbol{0} \tag{2.169b}$$

with the eigenvalue $\lambda_i = \omega_i^2$ and the matrix $\boldsymbol{C} = \boldsymbol{M}^{-1}\boldsymbol{K}$.

If the matrices $\boldsymbol{M}$ and $\boldsymbol{K}$ are symmetric, the eigenpairs $(\lambda_i, \boldsymbol{\Phi}_i)$ are real.

However, there are limitations to directly applying the formulation in (2.169) for complex systems in engineering practice. The first challenge is that the direct inversion of matrix $\boldsymbol{M}$ is required to evaluate matrix $\boldsymbol{C}$. Although the mass matrix $\boldsymbol{M}$ is typically diagonal-dominant, making its inversion straightforward, this is not universally guaranteed. Additionally, ensuring the sparsity of matrix $\boldsymbol{C}$ becomes challenging for large-scale systems. Secondly, in many cases, only a small subset of the eigenvalues, usually those with the smallest amplitudes, is of interest. An iterative scheme is often preferred to efficiently address this requirement.

For a constrained undamped multibody system, we can assume the homogeneous solution for the Lagrange multipliers as $\delta\boldsymbol{\gamma} = \boldsymbol{\xi}_i e^{\jmath\omega_i t}$. Additionally, employing

$\boldsymbol{C_q}\boldsymbol{\Phi}_i = \mathbf{0}$ to enforce the constraints, the *Generalized Eigenvalue Problem* (GEP) is formulated as follows

$$-\begin{bmatrix}\boldsymbol{K} & \boldsymbol{C}_q^T\\ \boldsymbol{C_q} & \mathbf{0}\end{bmatrix}\hat{\boldsymbol{\Phi}}_i = \lambda_i\begin{bmatrix}\boldsymbol{M} & \mathbf{0}\\ \mathbf{0} & \mathbf{0}\end{bmatrix}\hat{\boldsymbol{\Phi}}_i \tag{2.170}$$

where $\hat{\boldsymbol{\Phi}}_i = \left[\boldsymbol{\Phi}_i^T, \boldsymbol{\xi}_i^T\right]^T \in \mathbb{R}^{n_q+n_c}$ is the augmented eigenvector, and $\lambda_i = -\omega_i^2$ is the eigenvalue.

The GEP in (2.170) produces a total of $n_q + n_c$ eigenvalues, of which only $n_q - n_c$ correspond to the physical system. The remaining $2n_c$ modes arise from the algebraic constraints, with their corresponding eigenvalues being infinite ($\lambda_i \approx \infty$) due to the absence of inertia in the constraints. The components $\boldsymbol{\xi}_i \in \mathbb{R}^{n_c}$ within the eigenvector represent the reaction forces and moments at the constraints during the system's periodic motion. Although these components are often of limited interest, they can provide valuable insight into the ratio between deflections and the reaction forces and moments during modal oscillations.

Alternatively, we can enforce the constraints at the acceleration level, leading to the following linearized DAEs

$$\begin{cases}\boldsymbol{M}\delta\ddot{\boldsymbol{q}} + \boldsymbol{K}\delta\boldsymbol{q} + \boldsymbol{C}_q^T\delta\ddot{\boldsymbol{\gamma}} = \mathbf{0} & \text{(2.171a)}\\ \boldsymbol{C_q}\delta\ddot{\boldsymbol{q}} = \mathbf{0} & \text{(2.171b)}\end{cases}$$

Substituting the homogeneous solutions of both the generalized coordinates and Lagrange multipliers into (2.171), the GEP can be reformulated in the below form

$$-\begin{bmatrix}\boldsymbol{K} & \mathbf{0}\\ \mathbf{0} & \mathbf{0}\end{bmatrix}\hat{\boldsymbol{\Phi}}_i = \lambda_i\begin{bmatrix}\boldsymbol{M} & \boldsymbol{C}_q^T\\ \boldsymbol{C_q} & \mathbf{0}\end{bmatrix}\hat{\boldsymbol{\Phi}}_i \tag{2.172}$$

where $\lambda_i = -\omega_i^2$ is the eigenvalue.

However, the formulation in (2.172) results in n_c spurious modes with $\lambda_i \approx 0$. While this is generally acceptable, it becomes challenging to distinguish these spurious modes from the rigid body modes, as the rigid body modes also exhibit zero or near-zero eigenvalues, which may arise due to numerical errors in the eigenvalue computation process.

The two distinct forms of the GEP in (2.170) and (2.172) can be expressed in a general form as follows

$$\boldsymbol{A}\hat{\boldsymbol{\Phi}}_i = \lambda_i\boldsymbol{B}\hat{\boldsymbol{\Phi}}_i \tag{2.173}$$

In the GEP (2.170), although $\boldsymbol{C_q}$ is always full rank, the $\boldsymbol{A}$ matrix cannot be guaranteed to be non-singular, as the $\boldsymbol{K}$ matrix may be rank-deficient by z in the presence of z rigid body modes. Additionally, the $\boldsymbol{B}$ matrix is inherently singular and therefore not invertible. Conversely, in the GEP (2.172), the $\boldsymbol{A}$ matrix is always singular, while the $\boldsymbol{B}$ matrix is guaranteed to be non-singular since $\boldsymbol{M}$ is positive definite. Although it might appear that GEP (2.172) is preferable because it allows transformation into a SEP via $\boldsymbol{C} = \boldsymbol{M}^{-1}\boldsymbol{K}$, this is not the case. We will later apply the shift-and-invert technique to resolve the singularity of the $\boldsymbol{A}$ matrix.

Damped Case

For an unconstrained damped system, the linearized equations of motion can be expressed as

$$\boldsymbol{M}\delta\ddot{\boldsymbol{q}} + \boldsymbol{D}\delta\dot{\boldsymbol{q}} + \boldsymbol{K}\delta\boldsymbol{q} = \boldsymbol{0} \tag{2.174}$$

Substituting the homogeneous solution $\delta\boldsymbol{q} = \boldsymbol{\Phi}_i e^{\lambda_i t}$ into (2.174), the *Quadratic Eigenvalue Problem* (QEP) is then formulated as follows

$$\left(\lambda_i^2\boldsymbol{M} + \lambda_i\boldsymbol{D} + \boldsymbol{K}\right)\boldsymbol{\Phi}_i = \boldsymbol{0} \tag{2.175}$$

Since the system matrices $\boldsymbol{M}$, $\boldsymbol{D}$, and $\boldsymbol{K}$ are all real, the eigenvalues must either be real or appear as complex conjugate pairs $\left(\lambda_i, \overline{\lambda}_i\right)$. The eigenvalue λ_i provides insights into the modal properties as follows:

- Complex conjugate eigenvalue pairs $\left(\lambda_i, \overline{\lambda}_i\right)$ indicate subcritically damped modes, characterized by oscillatory motion with a decaying amplitude when $\mathrm{Re}\left(\lambda_i\right) < 0$.
- Purely imaginary conjugate pairs $\left(\lambda_i, \overline{\lambda}_i\right)$, where $\mathrm{Re}\left(\lambda_i\right) = 0$, correspond to undamped modes that exhibit purely harmonic motion without decay.
- Real eigenvalues with $\mathrm{Re}\left(\lambda_i\right) < 0$ and $\mathrm{Im}\left(\lambda_i\right) = 0$ represent supercritically damped modes, showing no oscillatory motion but exhibiting exponential decay.
- In all cases, $\mathrm{Re}\left(\lambda_i\right) > 0$ indicates an unstable mode.

The natural (undamped) frequency ω_i, the damped frequency ω_{d_i}, and the damping ratio ζ_i for mode i can be derived from the eigenvalue λ_i as follows

$$\omega_i = \|\lambda_i\|, \qquad f_i = \omega_i/2\pi \tag{2.176a}$$
$$\omega_{d_i} = \mathrm{Im}\left(\lambda_i\right), \qquad f_{d_i} = \omega_{d_i}/2\pi \tag{2.176b}$$
$$\zeta_i = -\mathrm{Re}\left(\lambda_i\right)/\omega_i \tag{2.176c}$$
$$\omega_{d_i} = \omega_i\sqrt{1-\zeta_i^2} \tag{2.176d}$$

The QEP in (2.175) can be converted into a GEP by reformulating the problem in state space, although at the cost of doubling the problem size. By introducing the augmented eigenvector $\underline{\boldsymbol{\Phi}}_i = \left[\boldsymbol{\Phi}_i^T, \lambda_i\boldsymbol{\Phi}_i^T\right]^T \in \mathbb{C}^{2n_q}$, the GEP is formulated as follows

$$\begin{bmatrix} \boldsymbol{0} & \boldsymbol{I} \\ -\boldsymbol{K} & -\boldsymbol{D} \end{bmatrix}\underline{\boldsymbol{\Phi}}_i = \lambda_i \begin{bmatrix} \boldsymbol{I} & \boldsymbol{0} \\ \boldsymbol{0} & \boldsymbol{M} \end{bmatrix}\underline{\boldsymbol{\Phi}}_i \tag{2.177}$$

Furthermore, the constraints can be incorporated by extending the eigenvectors to include the components $\boldsymbol{\xi}_i \in \mathbb{C}^{n_c}$ for the Lagrange multipliers, and by enforcing the constraints at the configuration level using $\boldsymbol{C_q}\boldsymbol{\Phi}_i = \boldsymbol{0}$. This results in a constrained QEP formulated as follows

$$\begin{cases} \lambda_i^2 \boldsymbol{M}\boldsymbol{\Phi}_i + \lambda_i \boldsymbol{D}\boldsymbol{\Phi}_i + \boldsymbol{K}\boldsymbol{\Phi}_i + \boldsymbol{C}_{\boldsymbol{q}}^T \boldsymbol{\xi}_i = \boldsymbol{0} & \text{(2.178a)} \\ -\boldsymbol{C_q}\boldsymbol{\Phi}_i = \boldsymbol{0} & \text{(2.178b)} \end{cases}$$

By introducing the augmented eigenvector, which includes the components for generalized coordinates, generalized velocities, and Lagrange multipliers, in the form $\hat{\underline{\boldsymbol{\Phi}}}_i = \left[\boldsymbol{\Phi}_i^T, \lambda_i \boldsymbol{\Phi}_i^T, \boldsymbol{\xi}_i^T\right]^T \in \mathbb{C}^{2n_q+n_c}$, the constrained QEP from (2.178) can be reformulated as a constrained GEP through simple linear algebra, as shown below

$$\begin{bmatrix} \boldsymbol{0} & \boldsymbol{I} & \boldsymbol{0} \\ -\boldsymbol{K} & -\boldsymbol{D} & -\boldsymbol{C}_{\boldsymbol{q}}^T \\ -\boldsymbol{C_q} & \boldsymbol{0} & \boldsymbol{0} \end{bmatrix} \hat{\underline{\boldsymbol{\Phi}}}_i = \lambda_i \begin{bmatrix} \boldsymbol{I} & \boldsymbol{0} & \boldsymbol{0} \\ \boldsymbol{0} & \boldsymbol{M} & \boldsymbol{0} \\ \boldsymbol{0} & \boldsymbol{0} & \boldsymbol{0} \end{bmatrix} \hat{\underline{\boldsymbol{\Phi}}}_i \tag{2.179}$$

Alternatively, similar to the formulation in (2.172), we can enforce the constraints at the velocity level and reformulate the constrained GEP in the following form

$$\begin{bmatrix} \boldsymbol{0} & \boldsymbol{I} & \boldsymbol{0} \\ -\boldsymbol{K} & -\boldsymbol{D} & \boldsymbol{0} \\ \boldsymbol{0} & \boldsymbol{0} & \boldsymbol{0} \end{bmatrix} \hat{\underline{\boldsymbol{\Phi}}}_i = \lambda_i \begin{bmatrix} \boldsymbol{I} & \boldsymbol{0} & \boldsymbol{0} \\ \boldsymbol{0} & \boldsymbol{M} & \boldsymbol{C}_{\boldsymbol{q}}^T \\ \boldsymbol{C_q} & \boldsymbol{0} & \boldsymbol{0} \end{bmatrix} \hat{\underline{\boldsymbol{\Phi}}}_i \tag{2.180}$$

The two distinct forms of the GEP in (2.179) and (2.180) can be expressed in the general form $\boldsymbol{A}\hat{\underline{\boldsymbol{\Phi}}}_i = \lambda_i \boldsymbol{B}\hat{\underline{\boldsymbol{\Phi}}}_i$. In the GEP (2.179), the $\boldsymbol{A}$ matrix is singular in the presence of rigid body modes, whereas $\boldsymbol{B}$ is always singular but remains symmetric. In contrast, for the GEP (2.180), the $\boldsymbol{A}$ matrix is singular while $\boldsymbol{B}$ is always full rank; however, both $\boldsymbol{A}$ and $\boldsymbol{B}$ are asymmetric. Our experience indicates that the most efficient approach for computing the eigenpairs of the constrained damped system is using the first formulation, i.e., the GEP (2.179).

Summary

The eigenvalue problem of a multibody system can always be expressed as a GEP. All possible options for damped or undamped, constrained or unconstrained systems are summarized in Table 2.3.

2.10.3 Implementation of the Krylov-Schur Solver

When the DOFs in a flexible multibody system reach the order of thousands, obtaining all eigenmodes becomes challenging due to the substantial memory requirements for storing all the eigenvectors, as well as the excessive computational time

Table 2.3: Different formulations for the eigenpair computation.

Systems	GEP	Notes
Undamped	$\boldsymbol{A} = \begin{bmatrix}\boldsymbol{K}\end{bmatrix} \quad \boldsymbol{B} = \begin{bmatrix}\boldsymbol{M}\end{bmatrix}$	real eigenpairs, $\omega_i = \sqrt{\lambda_i}$ $\boldsymbol{A}$ singular if rigid body modes
	$\boldsymbol{A} = \begin{bmatrix}-\boldsymbol{K}\end{bmatrix} \quad \boldsymbol{B} = \begin{bmatrix}\boldsymbol{M}\end{bmatrix}$	real eigenpairs, $\omega_i = \sqrt{-\lambda_i}$ $\boldsymbol{A}$ singular if rigid body modes
Undamped Constrained	$\boldsymbol{A} = \begin{bmatrix}-\boldsymbol{K} & -\boldsymbol{C}_q^T \\ -\boldsymbol{C}_q & \boldsymbol{0}\end{bmatrix}, \quad \boldsymbol{B} = \begin{bmatrix}\boldsymbol{M} & \boldsymbol{0} \\ \boldsymbol{0} & \boldsymbol{0}\end{bmatrix}$	real eigenpairs, $\omega_i = \sqrt{-\lambda_i}$ $\|\lambda_i\| = \infty$ for each constraint $\boldsymbol{A}$ singular if rigid body modes $\boldsymbol{B}$ singular
	$\boldsymbol{A} = \begin{bmatrix}-\boldsymbol{K} & \boldsymbol{0} \\ \boldsymbol{0} & \boldsymbol{0}\end{bmatrix}, \quad \boldsymbol{B} = \begin{bmatrix}\boldsymbol{M} & \boldsymbol{C}_q^T \\ \boldsymbol{C}_q & \boldsymbol{0}\end{bmatrix}$	real eigenpairs, $\omega_i = \sqrt{-\lambda_i}$ $\lambda_i = 0$ for each constraint $\boldsymbol{A}$ singular $\boldsymbol{B}$ nonsingular
Damped	$\boldsymbol{A} = \begin{bmatrix}\boldsymbol{0} & \boldsymbol{I} \\ -\boldsymbol{K} & -\boldsymbol{D}\end{bmatrix}, \quad \boldsymbol{B} = \begin{bmatrix}\boldsymbol{I} & \boldsymbol{0} \\ \boldsymbol{0} & \boldsymbol{M}\end{bmatrix}$	complex eigenpairs, $\omega_i = \|\lambda_i\|$ $\boldsymbol{A}$ singular if rigid body modes $\boldsymbol{B}$ singular
Damped Constrained	$\boldsymbol{A} = \begin{bmatrix}\boldsymbol{0} & \boldsymbol{I} & \boldsymbol{0} \\ -\boldsymbol{K} & -\boldsymbol{D} & -\boldsymbol{C}_q^T \\ -\boldsymbol{C}_q & \boldsymbol{0} & \boldsymbol{0}\end{bmatrix}, \boldsymbol{B} = \begin{bmatrix}\boldsymbol{I} & \boldsymbol{0} & \boldsymbol{0} \\ \boldsymbol{0} & \boldsymbol{M} & \boldsymbol{0} \\ \boldsymbol{0} & \boldsymbol{0} & \boldsymbol{0}\end{bmatrix}$	complex eigenpairs, $\omega_i = \|\lambda_i\|$ $\|\lambda_i\| = \infty$ for each constraint $\boldsymbol{A}$ singular if rigid body modes $\boldsymbol{B}$ singular
	$\boldsymbol{A} = \begin{bmatrix}\boldsymbol{0} & \boldsymbol{I} & \boldsymbol{0} \\ -\boldsymbol{K} & -\boldsymbol{D} & \boldsymbol{0} \\ \boldsymbol{0} & \boldsymbol{0} & \boldsymbol{0}\end{bmatrix}, \boldsymbol{B} = \begin{bmatrix}\boldsymbol{I} & \boldsymbol{0} & \boldsymbol{0} \\ \boldsymbol{0} & \boldsymbol{M} & \boldsymbol{C}_q^T \\ \boldsymbol{C}_q & \boldsymbol{0} & \boldsymbol{0}\end{bmatrix}$	complex eigenpairs, $\omega_i = \|\lambda_i\|$ $\lambda_i = 0$ for each constraint $\boldsymbol{A}$ singular $\boldsymbol{B}$ nonsingular

involved. In engineering practice, interest typically lies in a small subset of eigenmodes, often those with the lowest frequencies or those within a specific frequency range. To address this, the Krylov-Schur method has been proposed [254].

However, the Krylov subspace method naturally converges towards eigenvectors associated with the largest eigenvalues, which is contrary to our objective. To overcome this, a Möbius transformation of the eigenvalue problem is required. Additionally, to mitigate potential numerical difficulties caused by the singularity or ill-conditioning of the matrix $\boldsymbol{A}$, a shift technique is also necessary in the implementation.

At the highest level of generality, the GEP is expressed as $\boldsymbol{A}\hat{\underline{\boldsymbol{\Phi}}}_i = \lambda_i \boldsymbol{B}\hat{\underline{\boldsymbol{\Phi}}}_i$. The *shift-and-invert* technique reformulates the eigenvalue problem as follows

$$(\boldsymbol{C} - \mu_i \boldsymbol{I})\,\hat{\underline{\boldsymbol{\Phi}}}_i = 0 \tag{2.181a}$$

$$\boldsymbol{C} = (\boldsymbol{A} - \sigma \boldsymbol{B})^{-1}\,\boldsymbol{B} \tag{2.181b}$$

$$\lambda_i = \frac{1}{\mu_i} + \sigma \tag{2.181c}$$

where μ_i represents the eigenvalue of the transformed eigenvalue problem in (2.181a), and σ denotes the shift parameter specified by the user.

In the Krylov subspace iteration, the largest eigenvalue is naturally obtained first. To target eigenvalues with the smallest magnitude, a small value of σ can be applied, which also improves the conditioning of the linear problem in (2.181b), particularly when $\boldsymbol{A}$ is singular. If a specific range of modal frequencies is of interest, σ can be set to the central frequency of that range. In our experience, a shift value of $\sigma = 1 \times 10^{-3}$ effectively extracts the lower-order modes, including rigid body modes where $\lambda_i \approx 0$, while also addressing issues of ill-conditioning. Notably, the eigenvector $\hat{\underline{\boldsymbol{\Phi}}}_i$ remains unchanged during the shift-and-invert process.

The computation of matrix $\boldsymbol{C}$ in (2.181b) requires the inversion of a large sparse matrix: $(\boldsymbol{A} - \sigma \boldsymbol{B})^{-1}$. This operation is prohibitively expensive for large systems and destroys the sparsity of matrices. However, since only the product $\boldsymbol{b} = \boldsymbol{C}\boldsymbol{v}$ is needed for the iterative solver, an efficient approach is to split this computation into two steps:

$$\boldsymbol{z} = \boldsymbol{B}\boldsymbol{v} \tag{2.182a}$$

$$\boldsymbol{b} = (\boldsymbol{A} - \sigma \boldsymbol{B})^{-1} \boldsymbol{z} \tag{2.182b}$$

We observe that the linear problem in (2.182b) can become a performance bottleneck. A feasible optimization is to factorize the coefficient matrix $(\boldsymbol{A} - \sigma \boldsymbol{B})$ once at the beginning of the Krylov-Schur iterations, since this matrix remains constant throughout. This initial factorization can then be reused multiple times for the computation in (2.182b). For cases involving millions of unknowns, computational efficiency can be further improved by solving the linear problem in (2.182b) using iterative methods such as truncated MINRES or GMRES. However, for problems with tens of thousands of unknowns, our experience suggests that a direct method is more efficient due to the relatively smaller problem size.

It is worth noting that the entries in the stiffness and damping matrices are typically on the order of 10^6 or higher, while the Jacobian matrix of constraints is usually on the order of 10^0. This discrepancy worsens the conditioning of the $\boldsymbol{A}$ matrix. To enhance the robustness of the method, a simple and inexpensive preconditioning of the Jacobian matrix $\boldsymbol{C_q}$ is applied. This is achieved by scaling it with $\text{trace}(\boldsymbol{K})/n_q$, thereby adjusting the Lagrange multipliers $\delta\boldsymbol{\gamma}$ to be on the same order of magnitude as the displacements $\delta\boldsymbol{q}$.

The Krylov-Schur method, introduced in 2001 [254], is implemented following the guidelines in [68], as detailed in Algorithm 1. It has been extended to handle cases involving complex and sparse matrices and has been integrated into the open-source multibody dynamics library CHRONO [260].

The code allows users to specify different problem formulations, either in direct or shift-invert mode, by providing different OP_CV($\boldsymbol{v}$) operators in Algorithm 2. For example, Algorithm 3 illustrates the implementation for the shift-invert case, following equations (2.182) and (2.182b).

The linear problem in (2.182b) can theoretically be solved by any linear solver that supports complex values. For smaller problems, the choice of solver is not critical; for instance, SparseLU and SparseQR functions from the popular C++ linear algebra library EIGEN [102] are suitable options. However, for most practical engineering applications, the presence of ill-conditioned matrices and the requirement for high accuracy and robustness make it necessary to employ more advanced solvers, such as Pardiso MKL or MUMPS [64]. Given the importance of solver selection, our Krylov-Schur implementation allows users to choose the most appropriate solver for their specific application requirements.

Algorithm 1 Krylov-Schur

procedure KRYLOV-SCHUR(OP_CV(),k, m)
  $Q(:,1) := v1/norm(v1)$
  $p := 1$
  $isC := 0$
  $[Q, H] :=$ KRYLOVEXPANSION(OP_CV(),$Q, H, 0, k$)
  while $i < i_{\max}$ & $p < k$ **do**
    $i++$
    $isC := 0$
    $[Q, H] :=$ KRYLOVEXPANSION(OP_CV(),$Q, H, k + isC, m$)
    $[U, T, isC] :=$ SORTSCHUR($H(p:m, p:m), k - p + 1$)
    $H(p:m, p:m) := T$
    $H(1:p-1, p:m) := H(1:p-1, p:m)\,U$
    $Q(:, p:m) := Q(:, p:m)\,U$
    $H(m+1, p:m) := H(m+1, m)\,U(end, :)$
    $Q := [Q(:, 1:k), Q(:, m+1)]$
    $H := [H(1:k, 1:k); H(m+1, 1:k)]$
    CHECKCONVERGENCE(H, $k + isC$, p, tol)
  end while
  $[\mu, \mathbf{\Phi}_H] :=$ EIG($H(1:k+isC, 1:k+isC)$)
  $\mathbf{\Phi} = Q(:, k+isC)\mathbf{\Phi}_H$
  return $\mu, \mathbf{\Phi}$
end procedure

Algorithm 2 Krylov Expansion

procedure KRYLOVEXPANSION(OP_CV(),Q, H, k_s, k_e)
  for $k = k_s + 1 : k_e$ **do**
    v :=OP_CV($Q(:, k)$)
    $isC := 0$
    $w := Q(:, 1 : k)' \, v$
    $v -= Q(:, 1 : k) \, w$
    $w2 := Q(:, 1 : k)' \, v$
    $v -= Q(:, 1 : k) \, w2$
    $w += w2$
    $nv := norm(v)$
    $Q(:, k + 1) := v/nv$
    $H(1 : k + 1, k) := [w; nv]$
  end for
end procedure

Algorithm 3 Op_Cv operator

procedure OP_CV(v)
  $\boldsymbol{z} = B\boldsymbol{v}$
  $\boldsymbol{r} = (A - \sigma B)^{-1}\boldsymbol{z}$
  return $\boldsymbol{r}$
end procedure

Chapter 3

Linearization

The generic form of the linearized index-3 DAEs has been outlined in Section 2.6. In this chapter, the linearization procedure is presented in detail, along with the corresponding expressions for various terms, including the tangent stiffness matrix of the constraints $\boldsymbol{K}_c$, the aerodynamic damping and stiffness matrices $\boldsymbol{D}_a$ and $\boldsymbol{K}_a$, as well as the inertial damping and stiffness matrices $\boldsymbol{D}_i$ and $\boldsymbol{K}_i$. The multi-bladed rotor system exhibits time-varying properties due to continuous rotation. To perform a proper eigenvalue analysis, it is necessary to transform the generalized coordinates of the blade beam nodes into an auxiliary basis defined in a floating frame of reference at the rotor's rotating center. This coordinate transformation is discussed in detail. In the end, the *Multi-Blade Coordinate* (MBC) transformation is introduced, resulting in linear time-invariant DAEs that are well-suited for the subsequent eigenvalue analysis. An interpretation of the modal dynamics of wind turbines is also provided.

3.1 Tangent stiffness matrix of constraints

We recall the general expression of the *tangent stiffness matrix of constraints*:

$$\boldsymbol{K}_c = \frac{\partial \boldsymbol{C}_{\boldsymbol{q}}(\boldsymbol{q}, t)^T}{\partial \boldsymbol{q}} \boldsymbol{\gamma} \tag{3.1}$$

The expression for the Jacobian matrix of constraints, $\boldsymbol{C}_{\boldsymbol{q}}(\boldsymbol{q}, t)$, has been introduced in Section 2.5. In this section, we derive the Jacobian matrix of $\boldsymbol{C}_{\boldsymbol{q}}$ with respect to $\boldsymbol{q}$, yielding a unified analytical expression for the tangent stiffness matrix of holonomic constraints. To illustrate the significance and practical applications of this matrix, an example involving an anchor chain is provided. This example demonstrates the relevance of the tangent stiffness matrix of constraints in both static equilibrium analysis and eigenvalue analysis for systems that exhibit rigid-body motion.

3.1.1 Introduction

The tangent stiffness matrix of constraints, $\boldsymbol{K}_c$, stems from changes in the direction of reaction forces and moments of the joints, representing a geometric nonlinear phenomenon. This is different from the stiffness contribution provided by the material properties of the joints [170], which is associated with the deformation of bodies.

In many applications of flexible multibody system dynamics, the structural material stiffness matrix $\boldsymbol{K}_m$ and the structural geometric stiffness matrix $\boldsymbol{K}_g$ are typically the primary factors driving the analysis. In contrast, the contribution of the tangent stiffness matrix of constraints, $\boldsymbol{K}_c$, is often negligible. However, this matrix can become significant in case of extremely-soft flexible bodies or in rigid-body systems under heavy loading.

A classic example is a pendulum hinged at a fixed point and subjected to gravitational forces. If the tangent stiffness matrix of constraints $\boldsymbol{K}_c$ is neglected, the system stiffness matrix becomes zero, as shown in Equation (2.159). Consequently, during the static equilibrium analysis, the Newton-Raphson method lacks the necessary directional information to search for the equilibrium state, leading to divergence. Additionally, the eigenvalues of the system would be zero because of the zero stiffness matrix. This result is incorrect, as it is well-known that a pendulum exhibits oscillatory motion around the static equilibrium state.

It is true that the same dynamics model can be simulated without incorporating the tangent stiffness matrix of constraints. This is because dynamic simulations can still converge to reasonable solutions with only an approximate stiffness matrix [73]. Nonetheless, even in cases where iterative schemes provide increasingly accurate approximations, incorporating $\boldsymbol{K}_c$ can enhance the stability, convergence, and, in some cases, the performance of numerical methods. For instance, in computer graphics applications, such as those in the film and gaming industries where performance is prioritized over accuracy, the inclusion of this matrix can effectively improve the stability of dynamic simulations, especially for systems with inextensible objects or articulated chains [269].

In these applications, the symmetric form $\left(\boldsymbol{K}_c + \boldsymbol{K}_c^T\right)/2$ is employed to maintain matrix symmetry in implicit integrators, leading to faster solutions for linear equations. Inspired by the discovery of Tournier [269], Andrews [4] developed a diagonal approximation of the tangent stiffness matrix of constraints to reduce energy dissipation during simulations and derived closed-form expressions for a range of joints commonly used in articulated rigid-body simulations. However, no unified expression has been presented. Building on these developments, Macklin [175] further refined the diagonal approximation of $\boldsymbol{K}_c$ using successive finite differences from the last two Newton iterations, clamping the shift to ensure the matrix positive definiteness.

Although many studies [195, 95, 178] in the field of linearizing the equations

of motion for constrained multibody systems have pointed out the existence of the tangent stiffness matrix of constraints, unified analytical expressions for this matrix have not been clearly reported.

Bauchau [11] introduced the concept of the tangent stiffness matrix (referred to as the *equivalent stiffness matrix* in his work), though his formulation was based on Euler parametrization rather than quaternions. Similarly, Géradin and Cardona [104] mention the tangent stiffness matrix of constraints, but they do not provide a detailed expansion of this term.

Minaker [188] derived analytical expressions for the tangent stiffness matrix for several types of constraints, including the revolute joint, point-on-plane contact, and rolling disk contact. His work highlighted the significant influence of the tangent stiffness matrix on the eigenvalues of the A-arm suspension system, thereby demonstrating its importance in vehicle dynamics analysis. Furthermore, Minaker suggested that a generic expression for the tangent stiffness matrix of constraints might exist due to the similarities observed in the forms of the stiffness matrices for the studied constraints. In a later study, Minaker [189] calculated the tangent stiffness matrix for a constant velocity joint and verified his results through a comparison of different modeling approaches.

To derive the tangent stiffness matrix of constraints (3.1), we need to linearize the reaction forces and moments $\boldsymbol{C_q}(\boldsymbol{q},t)^T\boldsymbol{\gamma}$ with respect to the generalized coordinates $\delta\boldsymbol{q} = \left[\delta\boldsymbol{r}_{B_1}^T, \delta\boldsymbol{\theta}_{l_{B_1}}^T, \delta\boldsymbol{r}_{B_2}^T, \delta\boldsymbol{\theta}_{l_{B_2}}^T\right]^T$. In this linearization process, the Lagrange multipliers $\boldsymbol{\gamma}$ are assumed to remain constant because their variations are already accounted for in the other linearization term, $\boldsymbol{C_q}(\boldsymbol{q},t)^T\delta\boldsymbol{\gamma}$, as shown in Equation (2.76a).

3.1.2 Scleronomic constraints

Main Part

The Lagrange multipliers $\boldsymbol{\gamma}$ can be split into two parts

$$\boldsymbol{\gamma} = \left[\boldsymbol{\gamma}_{f\ (F_2)}^T, \boldsymbol{\gamma}_{m(F_2)}^T\right]^T \tag{3.2}$$

where $\boldsymbol{\gamma}_{f_{(F_2)}}, \boldsymbol{\gamma}_{m_{(F_2)}} \in \mathbb{R}^3$ are the reaction forces and moments of the joint expressed in the main frame F_2, respectively.

Recalling the expression (2.60), the transpose of the Jacobian matrix of constraint can be written in the following compact form

$$\boldsymbol{C}_{\boldsymbol{q}}^T = \begin{bmatrix} \boldsymbol{J}_{x_1}^T & \boldsymbol{0} \\ \boldsymbol{J}_{r_1}^T & \boldsymbol{J}_{w_1}^T \\ \boldsymbol{J}_{x_2}^T & \boldsymbol{0} \\ \boldsymbol{J}_{r_2}^T & \boldsymbol{J}_{w_2}^T \end{bmatrix} \tag{3.3}$$

where the sub-blocks are

$$\boldsymbol{J}_{x_1}^T = \boldsymbol{R}_{F_2} \tag{3.4a}$$
$$\boldsymbol{J}_{r_1}^T = \widetilde{\boldsymbol{r}}_{B_1.F_{1(B_1)}} \boldsymbol{R}_{B_1}^T \boldsymbol{R}_{F_2} \tag{3.4b}$$
$$\boldsymbol{J}_{w_1}^T = \boldsymbol{R}_{B_1}^T \boldsymbol{R}_{F_2} \boldsymbol{P}\left(\boldsymbol{\rho}_{F_{1(F_2)}}\right) \tag{3.4c}$$
$$\boldsymbol{J}_{x_2}^T = -\boldsymbol{R}_{F_2} \tag{3.4d}$$
$$\boldsymbol{J}_{r_2}^T = -\widetilde{\boldsymbol{r}}_{B_2.F_{2(B_2)}} \boldsymbol{R}_{B_2}^T \boldsymbol{R}_{F_2} - \widetilde{\boldsymbol{r}_{21}}_{(B_2)} \boldsymbol{R}_{B_2}^T \boldsymbol{R}_{F_2} \tag{3.4e}$$
$$\boldsymbol{J}_{w_2}^T = -\boldsymbol{R}_{B_2}^T \boldsymbol{R}_{F_2} \boldsymbol{P}\left(\boldsymbol{\rho}_{F_{1(F_2)}}\right) \tag{3.4f}$$

Since F_1, F_2 are rigidly attached on B_1, B_2, respectively, we have $\delta \boldsymbol{r}_{B_1.F_{1(B_1)}} = \boldsymbol{0}$, $\delta \boldsymbol{r}_{B_2.F_{2(B_2)}} = \boldsymbol{0}$, $\delta \boldsymbol{R}_{F_{1(B_1)}} = \boldsymbol{0}$, $\delta \boldsymbol{R}_{F_{2(B_2)}} = \boldsymbol{0}$. Meanwhile, recalling the equality (2.15b), and the property of the skew-symmetric matrix (2.1a), the variations of the sub-blocks are calculated as

$$\delta \boldsymbol{J}_{x_1}^T = \boldsymbol{R}_{B_2} \widetilde{\delta \boldsymbol{\theta}}_{l_{B_2}} \boldsymbol{R}_{B_2}^T \boldsymbol{R}_{F_2} \tag{3.5a}$$
$$\delta \boldsymbol{J}_{r_1}^T = \widetilde{\boldsymbol{r}}_{B_1.F_{1(B_1)}} \left(-\widetilde{\delta \boldsymbol{\theta}}_{l_{B_1}} \boldsymbol{R}_{B_1}^T \boldsymbol{R}_{F_2} + \boldsymbol{R}_{B_1}^T \boldsymbol{R}_{B_2} \widetilde{\delta \boldsymbol{\theta}}_{l_{B_2}} \boldsymbol{R}_{B_2}^T \boldsymbol{R}_{F_2}\right) \tag{3.5b}$$
$$\begin{aligned} \delta \boldsymbol{J}_{w_1}^T = &\left(-\widetilde{\delta \boldsymbol{\theta}}_{l_{B_1}} \boldsymbol{R}_{B_1}^T \boldsymbol{R}_{F_2} + \boldsymbol{R}_{B_1}^T \boldsymbol{R}_{B_2} \widetilde{\delta \boldsymbol{\theta}}_{l_{B_2}} \boldsymbol{R}_{B_2}^T \boldsymbol{R}_{F_2}\right) \boldsymbol{P}\left(\boldsymbol{\rho}_{F_{1(F_2)}}\right) \\ &+ \left(\boldsymbol{R}_{B_1}^T \boldsymbol{R}_{F_2}\right) \delta \boldsymbol{P}\left(\boldsymbol{\rho}_{F_{1(F_2)}}\right) \end{aligned} \tag{3.5c}$$
$$\delta \boldsymbol{J}_{x_2}^T = -\boldsymbol{R}_{B_2} \widetilde{\delta \boldsymbol{\theta}}_{l_{B_2}} \boldsymbol{R}_{B_2}^T \boldsymbol{R}_{F_2} \tag{3.5d}$$
$$\delta \boldsymbol{J}_{r_2}^T = -\widetilde{\delta \boldsymbol{r}_{21}}_{(B_2)} \boldsymbol{R}_{B_2}^T \boldsymbol{R}_{F_2} \tag{3.5e}$$
$$\delta \boldsymbol{J}_{w_2}^T = -\boldsymbol{R}_{B_2}^T \boldsymbol{R}_{F_2} \delta \boldsymbol{P}\left(\boldsymbol{\rho}_{F_{1(F_2)}}\right) \tag{3.5f}$$

Recalling the definition of $\boldsymbol{r}_{21_{(B_2)}}$ in (2.51), and using the properties (2.1b) and (2.1c), its variation $\delta \boldsymbol{r}_{21_{(B_2)}}$ is calculated as

$$\begin{aligned} \delta \boldsymbol{r}_{21_{(B_2)}} = &\boldsymbol{R}_{B_2}^T \delta \boldsymbol{r}_{B_1} - \boldsymbol{R}_{B_2}^T \boldsymbol{R}_{B_1} \widetilde{\boldsymbol{r}}_{B_1.F_{1(B_1)}} \delta \boldsymbol{\theta}_{l_{B_1}} \\ &- \boldsymbol{R}_{B_2}^T \delta \boldsymbol{r}_{B_2} + \left(\widetilde{\boldsymbol{r}_{21}}_{(B_2)} + \widetilde{\boldsymbol{r}}_{B_2.F_{2(B_2)}}\right) \delta \boldsymbol{\theta}_{l_{B_2}} \end{aligned} \tag{3.6}$$

Consequently, its skew-symmetric matrix is given by

$$\begin{aligned} \widetilde{\delta \boldsymbol{r}_{21}}_{(B_2)} = &\boldsymbol{R}_{B_2}^T \widetilde{\delta \boldsymbol{r}}_{B_1} \boldsymbol{R}_{B_2} - \boldsymbol{R}_{B_2}^T \boldsymbol{R}_{B_1} \widetilde{\left(\widetilde{\boldsymbol{r}}_{B_1.F_{1(B_1)}} \delta \boldsymbol{\theta}_{l_{B_1}}\right)} \boldsymbol{R}_{B_1}^T \boldsymbol{R}_{B_2} \\ &- \boldsymbol{R}_{B_2}^T \widetilde{\delta \boldsymbol{r}}_{B_2} \boldsymbol{R}_{B_2} + \widetilde{\left(\left(\widetilde{\boldsymbol{r}_{21}}_{(B_2)} + \widetilde{\boldsymbol{r}}_{B_2.F_{2(B_2)}}\right) \delta \boldsymbol{\theta}_{l_{B_2}}\right)} \end{aligned} \tag{3.7}$$

where the properties (2.1b) and (2.1e) are used.

Substituting (3.7) into (3.5e), the calculation of $\delta \boldsymbol{J}_{r_2}^T$ follows as

$$\begin{aligned}\delta \boldsymbol{J}_{r_2}^T = &- \boldsymbol{R}_{B_2}^T \widetilde{\delta \boldsymbol{r}}_{B_1} \boldsymbol{R}_{F_2} + \boldsymbol{R}_{B_2}^T \boldsymbol{R}_{B_1} \left(\widetilde{\widetilde{\boldsymbol{r}}_{B_1.F_{1(B_1)}} \delta \boldsymbol{\theta}_{l_{B_1}}} \right) \boldsymbol{R}_{B_1}^T \boldsymbol{R}_{F_2} \\ &+ \boldsymbol{R}_{B_2}^T \widetilde{\delta \boldsymbol{r}}_{B_2} \boldsymbol{R}_{F_2} - \left(\left(\widetilde{\boldsymbol{r}_{21}}_{(B_2)} + \widetilde{\widetilde{\boldsymbol{r}}_{B_2.F_{2(B_2)}} \delta \boldsymbol{\theta}_{l_{B_2}}} \right) \right) \boldsymbol{R}_{B_2}^T \boldsymbol{R}_{F_2}\end{aligned} \tag{3.8}$$

Recalling (3.2) and (3.3), the variation of the reaction forces and moments of the joint is expressed as

$$\delta \boldsymbol{C}_{\boldsymbol{q}}^T \boldsymbol{\gamma} = \begin{bmatrix} \delta \boldsymbol{J}_{x_1}^T \boldsymbol{\gamma}_{f_{(F_2)}} \\ \delta \boldsymbol{J}_{r_1}^T \boldsymbol{\gamma}_{f_{(F_2)}} + \delta \boldsymbol{J}_{w_1}^T \boldsymbol{\gamma}_{m_{(F_2)}} \\ \delta \boldsymbol{J}_{x_2}^T \boldsymbol{\gamma}_{f_{(F_2)}} \\ \delta \boldsymbol{J}_{r_2}^T \boldsymbol{\gamma}_{f_{(F_2)}} + \delta \boldsymbol{J}_{w_2}^T \boldsymbol{\gamma}_{m_{(F_2)}} \end{bmatrix} \tag{3.9}$$

Substituting (3.5) and (3.8) into (3.9), and remembering the properties (2.1c) and (2.1e) from which follows the useful property $\widetilde{\delta \boldsymbol{\theta}}_l \boldsymbol{R} \boldsymbol{\gamma} = -\boldsymbol{R} \widetilde{\boldsymbol{\gamma}} \boldsymbol{R}^T \delta \boldsymbol{\theta}_l$, the four rows are calculated as

$$\delta \boldsymbol{J}_{x_1}^T \boldsymbol{\gamma}_{f_{(F_2)}} = -\boldsymbol{R}_{F_2} \widetilde{\boldsymbol{\gamma}}_{f_{(F_2)}} \boldsymbol{R}_{F_2}^T \boldsymbol{R}_{B_2} \delta \boldsymbol{\theta}_{l_{B_2}} \tag{3.10a}$$

$$\begin{aligned}\delta \boldsymbol{J}_{r_1}^T \boldsymbol{\gamma}_{f_{(F_2)}} + \delta \boldsymbol{J}_{w_1}^T \boldsymbol{\gamma}_{m_{(F_2)}} = &\ \widetilde{\boldsymbol{r}}_{B_1.F_{1(B_1)}} \boldsymbol{R}_{B_1}^T \boldsymbol{R}_{F_2} \widetilde{\boldsymbol{\gamma}}_{f_{(F_2)}} \boldsymbol{R}_{F_2}^T \boldsymbol{R}_{B_1} \delta \boldsymbol{\theta}_{l_{B_1}} \\ &- \widetilde{\boldsymbol{r}}_{B_1.F_{1(B_1)}} \boldsymbol{R}_{B_1}^T \boldsymbol{R}_{F_2} \widetilde{\boldsymbol{\gamma}}_{f_{(F_2)}} \boldsymbol{R}_{F_2}^T \boldsymbol{R}_{B_2} \delta \boldsymbol{\theta}_{l_{B_2}} \\ &+ \boldsymbol{R}_{B_1}^T \boldsymbol{R}_{F_2} \left(\boldsymbol{P} \left(\widetilde{\boldsymbol{\rho}_{F_{1(F_2)}}} \right) \boldsymbol{\gamma}_{m_{(F_2)}} \right) \boldsymbol{R}_{F_2}^T \boldsymbol{R}_{B_1} \delta \boldsymbol{\theta}_{l_{B_1}} \\ &- \boldsymbol{R}_{B_1}^T \boldsymbol{R}_{F_2} \left(\boldsymbol{P} \left(\widetilde{\boldsymbol{\rho}_{F_{1(F_2)}}} \right) \boldsymbol{\gamma}_{m_{(F_2)}} \right) \boldsymbol{R}_{F_2}^T \boldsymbol{R}_{B_2} \delta \boldsymbol{\theta}_{l_{B_2}} \\ &+ \boldsymbol{R}_{B_1}^T \boldsymbol{R}_{F_2} \delta \boldsymbol{P} \left(\boldsymbol{\rho}_{F_{1(F_2)}} \right) \boldsymbol{\gamma}_{m_{(F_2)}}\end{aligned} \tag{3.10b}$$

$$\delta \boldsymbol{J}_{x_2}^T \boldsymbol{\gamma}_{f_{(F_2)}} = \boldsymbol{R}_{F_2} \widetilde{\boldsymbol{\gamma}}_{f_{(F_2)}} \boldsymbol{R}_{F_2}^T \boldsymbol{R}_{B_2} \delta \boldsymbol{\theta}_{l_{B_2}} \tag{3.10c}$$

$$\begin{aligned}\delta \boldsymbol{J}_{r_2}^T \boldsymbol{\gamma}_{f_{(F_2)}} + \delta \boldsymbol{J}_{w_2}^T \boldsymbol{\gamma}_{m_{(F_2)}} = &\ \boldsymbol{R}_{B_2}^T \boldsymbol{R}_{F_2} \widetilde{\boldsymbol{\gamma}}_{f_{(F_2)}} \boldsymbol{R}_{F_2}^T \delta \boldsymbol{r}_{B_1} \\ &- \boldsymbol{R}_{B_2}^T \boldsymbol{R}_{F_2} \widetilde{\boldsymbol{\gamma}}_{f_{(F_2)}} \boldsymbol{R}_{F_2}^T \delta \boldsymbol{r}_{B_2} \\ &- \boldsymbol{R}_{B_2}^T \boldsymbol{R}_{F_2} \widetilde{\boldsymbol{\gamma}}_{f_{(F_2)}} \boldsymbol{R}_{F_2}^T \boldsymbol{R}_{B_1} \widetilde{\boldsymbol{r}}_{B_1.F_{1(B_1)}} \delta \boldsymbol{\theta}_{l_{B_1}} \\ &+ \boldsymbol{R}_{B_2}^T \boldsymbol{R}_{F_2} \widetilde{\boldsymbol{\gamma}}_{f_{(F_2)}} \boldsymbol{R}_{F_2}^T \boldsymbol{R}_{B_2} \left(\widetilde{\boldsymbol{r}_{21}}_{(B_2)} + \widetilde{\boldsymbol{r}}_{B_2.F_{2(B_2)}} \right) \delta \boldsymbol{\theta}_{l_{B_2}} \\ &- \boldsymbol{R}_{B_2}^T \boldsymbol{R}_{F_2} \delta \boldsymbol{P} \left(\boldsymbol{\rho}_{F_{1(F_2)}} \right) \boldsymbol{\gamma}_{m_{(F_2)}}\end{aligned} \tag{3.10d}$$

Substituting (3.10) into (3.9), and grouping the coefficient terms according to the generalized coordinates $\delta \boldsymbol{q} = \left[\delta \boldsymbol{r}_{B_1}^T, \delta \boldsymbol{\theta}_{l_{B_1}}^T, \delta \boldsymbol{r}_{B_2}^T, \delta \boldsymbol{\theta}_{l_{B_2}}^T \right]^T$, one obtains

$$\delta \boldsymbol{C}_{\boldsymbol{q}}^T \boldsymbol{\gamma} = \boldsymbol{K}_c^{(M)} \delta \boldsymbol{q} + \delta \boldsymbol{\Gamma} \tag{3.11}$$

where the main part of the tangent stiffness matrix of constraints is expressed as

$$\boldsymbol{K}_c^{(M)} = \begin{bmatrix} \mathbf{0} & \mathbf{0} & \mathbf{0} & \boldsymbol{K}_{c_{14}}^{(M)} \\ \mathbf{0} & \boldsymbol{K}_{c_{22}}^{(M)} & \mathbf{0} & \boldsymbol{K}_{c_{24}}^{(M)} \\ \mathbf{0} & \mathbf{0} & \mathbf{0} & \boldsymbol{K}_{c_{34}}^{(M)} \\ \boldsymbol{K}_{c_{41}}^{(M)} & \boldsymbol{K}_{c_{42}}^{(M)} & \boldsymbol{K}_{c_{43}}^{(M)} & \boldsymbol{K}_{c_{44}}^{(M)} \end{bmatrix} \tag{3.12}$$

in which the sub-blocks are given by

$$\boldsymbol{K}_{c_{14}}^{(M)} = -\boldsymbol{R}_{F_2}\widetilde{\boldsymbol{\gamma}}_{f_{(F_2)}}\boldsymbol{R}_{F_2}^T\boldsymbol{R}_{B_2} \tag{3.13a}$$

$$\boldsymbol{K}_{c_{22}}^{(M)} = \widetilde{\boldsymbol{r}}_{B_1.F_{1(B_1)}}\boldsymbol{R}_{B_1}^T\boldsymbol{R}_{F_2}\widetilde{\boldsymbol{\gamma}}_{f_{(F_2)}}\boldsymbol{R}_{F_2}^T\boldsymbol{R}_{B_1} + \boldsymbol{R}_{B_1}^T\boldsymbol{R}_{F_2}\Big(\boldsymbol{P}\Big(\widetilde{\boldsymbol{\rho}_{F_{1(F_2)}}}\Big)\boldsymbol{\gamma}_{m_{(F_2)}}\Big)\boldsymbol{R}_{F_2}^T\boldsymbol{R}_{B_1} \tag{3.13b}$$

$$\boldsymbol{K}_{c_{24}}^{(M)} = -\widetilde{\boldsymbol{r}}_{B_1.F_{1(B_1)}}\boldsymbol{R}_{B_1}^T\boldsymbol{R}_{F_2}\widetilde{\boldsymbol{\gamma}}_{f_{(F_2)}}\boldsymbol{R}_{F_2}^T\boldsymbol{R}_{B_2} - \boldsymbol{R}_{B_1}^T\boldsymbol{R}_{F_2}\Big(\boldsymbol{P}\Big(\widetilde{\boldsymbol{\rho}_{F_{1(F_2)}}}\Big)\boldsymbol{\gamma}_{m_{(F_2)}}\Big)\boldsymbol{R}_{F_2}^T\boldsymbol{R}_{B_2} \tag{3.13c}$$

$$\boldsymbol{K}_{c_{34}}^{(M)} = \boldsymbol{R}_{F_2}\widetilde{\boldsymbol{\gamma}}_{f_{(F_2)}}\boldsymbol{R}_{F_2}^T\boldsymbol{R}_{B_2} \tag{3.13d}$$

$$\boldsymbol{K}_{c_{41}}^{(M)} = \boldsymbol{R}_{B_2}^T\boldsymbol{R}_{F_2}\widetilde{\boldsymbol{\gamma}}_{f_{(F_2)}}\boldsymbol{R}_{F_2}^T \tag{3.13e}$$

$$\boldsymbol{K}_{c_{42}}^{(M)} = -\boldsymbol{R}_{B_2}^T\boldsymbol{R}_{F_2}\widetilde{\boldsymbol{\gamma}}_{f_{(F_2)}}\boldsymbol{R}_{F_2}^T\boldsymbol{R}_{B_1}\widetilde{\boldsymbol{r}}_{B_1.F_{1(B_1)}} \tag{3.13f}$$

$$\boldsymbol{K}_{c_{43}}^{(M)} = -\boldsymbol{R}_{B_2}^T\boldsymbol{R}_{F_2}\widetilde{\boldsymbol{\gamma}}_{f_{(F_2)}}\boldsymbol{R}_{F_2}^T \tag{3.13g}$$

$$\boldsymbol{K}_{c_{44}}^{(M)} = \boldsymbol{R}_{B_2}^T\boldsymbol{R}_{F_2}\widetilde{\boldsymbol{\gamma}}_{f_{(F_2)}}\boldsymbol{R}_{F_2}^T\boldsymbol{R}_{B_2}\left(\widetilde{\boldsymbol{r}_{21}}_{(B_2)} + \widetilde{\boldsymbol{r}}_{B_2.F_{2(B_2)}}\right) \tag{3.13h}$$

The remaining part in (3.11) is read as

$$\delta\boldsymbol{\Gamma} = \begin{bmatrix} \mathbf{0} \\ \boldsymbol{R}_{B_1}^T\boldsymbol{R}_{F_2}\delta\boldsymbol{P}\left(\boldsymbol{\rho}_{F_{1(F_2)}}\right)\boldsymbol{\gamma}_{m_{(F_2)}} \\ \mathbf{0} \\ -\boldsymbol{R}_{B_2}^T\boldsymbol{R}_{F_2}\delta\boldsymbol{P}\left(\boldsymbol{\rho}_{F_{1(F_2)}}\right)\boldsymbol{\gamma}_{m_{(F_2)}} \end{bmatrix} \tag{3.14}$$

When F_1 and F_2 are coincident, for instance when the constraints of a fixed joint are satisfied, the relative quaternion $\boldsymbol{\rho}_{F_{1(F_2)}}$ is identity quaternion, and the projection matrix boils down to $\boldsymbol{P}\left(\boldsymbol{\rho}_{F_{1(F_2)}}\right) = \frac{1}{2}\boldsymbol{I}_{3\times 3}$.

Projection Part

The matrix $\boldsymbol{P}\left(\boldsymbol{\rho}_{F_{1(F_2)}}\right)$ present in (2.60) – originated from the variation of the quaternion of (A.2) – can map the Lagrange multipliers $\boldsymbol{\gamma}_{m_{(F_2)}}$ to a part of the reaction moments in the basis of the main frame F_2, thus we call it *projection matrix*. Consequently, the remaining term (3.14) is called the *projection part* of the tangent stiffness matrix of constraints.

Employing the equality (A.12) and the equation (2.56), the expression (3.14) is further derived as

$$\delta\boldsymbol{\Gamma} = \begin{bmatrix} \mathbf{0} \\ \boldsymbol{R}_{B_1}^T \boldsymbol{R}_{F_2} \boldsymbol{G}\left(\boldsymbol{\rho}_{F_1(F_2)}, \boldsymbol{\gamma}_{m_{(F_2)}}\right) \boldsymbol{R}_{F_1}^T \left(\boldsymbol{R}_{B_1} \delta\boldsymbol{\theta}_{l_{B_1}} - \boldsymbol{R}_{B_2} \delta\boldsymbol{\theta}_{l_{B_2}}\right) \\ \mathbf{0} \\ -\boldsymbol{R}_{B_2}^T \boldsymbol{R}_{F_2} \boldsymbol{G}\left(\boldsymbol{\rho}_{F_1(F_2)}, \boldsymbol{\gamma}_{m_{(F_2)}}\right) \boldsymbol{R}_{F_1}^T \left(\boldsymbol{R}_{B_1} \delta\boldsymbol{\theta}_{l_{B_1}} - \boldsymbol{R}_{B_2} \delta\boldsymbol{\theta}_{l_{B_2}}\right) \end{bmatrix} \tag{3.15}$$

Grouping the coefficient terms according to the generalized coordinates $\delta\boldsymbol{q} = \left[\delta\boldsymbol{r}_{B_1}^T, \delta\boldsymbol{\theta}_{l_{B_1}}^T, \delta\boldsymbol{r}_{B_2}^T, \delta\boldsymbol{\theta}_{l_{B_2}}^T\right]^T$, one obtains the projection part of the tangent stiffness matrix of constraints as

$$\boldsymbol{K}_c^{(P)} = \begin{bmatrix} \mathbf{0} & \mathbf{0} & \mathbf{0} & \mathbf{0} \\ \mathbf{0} & \boldsymbol{K}_{c_{22}}^{(P)} & \mathbf{0} & \boldsymbol{K}_{c_{24}}^{(P)} \\ \mathbf{0} & \mathbf{0} & \mathbf{0} & \mathbf{0} \\ \mathbf{0} & \boldsymbol{K}_{c_{42}}^{(P)} & \mathbf{0} & \boldsymbol{K}_{c_{44}}^{(P)} \end{bmatrix} \tag{3.16}$$

in which the sub-blocks are

$$\boldsymbol{K}_{c_{22}}^{(P)} = \boldsymbol{R}_{B_1}^T \boldsymbol{R}_{F_2} \boldsymbol{G}\left(\boldsymbol{\rho}_{F_1(F_2)}, \boldsymbol{\gamma}_{m_{(F_2)}}\right) \boldsymbol{R}_{F_1}^T \boldsymbol{R}_{B_1} \tag{3.17a}$$

$$\boldsymbol{K}_{c_{24}}^{(P)} = -\boldsymbol{R}_{B_1}^T \boldsymbol{R}_{F_2} \boldsymbol{G}\left(\boldsymbol{\rho}_{F_1(F_2)}, \boldsymbol{\gamma}_{m_{(F_2)}}\right) \boldsymbol{R}_{F_1}^T \boldsymbol{R}_{B_2} \tag{3.17b}$$

$$\boldsymbol{K}_{c_{42}}^{(P)} = -\boldsymbol{R}_{B_2}^T \boldsymbol{R}_{F_2} \boldsymbol{G}\left(\boldsymbol{\rho}_{F_1(F_2)}, \boldsymbol{\gamma}_{m_{(F_2)}}\right) \boldsymbol{R}_{F_1}^T \boldsymbol{R}_{B_1} \tag{3.17c}$$

$$\boldsymbol{K}_{c_{44}}^{(P)} = \boldsymbol{R}_{B_2}^T \boldsymbol{R}_{F_2} \boldsymbol{G}\left(\boldsymbol{\rho}_{F_1(F_2)}, \boldsymbol{\gamma}_{m_{(F_2)}}\right) \boldsymbol{R}_{F_1}^T \boldsymbol{R}_{B_2} \tag{3.17d}$$

If F_1, F_2 are coincident, for instance, when the constraints of a fixed joint are satisfied, the relative quaternion $\boldsymbol{\rho}_{F_1(F_2)}$ is identity quaternion, one has a simple matrix $\boldsymbol{G}\left(\boldsymbol{\rho}_{F_1(F_2)}, \boldsymbol{\gamma}_{m_{(F_2)}}\right) = -\frac{1}{4}\widetilde{\boldsymbol{\gamma}_{m_{(F_2)}}}$.

Complete Form

The complete form of the tangent stiffness matrix of constraints is the summation of the main part (3.12) and the projection part (3.16), i.e.,

$$\boldsymbol{K}_c = \boldsymbol{K}_c^{(M)} + \boldsymbol{K}_c^{(P)} \tag{3.18}$$

The block patterns of $\boldsymbol{K}_c^{(M)}$ and $\boldsymbol{K}_c^{(P)}$ are symmetric, but in general both of them are neither symmetric nor skew-symmetric.

The tangent stiffness matrix of constraints of other types of joints in Table 2.1 can be calculated using (3.18) directly. The reaction forces and moments associated with the free DOFs are zero, thus the corresponding rows in the Jacobian matrix of constraints can be eliminated automatically.

3.1.3 Rheonomic constraints

The Jacobian matrix of translational rheonomic constraints is the same as the scleronomic constraints, hence the tangent stiffness matrix is the same.

There is a difference in the rotational rheonomic constraints. By comparing the expression (2.60) and (2.68), one can note that the only discrepancy between the scleronomic and rheonomic constraints is the projection matrix $\boldsymbol{P}$: replacing $\boldsymbol{P}\left(\boldsymbol{\rho}_{F_{1(F_2)}}\right)$ in (2.60) with $\boldsymbol{P}\left(\boldsymbol{\rho}_{F_1^{\Diamond}(F_2)}\right)$ yields the expression (2.68). Thus one just needs to replace $\boldsymbol{P}\left(\boldsymbol{\rho}_{F_{1(F_2)}}\right)$ in (3.12) with $\boldsymbol{P}\left(\boldsymbol{\rho}_{F_1^{\Diamond}(F_2)}\right)$ to revise the main part of the tangent stiffness matrix of rheonomic constraints and replace the quaternion $\boldsymbol{\rho}_{F_{1(F_2)}}$ with $\boldsymbol{\rho}_{F_1^{\Diamond}(F_2)}$ in (3.15) to obtain the projection part of the tangent stiffness matrix of rheonomic constraints.

3.1.4 Example: anchor chain

An anchor chain is modeled as a series of rigid bodies connected by joints (Figure 3.1). The left and right ends of the chain are hinged at coordinates $A(0,0,0)$ and $B(10,0,0)$, respectively, with the middle point located at $C(5,0,-6)$. A series of rigid bodies connected through double revolute joints, where the two bending DOFs are unconstrained, are constructed between points A and C as well as between points B and C. The chain is initialized in a 'V'-shaped configuration. The axial flexibility of the chain is neglected, as the primary focus is to investigate the influence of the tangent stiffness matrix of constraints. Nevertheless, the assumption of inextensibility can be considered a reasonable approximation from a practical perspective [210].

Static equilibrium analysis

The assembly and static equilibrium analyses are carried out, and the anchor chain is observed to sag under the influence of gravity, as shown in Figure 3.1. The horizontal components of the reaction forces at the joints, expressed in the inertial frame, are found to be constant, which is a typical characteristic of the catenary curve.

The analytical expression for a catenary curve is given by $z = a\cosh(x/a + x_0) + z_0$, where x_0 and z_0 are the coordinate offsets of the origin, and $a = T_0/(mg)$ is the constant parameter of the catenary curve. Here, T_0 represents the horizontal internal force, m is the mass per unit length, and g is the gravitational acceleration.

The coordinates of the rigid bodies along the anchor chain in the static equilibrium configuration are compared with the analytical catenary curve, as illustrated in Figure 3.2.

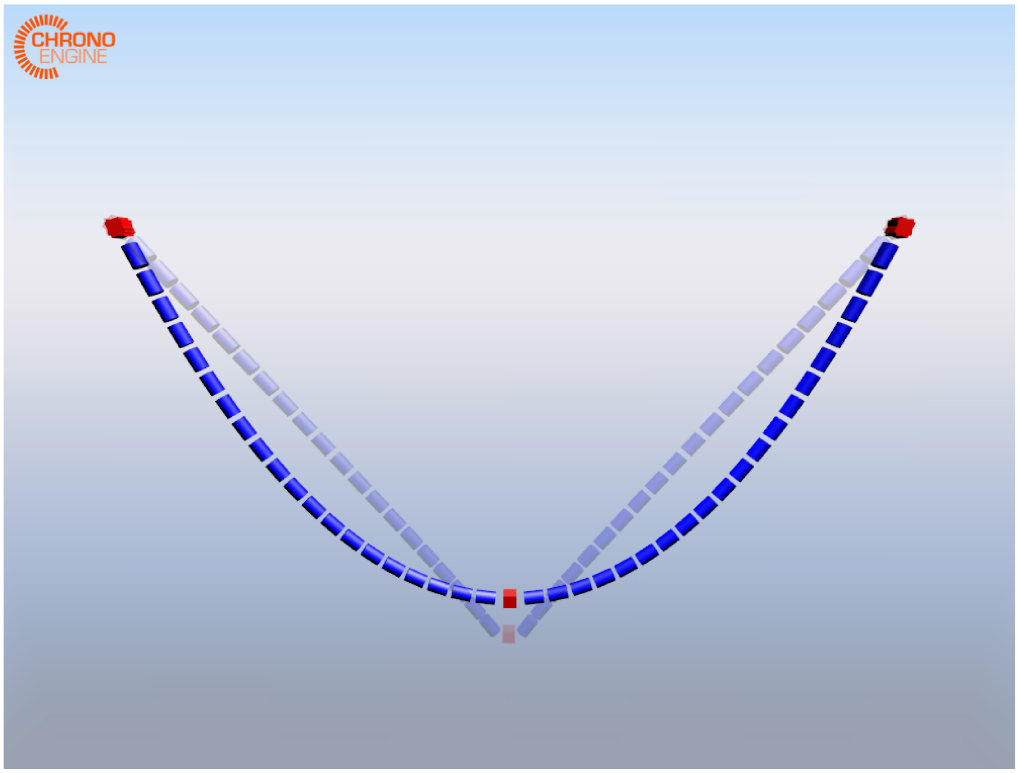

Figure 3.1: An anchor chain hinged at two ends under gravity in its initial and static equilibrium configuration.

Eigenvalue analysis

An eigenvalue analysis of the anchor chain in its equilibrium state is also conducted. The modal frequencies of the first four modes are presented in Table 3.1, with the corresponding mode shapes illustrated in Figure 3.3.

Table 3.1: Modal frequencies of the anchor chain.

No.	Frequency [Hz]
1	0.240
2	0.309
3	0.504
4	0.551

Nonlinear time-domain simulations are performed to identify the first four modal frequencies. A constant force $\boldsymbol{f}$ is applied at point C for the first 5 seconds to induce vibrations in the anchor chain around its static equilibrium configuration. Afterward, the force is removed, allowing the system to undergo free vibration.

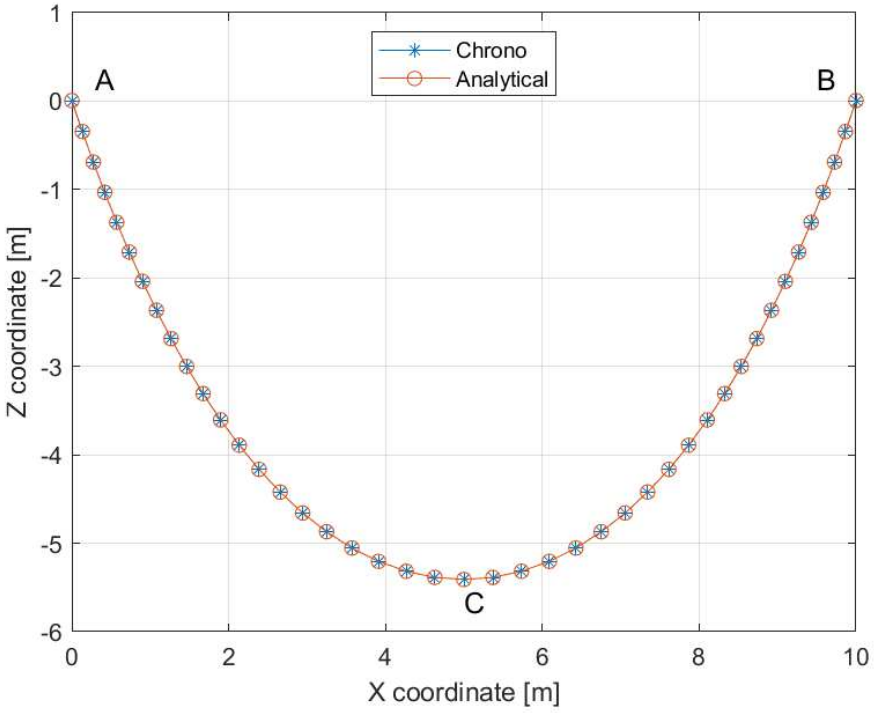

Figure 3.2: The validation of the catenary curve.

The amplitude spectrum obtained from the fast Fourier transform (FFT) analysis is presented in Figure 3.4, with the data from the initial 10 seconds discarded to eliminate the influence of transient impulses at the start of the simulation.

The constant force is applied in the X (longitudinal), Y (lateral), and Z (vertical) directions, respectively, to excite vibrations in the corresponding modes:

- When the excitation force $\boldsymbol{f}$ is applied in the $+X$ direction, as shown in Figure 3.4a, the anchor chain oscillates at a frequency of 0.311 Hz, which corresponds to the second modal frequency listed in Table 3.1.
- When the excitation force $\boldsymbol{f}$ is applied in the $+Y$ direction, as shown in Figure 3.4b, the dominant frequency is 0.244 Hz, with a secondary peak observed at 0.544 Hz, although with lower amplitude. These frequencies correspond to the first and fourth modal frequencies in Table 3.1, respectively.
- When the excitation force $\boldsymbol{f}$ is applied in the $-Z$ direction, as shown in Figure 3.4c, the anchor chain oscillates at a frequency of 0.5 Hz, matching the third modal frequency listed in Table 3.1.

The oscillations in all three test cases follow the directions of the applied excitation forces and align with the dominant directions of the corresponding modal

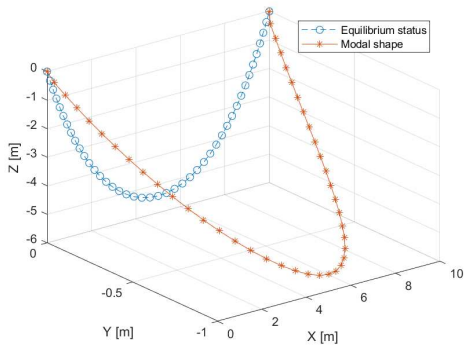

(a) *No.1, out-of-plane swinging mode.*

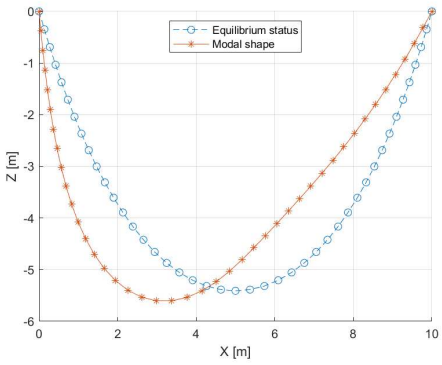

(b) *No.2, in-plane swinging mode.*

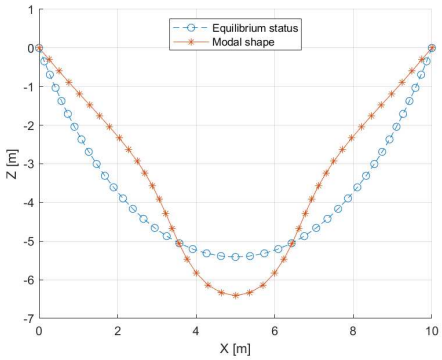

(c) *No.3, in-plane bending mode.*

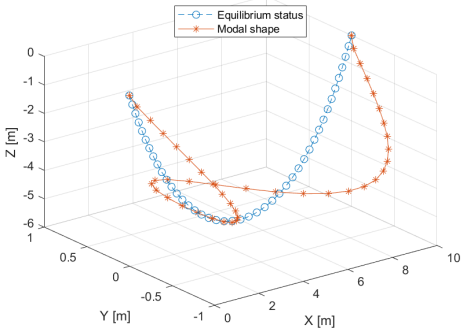

(d) *No.4, out-of-plane bending mode.*

Figure 3.3: Modal shapes of the anchor chain.

shapes. This demonstrates a strong agreement between the results of the eigenvalue analysis and the nonlinear time-domain simulations.

3.2 Linearization of wind turbine aerodynamics

A wind turbine is a rotating machine designed to extract kinetic energy from the incoming wind flow. The aerodynamic forces acting on the blades depend on both the blade configuration and its velocity, resulting in equivalent aerodynamic stiffness and damping matrices. These matrices are of crucial importance for the modal and stability analyses of wind turbines.

3.2.1 Aerodynamics model

Blade Element Momentum (BEM) theory has been extensively utilized in the wind energy industry due to its reasonable accuracy and exceptional computational efficiency.

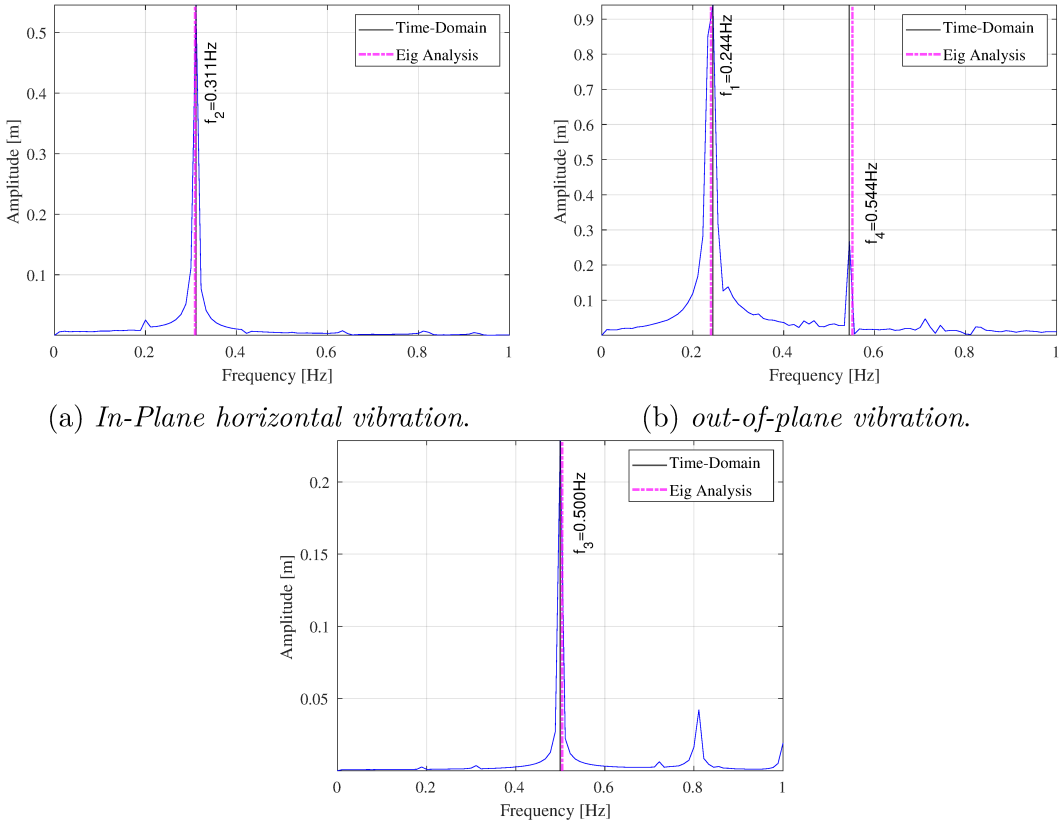

(a) *In-Plane horizontal vibration.* (b) *out-of-plane vibration.*

(c) *In-Plane vertical vibration.*

Figure 3.4: The vibration of the middle point C of the anchor chain.

The BEM theory combines two fundamental concepts: momentum theory and blade element theory. In momentum theory, the rotor plane is treated as an actuator disc. By applying the principles of axial and angular momentum conservation, the axial and tangential induction factors are determined when the wind flow passes through the actuator disc. Taking into account the position, orientation, and velocities of the blade station, the induced velocities, relative inflow velocity, and local angle of attack at a given airfoil section are subsequently computed. Blade element theory involves discretizing the rotor plane into concentric annular rings along the radial direction, effectively dividing the blades into a series of aerodynamic elements in the spanwise direction. Each annular ring is treated separately. Two-dimensional airfoil theory is then applied to compute the aerodynamic forces on each element, based on the relative inflow velocity, the local angle of attack, and the aerodynamic characteristics of the airfoil. These characteristics include lift, drag, and moment coefficients as functions of the angle of attack, as well as the airfoil's thickness and chord length.

Due to the complex interaction between induction velocities, angle of attack,

and aerodynamic forces, an iterative procedure is typically required to achieve a converged solution. When the wind inflow is misaligned with the rotor plane, a skewed wake model is employed to deal with azimuth variations of the induced velocities. At low wind speeds, higher axial induction factors are expected, necessitating a correction to the thrust coefficient to prevent non-physical predictions of flow reversal. In this case, the Glauert's empirical correction can be applied [94]. To ensure accurate thrust coefficient predictions, tip-loss correction must also be applied. Additionally, a dynamic inflow model is required to capture the time lag effect in the induction response to the change of wind conditions. A dynamic stall model is necessary to accurately compute the aerodynamic forces acting on the blade in unsteady wind conditions.

Readers are referred to Burton (2011) [43] and Madsen (2020) [176] for a detailed description of the BEM theory.

3.2.2 Assumptions for linearization

For the linearization of the aerodynamics of wind turbine rotors, some assumptions are introduced to ensure circumferential symmetric aerodynamic properties within the rotor plane. In detail, it is assumed that gravity acting on the blades and the tower shadow effect are neglected. The normal wind profile (NWP) model is employed, with the free inflow assumed to be perfectly aligned with the rotor's axis of rotation. The wind shear is also disregarded. The dynamic inflow and dynamic stall effects, particularly the latter, can influence the aeroelastic modes of wind turbines [40] and are therefore important considerations in the linearization of aerodynamic models. For those interested in implementing a linearized dynamic stall model, a state-space formulation based on the Beddoes-Leishman dynamic stall model can be employed [117]. However, due to time constraints in this project, both dynamic inflow and dynamic stall effects are omitted from this thesis. Finally, Glauert's correction for highly loaded rotors is applied, along with a tip-loss correction. The assumptions in the linearization of rotor aerodynamics are listed in Table 3.2.

In the BEM theory, the relationships between the relative inflow velocity, the local angle of attack, and the DOFs of the blade station are prohibitively complex. Furthermore, the implementation of BEM theory can vary significantly between different codes [199, 198, 176]. These factors render the analytical derivation of the aerodynamic stiffness and damping matrices exceedingly challenging. To address this, a numerical differentiation method is employed to compute the gradients. This approach offers the advantage of decoupling the linearization procedure from the specific code implementation of BEM theory, allowing for greater flexibility in modifying the aerodynamic algorithm in future.

Table 3.2: Assumptions for aerodynamics linearization

Effects	Included ?
Gravity on blades	No
Tower shadow	No
Wind shear	No
Wind inflow angle	No
Yaw misalignment	No
Skewed wake model	No
Dynamic inflow	No
Dynamic stall	No
Glauert's correction for highly loaded rotors	Yes
Tip-loss correction	Yes

3.2.3 Quasi-static equilibrium analysis

The first step in the linearization process is to determine the quasi-static equilibrium configuration of the aeroelastic coupling dynamics system. The wind speed, rotor speed and pitch angles are specified as input parameters. To ensure an isotropic rotor system, identical pitch angles are applied to all three blades. The velocities $\{\dot{\boldsymbol{r}}_a, \boldsymbol{\omega}_l\}$ and accelerations $\{\ddot{\boldsymbol{r}}_a, \dot{\boldsymbol{\omega}}_l\}$ of all rotating components—including the blade nodes, pitch bearings, hub, and rotating shafts—are directly prescribed according to equations (2.39), (2.40), (2.42), and (2.44). Aerodynamic forces are calculated using the BEM theory, while inertial forces are evaluated based on (2.131) and incorporated into the external loads.

A static equilibrium analysis, as outlined in Section 2.9, is then conducted. Each time the structural configuration is updated, the velocities and accelerations of rotating components are adjusted accordingly. Simultaneously, the wind inflow is aligned with the rotor's axis of rotation, and the aerodynamic forces are recalculated using the equilibrium wake model, in which the induction responds instantaneously to structural changes. An iterative procedure is employed to achieve the quasi-static equilibrium configuration in both the structural and aerodynamic domains. Convergence is reached when the change of the blade tip deflection between successive iterations falls below 0.01 % of the blade length [120], at which point the iteration process is terminated.

3.2.4 Numerical differentiation in the local basis

At the aeroelastic quasi-static equilibrium configuration $\{\boldsymbol{q}_0, \dot{\boldsymbol{q}}_0\}$, a small-amplitude perturbation is applied in the local frame of blade nodes to maintain the isotropy of

the rotor system, as depicted in Figure 3.5. The perturbations in the three translational and three rotational directions are performed independently to prevent coupling; however, the perturbation in one direction can be executed simultaneously at all blade stations to improve computational efficiency, given that, in BEM theory, the aerodynamic elements are treated separately. The aerodynamic forces are recalculated using the frozen wake model, in which the induced velocities remain invariant. The gradients of the aerodynamic forces with respect to the blade structural position, orientation, and velocities are evaluated using a numerical differentiation method.

Let $\delta \boldsymbol{r}_l$ denote the infinitesimal perturbation of the position vector of a blade node, expressed in the local basis of the node frame. The relationship of the perturbation expressed in the local frame and the inertial frame is given by

$$\delta \boldsymbol{r}_l = \boldsymbol{R}_N^T \delta \boldsymbol{r}_a \tag{3.19}$$

where $\boldsymbol{R}_N$ is the rotation matrix of the node frame N.

Correspondingly, $\dot{\boldsymbol{r}}_l = \boldsymbol{R}_N^T \dot{\boldsymbol{r}}_a$ represents the translational velocity of the blade node, also expressed in its local basis. Applying variations to both sides, and recalling (2.15b), (2.1a),(2.1c), we obtain the following expression for the variation of velocity

$$\delta \dot{\boldsymbol{r}}_l = \boldsymbol{R}_N^T \delta \dot{\boldsymbol{r}}_a + \widetilde{\boldsymbol{R}_N^T \dot{\boldsymbol{r}}_a} \delta \boldsymbol{\theta}_l \tag{3.20}$$

Let $\boldsymbol{f}_{ll} = \left[\boldsymbol{f}_l^T, \boldsymbol{m}_l^T\right]^T$ represent the wrench consisting of aerodynamic forces and moments, expressed in the local frame of the blade node. The aerodynamic forces and moments are initially computed at the aerodynamic center of the cross-section and subsequently transformed to the reference center, which is typically the elastic center. The aerodynamic force in the spanwise direction is zero if the spanwise flow is neglected, resulting in the typical form $\boldsymbol{f}_l = [0, f_y, f_z]^T$. According to 2D airfoil theory, the aerodynamic moment acts only orthogonal to the cross-section, giving $\boldsymbol{m}_l = [m_x, 0, 0]^T$ as the typical form.

The aerodynamic stiffness and damping matrices can be computed using the numerical differentiation method, as expressed in (3.21).

$$\boldsymbol{D}_{ll} = -\left.\frac{\partial \boldsymbol{f}_{ll}}{\partial \dot{\boldsymbol{q}}_{ll}^T}\right|_{\boldsymbol{q}_0, \dot{\boldsymbol{q}}_0} \approx -\frac{\boldsymbol{f}_{ll}\left(\boldsymbol{q}_0, \dot{\boldsymbol{q}}_0 + \Delta \dot{\boldsymbol{q}}_{ll}\right) - \boldsymbol{f}_{ll}\left(\boldsymbol{q}_0, \dot{\boldsymbol{q}}_0\right)}{\Delta \dot{\boldsymbol{q}}_{ll}^T} \tag{3.21a}$$

$$\boldsymbol{K}_{ll} = -\left.\frac{\partial \boldsymbol{f}_{ll}}{\partial \boldsymbol{q}_{ll}^T}\right|_{\boldsymbol{q}_0, \dot{\boldsymbol{q}}_0} \approx -\frac{\boldsymbol{f}_{ll}\left(\boldsymbol{q}_0 + \Delta \boldsymbol{q}_{ll}, \dot{\boldsymbol{q}}_0\right) - \boldsymbol{f}_{ll}\left(\boldsymbol{q}_0, \dot{\boldsymbol{q}}_0\right)}{\Delta \boldsymbol{q}_{ll}^T} \tag{3.21b}$$

where $\Delta \boldsymbol{q}_{ll} = \left[\Delta \boldsymbol{r}_l^T, \boldsymbol{\phi}_{l_\Delta}^T\right]^T$, $\Delta \dot{\boldsymbol{q}}_{ll} = \left[\Delta \dot{\boldsymbol{r}}_l^T, \Delta \boldsymbol{\omega}_l^T\right]^T$ represent the small-amplitude perturbations in position, orientation and velocities. The perturbation in orientation is conducted via the rotation pseudovector $\boldsymbol{\phi}_{l_\Delta}$. The subscript '$ll$' indicates that both the translational and rotational quantities are expressed in the local basis.

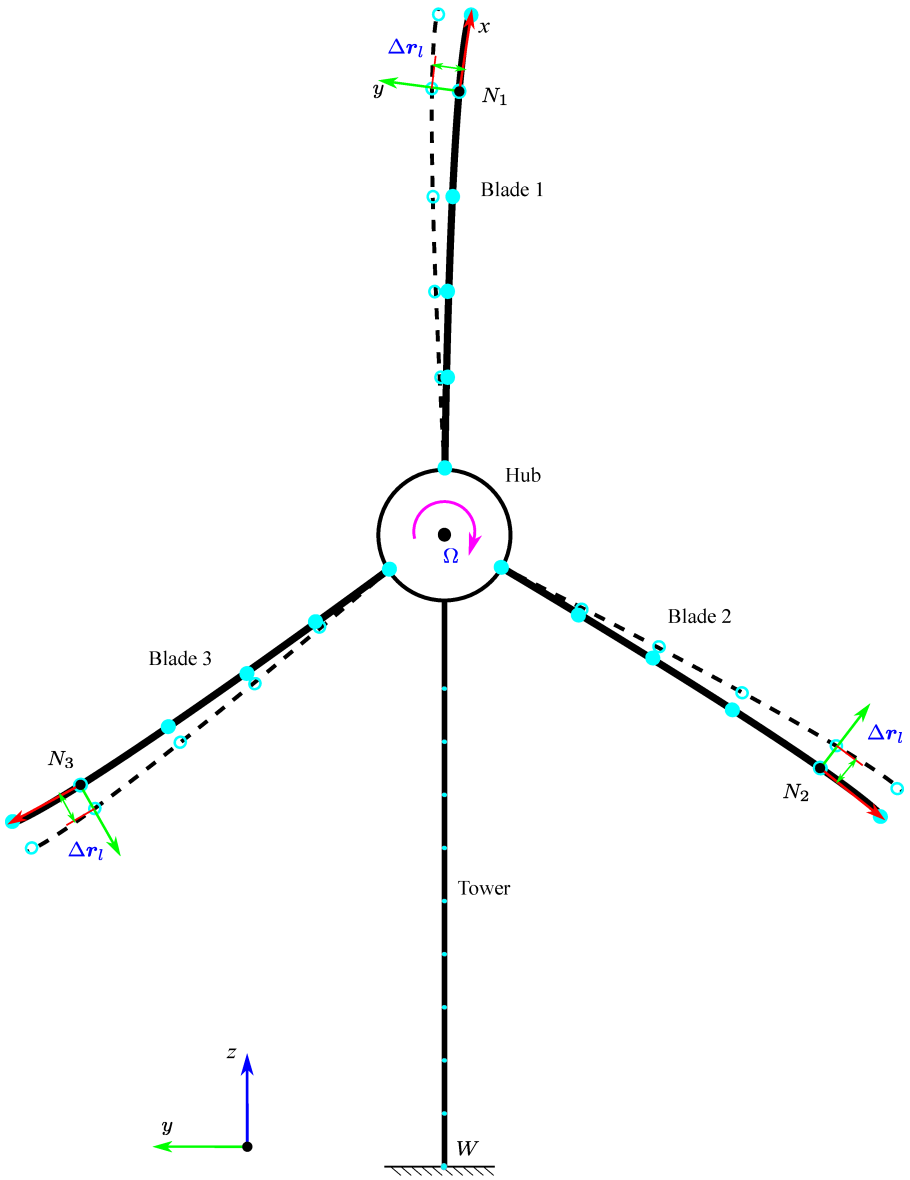

Figure 3.5: A small-amplitude perturbation in the local frame of blade nodes. 'x': from blade root to tip; 'y': from leading edge to trailing edge; 'z': toward wind inflow. In this figure, the perturbation $\Delta \boldsymbol{r}_l$ is applied in the y direction of the frame of blade nodes.

The perturbations are applied using several different small-amplitude values, followed by a linear regression fit to smooth out local aerodynamic nonlinearities around the quasi-static equilibrium state [69].

3.2.5 Rotate back to the mixed basis

The linearization of the wrench $\boldsymbol{f}_{ll}$ in the local basis can be expressed as

$$\delta \boldsymbol{f}_{ll} = \begin{pmatrix} \delta \boldsymbol{f}_l \\ \delta \boldsymbol{m}_l \end{pmatrix} = -\boldsymbol{D}_{ll} \begin{pmatrix} \delta \dot{\boldsymbol{r}}_l \\ \delta \boldsymbol{\omega}_l \end{pmatrix} - \boldsymbol{K}_{ll} \begin{pmatrix} \delta \boldsymbol{r}_l \\ \delta \boldsymbol{\theta}_l \end{pmatrix} \tag{3.22}$$

Substituting (3.19) and (3.20) into (3.22), and grouping the terms according to the generalized coordinates in the mixed basis, yields

$$\begin{pmatrix} \delta \boldsymbol{f}_l \\ \delta \boldsymbol{m}_l \end{pmatrix} = -\boldsymbol{D}_{ll} \begin{bmatrix} \boldsymbol{R}_N^T & \boldsymbol{0} \\ \boldsymbol{0} & \boldsymbol{I} \end{bmatrix} \begin{pmatrix} \delta \dot{\boldsymbol{r}}_a \\ \delta \boldsymbol{\omega}_l \end{pmatrix} - \left(\boldsymbol{D}_{ll} \begin{bmatrix} \boldsymbol{0} & \widetilde{\boldsymbol{R}_N^T \dot{\boldsymbol{r}}_a} \\ \boldsymbol{0} & \boldsymbol{0} \end{bmatrix} + \boldsymbol{K}_{ll} \begin{bmatrix} \boldsymbol{R}_N^T & \boldsymbol{0} \\ \boldsymbol{0} & \boldsymbol{I} \end{bmatrix} \right) \begin{pmatrix} \delta \boldsymbol{r}_a \\ \delta \boldsymbol{\theta}_l \end{pmatrix} \tag{3.23}$$

The aerodynamic forces expressed in the inertial frame are given by $\boldsymbol{f}_a = \boldsymbol{R}_N \boldsymbol{f}_l$. The corresponding variation is $\delta \boldsymbol{f}_a = \boldsymbol{R}_N \delta \boldsymbol{f}_l - \boldsymbol{R}_N \widetilde{\boldsymbol{f}_l} \delta \boldsymbol{\theta}_l$. The wrench, consisting of aerodynamic forces and moments in the mixed basis, is denoted as $\boldsymbol{f}_{al} = \left[\boldsymbol{f}_a^T, \boldsymbol{m}_l^T \right]^T$. This expression is then linearized as follows:

$$\delta \boldsymbol{f}_{al} = \begin{pmatrix} \delta \boldsymbol{f}_a \\ \delta \boldsymbol{m}_l \end{pmatrix} = -\boldsymbol{D}_{al} \begin{pmatrix} \delta \dot{\boldsymbol{r}}_a \\ \delta \boldsymbol{\omega}_l \end{pmatrix} - \left(\boldsymbol{K}_{al} + \boldsymbol{K}_{al_g} \right) \begin{pmatrix} \delta \boldsymbol{r}_a \\ \delta \boldsymbol{\theta}_l \end{pmatrix} \tag{3.24}$$

where the three matrices are detailed as follows:

$$\boldsymbol{D}_{al} = \begin{bmatrix} \boldsymbol{R}_N & \boldsymbol{0} \\ \boldsymbol{0} & \boldsymbol{I} \end{bmatrix} \boldsymbol{D}_{ll} \begin{bmatrix} \boldsymbol{R}_N^T & \boldsymbol{0} \\ \boldsymbol{0} & \boldsymbol{I} \end{bmatrix} \in \mathbb{R}^{6\times 6} \tag{3.25a}$$

$$\boldsymbol{K}_{al} = \begin{bmatrix} \boldsymbol{R}_N & \boldsymbol{0} \\ \boldsymbol{0} & \boldsymbol{I} \end{bmatrix} \boldsymbol{K}_{ll} \begin{bmatrix} \boldsymbol{R}_N^T & \boldsymbol{0} \\ \boldsymbol{0} & \boldsymbol{I} \end{bmatrix} \in \mathbb{R}^{6\times 6} \tag{3.25b}$$

$$\boldsymbol{K}_{al_g} = \begin{bmatrix} \boldsymbol{R}_N & \boldsymbol{0} \\ \boldsymbol{0} & \boldsymbol{I} \end{bmatrix} \boldsymbol{D}_{ll} \begin{bmatrix} \boldsymbol{0} & \widetilde{\boldsymbol{R}_N^T \dot{\boldsymbol{r}}_a} \\ \boldsymbol{0} & \boldsymbol{0} \end{bmatrix} + \begin{bmatrix} \boldsymbol{R}_N & \boldsymbol{0} \\ \boldsymbol{0} & \boldsymbol{I} \end{bmatrix} \begin{bmatrix} \boldsymbol{0} & \widetilde{\boldsymbol{f}_l} \\ \boldsymbol{0} & \boldsymbol{0} \end{bmatrix} \in \mathbb{R}^{6\times 6} \tag{3.25c}$$

The subscript 'al' indicates that the quantity is expressed in the mixed basis. The matrices $\boldsymbol{D}_{al}$ and $\boldsymbol{K}_{al}$ represent the aerodynamic damping matrix and aerodynamic stiffness matrix, respectively, in the mixed basis of the blade node.

The matrix $\boldsymbol{K}_{al_g}$ denotes the aerodynamic geometric stiffness matrix introduced by the 3D rotation of the cross-section, based on the assumption that the aerodynamic forces $\boldsymbol{f}_l$ behave as follower forces, adapting to the deflection of the blade station. However, this assumption does not fully reflect the actual conditions. For example, when applying BEM theory to coned rotors [59, 177] or swept blades [163, 82], additional complexities must be considered. From the author's perspective, it remains unclear whether the aerodynamic forces $\boldsymbol{f}_l$ can be definitively classified as follower forces. Consequently, as a higher-order term, $\boldsymbol{K}_{al_g}$ is neglected in the present work.

3.2.6 Flowchart of aerodynamics linearization

The overall linearization procedure of aerodynamic forces and moments acting on wind turbine rotors is summarized in a flowchart, as shown in Figure 3.6.

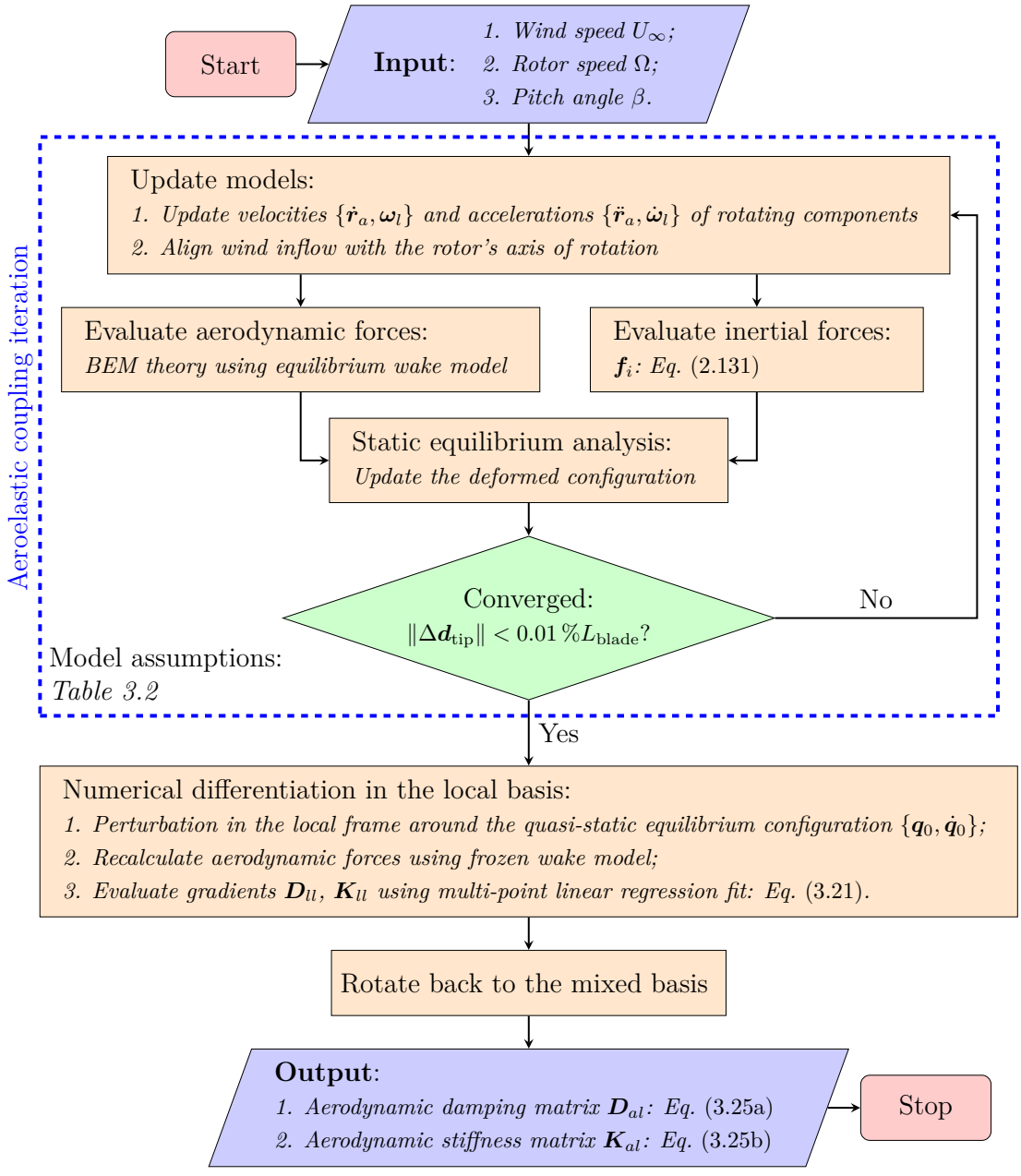

Figure 3.6: Flowchart of the linearization procedure of aerodynamic forces and moments acting on wind turbine rotors.

The input parameters—wind speed U_∞, rotor speed Ω, and pitch angle β—can

be obtained from a static power curve analysis, statistical results from time-domain dynamic simulations, or field measurement data.

3.3 Transformation to the rotor's rotating center

The linearized DAEs of wind turbines involve numerous rotation matrices, making them highly dependent on the azimuthal positions of the blades. Consequently, the dynamic system represented by the DAEs is time-varying, and hence unsuitable for modal analysis. To address this, three auxiliary reference frames at the rotor's center of rotation are introduced for the three blades, respectively. The aerodynamic, elastic, constraint and inertial terms are first transformed into these auxiliary coordinates, and then rotated back to the stationary reference frame at the hub center, resulting in linearized DAEs for the wind turbine system that are expressed within consistent reference frames.

3.3.1 Wind turbine model description

A modern wind turbine typically consists of three blades, a tower and a drive train, as depicted in Figure 3.7. The three blades and tower are discretized using corotational Timoshenko beam elements to achieve a good trade-off of computational performance and numerical accuracy. The drive train is simplified as a series of rigid bodies, including the hub, nacelle, low-speed shaft (LSS), high-speed shaft (HSS) and bedplate. Each blade is mounted on the hub via rheonomic revolute joints, characterized by the respective pitch angles $\beta_1, \beta_2, \beta_3$. The LSS and HSS are connected by a torsional spring with specified stiffness and damping properties to account for the mechanical flexibility and damping of the drive train. The rotational inertia of the HSS is transformed to the low-speed side by multiplication of the square of the gearbox transmission ratio. The HSS is attached to the bedplate through a revolute joint at point G, where a generator torque is applied to regulate the rotor speed Ω. The bedplate is connected to the tower top via a rheonomic revolute joint at point Y, defined by the yaw angle φ_{yaw}. Additionally, the nacelle is rigidly connected to the tower top, and the hub is fixed to the LSS using a fixed joint.

The bending stiffness of the drive train and yaw system may affect the modal dynamics of the rotor. Similarly, the stiffness properties of the foundation at the tower bottom are important for the tower modes. Additionally, the flexibility of the hub and pitch bearings could be relevant for the blade modal dynamics, particularly for very long blades. However, to simplify the discussion, these engineering details are not included in this work.

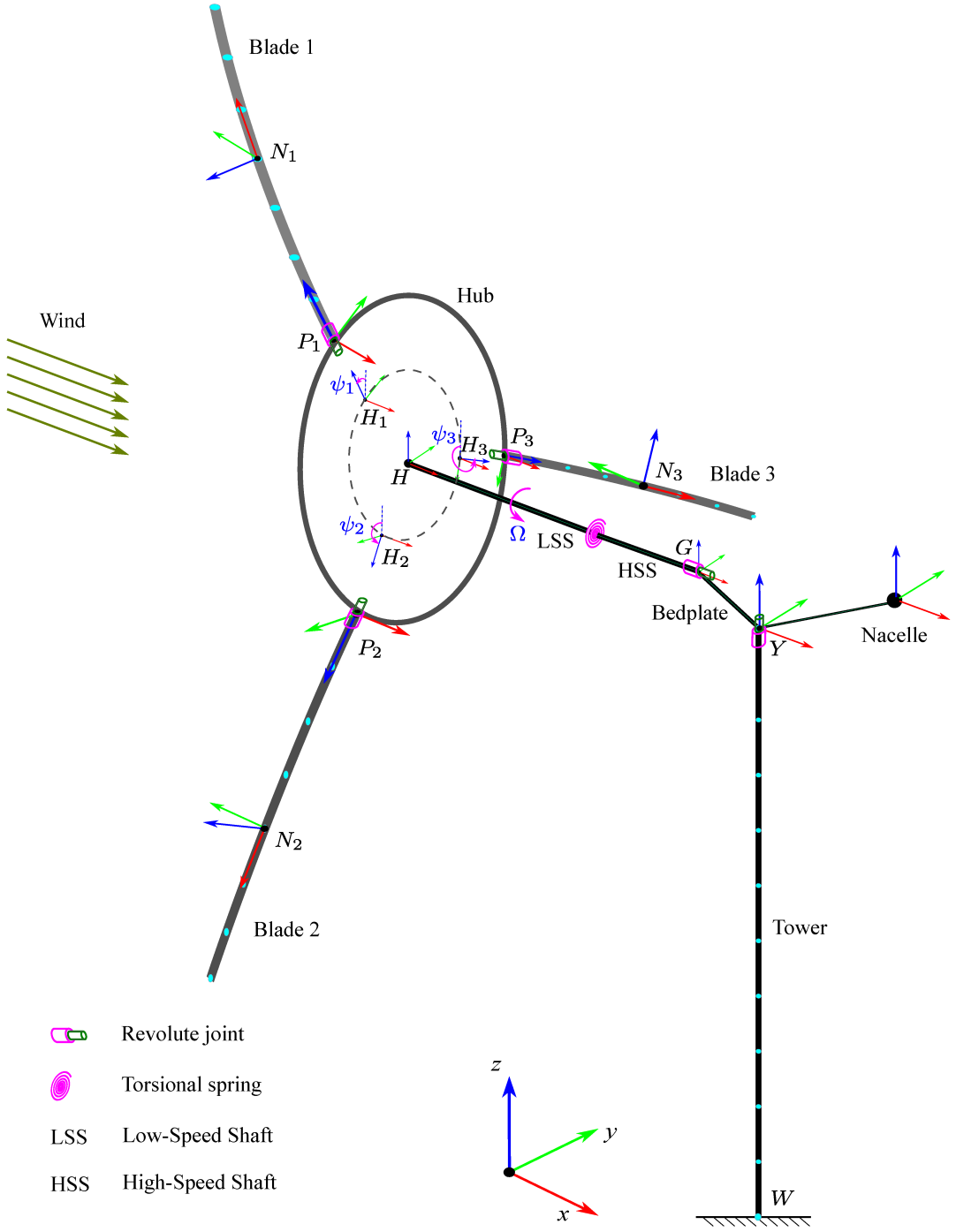

Figure 3.7: The scheme of a three-bladed wind turbine. The three blades are rotated by the corresponding azimuthal angles ψ_1, ψ_2, ψ_3. The three auxiliary reference frames H_1, H_2, H_3 are located at the same position as H, but shown separately to avoid mess.

3.3.2 Blade auxiliary coordinates

At the aeroelastic quasi-static equilibrium configuration $\{\boldsymbol{q}_0, \dot{\boldsymbol{q}}_0\}$, the three blades are isotropic with respect to the hub center. Specifically, the blades possess identical mass and stiffness properties, identical pitch angles, and are mounted on the hub at equally distributed azimuthal positions. Additionally, the aerodynamic forces and deflections of the three blades are also identical. As a result, from a physical perspective, the rotor can be considered *isotropic*. However, this isotropy does not extend to the mathematical model. For example, the position vectors of the corresponding nodes at the same spanwise locations on the three blades are not identical: $\boldsymbol{r}_{N_1} \neq \boldsymbol{r}_{N_2} \neq \boldsymbol{r}_{N_3}$. This breaks a key assumption required for the Multi-Blade Coordinate (MBC) transformation, which is necessary for performing a proper modal analysis of a rotating multi-bladed rotor system.

To address this issue, the generalized coordinates of the blade nodes must be expressed relative to a reference frame at the hub rotating center. To achieve this, we introduce three auxiliary reference frames, H_1, H_2, and H_3, as shown in Figure 3.7. These three auxiliary frames are located at the same position as the hub's reference frame H, but are rotated by the corresponding azimuthal angles of the three blades, ψ_1, ψ_2, ψ_3. The reference frame H is stationary in three-dimensional space, that means it does not rotate with the azimuthal motion of the rotor.

Coordinate transformation relationships

Taking node N_1 on the first blade as an example, the variations of the generalized coordinates of node N_1 in the mixed basis are represented as

$$\delta\boldsymbol{q}_{N_1} = \begin{pmatrix} \delta\boldsymbol{r}_{N_1} \\ \delta\boldsymbol{\theta}_{l_{N_1}} \end{pmatrix}, \qquad \delta\dot{\boldsymbol{q}}_{N_1} = \begin{pmatrix} \delta\dot{\boldsymbol{r}}_{N_1} \\ \delta\boldsymbol{\omega}_{l_{N_1}} \end{pmatrix}, \qquad \delta\ddot{\boldsymbol{q}}_{N_1} = \begin{pmatrix} \delta\ddot{\boldsymbol{r}}_{N_1} \\ \delta\dot{\boldsymbol{\omega}}_{l_{N_1}} \end{pmatrix} \tag{3.26}$$

For the reference frame H_1, the variations of its generalized coordinates are represented as

$$\delta\boldsymbol{q}_{H_1} = \begin{pmatrix} \delta\boldsymbol{r}_{H_1} \\ \delta\boldsymbol{\theta}_{l_{H_1}} \end{pmatrix}, \qquad \delta\dot{\boldsymbol{q}}_{H_1} = \begin{pmatrix} \delta\dot{\boldsymbol{r}}_{H_1} \\ \delta\boldsymbol{\omega}_{l_{H_1}} \end{pmatrix}, \qquad \delta\ddot{\boldsymbol{q}}_{H_1} = \begin{pmatrix} \delta\ddot{\boldsymbol{r}}_{H_1} \\ \delta\dot{\boldsymbol{\omega}}_{l_{H_1}} \end{pmatrix} \tag{3.27}$$

We introduce the auxiliary coordinates of node N_1, where the translational DOFs are expressed relative to the reference frame H_1, while the rotational DOFs remain in the local basis. The variations of the auxiliary coordinates are represented as

$$\delta\overline{\boldsymbol{q}}_{N_1} = \begin{pmatrix} \delta\boldsymbol{r}_{H_1.N_1(H_1)} \\ \delta\boldsymbol{\theta}_{l_{N_1}} \end{pmatrix}, \quad \delta\dot{\overline{\boldsymbol{q}}}_{N_1} = \begin{pmatrix} \delta\dot{\boldsymbol{r}}_{H_1.N_1(H_1)} \\ \delta\boldsymbol{\omega}_{l_{N_1}} \end{pmatrix}, \quad \delta\ddot{\overline{\boldsymbol{q}}}_{N_1} = \begin{pmatrix} \delta\ddot{\boldsymbol{r}}_{H_1.N_1(H_1)} \\ \delta\dot{\boldsymbol{\omega}}_{l_{N_1}} \end{pmatrix} \tag{3.28}$$

The position and translational velocity of node N_1 can be expressed relative to the reference frame H_1 as follows

$$\boldsymbol{r}_{N_1} = \boldsymbol{r}_{H_1} + \boldsymbol{R}_{H_1}\boldsymbol{r}_{H_1.N_{1(H_1)}} \tag{3.29a}$$

$$\dot{\boldsymbol{r}}_{N_1} = \dot{\boldsymbol{r}}_{H_1} + \boldsymbol{R}_{H_1}\widetilde{\boldsymbol{\omega}}_{l_{H_1}}\boldsymbol{r}_{H_1.N_{1(H_1)}} + \boldsymbol{R}_{H_1}\dot{\boldsymbol{r}}_{H_1.N_{1(H_1)}} \tag{3.29b}$$

Applying variations to (3.29), and recalling (2.15b) along with properties (2.1a) and (2.1c), we obtain the following variations

$$\delta\boldsymbol{r}_{N_1} = \delta\boldsymbol{r}_{H_1} + \boldsymbol{R}_{H_1}\delta\boldsymbol{r}_{H_1.N_{1(H_1)}} - \boldsymbol{R}_{H_1}\widetilde{\boldsymbol{r}}_{H_1.N_{1(H_1)}}\delta\boldsymbol{\theta}_{l_{H_1}} \tag{3.30a}$$

$$\begin{aligned}\delta\dot{\boldsymbol{r}}_{N_1} = {} & \delta\dot{\boldsymbol{r}}_{H_1} - \boldsymbol{R}_{H_1}\big(\widetilde{\boldsymbol{\omega}}_{l_{H_1}}\widetilde{\boldsymbol{r}_{H_1.N_{1(H_1)}}}\big)\delta\boldsymbol{\theta}_{l_{H_1}} - \boldsymbol{R}_{H_1}\widetilde{\boldsymbol{r}}_{H_1.N_{1(H_1)}}\delta\boldsymbol{\omega}_{l_{H_1}} \\ & + \boldsymbol{R}_{H_1}\widetilde{\boldsymbol{\omega}}_{l_{H_1}}\delta\boldsymbol{r}_{H_1.N_{1(H_1)}} - \boldsymbol{R}_{H_1}\widetilde{\dot{\boldsymbol{r}}}_{H_1.N_{1(H_1)}}\delta\boldsymbol{\theta}_{l_{H_1}} + \boldsymbol{R}_{H_1}\delta\dot{\boldsymbol{r}}_{H_1.N_{1(H_1)}}\end{aligned} \tag{3.30b}$$

Grouping the terms in (3.30) according to the generalized coordinates (3.26), (3.27) and (3.28), and extending the expressions to include the rotational coordinates, the following coordinate transformations are obtained

$$\delta\boldsymbol{q}_{N_1} = \boldsymbol{\Xi}_{H_1}\delta\boldsymbol{q}_{H_1} + \boldsymbol{\Xi}_{N_1}\delta\overline{\boldsymbol{q}}_{N_1} \tag{3.31a}$$

$$\delta\dot{\boldsymbol{q}}_{N_1} = \boldsymbol{\Xi}_{H_1}\delta\dot{\boldsymbol{q}}_{H_1} + \boldsymbol{\Xi}_{N_1}\delta\dot{\overline{\boldsymbol{q}}}_{N_1} + \boldsymbol{\Pi}_{H_1}\delta\boldsymbol{q}_{H_1} + \boldsymbol{\Pi}_{N_1}\delta\overline{\boldsymbol{q}}_{N_1} \tag{3.31b}$$

where the four transformation matrices are given by

$$\boldsymbol{\Xi}_{H_1} = \begin{bmatrix}\boldsymbol{I} & -\boldsymbol{R}_{H_1}\widetilde{\boldsymbol{r}}_{H_1.N_{1(H_1)}} \\ \boldsymbol{0} & \boldsymbol{0}\end{bmatrix} \in \mathbb{R}^{6\times 6} \tag{3.32a}$$

$$\boldsymbol{\Xi}_{N_1} = \begin{bmatrix}\boldsymbol{R}_{H_1} & \boldsymbol{0} \\ \boldsymbol{0} & \boldsymbol{I}\end{bmatrix} \in \mathbb{R}^{6\times 6} \tag{3.32b}$$

$$\boldsymbol{\Pi}_{H_1} = \begin{bmatrix}\boldsymbol{0} & -\boldsymbol{R}_{H_1}\big(\widetilde{\boldsymbol{\omega}}_{l_{H_1}}\widetilde{\boldsymbol{r}_{H_1.N_{1(H_1)}}}\big) - \boldsymbol{R}_{H_1}\widetilde{\dot{\boldsymbol{r}}}_{H_1.N_{1(H_1)}} \\ \boldsymbol{0} & \boldsymbol{0}\end{bmatrix} \in \mathbb{R}^{6\times 6} \tag{3.32c}$$

$$\boldsymbol{\Pi}_{N_1} = \begin{bmatrix}\boldsymbol{R}_{H_1}\widetilde{\boldsymbol{\omega}}_{l_{H_1}} & \boldsymbol{0} \\ \boldsymbol{0} & \boldsymbol{0}\end{bmatrix} \in \mathbb{R}^{6\times 6} \tag{3.32d}$$

The coordinate transformations (3.31) and corresponding transformation matrices (3.32) can be readily extended to node N_2, N_3 on the other two blades.

Rotate back to the consistent reference frame

The transformation relationships between the reference frames H_1, H_2, H_3, and H are given as follows

$$\boldsymbol{R}_{H_i} = \boldsymbol{R}_H\boldsymbol{R}_{\psi_i}, \qquad i = 1, 2, 3 \tag{3.33}$$

where $\boldsymbol{R}_{\psi_i}$ represents the rotation about the 'x' axis of the reference frame H by the azimuthal angle ψ_i.

Applying variations to both sides of (3.33), and disregarding the variation of the rotation matrix $\boldsymbol{R}_{\psi_i}$—since there is no DOF associated with ψ_i—and recalling the property (2.1e), it follows that

$$\delta\boldsymbol{\theta}_{l_{H_i}} = \boldsymbol{R}_{\psi_i}^T \delta\boldsymbol{\theta}_{l_H}, \qquad i = 1, 2, 3 \tag{3.34}$$

Taking the time derivatives of both sides of (3.33), we obtain $\boldsymbol{\omega}_{l_{H_i}} = \boldsymbol{R}_{\psi_i}^T \boldsymbol{\omega}_{l_H}$, from which the relationship of the variations of angular velocities can be readily derived.

$$\delta\boldsymbol{\omega}_{l_{H_i}} = \boldsymbol{R}_{\psi_i}^T \delta\boldsymbol{\omega}_{l_H}, \qquad i = 1, 2, 3 \tag{3.35}$$

Since the positions of the reference frames H_1, H_2, and H_3 coincide with that of H, we have

$$\delta\boldsymbol{r}_{H_i} = \delta\boldsymbol{r}_H, \quad \delta\dot{\boldsymbol{r}}_{H_i} = \delta\dot{\boldsymbol{r}}_H, \quad \delta\ddot{\boldsymbol{r}}_{H_i} = \delta\ddot{\boldsymbol{r}}_H, \qquad i = 1, 2, 3 \tag{3.36}$$

By introducing the variations of generalized coordinates of the reference frame H, which is also the reference frame of the hub,

$$\delta\boldsymbol{q}_H = \begin{pmatrix} \delta\boldsymbol{r}_H \\ \delta\boldsymbol{\theta}_{l_H} \end{pmatrix}, \qquad \delta\dot{\boldsymbol{q}}_H = \begin{pmatrix} \delta\dot{\boldsymbol{r}}_H \\ \delta\boldsymbol{\omega}_{l_H} \end{pmatrix}, \qquad \delta\ddot{\boldsymbol{q}}_H = \begin{pmatrix} \delta\ddot{\boldsymbol{r}}_H \\ \delta\dot{\boldsymbol{\omega}}_{l_H} \end{pmatrix} \tag{3.37}$$

and considering (3.34), (3.35), (3.36), we obtain the coordinate transformations which rotate from the three auxiliary reference frames H_1, H_2, and H_3 back to the consistent reference frame H

$$\delta\boldsymbol{q}_{H_i} = \boldsymbol{\Psi}_{H_i} \delta\boldsymbol{q}_H \tag{3.38a}$$
$$\delta\dot{\boldsymbol{q}}_{H_i} = \boldsymbol{\Psi}_{H_i} \delta\dot{\boldsymbol{q}}_H \tag{3.38b}$$
$$\delta\ddot{\boldsymbol{q}}_{H_i} = \boldsymbol{\Psi}_{H_i} \delta\ddot{\boldsymbol{q}}_H \tag{3.38c}$$

for $i = 1, 2, 3$, where the transformation matrix is

$$\boldsymbol{\Psi}_{H_i} = \begin{bmatrix} \boldsymbol{I} & \boldsymbol{0} \\ \boldsymbol{0} & \boldsymbol{R}_{\psi_i}^T \end{bmatrix} \in \mathbb{R}^{6\times 6} \tag{3.39}$$

Substituting (3.38) into (3.31), yields

$$\delta\boldsymbol{q}_{N_1} = \boldsymbol{\Xi}_{H_1} \boldsymbol{\Psi}_{H_1} \delta\boldsymbol{q}_H + \boldsymbol{\Xi}_{N_1} \delta\overline{\boldsymbol{q}}_{N_1} \tag{3.40a}$$
$$\delta\dot{\boldsymbol{q}}_{N_1} = \boldsymbol{\Xi}_{H_1} \boldsymbol{\Psi}_{H_1} \delta\dot{\boldsymbol{q}}_H + \boldsymbol{\Xi}_{N_1} \delta\dot{\overline{\boldsymbol{q}}}_{N_1} + \boldsymbol{\Pi}_{H_1} \boldsymbol{\Psi}_{H_1} \delta\boldsymbol{q}_H + \boldsymbol{\Pi}_{N_1} \delta\overline{\boldsymbol{q}}_{N_1} \tag{3.40b}$$

3.3.3 Aerodynamic stiffness and damping matrices

Recalling the linearization in (3.24) and neglecting the aerodynamic geometric stiffness matrix $\boldsymbol{K}_{al_g}$, while also considering the interpretation of the generalized coordinates provided in Section 2.6.3, the discretized form of the incremental linearized aerodynamic forces acting on blade node N_1, expressed in the mixed basis, is given as follows

$$\Delta \boldsymbol{f}_{al_{N_1}} = -\boldsymbol{D}_{al}\Delta\dot{\boldsymbol{q}}_{N_1} - \left(\boldsymbol{K}_{al} + \cancel{\boldsymbol{K}_{al_g}}\right)\Delta\boldsymbol{q}_{N_1} \tag{3.41}$$

Employing the coordinate transformations in (3.31), the virtual work done by the linearized aerodynamic forces acting on node N_1 is derived as follows

$$\begin{aligned}
\delta W_{\text{aero}} = \delta\boldsymbol{q}_{N_1}^T\Delta\boldsymbol{f}_{al_{N_1}} &= -\delta\boldsymbol{q}_{N_1}^T\boldsymbol{D}_{al}\Delta\dot{\boldsymbol{q}}_{N_1} - \delta\boldsymbol{q}_{N_1}^T\boldsymbol{K}_{al}\Delta\boldsymbol{q}_{N_1} \\
&= -\begin{pmatrix}\delta\boldsymbol{q}_{H_1}^T & \delta\overline{\boldsymbol{q}}_{N_1}^T\end{pmatrix}\begin{bmatrix}\boldsymbol{\Xi}_{H_1}^T\boldsymbol{D}_{al}\boldsymbol{\Xi}_{H_1} & \boldsymbol{\Xi}_{H_1}^T\boldsymbol{D}_{al}\boldsymbol{\Xi}_{N_1} \\ \boldsymbol{\Xi}_{N_1}^T\boldsymbol{D}_{al}\boldsymbol{\Xi}_{H_1} & \boldsymbol{\Xi}_{N_1}^T\boldsymbol{D}_{al}\boldsymbol{\Xi}_{N_1}\end{bmatrix}\begin{pmatrix}\Delta\dot{\boldsymbol{q}}_{H_1} \\ \Delta\dot{\overline{\boldsymbol{q}}}_{N_1}\end{pmatrix} \\
&\quad -\begin{pmatrix}\delta\boldsymbol{q}_{H_1}^T & \delta\overline{\boldsymbol{q}}_{N_1}^T\end{pmatrix}\left(\begin{bmatrix}\boldsymbol{\Xi}_{H_1}^T\boldsymbol{K}_{al}\boldsymbol{\Xi}_{H_1} & \boldsymbol{\Xi}_{H_1}^T\boldsymbol{K}_{al}\boldsymbol{\Xi}_{N_1} \\ \boldsymbol{\Xi}_{N_1}^T\boldsymbol{K}_{al}\boldsymbol{\Xi}_{H_1} & \boldsymbol{\Xi}_{N_1}^T\boldsymbol{K}_{al}\boldsymbol{\Xi}_{N_1}\end{bmatrix}\right. \\
&\qquad \left. + \begin{bmatrix}\boldsymbol{\Xi}_{H_1}^T\boldsymbol{D}_{al}\boldsymbol{\Pi}_{H_1} & \boldsymbol{\Xi}_{H_1}^T\boldsymbol{D}_{al}\boldsymbol{\Pi}_{N_1} \\ \boldsymbol{\Xi}_{N_1}^T\boldsymbol{D}_{al}\boldsymbol{\Pi}_{H_1} & \boldsymbol{\Xi}_{N_1}^T\boldsymbol{D}_{al}\boldsymbol{\Pi}_{N_1}\end{bmatrix}\right)\begin{pmatrix}\Delta\boldsymbol{q}_{H_1} \\ \Delta\overline{\boldsymbol{q}}_{N_1}\end{pmatrix}
\end{aligned} \tag{3.42}$$

The aerodynamic damping and stiffness matrices associated with node N_1, evaluated in the auxiliary reference frame H_1, are obtained as follows:

$$\boldsymbol{D}_{a_{\text{aux}}} = \begin{bmatrix}\boldsymbol{\Xi}_{H_1}^T\boldsymbol{D}_{al}\boldsymbol{\Xi}_{H_1} & \boldsymbol{\Xi}_{H_1}^T\boldsymbol{D}_{al}\boldsymbol{\Xi}_{N_1} \\ \boldsymbol{\Xi}_{N_1}^T\boldsymbol{D}_{al}\boldsymbol{\Xi}_{H_1} & \boldsymbol{\Xi}_{N_1}^T\boldsymbol{D}_{al}\boldsymbol{\Xi}_{N_1}\end{bmatrix} \in \mathbb{R}^{12\times 12} \tag{3.43a}$$

$$\begin{aligned}
\boldsymbol{K}_{a_{\text{aux}}} = &\begin{bmatrix}\boldsymbol{\Xi}_{H_1}^T\boldsymbol{K}_{al}\boldsymbol{\Xi}_{H_1} & \boldsymbol{\Xi}_{H_1}^T\boldsymbol{K}_{al}\boldsymbol{\Xi}_{N_1} \\ \boldsymbol{\Xi}_{N_1}^T\boldsymbol{K}_{al}\boldsymbol{\Xi}_{H_1} & \boldsymbol{\Xi}_{N_1}^T\boldsymbol{K}_{al}\boldsymbol{\Xi}_{N_1}\end{bmatrix} \\
&+ \begin{bmatrix}\boldsymbol{\Xi}_{H_1}^T\boldsymbol{D}_{al}\boldsymbol{\Pi}_{H_1} & \boldsymbol{\Xi}_{H_1}^T\boldsymbol{D}_{al}\boldsymbol{\Pi}_{N_1} \\ \boldsymbol{\Xi}_{N_1}^T\boldsymbol{D}_{al}\boldsymbol{\Pi}_{H_1} & \boldsymbol{\Xi}_{N_1}^T\boldsymbol{D}_{al}\boldsymbol{\Pi}_{N_1}\end{bmatrix} \in \mathbb{R}^{12\times 12}
\end{aligned} \tag{3.43b}$$

where $\boldsymbol{D}_{al}$ and $\boldsymbol{K}_{al}$ are evaluated in (3.25).

The top-left sub-block matrices in (3.43) (colored in cyan) correspond to the hub block. However, they are associated with the generalized coordinates $\delta\boldsymbol{q}_{H_1}$, $\delta\boldsymbol{q}_{H_2}$, and $\delta\boldsymbol{q}_{H_3}$ for the three blades, respectively. Since the associated generalized coordinates are not consistent across the three blades, we cannot directly overlap the top-left sub-block matrices at the hub block. To resolve this issue, we need to rotate back to the consistent reference frame H for all three blades.

By substituting the coordinate transformations in (3.38) into the virtual work expression in (3.42), we can readily obtain the aerodynamic damping and stiffness

matrices for node N_1, expressed as follows:

$$\boxed{\begin{aligned} \boldsymbol{D}_{a_{\text{con}}} &= \begin{bmatrix} \boldsymbol{\Psi}_{H_1}^T & \mathbf{0} \\ \mathbf{0} & \boldsymbol{I}_{6\times 6} \end{bmatrix} \boldsymbol{D}_{a_{\text{aux}}} \begin{bmatrix} \boldsymbol{\Psi}_{H_1} & \mathbf{0} \\ \mathbf{0} & \boldsymbol{I}_{6\times 6} \end{bmatrix} \in \mathbb{R}^{12\times 12} && \text{(3.44a)} \\ \boldsymbol{K}_{a_{\text{con}}} &= \begin{bmatrix} \boldsymbol{\Psi}_{H_1}^T & \mathbf{0} \\ \mathbf{0} & \boldsymbol{I}_{6\times 6} \end{bmatrix} \boldsymbol{K}_{a_{\text{aux}}} \begin{bmatrix} \boldsymbol{\Psi}_{H_1} & \mathbf{0} \\ \mathbf{0} & \boldsymbol{I}_{6\times 6} \end{bmatrix} \in \mathbb{R}^{12\times 12} && \text{(3.44b)} \end{aligned}}$$

We can now assemble the system's aerodynamic damping and stiffness matrices according to the corresponding indices of blade nodes. The arrangement of the sub-block matrices within the aerodynamic damping and stiffness matrices is illustrated in Figure 3.8.

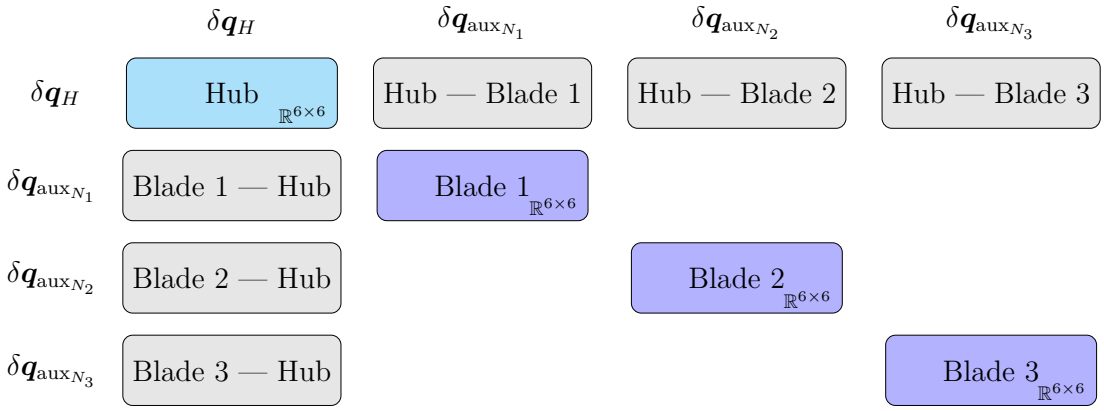

Figure 3.8: Arrangement of the sub-blocks in the aerodynamic damping and stiffness matrices.

3.3.4 Structural stiffness and damping matrices

The Timoshenko beam element developed in this study consists of two end nodes, yielding 12 DOFs per element. The tangent structural damping and stiffness matrices of the beam element (refer to (2.126b) and (2.126c)) are of size 12×12. The coordinate transformation relations outlined in (3.31) can be extended to accommodate the transformations required for beam elements.

Recalling the expressions provided in (3.32), the corresponding transformation matrices for the two nodes, A and B, of a beam element in the first blade are given

by

$$\boldsymbol{\Xi}_{H_A} = \begin{bmatrix} \boldsymbol{I} & -\boldsymbol{R}_{H_1}\widetilde{\boldsymbol{r}}_{H_1.N_{A(H_1)}} \\ \boldsymbol{0} & \boldsymbol{0} \end{bmatrix} \in \mathbb{R}^{6\times 6} \tag{3.45a}$$

$$\boldsymbol{\Xi}_{H_B} = \begin{bmatrix} \boldsymbol{I} & -\boldsymbol{R}_{H_1}\widetilde{\boldsymbol{r}}_{H_1.N_{B(H_1)}} \\ \boldsymbol{0} & \boldsymbol{0} \end{bmatrix} \in \mathbb{R}^{6\times 6} \tag{3.45b}$$

$$\boldsymbol{\Xi}_{N_A} = \boldsymbol{\Xi}_{N_B} = \begin{bmatrix} \boldsymbol{R}_{H_1} & \boldsymbol{0} \\ \boldsymbol{0} & \boldsymbol{I} \end{bmatrix} \in \mathbb{R}^{6\times 6} \tag{3.45c}$$

$$\boldsymbol{\Pi}_{H_A} = \begin{bmatrix} \boldsymbol{0} & -\boldsymbol{R}_{H_1}\big(\widetilde{\boldsymbol{\omega}}_{l_{H_1}}\widetilde{\boldsymbol{r}}_{H_1.N_{A(H_1)}}\big) - \boldsymbol{R}_{H_1}\widetilde{\dot{\boldsymbol{r}}}_{H_1.N_{A(H_1)}} \\ \boldsymbol{0} & \boldsymbol{0} \end{bmatrix} \in \mathbb{R}^{6\times 6} \tag{3.45d}$$

$$\boldsymbol{\Pi}_{H_B} = \begin{bmatrix} \boldsymbol{0} & -\boldsymbol{R}_{H_1}\big(\widetilde{\boldsymbol{\omega}}_{l_{H_1}}\widetilde{\boldsymbol{r}}_{H_1.N_{B(H_1)}}\big) - \boldsymbol{R}_{H_1}\widetilde{\dot{\boldsymbol{r}}}_{H_1.N_{B(H_1)}} \\ \boldsymbol{0} & \boldsymbol{0} \end{bmatrix} \in \mathbb{R}^{6\times 6} \tag{3.45e}$$

$$\boldsymbol{\Pi}_{N_A} = \boldsymbol{\Pi}_{N_B} = \begin{bmatrix} \boldsymbol{R}_{H_1}\widetilde{\boldsymbol{\omega}}_{l_{H_1}} & \boldsymbol{0} \\ \boldsymbol{0} & \boldsymbol{0} \end{bmatrix} \in \mathbb{R}^{6\times 6} \tag{3.45f}$$

Two extended transformation matrices are introduced as follows

$$\boldsymbol{\Xi}_{AB} = \begin{bmatrix} \boldsymbol{\Xi}_{H_A} & \boldsymbol{\Xi}_{N_A} & \boldsymbol{0} \\ \boldsymbol{\Xi}_{H_B} & \boldsymbol{0} & \boldsymbol{\Xi}_{N_B} \end{bmatrix} \in \mathbb{R}^{12\times 18} \tag{3.46a}$$

$$\boldsymbol{\Pi}_{AB} = \begin{bmatrix} \boldsymbol{\Pi}_{H_A} & \boldsymbol{\Pi}_{N_A} & \boldsymbol{0} \\ \boldsymbol{\Pi}_{H_B} & \boldsymbol{0} & \boldsymbol{\Pi}_{N_B} \end{bmatrix} \in \mathbb{R}^{12\times 18} \tag{3.46b}$$

Analogous to the derivation in (3.42), by evaluating the virtual work done by the structural damping and elastic forces in the beam element, the structural damping and stiffness matrices expressed in the auxiliary reference frame H_1 are derived as follows:

$$\boldsymbol{D}_{e_{\text{aux}}} = \boldsymbol{\Xi}_{AB}^T \boldsymbol{D}_m \boldsymbol{\Xi}_{AB} \in \mathbb{R}^{18\times 18} \tag{3.47a}$$

$$\boldsymbol{K}_{e_{\text{aux}}} = \boldsymbol{\Xi}_{AB}^T \left(\boldsymbol{K}_m + \boldsymbol{K}_g\right) \boldsymbol{\Xi}_{AB} + \boldsymbol{\Xi}_{AB}^T \boldsymbol{D}_m \boldsymbol{\Pi}_{AB} \in \mathbb{R}^{18\times 18} \tag{3.47b}$$

where $\boldsymbol{D}_m$, $\boldsymbol{K}_m$, and $\boldsymbol{K}_g$ are evaluated in accordance with (2.126b), (2.126c), and (2.128), respectively.

A similar rotation, as described in (3.44), can be applied to transform the top-left 6×6 sub-block matrices back to the consistent reference frame H, as shown below:

$$\boxed{\boldsymbol{D}_{e_{\text{con}}} = \begin{bmatrix} \boldsymbol{\Psi}_{H_1}^T & \boldsymbol{0} \\ \boldsymbol{0} & \boldsymbol{I}_{12\times 12} \end{bmatrix} \boldsymbol{D}_{e_{\text{aux}}} \begin{bmatrix} \boldsymbol{\Psi}_{H_1} & \boldsymbol{0} \\ \boldsymbol{0} & \boldsymbol{I}_{12\times 12} \end{bmatrix} \in \mathbb{R}^{18\times 18}} \tag{3.48a}$$

$$\boxed{\boldsymbol{K}_{e_{\text{con}}} = \begin{bmatrix} \boldsymbol{\Psi}_{H_1}^T & \boldsymbol{0} \\ \boldsymbol{0} & \boldsymbol{I}_{12\times 12} \end{bmatrix} \boldsymbol{K}_{e_{\text{aux}}} \begin{bmatrix} \boldsymbol{\Psi}_{H_1} & \boldsymbol{0} \\ \boldsymbol{0} & \boldsymbol{I}_{12\times 12} \end{bmatrix} \in \mathbb{R}^{18\times 18}} \tag{3.48b}$$

which are ready for assembly into the system's structural damping and stiffness matrices, following the corresponding indices of the blade nodes.

3.3.5 Constraints

The wind turbine blades are mounted on the hub through pitch bearings. In our simulation model, the blade root node N_r of the first blade is connected to the pitch bearing, modeled as a rigid body and labeled as P_1, via a rheonomic revolute joint, which is characterized by the pitch angle β_1. The pitch bearing P_1 is then rigidly linked with the hub through a fixed joint, as illustrated in Figure 3.7.

Both the Jacobian matrix of constraints $\boldsymbol{C_q}$ and the tangent stiffness matrix of constraints $\boldsymbol{K}_c$ are required to transform into the consistent reference frame H.

Constraints between pitch bearing and blade root node

Referring to (3.31a), the generalized coordinates of the pitch bearing P_1 and the blade root node N_r can be transformed into the blade auxiliary reference frame H_1 as follows

$$\delta \boldsymbol{q}_{P_1} = \boldsymbol{\Xi}_{H_{P_1}} \delta \boldsymbol{q}_{H_1} + \boldsymbol{\Xi}_{N_{P_1}} \delta \overline{\boldsymbol{q}}_{P_1} \tag{3.49a}$$

$$\delta \boldsymbol{q}_{N_r} = \boldsymbol{\Xi}_{H_{N_r}} \delta \boldsymbol{q}_{H_1} + \boldsymbol{\Xi}_{N_{N_r}} \delta \overline{\boldsymbol{q}}_{N_r} \tag{3.49b}$$

where the transformation matrices $\boldsymbol{\Xi}_{H_{P_1}}$, $\boldsymbol{\Xi}_{H_{N_r}}$, and $\boldsymbol{\Xi}_{N_{P_1}}$, $\boldsymbol{\Xi}_{N_{N_r}}$ are evaluated according to (3.32a) and (3.32b), respectively.

Similarly to the coordinate transformations for the beam element discussed in Section 3.3.4, an extended transformation matrix is introduced as follows:

$$\boldsymbol{\Xi}_{PN} = \begin{bmatrix} \boldsymbol{\Xi}_{H_{P_1}} & \boldsymbol{\Xi}_{N_{P_1}} & \boldsymbol{0} \\ \boldsymbol{\Xi}_{H_{N_r}} & \boldsymbol{0} & \boldsymbol{\Xi}_{N_{N_r}} \end{bmatrix} \in \mathbb{R}^{12\times 18} \tag{3.50}$$

In the generic form of the linearized DAEs (2.76), the second equation $\boldsymbol{C_q}\delta\boldsymbol{q} = \boldsymbol{0}$ enforces the satisfaction of constraints. For the constraints between the blade bearing P_1 and the blade root node N_r, let the original Jacobian matrix of constraints associated with the generalized coordinates $\delta \boldsymbol{q}_{PN} = \left[\delta \boldsymbol{q}_{P_1}^T, \delta \boldsymbol{q}_{N_r}^T\right]^T$ be denoted $\boldsymbol{C}_{\boldsymbol{q}_{PN}}$. By applying the coordinate transformations in (3.49), the linearized constraint equation can be derived as follows

$$\boldsymbol{C}_{\boldsymbol{q}_{PN}} \delta \boldsymbol{q}_{PN} = \boldsymbol{C}_{\boldsymbol{q}_{PN}} \boldsymbol{\Xi}_{PN} \begin{pmatrix} \delta \boldsymbol{q}_{H_1} \\ \delta \overline{\boldsymbol{q}}_{P_1} \\ \delta \overline{\boldsymbol{q}}_{N_r} \end{pmatrix} = \boldsymbol{0} \tag{3.51}$$

Substituting the rotation transformation (3.38a) into (3.51), the Jacobian matrix of constraints resolved in the consistent reference frame H can be obtained as follows

$$\boxed{\boldsymbol{C}_{\boldsymbol{q}_{PN\mathrm{con}}} = \boldsymbol{C}_{\boldsymbol{q}_{PN}} \boldsymbol{\Xi}_{PN} \begin{bmatrix} \boldsymbol{\Psi}_{H_1} & \boldsymbol{0} \\ \boldsymbol{0} & \boldsymbol{I}_{12\times 12} \end{bmatrix} \in \mathbb{R}^{6\times 18}} \tag{3.52}$$

Similarly to the derivation for (3.48), the tangent stiffness matrix of the constraints between the pitch bearing P_1 and the blade root node N_1, resolved in the consistent reference frame H, can be derived as follows

$$\boxed{\boldsymbol{K}_{c_{PN\mathrm{con}}} = \begin{bmatrix} \boldsymbol{\Psi}_{H_1}^T & \boldsymbol{0} \\ \boldsymbol{0} & \boldsymbol{I}_{12\times 12} \end{bmatrix} \boldsymbol{\Xi}_{PN}^T \boldsymbol{K}_{c_{PN}} \boldsymbol{\Xi}_{PN} \begin{bmatrix} \boldsymbol{\Psi}_{H_1} & \boldsymbol{0} \\ \boldsymbol{0} & \boldsymbol{I}_{12\times 12} \end{bmatrix} \in \mathbb{R}^{18\times 18}} \tag{3.53}$$

where $\boldsymbol{K}_{c_{PN}}$ is the original tangent stiffness matrix of constraints, expressed in the mixed basis and computed using the algorithm presented in Section 3.1.3.

Constraints between pitch bearing and hub

For the fixed constraints between the pitch bearing P_1 to the hub H, the generalized coordinates in the mixed basis are denoted as $\delta\boldsymbol{q}_{HP} = \left[\delta\boldsymbol{q}_H^T, \delta\boldsymbol{q}_{P_1}^T\right]^T$, and the Jacobian matrix of constraints in the mixed basis is represented as $\boldsymbol{C}_{\boldsymbol{q}_{HP}}$.

Recalling the coordinate transformation (3.49a) and the rotation transformation (3.38a), the linearized constraint equation $\boldsymbol{C}_{\boldsymbol{q}}\delta\boldsymbol{q} = \boldsymbol{0}$ can be derived as follows

$$\boldsymbol{C}_{\boldsymbol{q}_{HP}}\delta\boldsymbol{q}_{HP} = \boldsymbol{C}_{\boldsymbol{q}_{HP}} \begin{bmatrix} \boldsymbol{I}_{6\times 6} & \boldsymbol{0} \\ \boldsymbol{\Xi}_{H_{P_1}}\boldsymbol{\Psi}_{H_1} & \boldsymbol{\Xi}_{N_{P_1}} \end{bmatrix} \begin{pmatrix} \delta\boldsymbol{q}_H \\ \delta\overline{\boldsymbol{q}}_{P_1} \end{pmatrix} = \boldsymbol{0} \tag{3.54}$$

By introducing an extended transformation matrix

$$\boldsymbol{\Xi}_{HP} = \begin{bmatrix} \boldsymbol{I}_{6\times 6} & \boldsymbol{0} \\ \boldsymbol{\Xi}_{H_{P_1}}\boldsymbol{\Psi}_{H_1} & \boldsymbol{\Xi}_{N_{P_1}} \end{bmatrix} \in \mathbb{R}^{12\times 12} \tag{3.55}$$

the Jacobian matrix of constraints, resolved in the consistent reference frame H, is obtained as follows:

$$\boxed{\boldsymbol{C}_{\boldsymbol{q}_{HP\mathrm{con}}} = \boldsymbol{C}_{\boldsymbol{q}_{HP}}\boldsymbol{\Xi}_{HP} \in \mathbb{R}^{6\times 12}} \tag{3.56}$$

The tangent stiffness matrix of constraints, expressed in the consistent reference frame H, can be readily derived as follows:

$$\boxed{\boldsymbol{K}_{c_{HP\mathrm{con}}} = \boldsymbol{\Xi}_{HP}^T\boldsymbol{K}_{c_{HP}}\boldsymbol{\Xi}_{HP} \in \mathbb{R}^{12\times 12}} \tag{3.57}$$

where $\boldsymbol{K}_{c_{HP}}$ is the original tangent stiffness matrix of constraints expressed in the mixed basis and computed using the algorithm presented in Section 3.1.2.

3.3.6 Inertial mass, damping and stiffness matrices

According to (2.131), based on the lumped mass assumption, the inertial forces concentrated at node N_1 are expressed as

$$\boldsymbol{f}_{i_{N_1}} = \begin{pmatrix} \nu\ddot{\boldsymbol{r}}_{N_1} + \nu\boldsymbol{R}_{N_1}\widetilde{\boldsymbol{s}}_l^T\dot{\boldsymbol{\omega}}_{l_{N_1}} + \nu\boldsymbol{R}_{N_1}\widetilde{\boldsymbol{\omega}}_{l_{N_1}}\widetilde{\boldsymbol{\omega}}_{l_{N_1}}\boldsymbol{s}_l \\ \nu\widetilde{\boldsymbol{s}}_l\boldsymbol{R}_{N_1}^T\ddot{\boldsymbol{r}}_{N_1} + \boldsymbol{J}_l\dot{\boldsymbol{\omega}}_{l_{N_1}} + \widetilde{\boldsymbol{\omega}}_{l_{N_1}}\boldsymbol{J}_l\boldsymbol{\omega}_{l_{N_1}} \end{pmatrix} \tag{3.58}$$

where ν and $\boldsymbol{J}_l$ represent the lumped mass and the inertial tensor at node N_1, respectively, and $\boldsymbol{s}_l$ denotes the mass center offset in the nodal frame.

Referring to (2.42), the translational acceleration of node N_1 is read as

$$\begin{aligned}\ddot{\boldsymbol{r}}_{N_1} = \ddot{\boldsymbol{r}}_{H_1} + \boldsymbol{R}_{H_1}\widetilde{\dot{\boldsymbol{\omega}}}_{l_{H_1}}\boldsymbol{r}_{H_1.N_{1(H_1)}} + \boldsymbol{R}_{H_1}\widetilde{\boldsymbol{\omega}}_{l_{H_1}}\widetilde{\boldsymbol{\omega}}_{l_{H_1}}\boldsymbol{r}_{H_1.N_{1(H_1)}} \\ + 2\boldsymbol{R}_{H_1}\widetilde{\boldsymbol{\omega}}_{l_{H_1}}\dot{\boldsymbol{r}}_{H_1.N_{1(H_1)}} + \boldsymbol{R}_{H_1}\ddot{\boldsymbol{r}}_{H_1.N_{1(H_1)}}\end{aligned} \tag{3.59}$$

Applying variations to (3.59), yields

$$\begin{aligned}\delta\ddot{\boldsymbol{r}}_{N_1} = \delta\ddot{\boldsymbol{r}}_{H_1} - \boldsymbol{R}_{H_1}\widetilde{\boldsymbol{r}}_{H_1.N_{1(H_1)}}\delta\dot{\boldsymbol{\omega}}_{l_{H_1}} - \boldsymbol{R}_{H_1}\boldsymbol{\Upsilon}_1\delta\boldsymbol{\omega}_{l_{H_1}} - \boldsymbol{R}_{H_1}\boldsymbol{\Upsilon}_2\delta\boldsymbol{\theta}_{l_{H_1}} \\ + \boldsymbol{R}_{H_1}\delta\ddot{\boldsymbol{r}}_{H_1.N_{1(H_1)}} + 2\boldsymbol{R}_{H_1}\widetilde{\boldsymbol{\omega}}_{l_{H_1}}\delta\dot{\boldsymbol{r}}_{H_1.N_{1(H_1)}} + \boldsymbol{R}_{H_1}\boldsymbol{\Upsilon}_3\delta\boldsymbol{r}_{H_1.N_{1(H_1)}}\end{aligned} \tag{3.60}$$

where

$$\boldsymbol{\Upsilon}_1 = 2\widetilde{\boldsymbol{\omega}}_{l_{H_1}}\widetilde{\boldsymbol{r}}_{H_1.N_{1(H_1)}} - \widetilde{\boldsymbol{r}}_{H_1.N_{1(H_1)}}\widetilde{\boldsymbol{\omega}}_{l_{H_1}} + 2\widetilde{\dot{\boldsymbol{r}}}_{H_1.N_{1(H_1)}} \tag{3.61a}$$

$$\begin{aligned}\boldsymbol{\Upsilon}_2 = \Big(\widetilde{\boldsymbol{\omega}}_{l_{H_1}}\widetilde{\boldsymbol{\omega}}_{l_{H_1}}\boldsymbol{r}_{H_1.N_{1(H_1)}}\Big) \\ + \Big(\widetilde{\dot{\boldsymbol{\omega}}}_{l_{H_1}}\boldsymbol{r}_{H_1.N_{1(H_1)}}\Big) + 2\Big(\widetilde{\boldsymbol{\omega}}_{l_{H_1}}\dot{\boldsymbol{r}}_{H_1.N_{1(H_1)}}\Big) + \widetilde{\ddot{\boldsymbol{r}}}_{H_1.N_{1(H_1)}}\end{aligned} \tag{3.61b}$$

$$\boldsymbol{\Upsilon}_3 = \widetilde{\boldsymbol{\omega}}_{l_{H_1}}\widetilde{\boldsymbol{\omega}}_{l_{H_1}} + \widetilde{\dot{\boldsymbol{\omega}}}_{l_{H_1}} \tag{3.61c}$$

In the quasi-static equilibrium state of wind turbine rotors, the translational velocity and acceleration of node N_1 relative to the hub center H_1 are zero, i.e., $\dot{\boldsymbol{r}}_{H_1.N_{1(H_1)}} = \ddot{\boldsymbol{r}}_{H_1.N_{1(H_1)}} = \boldsymbol{0}$, and the angular acceleration of the hub center H_1 is also zero, i.e., $\dot{\boldsymbol{\omega}}_{l_{H_1}} = \boldsymbol{0}$. These conditions lead to simplified expressions for the three terms, as follows:

$$\boldsymbol{\Upsilon}_1 = 2\widetilde{\boldsymbol{\omega}}_{l_{H_1}}\widetilde{\boldsymbol{r}}_{H_1.N_{1(H_1)}} - \widetilde{\boldsymbol{r}}_{H_1.N_{1(H_1)}}\widetilde{\boldsymbol{\omega}}_{l_{H_1}} \tag{3.62a}$$

$$\boldsymbol{\Upsilon}_2 = \Big(\widetilde{\boldsymbol{\omega}}_{l_{H_1}}\widetilde{\boldsymbol{\omega}}_{l_{H_1}}\boldsymbol{r}_{H_1.N_{1(H_1)}}\Big) \tag{3.62b}$$

$$\boldsymbol{\Upsilon}_3 = \widetilde{\boldsymbol{\omega}}_{l_{H_1}}\widetilde{\boldsymbol{\omega}}_{l_{H_1}} \tag{3.62c}$$

Applying variations to (3.58), recalling (2.15b) and properties in (2.1), and substituting the variations from (3.30a), (3.30b) and (3.60), while grouping the terms according to the generalized coordinates, the linearized inertial forces in the

auxiliary coordinates are obtained after tedious manipulations, as follows

$$\begin{aligned}
\delta \boldsymbol{f}_{i_{N_1}} = & \begin{bmatrix} \nu \boldsymbol{I} & -\nu \boldsymbol{R}_{H_1} \widetilde{\overline{\boldsymbol{r}}} \\ \nu \widetilde{\boldsymbol{s}}_l \boldsymbol{R}_{N_1}^T & -\nu \widetilde{\boldsymbol{s}}_l \boldsymbol{R}_{N_1}^T \boldsymbol{R}_{H_1} \widetilde{\overline{\boldsymbol{r}}} \end{bmatrix} \delta \ddot{\boldsymbol{q}}_{H_1} \\
& + \begin{bmatrix} \boldsymbol{0} & -\nu \boldsymbol{R}_{H_1} \boldsymbol{\Upsilon}_1 \\ \boldsymbol{0} & -\nu \widetilde{\boldsymbol{s}}_l \boldsymbol{R}_{N_1}^T \boldsymbol{R}_{H_1} \boldsymbol{\Upsilon}_1 \end{bmatrix} \delta \dot{\boldsymbol{q}}_{H_1} \\
& + \begin{bmatrix} \boldsymbol{0} & -\nu \boldsymbol{R}_{H_1} \boldsymbol{\Upsilon}_2 \\ \boldsymbol{0} & -\nu \widetilde{\boldsymbol{s}}_l \boldsymbol{R}_{N_1}^T \boldsymbol{R}_{H_1} \boldsymbol{\Upsilon}_2 \end{bmatrix} \delta \boldsymbol{q}_{H_1} \\
& + \begin{bmatrix} \nu \boldsymbol{R}_{H_1} & -\nu \boldsymbol{R}_{N_1} \widetilde{\boldsymbol{s}}_l \\ \nu \widetilde{\boldsymbol{s}}_l \boldsymbol{R}_{N_1}^T \boldsymbol{R}_{H_1} & \boldsymbol{J}_l \end{bmatrix} \delta \ddot{\overline{\boldsymbol{q}}}_{N_1} \\
& + \begin{bmatrix} 2\nu \boldsymbol{R}_{H_1} \widetilde{\boldsymbol{\omega}}_{l_{H_1}} & -\nu \boldsymbol{R}_{N_1} \boldsymbol{\Upsilon}_4 \\ 2\nu \widetilde{\boldsymbol{s}}_l \boldsymbol{R}_{N_1}^T \boldsymbol{R}_{H_1} \widetilde{\boldsymbol{\omega}}_{l_{H_1}} & \widetilde{\boldsymbol{\omega}}_{l_{N_1}} \boldsymbol{J}_l - \widetilde{\boldsymbol{J}_l \boldsymbol{\omega}_{l_{N_1}}} \end{bmatrix} \delta \dot{\overline{\boldsymbol{q}}}_{N_1} \\
& + \begin{bmatrix} \nu \boldsymbol{R}_{H_1} \boldsymbol{\Upsilon}_3 & -\nu \boldsymbol{R}_{N_1} \boldsymbol{\Upsilon}_5 \\ \nu \widetilde{\boldsymbol{s}}_l \boldsymbol{R}_{N_1}^T \boldsymbol{R}_{H_1} \boldsymbol{\Upsilon}_3 & \nu \widetilde{\boldsymbol{s}}_l \boldsymbol{R}_{N_1}^T \ddot{\boldsymbol{r}}_{N_1} \end{bmatrix} \delta \overline{\boldsymbol{q}}_{N_1}
\end{aligned} \tag{3.63}$$

where

$$\boldsymbol{\Upsilon}_4 = 2\widetilde{\boldsymbol{\omega}}_{l_{N_1}} \widetilde{\boldsymbol{s}}_l - \widetilde{\boldsymbol{s}}_l \widetilde{\boldsymbol{\omega}}_{l_{N_1}} \tag{3.64a}$$

$$\boldsymbol{\Upsilon}_5 = \widetilde{\left(\widetilde{\boldsymbol{\omega}}_{l_{N_1}} \boldsymbol{s}_l\right)} + \widetilde{\left(\widetilde{\boldsymbol{\omega}}_{l_{N_1}} \widetilde{\boldsymbol{\omega}}_{l_{N_1}} \boldsymbol{s}_l\right)} \tag{3.64b}$$

Recalling the coordinate transformation in (3.31a), the virtual work done by the incremental linearized inertial forces $\Delta \boldsymbol{f}_{i_{N_1}}$ can be evaluated in the auxiliary coordinates as follows

$$\begin{aligned}
\delta W_{\text{iner}} &= \delta \boldsymbol{q}_{N_1} \Delta \boldsymbol{f}_{i_{N_1}} \\
&= \begin{pmatrix} \delta \boldsymbol{q}_{H_1}^T & \delta \overline{\boldsymbol{q}}_{N_1}^T \end{pmatrix} \left(\boldsymbol{M}_{\text{aux}} \begin{pmatrix} \Delta \ddot{\boldsymbol{q}}_{H_1} \\ \Delta \ddot{\overline{\boldsymbol{q}}}_{N_1} \end{pmatrix} + \boldsymbol{D}_{i_{\text{aux}}} \begin{pmatrix} \Delta \dot{\boldsymbol{q}}_{H_1} \\ \Delta \dot{\overline{\boldsymbol{q}}}_{N_1} \end{pmatrix} + \boldsymbol{K}_{i_{\text{aux}}} \begin{pmatrix} \Delta \boldsymbol{q}_{H_1} \\ \Delta \overline{\boldsymbol{q}}_{N_1} \end{pmatrix} \right)
\end{aligned} \tag{3.65}$$

where the inertial mass, damping and stiffness matrices are

$$\boldsymbol{M}_{\text{aux}} = \begin{bmatrix} \nu\boldsymbol{I} & -\nu\boldsymbol{R}_{H_1}\widetilde{\overline{\boldsymbol{r}}} & \nu\boldsymbol{R}_{H_1} & -\nu\boldsymbol{R}_{N_1}\widetilde{\boldsymbol{s}}_l \\ \nu\widetilde{\overline{\boldsymbol{r}}}\boldsymbol{R}_{H_1}^T & -\nu\widetilde{\overline{\boldsymbol{r}}}\widetilde{\overline{\boldsymbol{r}}} & \nu\widetilde{\overline{\boldsymbol{r}}} & -\nu\widetilde{\overline{\boldsymbol{r}}}\boldsymbol{R}_{H_1}^T\boldsymbol{R}_{N_1}\widetilde{\boldsymbol{s}}_l \\ \nu\boldsymbol{R}_{H_1}^T & -\nu\widetilde{\overline{\boldsymbol{r}}} & \nu\boldsymbol{I} & -\nu\boldsymbol{R}_{H_1}^T\boldsymbol{R}_{N_1}\widetilde{\boldsymbol{s}}_l \\ \nu\widetilde{\boldsymbol{s}}_l\boldsymbol{R}_{N_1}^T & -\nu\widetilde{\boldsymbol{s}}_l\boldsymbol{R}_{N_1}^T\boldsymbol{R}_{H_1}\widetilde{\overline{\boldsymbol{r}}} & \nu\widetilde{\boldsymbol{s}}_l\boldsymbol{R}_{N_1}^T\boldsymbol{R}_{H_1} & \boldsymbol{J}_l \end{bmatrix} \tag{3.66a}$$

$$\boldsymbol{D}_{i_{\text{aux}}} = \begin{bmatrix} \boldsymbol{0} & -\nu\boldsymbol{R}_{H_1}\boldsymbol{\Upsilon}_1 & 2\nu\boldsymbol{R}_{H_1}\widetilde{\boldsymbol{\omega}}_{l_{H_1}} & -\nu\boldsymbol{R}_{N_1}\boldsymbol{\Upsilon}_4 \\ \boldsymbol{0} & -\nu\widetilde{\overline{\boldsymbol{r}}}\boldsymbol{\Upsilon}_1 & 2\nu\widetilde{\overline{\boldsymbol{r}}}\widetilde{\boldsymbol{\omega}}_{l_{H_1}} & -\nu\widetilde{\overline{\boldsymbol{r}}}\boldsymbol{R}_{H_1}^T\boldsymbol{R}_{N_1}\boldsymbol{\Upsilon}_4 \\ \boldsymbol{0} & -\nu\boldsymbol{\Upsilon}_1 & 2\nu\widetilde{\boldsymbol{\omega}}_{l_{H_1}} & -\nu\boldsymbol{R}_{H_1}^T\boldsymbol{R}_{N_1}\boldsymbol{\Upsilon}_4 \\ \boldsymbol{0} & -\nu\widetilde{\boldsymbol{s}}_l\boldsymbol{R}_{N_1}^T\boldsymbol{R}_{H_1}\boldsymbol{\Upsilon}_1 & 2\nu\widetilde{\boldsymbol{s}}_l\boldsymbol{R}_{N_1}^T\boldsymbol{R}_{H_1}\widetilde{\boldsymbol{\omega}}_{l_{H_1}} & \widetilde{\boldsymbol{\omega}}_{l_{N_1}}\boldsymbol{J}_l - \widetilde{\boldsymbol{J}_l\boldsymbol{\omega}_{l_{N_1}}} \end{bmatrix} \tag{3.66b}$$

$$\boldsymbol{K}_{i_{\text{aux}}} = \begin{bmatrix} \boldsymbol{0} & -\nu\boldsymbol{R}_{H_1}\boldsymbol{\Upsilon}_2 & \nu\boldsymbol{R}_{H_1}\boldsymbol{\Upsilon}_3 & -\nu\boldsymbol{R}_{N_1}\boldsymbol{\Upsilon}_5 \\ \boldsymbol{0} & -\nu\widetilde{\overline{\boldsymbol{r}}}\boldsymbol{\Upsilon}_2 & \nu\widetilde{\overline{\boldsymbol{r}}}\boldsymbol{\Upsilon}_3 & -\nu\widetilde{\overline{\boldsymbol{r}}}\boldsymbol{R}_{H_1}^T\boldsymbol{R}_{N_1}\boldsymbol{\Upsilon}_5 \\ \boldsymbol{0} & -\nu\boldsymbol{\Upsilon}_2 & \nu\boldsymbol{\Upsilon}_3 & -\nu\boldsymbol{R}_{H_1}^T\widetilde{\boldsymbol{R}_{N_1}\boldsymbol{\Upsilon}_5} \\ \boldsymbol{0} & -\nu\widetilde{\boldsymbol{s}}_l\boldsymbol{R}_{N_1}^T\boldsymbol{R}_{H_1}\boldsymbol{\Upsilon}_2 & \nu\widetilde{\boldsymbol{s}}_l\boldsymbol{R}_{N_1}^T\boldsymbol{R}_{H_1}\boldsymbol{\Upsilon}_3 & \nu\widetilde{\boldsymbol{s}}_l\boldsymbol{R}_{N_1}^T\ddot{\boldsymbol{r}}_{N_1} \end{bmatrix} \tag{3.66c}$$

with $\overline{\boldsymbol{r}} = \boldsymbol{r}_{H_1.N_{1(H_1)}}$ being introduced to reduce the width of matrix notation.

It is worth noting that the mass matrix $\boldsymbol{M}_{\text{aux}}$ is symmetric, while both the inertial damping matrix $\boldsymbol{D}_{i_{\text{aux}}}$ and the inertial stiffness matrix $\boldsymbol{K}_{i_{\text{aux}}}$ are neither symmetric nor skew-symmetric.

If the mass center coincides with the reference center of the cross-section (which is typically the elastic center), resulting in $\boldsymbol{s}_l = \boldsymbol{0}$ and $\boldsymbol{\Upsilon}_4 = \boldsymbol{\Upsilon}_5 = \boldsymbol{0}$, the inertial mass, damping, and stiffness matrices in the auxiliary coordinates simplify to the following expressions:

$$\boldsymbol{M}_{\text{aux}} = \begin{bmatrix} \nu\boldsymbol{I} & -\nu\boldsymbol{R}_{H_1}\widetilde{\overline{\boldsymbol{r}}} & \nu\boldsymbol{R}_{H_1} & \boldsymbol{0} \\ \nu\widetilde{\overline{\boldsymbol{r}}}\boldsymbol{R}_{H_1}^T & -\nu\widetilde{\overline{\boldsymbol{r}}}\widetilde{\overline{\boldsymbol{r}}} & \nu\widetilde{\overline{\boldsymbol{r}}} & \boldsymbol{0} \\ \nu\boldsymbol{R}_{H_1}^T & -\nu\widetilde{\overline{\boldsymbol{r}}} & \nu\boldsymbol{I} & \boldsymbol{0} \\ \boldsymbol{0} & \boldsymbol{0} & \boldsymbol{0} & \boldsymbol{J}_l \end{bmatrix} \tag{3.67a}$$

$$\boldsymbol{D}_{i_{\text{aux}}} = \begin{bmatrix} \boldsymbol{0} & -\nu\boldsymbol{R}_{H_1}\boldsymbol{\Upsilon}_1 & 2\nu\boldsymbol{R}_{H_1}\widetilde{\boldsymbol{\omega}}_{l_{H_1}} & \boldsymbol{0} \\ \boldsymbol{0} & -\nu\widetilde{\overline{\boldsymbol{r}}}\boldsymbol{\Upsilon}_1 & 2\nu\widetilde{\overline{\boldsymbol{r}}}\widetilde{\boldsymbol{\omega}}_{l_{H_1}} & \boldsymbol{0} \\ \boldsymbol{0} & -\nu\boldsymbol{\Upsilon}_1 & 2\nu\widetilde{\boldsymbol{\omega}}_{l_{H_1}} & \boldsymbol{0} \\ \boldsymbol{0} & \boldsymbol{0} & \boldsymbol{0} & \widetilde{\boldsymbol{\omega}}_{l_{N_1}}\boldsymbol{J}_l - \widetilde{\boldsymbol{J}_l\boldsymbol{\omega}_{l_{N_1}}} \end{bmatrix} \tag{3.67b}$$

$$\boldsymbol{K}_{i_{\text{aux}}} = \begin{bmatrix} \boldsymbol{0} & -\nu\boldsymbol{R}_{H_1}\boldsymbol{\Upsilon}_2 & \nu\boldsymbol{R}_{H_1}\boldsymbol{\Upsilon}_3 & \boldsymbol{0} \\ \boldsymbol{0} & -\nu\widetilde{\overline{\boldsymbol{r}}}\boldsymbol{\Upsilon}_2 & \nu\widetilde{\overline{\boldsymbol{r}}}\boldsymbol{\Upsilon}_3 & \boldsymbol{0} \\ \boldsymbol{0} & -\nu\boldsymbol{\Upsilon}_2 & \nu\boldsymbol{\Upsilon}_3 & \boldsymbol{0} \\ \boldsymbol{0} & \boldsymbol{0} & \boldsymbol{0} & \boldsymbol{0} \end{bmatrix} \tag{3.67c}$$

The top-left 6×6 sub-block matrices in (3.66) are expressed in the three auxiliary reference frames H_1, H_2 and H_3 for the three blades, respectively. A similar rotation, as described in (3.44), can be applied to transform these top-left 6×6

sub-block matrices back to the consistent reference frame H, as shown below:

$$\boxed{\begin{aligned}
\boldsymbol{M}_{\text{con}} &= \begin{bmatrix} \boldsymbol{\Psi}_{H_1}^T & \boldsymbol{0} \\ \boldsymbol{0} & \boldsymbol{I}_{6\times 6} \end{bmatrix} \boldsymbol{M}_{\text{aux}} \begin{bmatrix} \boldsymbol{\Psi}_{H_1} & \boldsymbol{0} \\ \boldsymbol{0} & \boldsymbol{I}_{6\times 6} \end{bmatrix} \in \mathbb{R}^{12\times 12} && \text{(3.68a)} \\
\boldsymbol{D}_{i_{\text{con}}} &= \begin{bmatrix} \boldsymbol{\Psi}_{H_1}^T & \boldsymbol{0} \\ \boldsymbol{0} & \boldsymbol{I}_{6\times 6} \end{bmatrix} \boldsymbol{D}_{i_{\text{aux}}} \begin{bmatrix} \boldsymbol{\Psi}_{H_1} & \boldsymbol{0} \\ \boldsymbol{0} & \boldsymbol{I}_{6\times 6} \end{bmatrix} \in \mathbb{R}^{12\times 12} && \text{(3.68b)} \\
\boldsymbol{K}_{i_{\text{con}}} &= \begin{bmatrix} \boldsymbol{\Psi}_{H_1}^T & \boldsymbol{0} \\ \boldsymbol{0} & \boldsymbol{I}_{6\times 6} \end{bmatrix} \boldsymbol{K}_{i_{\text{aux}}} \begin{bmatrix} \boldsymbol{\Psi}_{H_1} & \boldsymbol{0} \\ \boldsymbol{0} & \boldsymbol{I}_{6\times 6} \end{bmatrix} \in \mathbb{R}^{12\times 12} && \text{(3.68c)}
\end{aligned}}$$

which are ready for assembly into the system's inertial mass, damping and stiffness matrices, following the corresponding indices of the blade nodes.

3.3.7 Coaxial components

As illustrated in Figure 3.7, the coaxial components, including the hub, LSS and HSS, are modeled as rigid bodies. Their mass centers are aligned with the rotor's axis of rotation, i.e., $\boldsymbol{s}_l = \boldsymbol{0}$. Referring to (2.127) and (2.137), the inertial mass, damping and stiffness matrices are already independent of time, rendering them suitable for modal analysis. Therefore, no additional manipulation is required.

3.4 Modal analysis in multi-blade coordinates

The aerodynamic damping and stiffness matrices in (3.44), the structural damping and stiffness matrices in (3.48), the tangent stiffness matrix of constraints in (3.53) and (3.57), the Jacobian matrix of constraints in (3.52) and (3.56), as well as the inertial mass, damping and stiffness matrices in (3.68), are all expressed in the consistent reference frame H at the hub center. Consequently, the linearized DAEs of wind turbine rotors can be assembled.

Recalling the generic form of the linearized DAEs in (2.76) and accounting for the remaining stationary components of the wind turbine—including the bedplate, nacelle and tower—as depicted in Figure 3.7, the complete form of the linearized DAEs for the wind turbine system, resolved in consistent reference frames, which essentially are stationary reference frames, can be presented as follows

$$\begin{cases}
\boldsymbol{M}_{\text{con}}\delta\ddot{\boldsymbol{q}}_{\text{con}} + \boldsymbol{D}_{\text{con}}\delta\dot{\boldsymbol{q}}_{\text{con}} + \boldsymbol{K}_{\text{con}}\delta\boldsymbol{q}_{\text{con}} + \boldsymbol{C}_{\boldsymbol{q}_{\text{con}}}^T\delta\boldsymbol{\gamma}_{\boldsymbol{q}} = \boldsymbol{0} & \text{(3.69a)} \\
\boldsymbol{C}_{\boldsymbol{q}_{\text{con}}}\delta\boldsymbol{q}_{\text{con}} = \boldsymbol{0} & \text{(3.69b)}
\end{cases}$$

where the consistent damping and stiffness matrices are

$$\begin{aligned}
\boldsymbol{D}_{\text{con}} &= \boldsymbol{D}_{a_{\text{con}}} + \boldsymbol{D}_{e_{\text{con}}} + \boldsymbol{D}_{i_{\text{con}}} && \text{(3.70a)} \\
\boldsymbol{K}_{\text{con}} &= \boldsymbol{K}_{a_{\text{con}}} + \boldsymbol{K}_{e_{\text{con}}} + \boldsymbol{K}_{i_{\text{con}}} + \boldsymbol{K}_{c_{\text{con}}} && \text{(3.70b)}
\end{aligned}$$

The consistent generalized coordinates and Lagrange multipliers are composed of

$$\delta \boldsymbol{q}_{\text{con}} = \begin{bmatrix} \delta \overline{\boldsymbol{q}}_{B_1}^T & \delta \overline{\boldsymbol{q}}_{B_2}^T & \delta \overline{\boldsymbol{q}}_{B_3}^T & \delta \boldsymbol{q}_H^T & \delta \boldsymbol{q}_S^T \end{bmatrix}^T \tag{3.71a}$$

$$\delta \boldsymbol{\gamma}_{\boldsymbol{q}} = \begin{bmatrix} \delta \boldsymbol{\gamma}_{B_1}^T & \delta \boldsymbol{\gamma}_{B_2}^T & \delta \boldsymbol{\gamma}_{B_3}^T & \delta \boldsymbol{\gamma}_S^T \end{bmatrix}^T \tag{3.71b}$$

where

- $\delta \overline{\boldsymbol{q}}_{B_1}$, $\delta \overline{\boldsymbol{q}}_{B_2}$, $\delta \overline{\boldsymbol{q}}_{B_3}$, defined as in (3.28), are the auxiliary generalized coordinates of beam nodes for the three blades, respectively.

- $\delta \boldsymbol{q}_H$ are the generalized coordinates of the hub expressed in the mixed basis, as defined in (3.37).

- $\delta \boldsymbol{q}_S$ are the generalized coordinates of the remaining coaxial rotating components and the stationary parts, including the bedplate, nacelle, and tower.

- $\delta \boldsymbol{\gamma}_{B_1}$, $\delta \boldsymbol{\gamma}_{B_2}$, $\delta \boldsymbol{\gamma}_{B_3}$ are the Lagrange multipliers of the joints associated with the three blades, respectively, including the rheonomic revolute joints between the pitch bearings and the blade root nodes, as well as the fixed joints between the pitch bearings and the hub.

- $\delta \boldsymbol{\gamma}_S$ are the Lagrange multipliers of the remaining joints in the dynamic model.

Although the linearized DAEs in (3.69) are described within consistent reference frames, they still depend on the azimuthal positions of the three blades, resulting in a time-dependent system. To eliminate this dependency, the Multi-Blade Coordinate (MBC) transformation is introduced, converting the system into a Linear Time-Invariant (LTI) form suitable for modal analysis.

3.4.1 MBC transformation

The MBC transformations are applied to both the generalized coordinates $\delta \boldsymbol{q}_{\text{con}}$ and the Lagrange multipliers $\delta \boldsymbol{\gamma}_{\boldsymbol{q}}$, as follows

$$\delta \boldsymbol{q}_{\text{con}} = \boldsymbol{T}_{\boldsymbol{q}}(t)\, \delta \boldsymbol{z} \tag{3.72a}$$

$$\delta \boldsymbol{\gamma}_{\boldsymbol{q}} = \boldsymbol{T}_{\gamma}(t)\, \delta \boldsymbol{\gamma}_{\boldsymbol{z}} \tag{3.72b}$$

where $\boldsymbol{T_q}(t)$ and $\boldsymbol{T_\gamma}(t)$ are transformation matrices dependent on time, given by

$$\boldsymbol{T_q}(t) = \begin{bmatrix} \boldsymbol{I}_{n_b} & \boldsymbol{I}_{n_b}\cos(\psi_1) & \boldsymbol{I}_{n_b}\sin(\psi_1) & \boldsymbol{0} \\ \boldsymbol{I}_{n_b} & \boldsymbol{I}_{n_b}\cos(\psi_2) & \boldsymbol{I}_{n_b}\sin(\psi_2) & \boldsymbol{0} \\ \boldsymbol{I}_{n_b} & \boldsymbol{I}_{n_b}\cos(\psi_3) & \boldsymbol{I}_{n_b}\sin(\psi_3) & \boldsymbol{0} \\ \boldsymbol{0} & \boldsymbol{0} & \boldsymbol{0} & \boldsymbol{I}_{n_s} \end{bmatrix} \tag{3.73a}$$

$$\boldsymbol{T_\gamma}(t) = \begin{bmatrix} \boldsymbol{I}_{12} & \boldsymbol{I}_{12}\cos(\psi_1) & \boldsymbol{I}_{12}\sin(\psi_1) & \boldsymbol{0} \\ \boldsymbol{I}_{12} & \boldsymbol{I}_{12}\cos(\psi_2) & \boldsymbol{I}_{12}\sin(\psi_2) & \boldsymbol{0} \\ \boldsymbol{I}_{12} & \boldsymbol{I}_{12}\cos(\psi_3) & \boldsymbol{I}_{12}\sin(\psi_3) & \boldsymbol{0} \\ \boldsymbol{0} & \boldsymbol{0} & \boldsymbol{0} & \boldsymbol{I}_{n_c} \end{bmatrix} \tag{3.73b}$$

in which n_b is the number of DOFs corresponding to one blade, including the pitch bearing; n_s is the number of the remaining DOFs in the entire model, including the coaxial components and stationary parts; n_c is the number of constraints associated with the Lagrange multipliers $\delta\boldsymbol{\gamma}_S$. $\boldsymbol{I}_{n_b}$, $\boldsymbol{I}_{n_s}$, $\boldsymbol{I}_{n_c}$ and $\boldsymbol{I}_{12}$ are identity matrices of corresponding sizes.

The azimuthal angles of three blades can be expressed as

$$\psi_i = \Omega t + \frac{2\pi}{3}(i-1), \qquad i = 1, 2, 3 \tag{3.74}$$

where Ω is the mean rotational speed of the rotor, specified as an input parameter in the linearization and modal analysis.

The MBC transformations presented in (3.72) convert the physical coordinates into the generalized multi-blade coordinates expressed in the inertial frame, facilitating the modal analysis and the interpretation on the modal dynamics.

By introducing three auxiliary matrices [112]

$$\boldsymbol{S} = \begin{bmatrix} \boldsymbol{0}_{n_b} & \boldsymbol{0}_{n_b} & \boldsymbol{0}_{n_b} & \boldsymbol{0} \\ \boldsymbol{0}_{n_b} & \boldsymbol{0}_{n_b} & \Omega\boldsymbol{I}_{n_b} & \boldsymbol{0} \\ \boldsymbol{0}_{n_b} & -\Omega\boldsymbol{I}_{n_b} & \boldsymbol{0}_{n_b} & \boldsymbol{0} \\ \boldsymbol{0} & \boldsymbol{0} & \boldsymbol{0} & \boldsymbol{0}_{n_s} \end{bmatrix} \tag{3.75a}$$

$$\boldsymbol{\mu_q} = \begin{bmatrix} \frac{1}{3}\boldsymbol{I}_{n_b} & \boldsymbol{0} & \boldsymbol{0} & \boldsymbol{0} \\ \boldsymbol{0} & \frac{2}{3}\boldsymbol{I}_{n_b} & \boldsymbol{0} & \boldsymbol{0} \\ \boldsymbol{0} & \boldsymbol{0} & \frac{2}{3}\boldsymbol{I}_{n_b} & \boldsymbol{0} \\ \boldsymbol{0} & \boldsymbol{0} & \boldsymbol{0} & \boldsymbol{I}_{n_s} \end{bmatrix}, \quad \boldsymbol{\mu_\gamma} = \begin{bmatrix} \frac{1}{3}\boldsymbol{I}_{12} & \boldsymbol{0} & \boldsymbol{0} & \boldsymbol{0} \\ \boldsymbol{0} & \frac{2}{3}\boldsymbol{I}_{12} & \boldsymbol{0} & \boldsymbol{0} \\ \boldsymbol{0} & \boldsymbol{0} & \frac{2}{3}\boldsymbol{I}_{12} & \boldsymbol{0} \\ \boldsymbol{0} & \boldsymbol{0} & \boldsymbol{0} & \boldsymbol{I}_{n_c} \end{bmatrix} \tag{3.75b}$$

the transformation matrices $\boldsymbol{T_q}$ and $\boldsymbol{T_\gamma}$ have the following properties:

$$\begin{aligned} \dot{\boldsymbol{T}}_{\boldsymbol{q}} &= \boldsymbol{T_q}\boldsymbol{S} & \boldsymbol{T}_{\boldsymbol{q}}^{-1} &= \boldsymbol{\mu_q}\boldsymbol{T}_{\boldsymbol{q}}^{T} \\ \ddot{\boldsymbol{T}}_{\boldsymbol{q}} &= \boldsymbol{T_q}\boldsymbol{S}^2 & \boldsymbol{T}_{\boldsymbol{\gamma}}^{-1} &= \boldsymbol{\mu_\gamma}\boldsymbol{T}_{\boldsymbol{\gamma}}^{T} \end{aligned} \tag{3.76}$$

Applying time derivatives to (3.72a), and utilizing the properties (3.76), yields

$$\delta\dot{\boldsymbol{q}}_{\mathrm{con}} = \boldsymbol{T}_{\boldsymbol{q}}\boldsymbol{S}\delta\boldsymbol{z} + \boldsymbol{T}_{\boldsymbol{q}}\delta\dot{\boldsymbol{z}} \tag{3.77a}$$

$$\delta\ddot{\boldsymbol{q}}_{\mathrm{con}} = \boldsymbol{T}_{\boldsymbol{q}}\boldsymbol{S}^2\delta\boldsymbol{z} + 2\boldsymbol{T}_{\boldsymbol{q}}\boldsymbol{S}\delta\dot{\boldsymbol{z}} + \boldsymbol{T}_{\boldsymbol{q}}\delta\ddot{\boldsymbol{z}} \tag{3.77b}$$

Substituting the coordinate transformations from (3.72) and (3.77) into the linearized DAEs (3.69), and subsequently left-multiplying (3.69a) by $\boldsymbol{T}_{\boldsymbol{q}}^{-1}$, and (3.69b) by $\boldsymbol{T}_{\gamma}^{-1}$, the linearized DAEs in the multi-blade coordinates are obtained as

$$\begin{cases} \boldsymbol{M}_{\boldsymbol{z}}\delta\ddot{\boldsymbol{z}} + \boldsymbol{D}_{\boldsymbol{z}}\delta\dot{\boldsymbol{z}} + \boldsymbol{K}_{\boldsymbol{z}}\delta\boldsymbol{z} + \boldsymbol{C}_{\boldsymbol{q}_{\boldsymbol{z}}}^{T}\delta\boldsymbol{\gamma}_{\boldsymbol{z}} = \boldsymbol{0} & (3.78a) \\ \boldsymbol{C}_{\boldsymbol{q}_{\boldsymbol{\gamma}}}\delta\boldsymbol{z} = \boldsymbol{0} & (3.78b) \end{cases}$$

where four intermediate matrices are introduced as follows

$$\begin{aligned} \boldsymbol{M}_{\mathrm{T}} &= \boldsymbol{\mu}_{\boldsymbol{q}}\boldsymbol{T}_{\boldsymbol{q}}^{T}\boldsymbol{M}_{\mathrm{con}}\boldsymbol{T}_{\boldsymbol{q}} & \boldsymbol{K}_{\mathrm{T}} &= \boldsymbol{\mu}_{\boldsymbol{q}}\boldsymbol{T}_{\boldsymbol{q}}^{T}\boldsymbol{K}_{\mathrm{con}}\boldsymbol{T}_{\boldsymbol{q}} \\ \boldsymbol{D}_{\mathrm{T}} &= \boldsymbol{\mu}_{\boldsymbol{q}}\boldsymbol{T}_{\boldsymbol{q}}^{T}\boldsymbol{D}_{\mathrm{con}}\boldsymbol{T}_{\boldsymbol{q}} & \boldsymbol{C}_{\boldsymbol{q}_{\mathrm{T}}} &= \boldsymbol{T}_{\boldsymbol{\gamma}}^{T}\boldsymbol{C}_{\boldsymbol{q}_{\mathrm{con}}}\boldsymbol{T}_{\boldsymbol{q}} \end{aligned} \tag{3.79}$$

and the system matrices in the multi-blade coordinates are

$$\begin{aligned} \boldsymbol{M}_{\boldsymbol{z}} &= \boldsymbol{M}_{\mathrm{T}} & \boldsymbol{K}_{\boldsymbol{z}} &= \boldsymbol{M}_{\mathrm{T}}\boldsymbol{S}^2 + \boldsymbol{D}_{\mathrm{T}}\boldsymbol{S} + \boldsymbol{K}_{\mathrm{T}} \\ \boldsymbol{D}_{\boldsymbol{z}} &= 2\boldsymbol{M}_{\mathrm{T}}\boldsymbol{S} + \boldsymbol{D}_{\mathrm{T}} & \boldsymbol{C}_{\boldsymbol{q}_{\boldsymbol{z}}} &= \boldsymbol{C}_{\boldsymbol{q}_{\mathrm{T}}}\boldsymbol{\mu}_{\boldsymbol{q}}, \quad \boldsymbol{C}_{\boldsymbol{q}_{\boldsymbol{\gamma}}} = \boldsymbol{\mu}_{\boldsymbol{\gamma}}\boldsymbol{C}_{\boldsymbol{q}_{\mathrm{T}}} \end{aligned} \tag{3.80}$$

It is important to note that the Jacobian matrices of constraints in (3.78a) and (3.78b) are distinct, i.e., $\boldsymbol{C}_{\boldsymbol{q}_{\boldsymbol{z}}} \neq \boldsymbol{C}_{\boldsymbol{q}_{\boldsymbol{\gamma}}}$.

For wind turbine systems with isotropic rotors, the linearized DAEs (3.78) is time-invariant, and hence suitable for modal analysis.

3.4.2 Mode Interpretation

Referring to (2.179), based on the linearized DAEs in (3.78), the GEP can be set up as follows

$$\begin{bmatrix} \boldsymbol{0} & \boldsymbol{I} & \boldsymbol{0} \\ -\boldsymbol{K}_{\boldsymbol{z}} & -\boldsymbol{D}_{\boldsymbol{z}} & -\boldsymbol{C}_{\boldsymbol{q}_{\boldsymbol{z}}}^{T} \\ -\boldsymbol{C}_{\boldsymbol{q}_{\boldsymbol{\gamma}}} & \boldsymbol{0} & \boldsymbol{0} \end{bmatrix} \underline{\hat{\boldsymbol{\Phi}}}_{k} = \lambda_{k} \begin{bmatrix} \boldsymbol{I} & \boldsymbol{0} & \boldsymbol{0} \\ \boldsymbol{0} & \boldsymbol{M}_{\boldsymbol{z}} & \boldsymbol{0} \\ \boldsymbol{0} & \boldsymbol{0} & \boldsymbol{0} \end{bmatrix} \underline{\hat{\boldsymbol{\Phi}}}_{k} \tag{3.81}$$

where $\left(\lambda_k, \underline{\hat{\boldsymbol{\Phi}}}_{k}\right)$ are the eigenpairs of mode k.

The eigenvalue of mode k is generally a complex value:

$$\lambda_k = \sigma_k + \jmath\omega_{d_k} \tag{3.82}$$

where $\jmath = \sqrt{-1}$ is the imaginary unit.

By introducing the extended eigenvector of mode k as $\underline{\hat{\mathbf{\Phi}}}_k = \left[\mathbf{\Phi}_k^T, \lambda_k \mathbf{\Phi}_k^T, \boldsymbol{\xi}_k\right]^T$, the periodical motion in the multi-blade coordinates can be expressed as

$$\delta \boldsymbol{z} = \mathbf{\Phi}_k e^{\lambda_k t} \tag{3.83}$$

The eigenvector $\mathbf{\Phi}_k$ is composed of symmetric components $\mathbf{w}_0$, cosine components $\mathbf{w}_c$ and sine components $\mathbf{w}_s$ corresponding to the three blades, and the additional components $\mathbf{w}_g$, as shown below

$$\mathbf{\Phi}_k = \begin{bmatrix} \mathbf{w}_0 & \mathbf{w}_c & \mathbf{w}_s & \mathbf{w}_g \end{bmatrix}^T \tag{3.84}$$

where the four components are detailed as

$$\mathbf{w}_0 = \begin{bmatrix} \mathrm{w}_{0,1} & \mathrm{w}_{0,2} & \cdots & \mathrm{w}_{0,n_b} \end{bmatrix}^T \tag{3.85a}$$

$$\mathbf{w}_c = \begin{bmatrix} \mathrm{w}_{c,1} & \mathrm{w}_{c,2} & \cdots & \mathrm{w}_{c,n_b} \end{bmatrix}^T \tag{3.85b}$$

$$\mathbf{w}_s = \begin{bmatrix} \mathrm{w}_{s,1} & \mathrm{w}_{s,2} & \cdots & \mathrm{w}_{s,n_b} \end{bmatrix}^T \tag{3.85c}$$

$$\mathbf{w}_g = \begin{bmatrix} \mathrm{w}_{g,1} & \mathrm{w}_{g,2} & \cdots & \mathrm{w}_{g,n_s} \end{bmatrix}^T \tag{3.85d}$$

in which $\mathrm{w}_{0,j}$, $\mathrm{w}_{c,j}$, $\mathrm{w}_{s,j}$ and $\mathrm{w}_{g,j}$ are complex values.

Substituting (3.83) into the MBC transformation relation (3.72a), and recalling the MBC transformation matrix (3.73a) along with the representation of the generalized coordinates in the auxiliary reference frames H_i from (3.71a), the periodical motion of blade i in the physical coordinates can be expressed as

$$\delta \overline{\boldsymbol{q}}_{B_i} = e^{\lambda_k t} \left(\mathbf{w}_0 + \mathbf{w}_c \cos(\psi_i) + \mathbf{w}_s \sin(\psi_i)\right) \tag{3.86}$$

where $i = 1, 2, 3$ corresponds to the three blades, respectively.

From (3.86), it is evident that the symmetric components $\mathbf{w}_0$ directly contribute to the blade relative motion in the auxiliary reference frames H_i (which can be regarded as the blade root reference frames). In contrast, the cosine components $\mathbf{w}_c$ and sine components $\mathbf{w}_s$ contribute to the blade relative motion through modulation by the cosine and sine functions of the azimuthal angle ψ_i, respectively. This can be intuitively visualized, as depicted in Figure 3.9. The symmetric components $\mathbf{w}_0$, coupling with the drivetrain torsional mode, produce a circular reaction torque on the rotor system, while the cosine and sine components generate horizontal and vertical reaction forces on the rotor system, respectively. A conceptual interpretation of multi-blade coordinates in a three-bladed rotor system is that the motion is described in the inertial frame (also known as the ground-fixed frame) and decomposed into circular, horizontal, and vertical components.

Substituting the azimuthal angles (3.74) and the eigenvalue (3.82) into (3.86), using Euler's formula to proceed with the derivation, and subsequently extracting

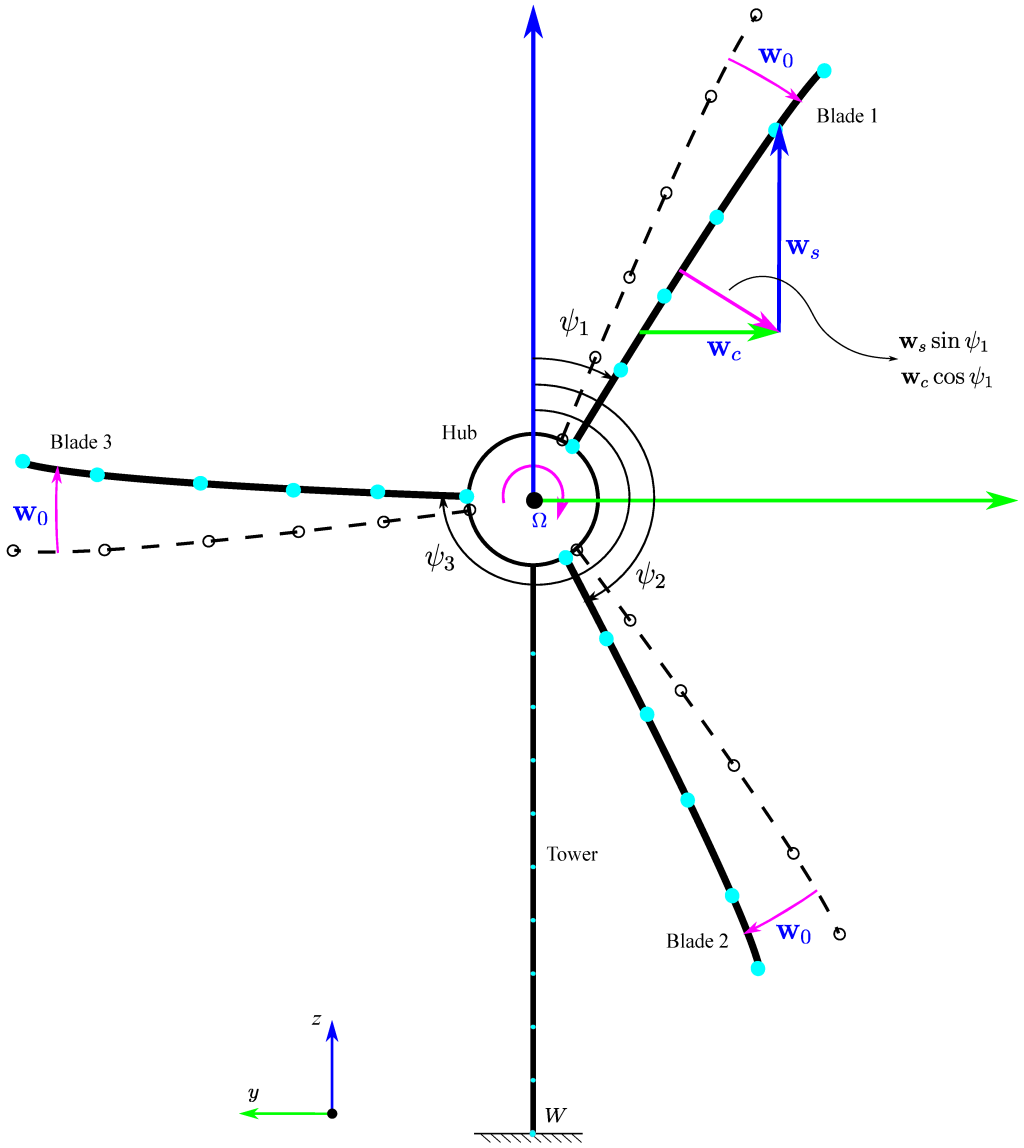

Figure 3.9: The symmetric ($\mathbf{w}_0$), cosine ($\mathbf{w}_c$), and sine ($\mathbf{w}_s$) components of the rotor's motion in the multi-bladed coordinates.

the real parts from the complex exponential forms, the periodical motion of blade i in the auxiliary reference frame H_i can be reformulated as

$$\begin{aligned}\delta\overline{\boldsymbol{q}}_{B_i} = e^{\sigma_k t}\,&\Big(\mathbf{A}_{\mathrm{COL}}\cos\left(\omega_{d_k}t+\boldsymbol{\phi}_{\mathrm{COL}}\right)\\ &+\mathbf{A}_{\mathrm{BW}}\cos\left((\omega_{d_k}+\Omega)t+\frac{2\pi}{3}(i-1)+\boldsymbol{\phi}_{\mathrm{BW}}\right)\\ &+\mathbf{A}_{\mathrm{FW}}\cos\left((\omega_{d_k}-\Omega)t-\frac{2\pi}{3}(i-1)+\boldsymbol{\phi}_{\mathrm{FW}}\right)\Big)\end{aligned} \tag{3.87}$$

where the amplitudes are evaluated as

$$\mathbf{A}_{\mathrm{COL}} = \|\mathbf{w}_0\| \tag{3.88a}$$

$$\mathbf{A}_{\mathrm{BW}} = \frac{1}{2}\|(\mathbf{w}_c - \jmath\mathbf{w}_s)\| \tag{3.88b}$$

$$\mathbf{A}_{\mathrm{FW}} = \frac{1}{2}\|(\mathbf{w}_c + \jmath\mathbf{w}_s)\| \tag{3.88c}$$

and the phase angles are computed as

$$\boldsymbol{\phi}_{\mathrm{COL}} = \tan^{-1}\frac{\mathrm{Im}\,(\mathbf{w}_0)}{\mathrm{Re}\,(\mathbf{w}_0)} \tag{3.89a}$$

$$\boldsymbol{\phi}_{\mathrm{BW}} = \tan^{-1}\frac{\mathrm{Im}\,(\mathbf{w}_c) - \mathrm{Re}\,(\mathbf{w}_s)}{\mathrm{Re}\,(\mathbf{w}_c) + \mathrm{Im}\,(\mathbf{w}_s)} \tag{3.89b}$$

$$\boldsymbol{\phi}_{\mathrm{FW}} = \tan^{-1}\frac{\mathrm{Im}\,(\mathbf{w}_c) + \mathrm{Re}\,(\mathbf{w}_s)}{\mathrm{Re}\,(\mathbf{w}_c) - \mathrm{Im}\,(\mathbf{w}_s)} \tag{3.89c}$$

In (3.87), the modal frequency ω_{d_k} is measured in the ground-fixed frame, as it is obtained by solving the GEP in (3.81).

From (3.87), we can see that the blade relative motion observed in the blade root reference frame consists of three components: a collective component where all blades deflect in phase with an amplitude of $\mathbf{A}_{\mathrm{COL}}$, and two asymmetric components where the blades vibrate with phase shifts of $2\pi/3$ and amplitudes of $\mathbf{A}_{\mathrm{BW}}$ and $\mathbf{A}_{\mathrm{FW}}$. When the amplitude $\mathbf{A}_{\mathrm{COL}}$ dominates, the mode k is referred to as the *rotor collective mode*, with its modal frequency denoted as ω_{COL}. If $\mathbf{A}_{\mathrm{BW}}$ dominates, it is termed the *rotor backward whirling mode*, with a modal frequency of ω_{BW}. Conversely, if $\mathbf{A}_{\mathrm{FW}}$ dominates, it is called the *rotor forward whirling mode*, with the modal frequency denoted as ω_{FW}. Regardless of which component is dominant, the blade vibration in the blade root reference frame includes contributions from all three modes simultaneously.

From (3.88), it is evident that the amplitude of the rotor collective mode corresponds directly to the symmetric components $\mathbf{w}_0$ in the multi-blade coordinates. In contrast, the amplitudes of the rotor edgewise backward and forward whirling modes stem from contributions of both the cosine and sine components within the multi-blade coordinates.

For the rotor edgewise collective mode, the vibration frequency measured in both the ground-fixed frame and the blade root reference frame is identical, i.e., $\omega_{\mathrm{COL}} = \omega_{d_k}$. In this mode, the blade edgewise vibration frequency in the blade root reference frame differs from the isolated blade frequency ω_{E}, which might be identified from a modal test on a blade test rig, due to the coupling between the rotor and drivetrain. In engineering practice, the rotor edgewise collective mode is often labeled as the drivetrain torsional mode, particularly for systems with a gearbox transmission.

For the rotor edgewise backward and forward whirling modes, the vibration frequencies observed in the blade root reference frame are close to the isolated blade edgewise frequency ω_{E}, i.e., $\omega_{\mathrm{BW}}+\Omega \approx \omega_{\mathrm{E}}$ and $\omega_{\mathrm{FW}}-\Omega \approx \omega_{\mathrm{E}}$, leading to the approximations $\omega_{\mathrm{BW}} \approx \omega_{\mathrm{E}}-\Omega$ and $\omega_{\mathrm{FW}} \approx \omega_{\mathrm{E}}+\Omega$. In fact, the frequency difference between the rotor edgewise backward and forward whirling modes is exactly 2Ω, while their central frequency is $\omega_{\mathrm{Cen}} = \frac{1}{2}(\omega_{\mathrm{BW}}+\omega_{\mathrm{FW}}) \approx \omega_{\mathrm{E}}$. The deviation between the central frequency ω_{Cen} and the isolated blade edgewise frequency ω_{E} arises from the effects of geometric stiffness $\boldsymbol{K}_g$, inertial stiffness $\boldsymbol{K}_i$, and the coupling with the hub, drivetrain, and tower.

Additionally, from (3.87), we observe that the envelope of the blade vibration measured in the blade root reference frame depends on the damping factor σ_k. The vibration amplitude will increase exponentially if σ_k is positive, in which case the damping ratio $\zeta_k = -\sigma_k/\sqrt{\sigma_k^2+\omega_{d_k}^2}$ is negative.

The rotor edgewise collective mode can be identified through drivetrain measurements, such as generator rotational speed or main shaft torque signals. In contrast, the rotor edgewise backward and forward whirling modes are more easily detected in tower measurements, for instance, through tower top acceleration or tower bottom moment signals in the side-side direction.

Finally, the collective, backward, and forward whirling modes can also be distinguished by analyzing the phase relationships in the time series of blade root signals, such as the blade root edgewise moment. As illustrated in Figure 3.10, the blade vibration signals, measured in the blade root reference frame, exhibit distinct phase patterns for each mode. In the rotor collective mode, the signals are in phase. For those rotors rotating in clockwise direction, the backward whirling mode exhibits a phase sequence of $1-3-2-1-3-2\cdots$, while the forward whirling mode follows a sequence of $1-2-3-1-2-3\cdots$. These characteristic phase relationships between the three blades provide a straightforward method for identifying the collective, backward whirling, and forward whirling modes.

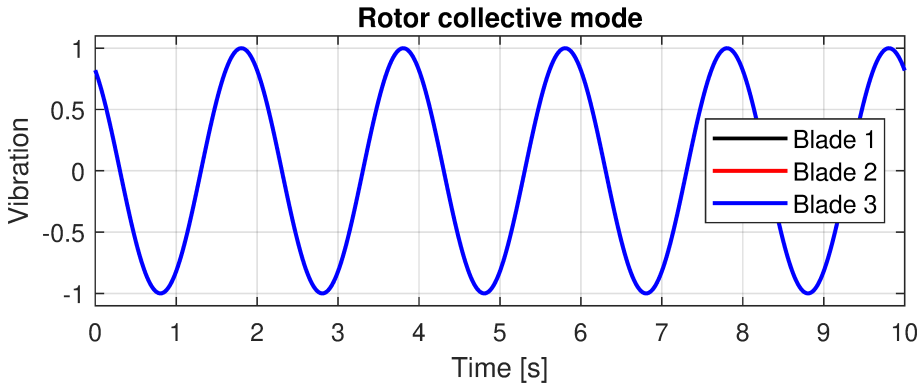

(a) In-phase vibration of the three blades in the rotor collective mode.

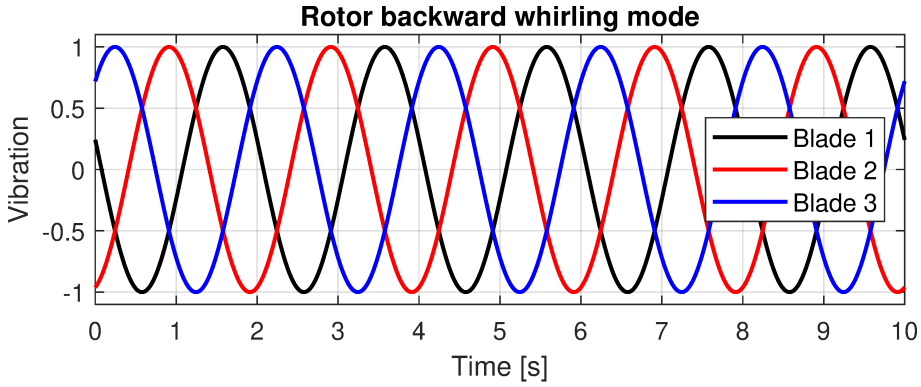

(b) Phase sequence of $1-3-2-1-3-2\cdots$ for the three blades in the rotor backward whirling mode.

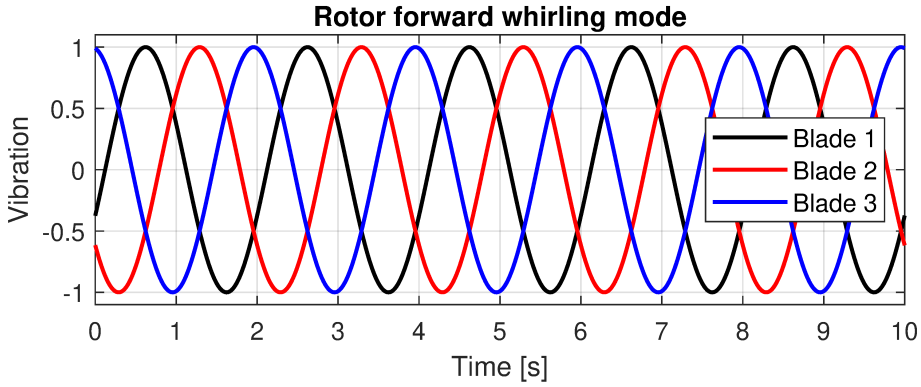

(c) Phase sequence of $1-2-3-1-2-3\cdots$ for the three blades in the rotor forward whirling mode.

Figure 3.10: Blade vibration signals for the rotor collective, backward whirling, and forward whirling modes, measured in the blade root reference frame for a clockwise-rotating rotor.

Chapter 4

Stability analysis

In Chapter (3), a linearization procedure and eigenvalue analysis method for multi-bladed rotor systems are developed. This chapter applies the proposed method to the eigenvalue problem of a free-rotating three-bladed rotor, with particular emphasis on the rotor's free rotation mode, as this is relevant to the state-space representation of wind turbines and, by extension, to controller design. A comprehensive verification and validation analysis of the proposed aeroelastic stability assessment using the eigenvalue approach is then presented. The analysis begins with a steady-state aeroelastic comparison using an open-source reference wind turbine, followed by a modal analysis to demonstrate the aeroelastic stability assessment. Next, the aeroelastic stability predictions are verified through a series of virtual wind turbine simulations, where the blade torsional stiffness is scaled. These predictions are then validated against experimental measurements from two offshore prototype wind turbines. Finally, the chapter concludes with a summary of the key findings and conclusions.

4.1 Eigenvalues of a rotor's free rotation mode

A multi-bladed rotor system inherently possesses a rotational DOF about its axis. For instance, wind turbines and helicopter rotors can rotate freely, allowing the exchange of kinetic energy between the rotor structure and the surrounding airflow. This rotational DOF introduces the so-called *rigid body mode*, also referred to as the *free-free mode*, which is commonly assumed to have zero eigenvalues [87]. However, our analysis indicates that these eigenvalues are not necessarily zero; therefore, we refer to this as the *free rotation mode*.

In controller design, the linearized equations of motion are crucial for representing controlled systems. The accuracy of linearizing the nonlinear dynamics system can significantly impact the controller's performance and robustness. In the case of

wind turbines, the near-zero frequency bandwidth, which corresponds to the overall rotational characteristics of the rotor system, is particularly important for the controller design to stabilize the rotor speed and optimize the power capture [101]. The transfer functions within this bandwidth are directly related to the eigenvalues of the free rotation mode in the rotor dynamics.

El-Absy [74] investigated the stability of the rigid body mode of a rotating rotor through time-marching simulations. The study examined simple rotor models, with and without the effects of longitudinal displacement due to bending, in the inertia and elastic forces. The results demonstrated that the geometric centrifugal stiffening term in the inertia forces is not essential for achieving a stable solution. However, the focus was primarily on the beam displacement time series, and the eigenvalues were not explicitly reported.

Numerous studies have investigated the stability of multi-bladed rotor systems, though most [28, 117, 87, 88, 248] have focused on higher-order modes, particularly the rotor's bending modes, which are critical in rotor design for avoiding potential resonances and instabilities. Both the centrifugal stiffening effect in rotating beams [136, 135] and the centrifugal softening effect [88, 265, 296] have been extensively studied for their influence on rotor modal dynamics.

In this section, we investigate the eigenvalues of a rotor's free rotation mode through a series of numerical experiments on rotors with increasing complexity. For all experiments discussed in this section, gravitational forces are not considered. The impacts of the geometric stiffness matrix, inertial stiffness matrix, and tangent stiffness matrix of constraints on the eigenvalues of the free rotation mode are thoroughly examined.

4.1.1 Single rigid body

The investigation begins with the analysis of a single rotating rigid body.

We first recall the *intermediate axis theorem*, also known as the *tennis racket theorem*, which addresses the dynamics of a freely rotating rigid body with three distinct principal moments of inertia. According to this theorem, rotation around the body's minor and major principal axes is stable, while rotation about the intermediate principal axis is unstable [162]. This theorem provides a fundamental reference for the eigenvalue analysis of rotating bodies.

For a single rotating rigid body, the mass matrix is expressed as

$$\boldsymbol{M} = \begin{bmatrix} \nu \boldsymbol{I}_{3\times 3} & \boldsymbol{0} \\ \boldsymbol{0} & \boldsymbol{J}_l \end{bmatrix} \tag{4.1}$$

where ν represents the mass, and $\boldsymbol{J}_l = \operatorname{diag}[J_{xx}, J_{yy}, J_{zz}]$ is the inertia tensor in the local frame, with J_{xx}, J_{yy}, J_{zz} denoting the moments of inertia about the three principal axes, respectively. Assuming the rotating center coincides with the mass center, the off-diagonal term J_{yz} is zero.

Referring to (2.137), the damping and stiffness matrices are read as

$$\boldsymbol{D} = \begin{bmatrix} \mathbf{0} & \mathbf{0} \\ \mathbf{0} & \widetilde{\boldsymbol{\omega}}_l \boldsymbol{J}_l - \widetilde{\boldsymbol{J}_l \boldsymbol{\omega}_l} \end{bmatrix} \tag{4.2a}$$

$$\boldsymbol{K} = \mathbf{0} \tag{4.2b}$$

where $\boldsymbol{\omega}_l = [\omega_x, \omega_y, \omega_z]^T$ is the local angular velocity vector.

The eigenvalues are examined for two cases: (1) free rotation about all three axes, and (2) free rotation constrained to the X axis. The Jacobian matrix of constraints is computed based on the corresponding joints, following the algorithm presented in Section 2.5.

Free rotation about all three axes

In this case, the rigid body is set to rotate freely about all three axes. The corresponding eigenvalues are presented in Table 4.1.

When the three principal moments of inertia are distinct, with $J_{xx} > J_{yy} > J_{zz}$, the eigenvalues for rotation about the X axis (the major principal axis) and the Z axis (the minor principal axis) are a pair of pure imaginary numbers, indicating constant-amplitude oscillations. In contrast, the eigenvalues for rotation about the Y axis (the intermediate principal axis) are real, suggesting unstable motion. This result is consistent with the intermediate axis theorem.

In the case where the moments of inertia satisfy the relation $J_{xx} = 2J_{yy} = 2J_{zz}$, which mimics an isotropic three-bladed rigid rotor, the eigenvalues for rotation about the X axis (the major principal axis, which also serves as the rotor's axis of rotation) are a pair of pure imaginary numbers, with a natural frequency equal to the angular velocity π. The eigenvalues for rotation about the Y and Z axes are zero, indicating no unstable modes.

Table 4.1: Eigenvalues of a single rigid body undergoing free rotation about three axes. Only two eigenvalues are presented, as the remaining four eigenvalues are all zero.

Subcase	ν [kg]	J_{xx}	J_{yy}	J_{zz} [kgm^2]	ω_x	ω_y	ω_z [rad/s]	λ
$J_{xx} > J_{yy} > J_{zz}$	1.3	5.7	3.3	1.9	π	0	0	$\pm 3.79\jmath$
					0	π	0	± 1.75
					0	0	π	$\pm 1.67\jmath$
$J_{xx} = 2J_{yy} = 2J_{zz}$	1.3	5.7	2.85	2.85	π	0	0	$\pm\pi\jmath$
					0	π	0	$0, 0$
					0	0	π	$0, 0$

Free rotation constrained to the X axis

In this case, the rigid body is constrained to rotate exclusively about the X axis. The rotational DOFs around the Y and Z axes are restricted by a revolute joint. Consequently, the eigenvalues are zero, as presented in Table 4.2.

Table 4.2: Eigenvalues of a single rigid body subjected to free rotation constrained to the X axis.

Subcase	ν [kg]	J_{xx}	J_{yy} [kgm^2]	J_{zz}	ω_x	ω_y [rad/s]	ω_z	λ
$J_{xx} > J_{yy} > J_{zz}$	1.3	5.7	3.3	1.9	π	0	0	0, 0
$J_{xx} = 2J_{yy} = 2J_{zz}$	1.3	5.7	2.85	2.85	π	0	0	0, 0

4.1.2 Rigid rotor

An ideal isotropic rigid rotor is examined as the second model. As illustrated in Figure 4.1, the rigid rotor consists of four rigid bodies: the hub H, located at the center of rotation, and three bearings P_1, P_2, P_3, which are equally distributed at the same radial distance along the azimuthal positions. The bearings are connected to the hub via three fixed joints C_1, C_2, C_3, respectively. Additionally, the hub is anchored to the ground by joint C_R, which allows for the adjustment of its rotational DOFs, enabling either free rotation about all three axes or constrained to the X axis.

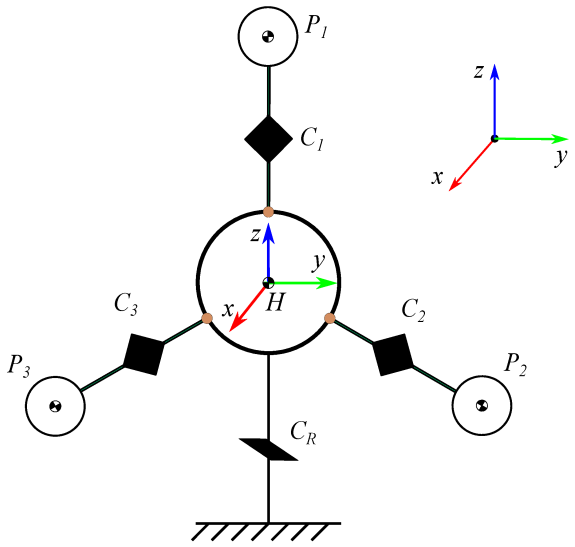

Figure 4.1: Schematic representation of a three-bladed rigid rotor.

The moments of inertia of the hub and bearings are set to zero to facilitate comparison with the single rigid body model. The masses of the hub and bearing are specified as 629 kg and 2222 kg, respectively, with a radius of 0.2 m between the hub and the bearings.

Since the rigid rotor does not incorporate any flexible finite elements, both the material stiffness matrix $\boldsymbol{K}_m$ and the geometric stiffness matrix $\boldsymbol{K}_g$ are absent. The impact of the inertial stiffness matrix $\boldsymbol{K}_i$, inertial damping matrix $\boldsymbol{D}_i$, and the constraint tangent stiffness matrix $\boldsymbol{K}_c$ on the eigenvalues is investigated by selectively including or excluding these matrices in the linearized DAEs (3.78).

Similarly, two cases with different rotational constraints are analyzed.

Table 4.3: Eigenvalues of a three-bladed rigid rotor. The '×' symbol denotes the inclusion of the corresponding matrix. For the case of free rotation about all three axes, the additional four eigenvalues are zero and therefore omitted.

Subcase	$\boldsymbol{K}_i$	$\boldsymbol{D}_i$	$\boldsymbol{K}_c$	ω_x	λ
Free rotation about all three axes		×		0	$0, 0$
				π	$\pm\pi\jmath$
	×	×	×	0	$0, 0$
				π	$\pm\pi\jmath$
Free rotation constrained to the X axis		×		0	$0, 0$
				π	$0, 0$
		×	×	0	$0, 0$
				π	$\pm\pi\jmath$
	×	×		0	$0, 0$
				π	$\pm\pi$
	×	×	×	0	$0, 0$
				π	$0, 0$

Since the ideal rigid rotor can be represented as a single rigid body characterized by the relationship $J_{xx} = 2J_{yy} = 2J_{zz}$, its eigenvalues should match those presented in Tables 4.1 and 4.2.

As shown in Table 4.3, when the rotational speed about the X axis is zero, both the centrifugal forces and gyroscopic torques vanish. Consequently, the matrices $\boldsymbol{K}_i, \boldsymbol{D}_i, \boldsymbol{K}_c$ reduce to zero, resulting in zero eigenvalues for both constraint conditions.

When the rotational speed is π, in the case of free rotation about all three axes, including the inertial damping matrix $\boldsymbol{D}_i$ results in eigenvalues of $\pm\pi\jmath$, meaning the natural frequency equals the rotational speed, which is consistent with the results in Table 4.1. In this scenario, the matrices $\boldsymbol{K}_i, \boldsymbol{K}_c$ must either be both included or both excluded; otherwise, the eigenvalues deviate from $\pm\pi\jmath$, producing erroneous results, which are not presented in Table 4.3 for the sake of clarity.

For free rotation constrained to the X axis with a rotational speed of π, if $\boldsymbol{D}_i$ is included and $\boldsymbol{K}_i, \boldsymbol{K}_c$ are either both absent or both present, the eigenvalues are zero, which is consistent with the results in Table 4.2. If only $\boldsymbol{K}_c$ is included along with $\boldsymbol{D}_i$, the eigenvalues become $\pm\pi\jmath$; if only $\boldsymbol{K}_i$ is included with $\boldsymbol{D}_i$, the eigenvalues shift to $\pm\pi$,

The tangent stiffness matrix of constraints $\boldsymbol{K}_c$ moves the eigenvalues away from zero along the imaginary axis, indicating a stiffening effect, whereas the inertial stiffness matrix $\boldsymbol{K}_i$ moves the eigenvalues away from zero along the real axis, indicating a softening effect. For the rigid rotor, the stiffening effect of $\boldsymbol{K}_c$ and the softening effect of $\boldsymbol{K}_i$ can fully counterbalance each other.

The agreement between the results in Table 4.3 and Tables 4.1 and 4.2 demonstrates that the formulation of linearization and eigenvalue problem presented in Chapter 3 are applicable to the eigenvalue analysis of three-bladed rotors.

4.1.3 Flexible rotor

In this case, three flexible blades are attached to the bearings via fixed joints, producing a structure that resembles a wind turbine rotor. Each blade features a straight geometry with a constant rectangular cross-section measuring $0.6\,\mathrm{m} \times 0.2\,\mathrm{m}$ and a total length of $6.0\,\mathrm{m}$. The blades are constructed from steel, characterized by an elastic modulus of $E = 2.1 \times 10^{11}\,\mathrm{Pa}$, a Poisson's ratio of $\mu = 0.3$, and a density of $\rho = 7800\,\mathrm{kg/m^3}$. Figure 4.2 presents a schematic of the flexible rotor.

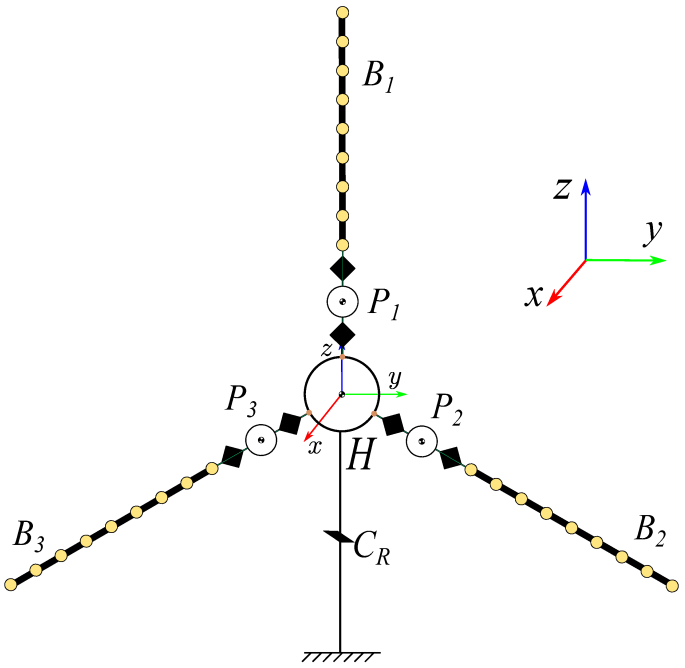

Figure 4.2: Schematic representation of a three-bladed flexible rotor.

Each blade is discretized into 10 Euler–Bernoulli beam elements. Two scenarios, with and without external forces, are examined. Only the eigenvalues corresponding to the rotor's free rotational mode are presented. The stiffening and softening effects of various stiffness terms are analyzed, followed by a parameter sweep to investigate the influence of the amplitudes of rotational speed and external forces.

Absence of external forces

In the absence of external forces acting on the blades, the eigenvalues of the rotor under two different constraint conditions are presented in Table 4.4.

Table 4.4: Eigenvalues of a three-bladed flexible rotor in the absence of external forces. The symbol '×' denotes that the corresponding matrix is included. The material stiffness matrix $\boldsymbol{K}_m$ is included in all cases.

Subcase	$\boldsymbol{K}_g$	$\boldsymbol{K}_i$	$\boldsymbol{D}_i$	$\boldsymbol{K}_c$	ω_x	λ		
Free rotation about all three axes			×		0	$0,0$	$0,0$	$0,0$
					π	$\pm\pi\jmath$	± 0.0063	$\pm 0.0139\jmath$
	×	×	×	×	0	$0,0$	$0,0$	$0,0$
					π	$\pm\pi\jmath$	± 0.0108	$\pm 0.0141\jmath$
Free rotation constrained to the X axis			×		0	$0,0$		
					π	± 0.0081		
	×		×		0	$0,0$		
					π	$\pm 3.0598\jmath$		
		×	×		0	$0,0$		
					π	± 3.1380		
			×	×	0	$0,0$		
					π	$\pm 0.6964\jmath$		
	×	×	×	×	0	$0,0$		
					π	$\pm 0.0072\jmath$		

When the rotational speed is π, for the case of free rotation about all three axes, the expected eigenvalues of $\pm\pi\jmath$ appear, while the remaining four eigenvalues deviate into two pairs of real and pure imaginary numbers with small magnitudes, likely due to numerical errors.

In the case of free rotation constrained to the X axis at a rotational speed of π, if only $\boldsymbol{D}_i$ is included, the eigenvalues shift to a pair of small real values, ± 0.0081. In contrast, when all four matrices $\boldsymbol{K}_g, \boldsymbol{K}_i, \boldsymbol{D}_i, \boldsymbol{K}_c$ are included, the eigenvalues become a pair of small pure imaginary numbers, $\pm 0.0072\jmath$. These results are considered to stem from numerical errors.

When either $\boldsymbol{K}_g$ or $\boldsymbol{K}_c$ are included alongside $\boldsymbol{D}_i$, the eigenvalues shift to a pair of imaginary numbers, indicating that $\boldsymbol{K}_g$ and $\boldsymbol{K}_c$ contribute a stiffening effect.

In contrast, when $\boldsymbol{K}_i$ is included with $\boldsymbol{D}_i$, the eigenvalues become a pair of real numbers, suggesting that $\boldsymbol{K}_i$ imparts a softening effect. For the flexible rotor without external forces, the stiffening effects of $\boldsymbol{K}_g$ and $\boldsymbol{K}_c$ and the softening effect of $\boldsymbol{K}_i$ appear to counteract each other completely.

Presence of external forces

In this case, out-of-plane forces of $\boldsymbol{F}_x = 725\,630.0\,\mathrm{N}$ and in-plane forces of $\boldsymbol{F}_y = 439\,010.0\,\mathrm{N}$ are applied, equally distributed across the blade nodes to mimic the aerodynamic loads on the rotor. These forces follow the orientation of the blade nodes as the rotor deflects, and are referred to as *follower forces*.

In the quasi-static equilibrium analysis, the hub is initially locked. Subsequently, the rotational DOF about the X axis is released for the eigenvalue analysis.

Since the wind turbine rotor has only one rigid-body motion DOF, i.e., rotation about the X axis, the case of free rotation about all three axes is not discussed here.

The out-of-plane and in-plane deflections of the blade tip for a rotational speed of $0\,\mathrm{rad/s}$ are $0.24\,\mathrm{m}$ and $0.016\,\mathrm{m}$, respectively. The ratio of these deflections to the blade length is less than $5\,\%$, indicating that the deflections remain within the range of small deformations.

The eigenvalues corresponding to the free rotation mode of the flexible rotor under external follower forces are presented in Table 4.5.

Table 4.5: Eigenvalues of a three-bladed flexible rotor under external follower forces. The symbol '×' denotes that the corresponding matrix is included. The material stiffness matrix $\boldsymbol{K}_m$ is included in all cases.

Subcase	$\boldsymbol{K}_g$	$\boldsymbol{K}_i$	$\boldsymbol{D}_i$	$\boldsymbol{K}_c$	ω_x	λ
Free rotation constrained to the X axis			×		0	$0, -0.0002$
					π	± 0.0002
	×		×		0	± 0.7034
					π	$\pm 2.9768\jmath$
		×	×		0	± 0.0001
					π	± 3.1379
			×	×	0	± 0.2800
					π	$\pm 0.6388\jmath$
	×	×	×	×	0	± 0.7570
					π	± 0.7598

When only $\boldsymbol{D}_i$ is included, the eigenvalues are near zero, with any deviation attributed to numerical errors.

When $\boldsymbol{K}_g$ is incorporated along with $\boldsymbol{D}_i$, for $\omega_x = 0$, the eigenvalues shift from near zero to a pair of real numbers ± 0.7034, indicating that the geometric stiffness term, induced by the transverse external follower forces $\boldsymbol{F}_x$ and $\boldsymbol{F}_y$, has a softening effect. For $\omega_x = \pi$, the eigenvalues become pure imaginary numbers $\pm 2.9768\jmath$, suggesting that increasing the rotational speed shifts the eigenvalues from the real axis to the imaginary axis, demonstrating the stiffening effect of the geometric stiffness term due to centrifugal forces.

When $\boldsymbol{K}_i$ is introduced alongside $\boldsymbol{D}_i$, for $\omega_x = 0$, the eigenvalues remain near zero because the quadratic velocity terms of the inertial forces are zero, resulting in $\boldsymbol{K}_i = \boldsymbol{0}$. However, for $\omega_x = \pi$, the eigenvalues become a pair of real numbers ± 3.1379, confirming the softening effect of $\boldsymbol{K}_i$.

Incorporating $\boldsymbol{K}_c$ with $\boldsymbol{D}_i$, for $\omega_x = 0$, shifts the eigenvalues from near zero to a pair of real numbers ± 0.2800, implying that the tangent stiffness matrix of constraints due to transverse external follower forces $\boldsymbol{F}_x$ and $\boldsymbol{F}_y$ exerts a softening effect. For $\omega_x = \pi$, the eigenvalues shift to pure imaginary numbers $\pm 0.6388\jmath$, confirming that the tangent stiffness matrix of constraints due to centrifugal forces has a stiffening effect as the rotational speed increases.

When all four matrices, $\boldsymbol{K}_g$, $\boldsymbol{K}_i$, $\boldsymbol{D}_i$, and $\boldsymbol{K}_c$, are included, the eigenvalues shift from near zero to a pair of real numbers, indicating that the rotor cannot rotate stably.

The eigenvalues of the rotor's free rotation mode, which correspond to the poles of the system matrix in the state-space representation of the linearized dynamics system, should be zero or close to zero for effective controller design using a classical PID model. To facilitate proper control design, the geometric stiffness matrix $\boldsymbol{K}_g$, the inertial stiffness matrix $\boldsymbol{K}_i$, and the tangent stiffness matrix of constraints $\boldsymbol{K}_c$ should be excluded, while the inertial damping matrix $\boldsymbol{D}_i$ can be retained.

Interpretation of stiffening and softening effects

The stiffening and softening effects of the geometric stiffness matrix $\boldsymbol{K}_g$, the tangent stiffness matrix of constraints $\boldsymbol{K}_c$, and the inertial stiffness matrix $\boldsymbol{K}_i$ are discussed in this section, respectively.

Geometric stiffness matrix The geometric stiffness matrix $\boldsymbol{K}_g$, derived from the linear assumptions of finite beam elements [216], is proportional to the internal axial forces within the beam elements. When these internal axial forces stretch the beams, as in the case of a pre-tensioned guitar string, $\boldsymbol{K}_g$ exhibits a stiffening effect, increasing the natural frequencies. Conversely, when the internal axial forces compress the beams, as seen in the cabled tower of a wind turbine, $\boldsymbol{K}_g$ induces a softening effect, lowering the natural frequencies and potentially leading to buckling instability under extreme conditions.

If the transverse external forces follow the orientation of the nodes as the beam

deflects, known as follower forces (illustrated in Figure 4.3a), the force $\boldsymbol{F}_j$ acting on node N_j induces an axial compression force $\boldsymbol{F}_p = \boldsymbol{F}_j \sin(\theta_j - \theta_i)$ on the inner node N_i. In this case, the geometric stiffness matrix $\boldsymbol{K}_g$ contributes a softening effect.

In contrast, if the transverse external forces maintain a constant direction relative to the inertial frame, regardless of beam deflection, these are referred to as *constant-directional forces* in this work (shown in Figure 4.3b). In this case, the force $\boldsymbol{F}_j$ acting on node N_j induces an axial stretching force $\boldsymbol{F}_p = \boldsymbol{F}_j \sin(\theta_j)$. Here, the geometric stiffness matrix $\boldsymbol{K}_g$ exhibits a stiffening effect.

To confirm this behavior, a numerical experiment is conducted on the flexible rotor subjected to external constant-directional forces, where only out-of-plane forces $\boldsymbol{F}_x = 725\,630.0\,\mathrm{N}$ are applied, with in-plane forces $\boldsymbol{F}_y = \boldsymbol{0}$ to preserve rotor isotropy. As shown in Table 4.6, the eigenvalues shift from zero to pure imaginary numbers upon the inclusion of $\boldsymbol{K}_g$, thereby confirming the stiffening effect.

Table 4.6: Eigenvalues of a three-bladed flexible rotor under external constant-directional forces. The symbol '×' denotes that the corresponding matrix is included. The material stiffness matrix $\boldsymbol{K}_m$ is included in all cases.

Subcase	$\boldsymbol{K}_g$	$\boldsymbol{K}_i$	$\boldsymbol{D}_i$	$\boldsymbol{K}_c$	ω_x	λ
Free rotation constrained to the X axis			×		0	0,0.0001
					π	± 0.0001
	×		×		0	$\pm 0.9740\jmath$
					π	$\pm 3.2068\jmath$

Since centrifugal forces consistently act to stretch the blades, the geometric stiffness matrix $\boldsymbol{K}_g$ resulting from these forces induces a stiffening effect on the rotating blades.

Tangent stiffness matrix of constraints The tangent stiffness matrix of constraints $\boldsymbol{K}_c$ arises from changes in the orientation of the reaction forces and moments at the joints, and is proportional to these reaction forces and moments.

In the case of a standard pendulum, as shown in Figure 4.4a, gravity generates a tensile force $\boldsymbol{F}_c$ at the root joint, analogous to the axial stretching force in a beam. Here, the tangent stiffness matrix of constraints $\boldsymbol{K}_c$ induces a stiffening effect, shifting the eigenvalues from zero to $\pm\jmath\sqrt{g/L}$.

In contrast, for an inverted pendulum, as illustrated in Figure 4.4b, gravity generates a compressive force $\boldsymbol{F}_c$ at the root joint, similar to the axial

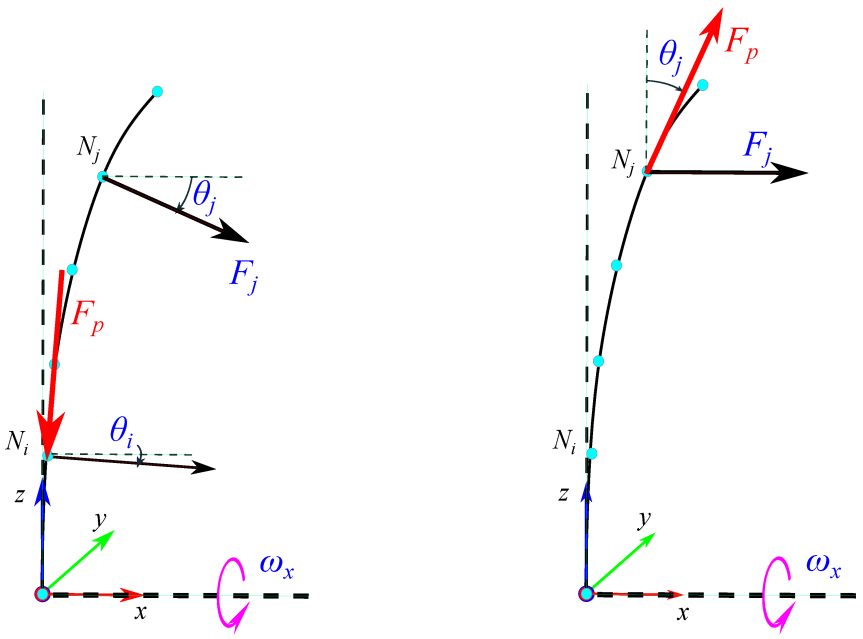

(a) *Follower forces.* (b) *Constant-directional forces.*

Figure 4.3: Effects of two distinct external forces on the deflected beam.

compression force in a beam. In this scenario, $\boldsymbol{K}_c$ induces a softening effect, altering the eigenvalues from zero to $\pm\sqrt{g/L}$, indicating an unstable motion.

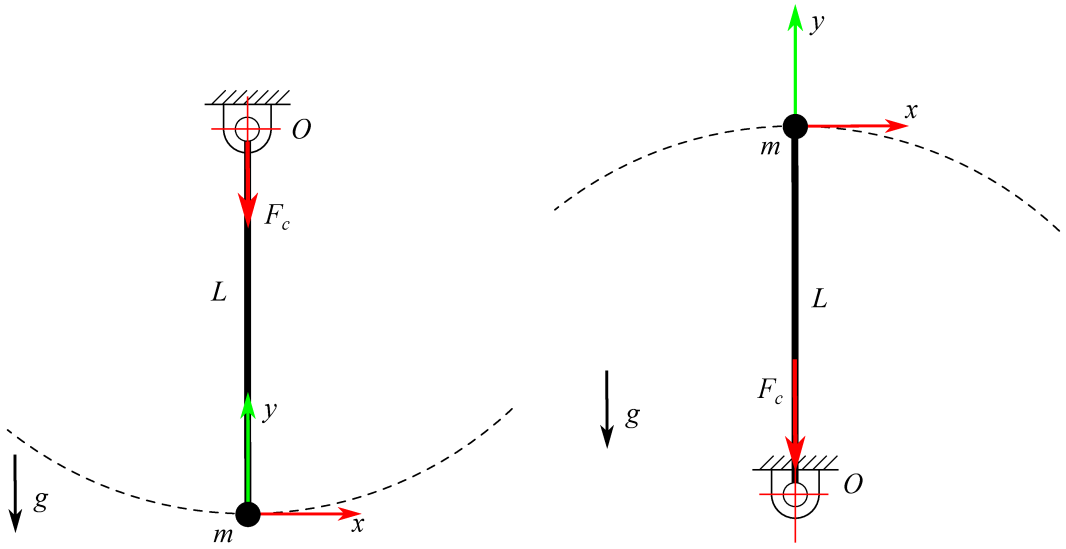

(a) *Standard pendulum.* (b) *Inverted pendulum.*

Figure 4.4: Two pendulum models. g represents gravitational acceleration, and L denotes the pendulum length.

When transverse external follower forces are applied, as in the case of the axial compression force $\boldsymbol{F}_p$ illustrated in Figure 4.3a, a compressive force $\boldsymbol{F}_c$ is generated at the root joint. By analogy with the inverted pendulum, the tangent stiffness matrix of constraints $\boldsymbol{K}_c$ induces a softening effect.

Conversely, centrifugal forces always produce a tensile force $\boldsymbol{F}_c$ at the root joint. Similar to the standard pendulum, the tangent stiffness matrix of constraints $\boldsymbol{K}_c$ induces a stiffening effect.

Inertial stiffness matrix The inertial stiffness matrix $\boldsymbol{K}_i$ contains a key term, $\boldsymbol{k}_{22} = -\widetilde{\boldsymbol{r}}_{H_1.N_{1(H_1)}}\widetilde{\boldsymbol{f}_c}$, in the hub block of the detailed expression (3.66c), where $\boldsymbol{f}_c = \nu\widetilde{\boldsymbol{\omega}}_{l_{H_1}}\widetilde{\boldsymbol{\omega}}_{l_{H_1}}\boldsymbol{r}_{H_1.N_{1(H_1)}}$ represents the centrifugal forces acting on the nodes of the rotating beams. Since the centrifugal forces are consistently directed towards the tips of the rotating beams, and due to the negative sign in $\boldsymbol{k}_{22}$, negative stiffness values accumulate in the hub block during the assembly of the system stiffness matrix. As a result, the inertial stiffness matrix $\boldsymbol{K}_i$ consistently contributes a softening effect.

The stiffening and softening effects of $\boldsymbol{K}_g$, $\boldsymbol{K}_c$, and $\boldsymbol{K}_i$ are summarized in Table 4.7.

Table 4.7: Stiffening and softening effects of the geometric stiffness matrix $\boldsymbol{K}_g$, the tangent stiffness matrix of constraints $\boldsymbol{K}_c$, and the inertial stiffness matrix $\boldsymbol{K}_i$ under various forces.

Matrix	Force	Effect
Geometric stiffness matrix $\boldsymbol{K}_g$	Transverse external follower forces	Softening
	Transverse external constant-directional forces	Stiffening
	Centrifugal forces	Stiffening
Tangent stiffness matrix of constraints $\boldsymbol{K}_c$	Transverse external follower forces	Softening
	Centrifugal forces	Stiffening
Inertial stiffness matrix $\boldsymbol{K}_i$	Centrifugal forces	Softening

Parameter sweep analysis

A parameter sweep analysis is performed to explore the relationship between the eigenvalues of the free rotation mode and the rotor's rotational speed and external forces.

The analysis is limited to the case where rotation is constrained to the X-axis. All four matrices—$\boldsymbol{K}_g$, $\boldsymbol{K}_i$, $\boldsymbol{D}_i$, and $\boldsymbol{K}_c$—are included in this parameter sweep.

Rotational speed Constant external follower forces of $\boldsymbol{F}_x = 725\,630.0\,\mathrm{N}$ and $\boldsymbol{F}_y = 439\,010.0\,\mathrm{N}$ are applied to the blade nodes, and the rotor's rotational speed is varied from 0 to $600\,\mathrm{r\,min^{-1}}$. As illustrated in Figure 4.5, as the rotor speed increases, the eigenvalues shift from a pair of real numbers toward zero, reaching zero at approximately $290\,\mathrm{r\,min^{-1}}$, before deviating into a pair of pure imaginary numbers. The stiffening effects of $\boldsymbol{K}_g$ and $\boldsymbol{K}_c$ due to centrifugal forces compete with the softening effect of $\boldsymbol{K}_i$. At low rotational speeds, the softening effect of $\boldsymbol{K}_i$ dominates, resulting in real eigenvalues. At higher rotational speeds, the stiffening effects of $\boldsymbol{K}_g$ and $\boldsymbol{K}_c$ prevail, producing imaginary eigenvalues. At a specific rotational speed, the effects cancel out, yielding zero eigenvalues.

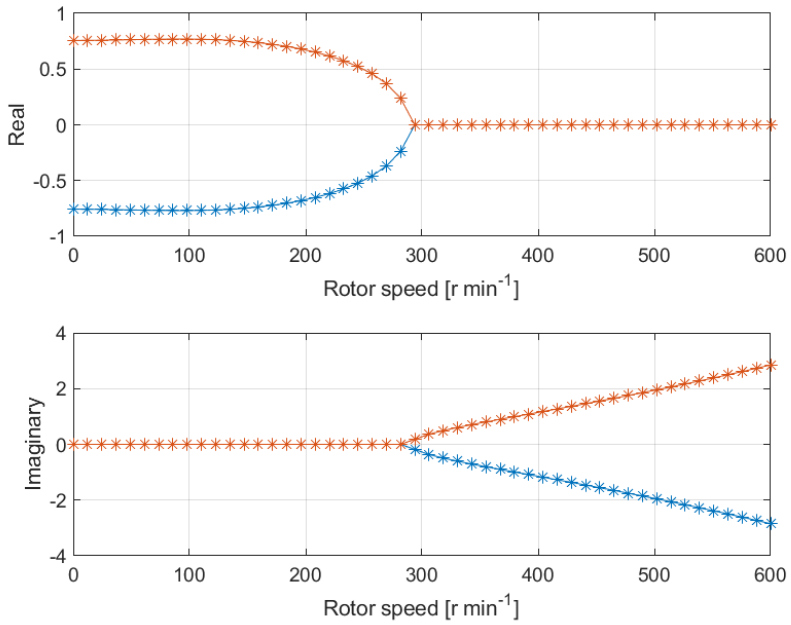

Figure 4.5: Eigenvalues of the rotor's free rotation mode with respect to the rotational speed.

External forces The rotor's rotational speed is set to $\pi\,\mathrm{rad/s}$. The external follower forces distributed along the blade nodes are linearly increased from 0 to $\boldsymbol{F}_x = 725\,630.0\,\mathrm{N}$ and $\boldsymbol{F}_y = 439\,010.0\,\mathrm{N}$. As shown in Figure 4.6, as the external follower forces increase, the eigenvalues shift proportionally along the real axis, moving further from zero as the force amplitude grows. This behavior is attributed to the increasing softening effect of $\boldsymbol{K}_g$, induced by the transverse

external follower forces. At zero applied forces, the eigenvalues are $\pm 0.0072\jmath$, which is due to numerical errors, as explained in Table 4.4.

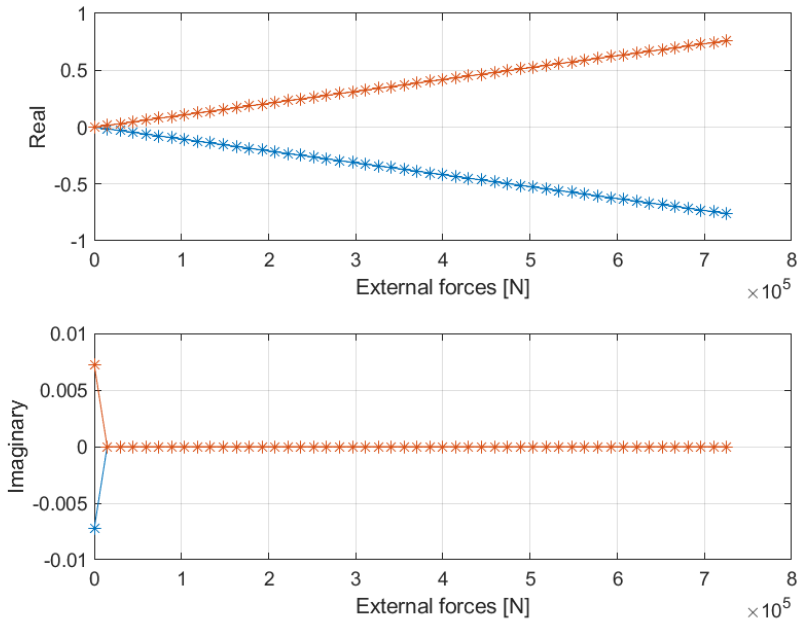

Figure 4.6: Eigenvalues of the rotor's free rotation mode with respect to the external follower forces applied to the blade nodes.

4.2 Aeroelastic verification using the IEA 15 MW reference wind turbine

The modal properties of wind turbine systems are significantly influenced by the accuracy of the structural model and the aeroelastic status in the static equilibrium configuration. Conducting a code-to-code verification of the structural properties and the aeroelastic computations enhances confidence in the proposed aeroelastic model. This section outlines a code-to-code verification between the current model and the commercial tool Bladed, utilizing an open-source reference wind turbine model.

Under the joint effort of the National Renewable Energy Laboratory (NREL) and the Technical University of Denmark (DTU), a 15 MW wind turbine model, designated IEA-15-240-RWT, was developed as part of the International Energy Agency (IEA) Wind Technology Collaboration Platform (TCP) Task 37 [84]. The IEA 15 MW turbine is designed as an offshore installation with a fixed-bottom monopile support structure, featuring a direct-drive system, a rotor diameter of

240 meters, and a hub height of 150 meters. DNV has released a reference model for the IEA 15 MW turbine [52], which corresponds to version 1.0 from the IEA Task 37. The numerical model employed in this work is directly converted from the Bladed reference model [52].

In Bladed, the blade is divided into five segments to effectively capture the geometric nonlinearity present in large deflections. Each segment is represented by ten modes, resulting in a total of 50 blade modes. The version of Bladed utilized in this study is v4.11.

4.2.1 Blade structural modes

An isolated blade clamped to the ground is analyzed. The blade is discretized into 50 Timoshenko beam elements. The modal analysis is conducted in the initial undeformed configuration. In the corotational formulation, a stiffness-proportional Rayleigh damping model is employed. The stiffness-proportional coefficient is tuned to achieve a damping ratio of 3 % for the blade first edgewise mode, consistent with the Bladed reference model [52].

The modal frequencies and damping ratios for the first ten modes are presented in Table 4.8. The relative differences between the present model and Bladed are calculated using the expression $\epsilon_{\text{rel}} = 2\,(f_{\text{CRF}} - f_{\text{Bladed}})\,/\,(f_{\text{CRF}} + f_{\text{Bladed}}) * 100\,\%$ [221]. The relative differences in the first ten modal frequencies are all less than 1 %, demonstrating excellent agreement with the Bladed model.

Table 4.8: Structural modal frequencies and damping ratios of the isolated blade of the IEA 15 MW wind turbine. 'CRF': Corotational Timoshenko beam element model in the present study; 'Bladed': Commercial tool.

No.	Modal frequency [Hz]			Damping ratio [-]	Suggested
	CRF	Bladed	Rel. diff [%]	CRF	mode name
1	0.520	0.525	−0.85	0.0255	1st flapwise
2	0.613	0.607	0.85	0.0300	1st edgewise
3	1.579	1.592	−0.88	0.0773	2nd flapwise
4	1.871	1.860	0.58	0.0916	2nd edgewise
5	3.175	3.197	−0.67	0.1555	3rd flapwise
6	3.857	3.854	0.08	0.1889	3rd edgewise
7	4.224	4.224	0.01	0.2069	1st torsion
8	5.394	5.429	−0.64	0.2642	4th flapwise
9	6.205	6.208	−0.05	0.3039	4th edgewise
10	7.506	7.531	−0.35	0.3676	2nd torsion

The modal shapes of the first edgewise mode and the first torsional mode of the blade are depicted in Figure 4.7. As shown in Figure 4.7a, coupling exists among

flapwise, edgewise, and torsional deflections in the first edgewise mode; in detail, a unit edgewise deflection is associated with a flapwise deflection of 0.1 m and a torsional deflection of −0.45°. Additionally, bending-twist coupling is also observed in the first torsional mode of the blade, as illustrated in Figure 4.7b.

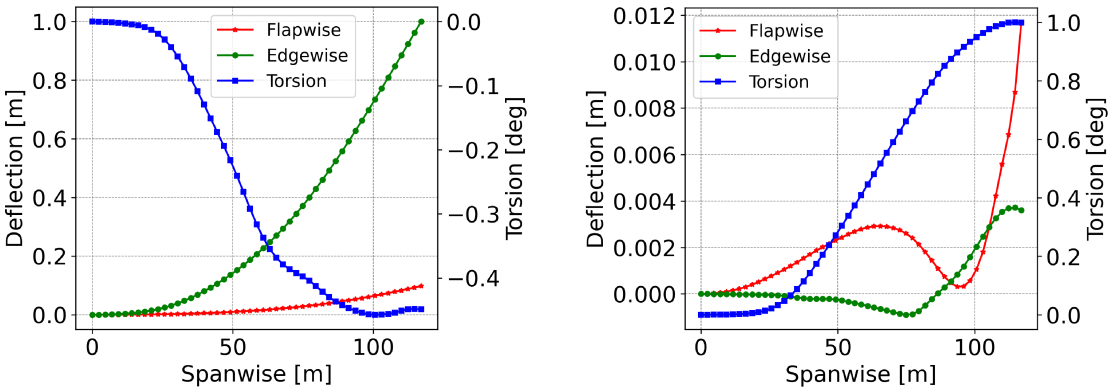

(a) 1st edgewise mode.

(b) 1st torsion mode.

Figure 4.7: Structural modal shapes of the isolated blade in the initial configuration.

It is important to note that the modal shapes illustrated in Figure 4.7 are evaluated in the initial undeformed configuration of the isolated blade. Due to the complex bending-twist coupling, these modal shapes may vary significantly in the deformed configuration. To compare the modal shapes from simulation with those from test rig experiments, it is essential to account for the influence of gravity on blade deflections during static equilibrium analysis. Subsequently, an eigenvalue analysis should be performed in the deformed configuration to extract the modal shapes, which can then be used for validation against modal experiments conducted on the blade test rig.

4.2.2 Blade aeroelastic steady states

The blade deflections, aerodynamic states and forces are analyzed in the aeroelastic equilibrium configurations across the operating wind speed range.

As detailed in Section 3.2, the rotor speed and pitch angle for a given wind speed are designated as input parameters in the linearization analysis of wind turbines. In the present study, these parameters are obtained from steady operational load calculations conducted in Bladed, thereby ensuring consistency in operational points between this study and Bladed. The rotor speed and pitch angle across the operating wind speed range are illustrated in Figure 4.8.

Only integer wind speeds are analyzed; therefore, the rated wind speed of 10.59 m/s [84] is not included in the operational points examined.

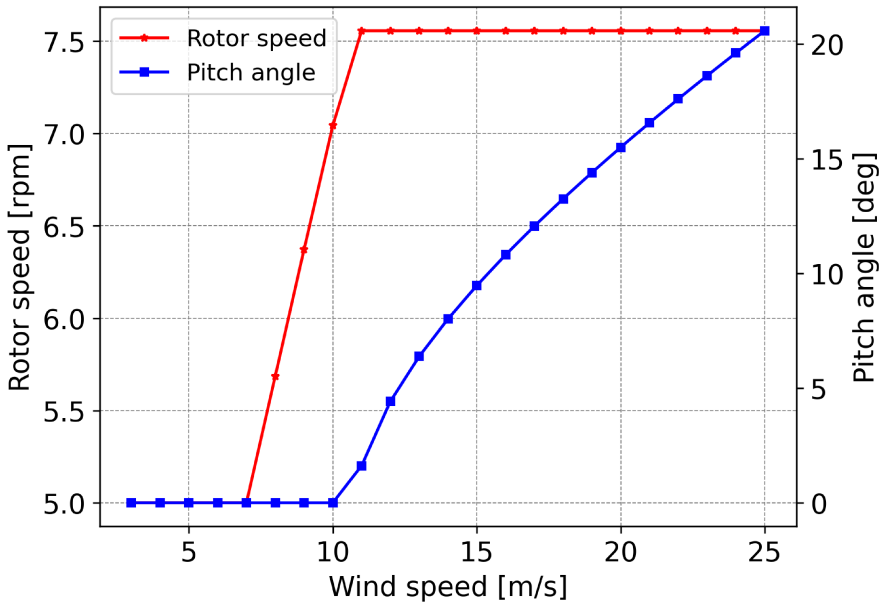

Figure 4.8: Rotor speed and pitch angle of the IEA 15 MW wind turbine across the operating wind speed range.

Blade deflections

The blade tip deflections in the flapwise, edgewise, and torsional directions across the operating wind speed range are illustrated in Figure 4.9a.

The maximum tip deflections in the flapwise and edgewise directions occur at a wind speed of 10 m/s, while the largest tip torsional angle is observed at approximately 21 m/s. A comparison of the maximum tip deflections in the flapwise, edgewise, and torsional directions between the present model and Bladed is provided in Table 4.9. The largest relative deviation in the edgewise deflection reaches 6.4 %; however, the absolute deviation of 0.003 m is considered negligible. Deviations in the flapwise and torsional directions are less than 3 %, indicating excellent agreement between the present model and the Bladed tool.

Table 4.9: Blade tip largest deflections.

		Present model	Bladed	Rel. diff [%]
Flapwise	[m]	13.443	13.050	3.0
Edgewise	[m]	0.053	0.050	6.4
Torsion	[deg]	-4.638	-4.509	2.8

The blade deflections in the spanwise direction at a wind speed of 10 m/s are illustrated in Figure 4.9b. The agreement between the present model and Bladed

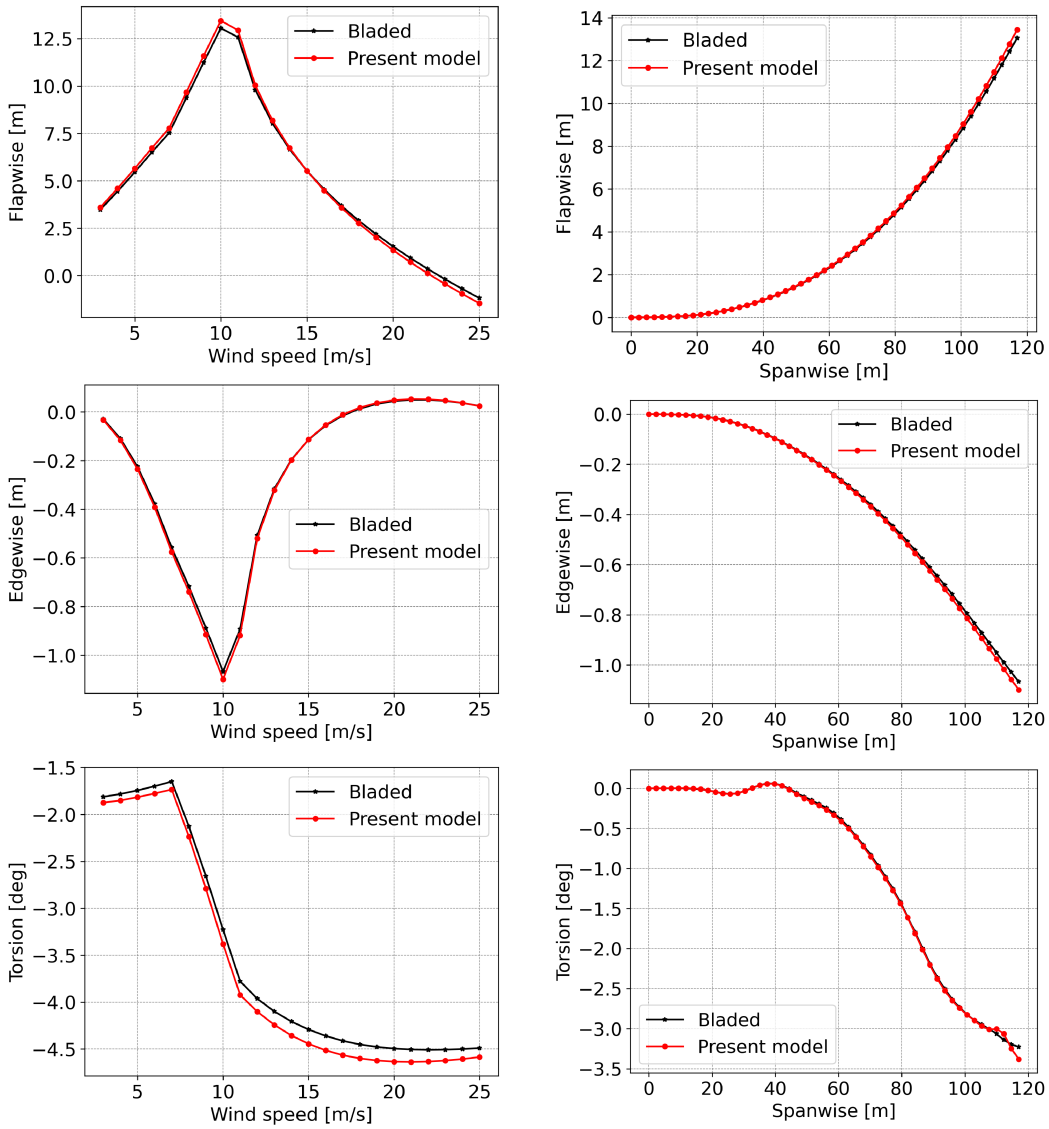

(a) Blade tip deflections across the operating wind speed range.

(b) Blade spanwise deflections at a wind speed of 10 m/s.

Figure 4.9: Blade deflection comparison between the present model and Bladed.

in the spanwise deflections is notably strong.

Figure 4.9b also reveals visible differences in the blade tip torsional angles, particularly where the torsional angles near the tip exhibit a lack of smoothness. This discrepancy is likely attributable to variations in the setup of the blade nodal orientation in the initial configuration for the prebend-pretwist blade design, as well as differences in the calculation methods for the torsional angle in three-dimensional rotation.

Blade aerodynamics

The aerodynamic states and forces acting on the blade in the aeroelastic equilibrium configuration are compared between the present model and Bladed. The analysis focuses on results obtained at a wind speed of 10 m/s, as this condition corresponds to the maximum deflections.

Figure 4.10a illustrates the angle of attack, as well as the axial and tangential induction factors along the spanwise direction at this wind speed. Additionally, Figure 4.10b presents the aerodynamic forces in the axial and tangential directions of the rotor plane, along with the aerodynamic twist moment exerted on the elastic center.

In Bladed, the aerodynamic forces at the blade tip are set to zero; however, these forces remain nonzero in the present model. Notably, the aerodynamic twist moment near the blade root, particularly for spans less than 20 m, exhibits a discrepancy between the present model and Bladed. This difference can likely be attributed to the distinct treatment of the aerodynamic center and elastic center in the context of tapered beam elements. Nevertheless, the observed deviations are minimal, and their influence on elastic deflections is limited, as demonstrated in Figure 4.9. Aside from these discrepancies, there is excellent overall agreement between the present model and Bladed regarding the blade aerodynamic states and forces.

4.2.3 Campbell diagram

Following the completion of the code-to-code verification between the present model and Bladed, which focused on blade structural modes as well as aeroelastic states and forces in the equilibrium configuration, a modal analysis of the entire aeroelastic model of the IEA 15 MW wind turbine is conducted across the operating wind speed range. The modal frequencies and damping ratios for the less damped modes, specifically the rotor edgewise modes and tower side-side modes, are extracted and subsequently plotted on the Campbell diagram, as illustrated in Figure 4.11.

For three-bladed wind turbines, the primary periodic excitation frequencies include 1P and 3P, which are associated with rotor rotation, as well as higher-order harmonic terms such as 6P, 9P, 12P, and so on. These periodic excitation frequencies are also illustrated in the Campbell diagram.

From Figure 4.11a, it can be observed that the 6P excitation intersects the rotor first edgewise backward whirling mode at a wind speed of 7.52 m/s, corresponding to a frequency of 0.536 Hz, thereby marking the first resonant point. The risk of resonance is mitigated since the rotor speed at this wind speed is dynamically regulated to track the optimal tip-speed ratio for enhanced power performance.

As the wind speed increases, the 6P excitation subsequently intersects the rotor first edgewise forward whirling mode at a wind speed of 10.68 m/s, with a frequency

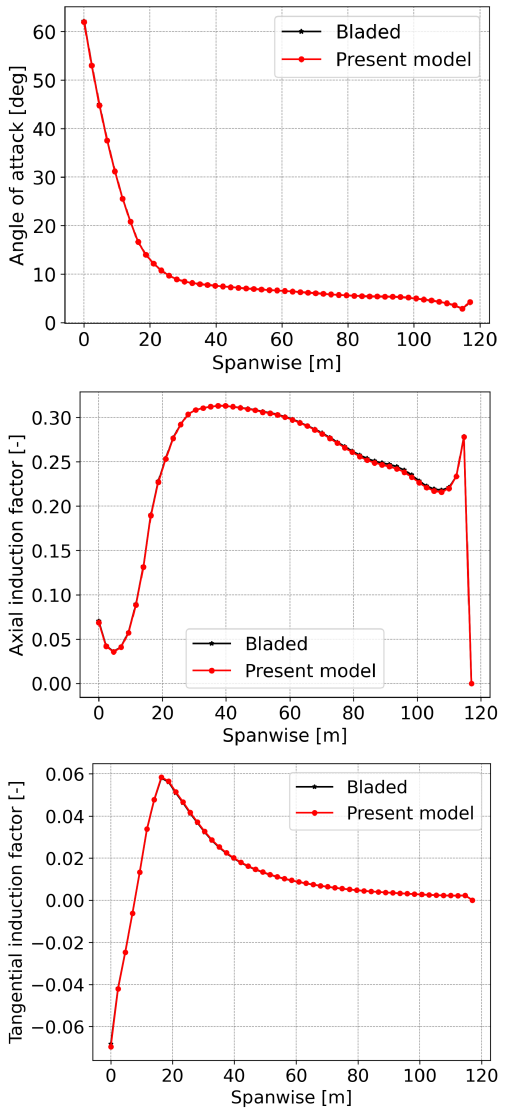

(a) Blade aerodynamic states.

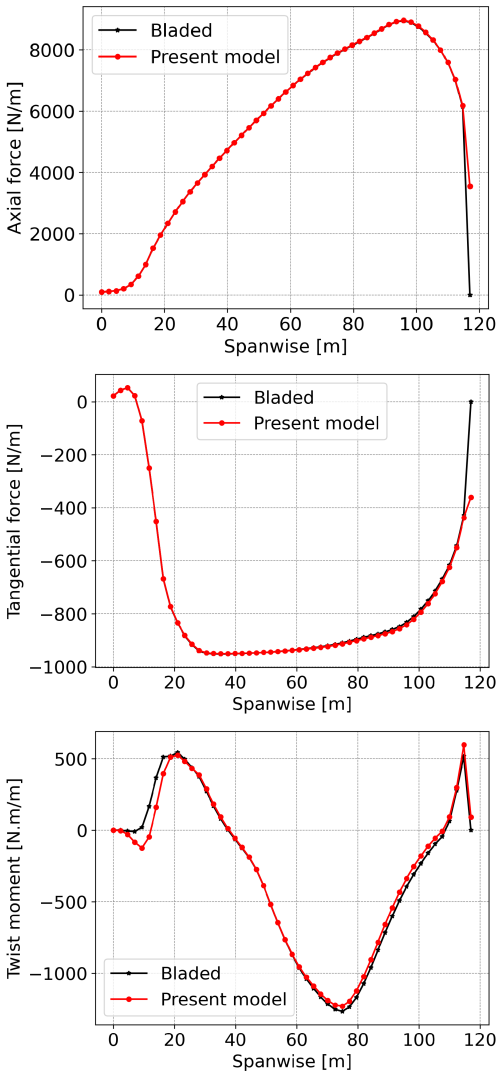

(b) Blade aerodynamic forces.

Figure 4.10: Blade aerodynamic comparison between the present model and Bladed at a wind speed of 10 m/s.

of 0.739 Hz, leading to the second resonant point. Notably, the designed rated wind speed is 10.59 m/s [84], indicating that the second resonant point occurs slightly above the rated wind speed. This suggests that the rotor speed remains relatively stable, which may heighten the risk of resonance development and potentially introduce significant fatigue loads.

As illustrated in Figure 4.11b, the minimum damping ratio observed across the operating wind speed range is 0.0219, attributed to the tower first side-side mode.

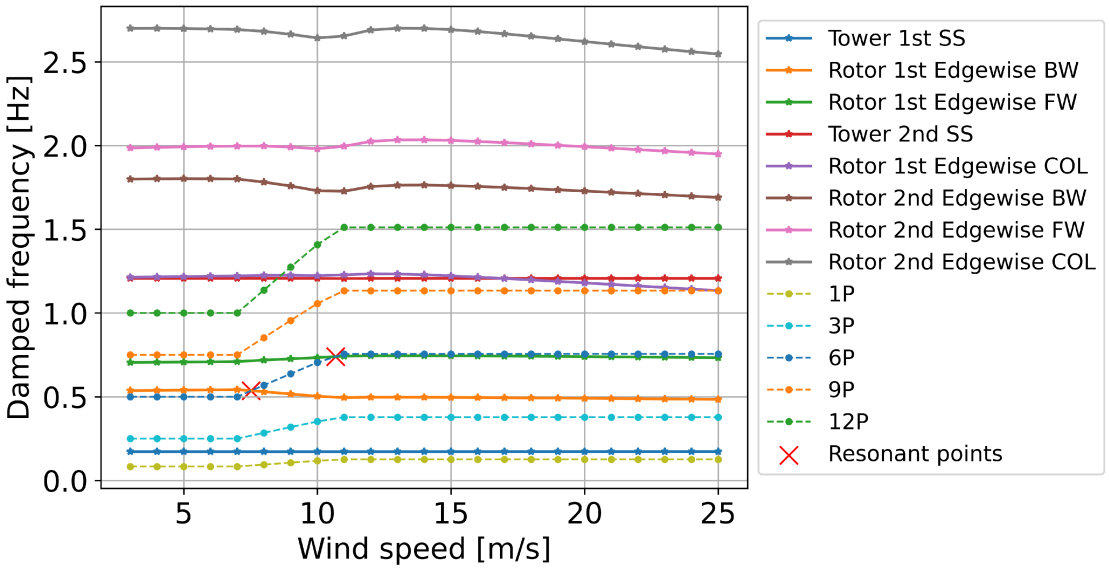

(a) Aeroelastic modal frequencies.

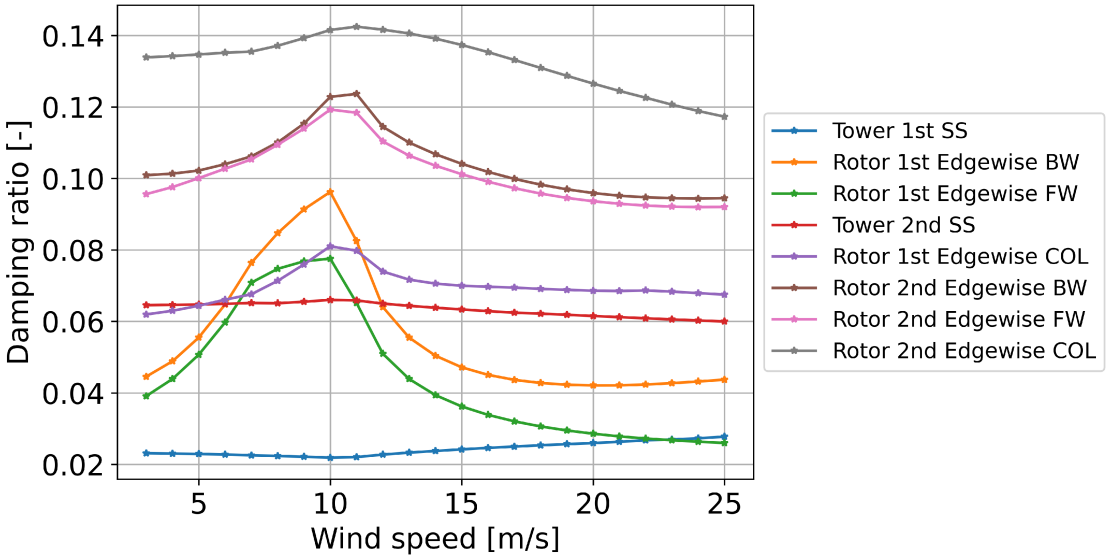

(b) Aeroelastic damping ratios.

Figure 4.11: Campbell diagram for the IEA 15 MW reference wind turbine. The tower fore-aft modes and rotor flapwise modes are excluded from the diagram due to their high damping. 'BW': Backward Whirling; 'FW': Forward Whirling; 'COL': Collective; 'SS': Side-Side.

This value indicates a sufficient stability margin regarding aeroelastic damping. However, it is important to note that the structural damping ratios for the blade and tower are set significantly higher than the typical values used in engineering

practice, which are usually around 0.005 or less. Therefore, caution is advised when utilizing the aeroelastic damping ratios of various modes in the Campbell diagram to assess the aeroelastic stability of the IEA 15 MW wind turbine.

4.3 Aeroelastic stability verification using simulation models

In the context of modal analysis and aeroelastic stability assessment, several code-to-code comparisons have been conducted. While modal frequencies generally exhibit good agreement across various codes, deviations are more pronounced in the damping ratios, particularly for the less damped rotor edgewise modes [63, 273, 55]. Damping ratios can be identified from time-domain nonlinear dynamic simulations and compared with results from eigenvalue analyses; however, achieving a strong agreement is not trivial [273]. The verification and validation of aeroelastic damping ratios remain an open challenge in the field of wind turbine aeroelasticity.

In this study, a quantitative indicator derived from the time series of the blade root edgewise moment is compared with the aeroelastic damping ratios of the rotor first edgewise backward whirling mode across various blade models, where torsional stiffness is scaled by a range of factors. This comparison aims to explore the correlation between blade edgewise vibrations in nonlinear time-domain simulations and the aeroelastic damping ratio obtained from eigenvalue analyses.

An aeroelastic simulation model for an intermediate-edition wind turbine, provided by Goldwind during the design phase, is employed in this investigation. Although the model does not represent the final system design, it closely approximates the final configuration in industrial practice, offering a valuable reference for the wind turbine industry. Due to confidentiality agreements with Goldwind, many key parameters of the wind turbine model and important results (primarily modal frequencies) are not disclosed here. The wind turbine is designed to deliver a power capacity exceeding 6 MW, featuring blades longer than 90 m and a tubular tower.

4.3.1 Description of the blade vibration

During the design phase of a new wind turbine, a series of load cases under normal operational conditions are simulated across the wind speed range from cut-in to cut-out limits. In the design iterations of an intermediate-edition turbine, concerns arose due to excessive blade fatigue loads. Engineers reviewed the time series data and observed that the blades exhibited significant edgewise vibrations at certain wind speeds under normal operational conditions. The time series of the blade root edgewise moment (M_x) at wind speeds of 3 m/s and 13 m/s are presented in Figure 4.12, along with the corresponding power spectral density (PSD) plots.

Although the full time series span 600 s, only 100 s segments are shown here to highlight the oscillatory behavior more clearly.

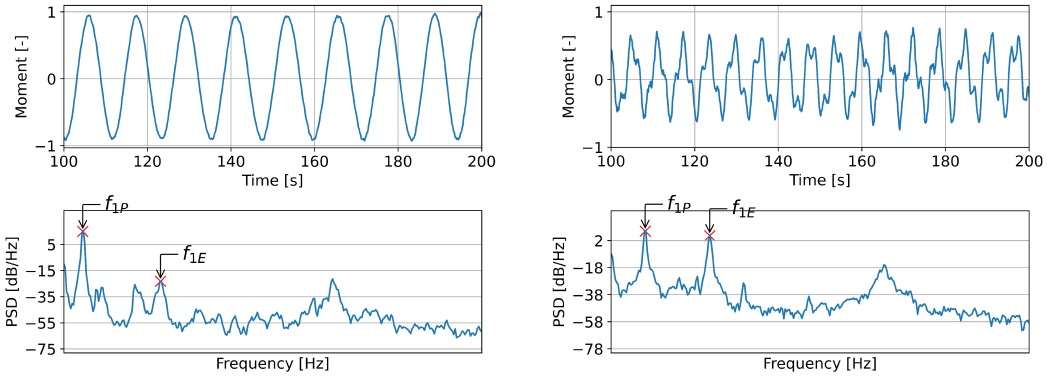

(a) Stable at wind speed 3 m/s. (b) Unstable at wind speed 13 m/s.

Figure 4.12: Blade root edgewise moment under stable and unstable operating conditions. The maximum amplitudes of the edgewise moment are normalized to unity. Frequency ticks in the power spectral density (PSD) subplots are omitted due to confidentiality restrictions.

The time series of the blade root edgewise moment at a wind speed of 3 m/s consists of a smooth sinusoidal curve, primarily generated by the blade gravitational force at various azimuth positions, which is the dominant contributor to the blade edgewise moment. As shown in the PSD subplot in Figure 4.12a, the peak corresponding to the blade first edgewise mode ($f_{1\mathrm{E}}$) is significantly lower than that of $f_{1\mathrm{P}}$, indicating a stable blade response. In contrast, the time series of the blade root edgewise moment at a wind speed of 13 m/s, as depicted in Figure 4.12b, exhibits significant local oscillations. The PSD subplot in Figure 4.12b reveals that the peak of the blade first edgewise mode ($f_{1\mathrm{E}}$) aligns closely with that of $f_{1\mathrm{P}}$, suggesting a severe vibration in the blade first edgewise mode, which is indicative of an unstable operating condition.

To better understand the vibration mechanism, time-domain simulations are re-run using a finer wind speed bin interval of 1 m/s. Six random turbulent wind seeds are used for each wind speed bin. The average longitudinal wind speed at the hub center, average rotor speed, and average pitch angles for each wind speed bin are extracted from the simulation time series to create an operational table, which is then used as input for subsequent linearization and eigenvalue analyses. The Campbell diagram for the wind turbine model under normal operational conditions is shown in Figure 4.13.

From Figure 4.13a, several resonant points across the operating wind speed range are evident. For those resonant points occurring below 9 m/s, resonance is less likely to develop due to the rapid change in rotor speed caused by turbulent wind

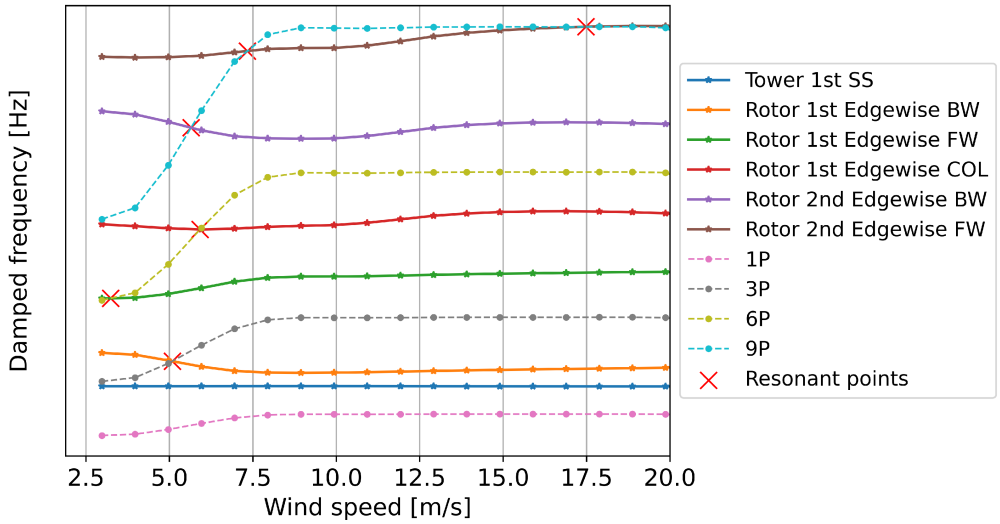

(a) Aeroelastic modal frequencies.

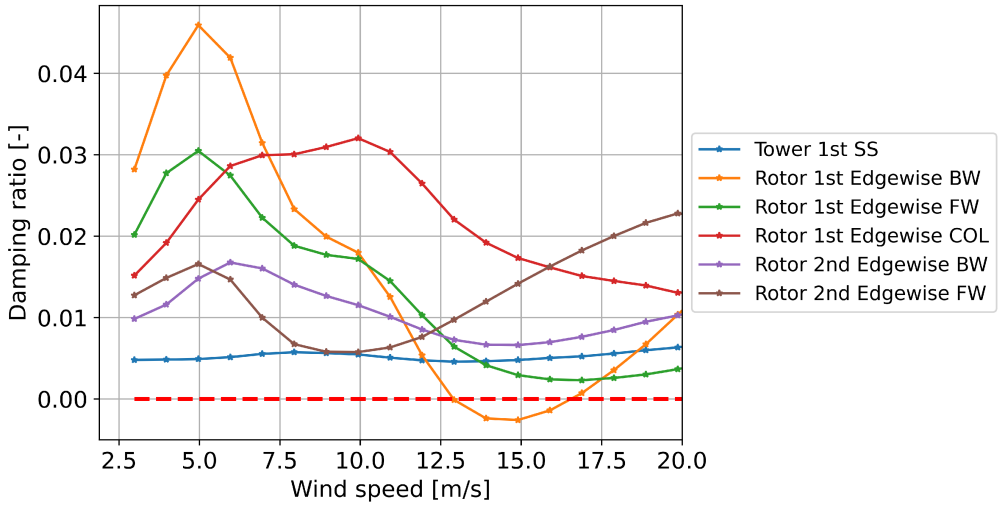

(b) Aeroelastic damping ratios.

Figure 4.13: Campbell diagram for a wind turbine model in the design phase. Only less damped modes are presented. The modal frequencies are omitted due to confidentiality requirements. 'BW': Backward Whirling; 'FW': Forward Whirling; 'COL': Collective; 'SS': Side-Side.

conditions. Another resonant point is observed at a wind speed of approximately 18 m/s, where the 9P rotor rotational frequency intersects with the rotor second edgewise forward whirling mode. The excitation energy of the 9P rotor rotational frequency is expected to be limited due to its high order. Additionally, the damping ratio of the rotor second edgewise forward whirling mode at 18 m/s, as shown in

Figure 4.13b, is approximately 0.02, indicating a relatively high damping level. Considering both aspects, the resonant risk at 18 m/s is expected to be minimal.

However, as shown in Figure 4.13b, the damping ratios of the rotor first edgewise backward whirling mode in the wind speed range from 13 m/s to 16.5 m/s are negative, suggesting a significant risk of blade edgewise vibration in this range. This finding provides an explanation for the blade edgewise vibration observed in Figure 4.12b.

4.3.2 Numerical experiment

In this study, it is assumed that time-domain dynamic simulations provide more reliable results than modal analyses based on linearization. This is because the former can more accurately capture geometric nonlinearities and incorporates unsteady aerodynamic effects, by utilizing the Øye dynamic inflow model and the Beddoes-Leishman dynamic stall model [69].

The procedure outlined below is used to quantify the blade edgewise vibration level in this study:

1. A low-pass Butterworth filter with a cutoff frequency of $1.5f_{1\mathrm{P}}$ is applied to the time series of the blade root edgewise moment (M_x) to isolate the 1P excitation component. The standard deviation (STD) of the filtered time series is then computed, denoted as $\sigma_{1\mathrm{P}}$.

2. A band-pass Butterworth filter with cutoff frequencies of $f_{1\mathrm{E}} - 0.1\,\mathrm{Hz}$ and $f_{1\mathrm{E}} + 0.1\,\mathrm{Hz}$ is applied to the time series of the blade root edgewise moment (M_x) to extract the component corresponding to the blade first edgewise mode ($f_{1\mathrm{E}}$). The standard deviation of the filtered time series is then calculated, denoted as $\sigma_{1\mathrm{E}}$.

3. The ratio of the standard deviations for the two components is computed as $r_{j,1\mathrm{E}/1\mathrm{P}} = \sigma_{1\mathrm{E}}/\sigma_{1\mathrm{P}}$ for a time series from a single load case simulation with a wind seed j in the corresponding wind speed bin.

4. The root mean square (RMS) of the standard deviation ratios from six time-domain simulations, corresponding to six different wind seeds within each wind speed bin, is then calculated as $r_{1\mathrm{E}/1\mathrm{P}} = \sqrt{\frac{1}{6}\sum_{j=1}^{6} r_{j,1\mathrm{E}/1\mathrm{P}}^2}$. This RMS value $r_{1\mathrm{E}/1\mathrm{P}}$ is used as a quantitative indicator of the blade edgewise vibration level at the analyzed average wind speed.

It is well established that the blade torsional stiffness, denoted as GJ, significantly influences the damping ratios of rotor edgewise modes [273, 34]. In this numerical experiment, the blade torsional stiffness is scaled uniformly across all spanwise cross-sections using various scaling factors. The time-domain simulations and modal analyses are performed for a series of scaling factors, denoted as c_{GJ},

which range from 0.8 to 1.2 in increments of 0.05. The standard deviation ratios $r_{1E/1P}$ across the operating wind speed range are computed from the results of the time-domain simulations. The damping ratios of the rotor first edgewise backward whirling mode, denoted as ζ_{1E}, are extracted from the eigenvalue analyses. These results are presented together in Figure 4.14.

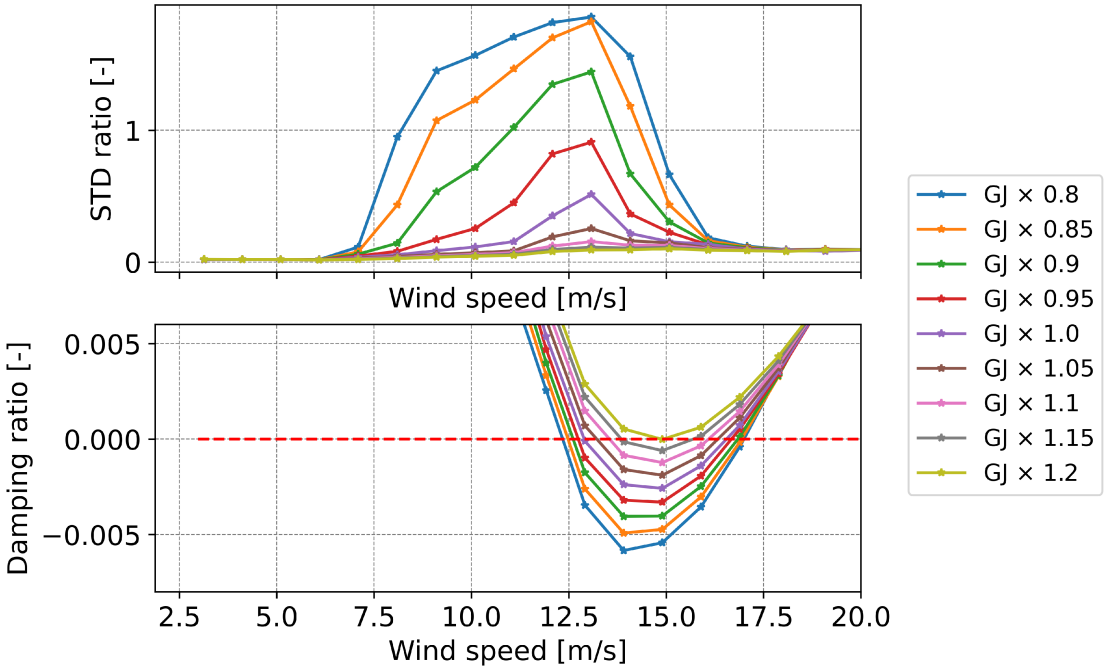

Figure 4.14: Correlation between the standard deviation (STD) ratios $r_{1E/1P}$ and the damping ratios of the rotor first edgewise backward whirling mode ζ_{1E} for various scaling factors $c_{GJ} = 0.8, 0.85, \ldots, 1.2$ on the blade torsional stiffness.

From Figure 4.14, it is observed that as the blade torsional stiffness increases, the damping ratios of the rotor first edgewise backward whirling mode also increase, resulting in a narrower wind speed range with negative damping ratios. Correspondingly, the standard deviation ratios $r_{1E/1P}$ decrease, and the wind speed range exhibiting higher standard deviation ratios becomes smaller, indicating a reduction in the blade edgewise vibration amplitude. This also implies that the wind speed range over which blade edgewise vibration occurs is further constrained. When the blade torsional stiffness is scaled by 1.2, the minimum damping ratio approaches zero, and the standard deviation ratios $r_{1E/1P}$ remain relatively flat across the operating wind speed range, suggesting that the blade edgewise vibration has been effectively suppressed.

The peaks of the standard deviation ratios $r_{1E/1P}$ for various scaling factors c_{GJ} consistently occur at a wind speed of 13 m/s. In contrast, the minimum damping ratios for these scaling factors are observed at wind speeds between 14 m/s and

15 m/s. Although the most critical wind speeds for blade edgewise vibration identified from the time-domain simulations and modal analyses of the wind turbine do not exactly overlap, the deviation is minimal, typically within 1 to 2 m/s. It can be concluded that there is a strong correlation between the standard deviation ratios $r_{1E/1P}$ and the damping ratios of the rotor first edgewise backward whirling mode ζ_{1E}.

The standard deviation ratios $r_{1E/1P}$ at the critical wind speed of 13 m/s, and the minimum damping ratios of the rotor first edgewise backward whirling mode ζ_{1E} at the critical wind speed range of 14 m/s to 15 m/s, are summarized and plotted in Figure 4.15.

As the blade torsional stiffness decreases, the minimum damping ratio ζ_{1E} becomes increasingly negative. When $\zeta_{1E} < -0.005$, the increase in the standard deviation ratio $r_{1E/1P}$ tends to level off, suggesting that the blade edgewise vibration amplitude reaches a limit and no longer increases. When the minimum damping ratio approaches zero, the standard deviation ratio $r_{1E/1P}$ also begins to stabilize. In cases where sufficient damping is present, the remaining blade edgewise vibration is primarily attributed to gravitational forces and stochastic aerodynamic forces induced by turbulent wind.

c_{GJ}	$r_{1E/1P}$	ζ_{1E}
0.80	1.858	-0.00584
0.85	1.823	-0.00492
0.90	1.443	-0.00405
0.95	0.909	-0.00331
1.00	0.513	-0.00258
1.05	0.255	-0.00190
1.10	0.155	-0.00123
1.15	0.114	-0.00061
1.20	0.092	-0.00002

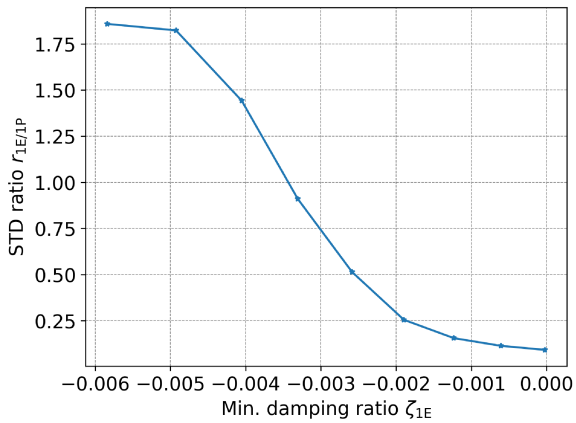

Figure 4.15: Correlation between the standard deviation (STD) ratios $r_{1E/1P}$ at a wind speed of 13 m/s and the minimum damping ratios ζ_{1E} of the rotor first edgewise backward whirling mode, for various scaling factors c_{GJ} of the blade torsional stiffness.

4.4 Aeroelastic stability validation using prototype turbines

In this section, standard load measurements are performed on two prototype offshore wind turbines to establish a reference for the aeroelastic stability assessment presented in this study. The two turbines, manufactured by Goldwind, are equipped with blades longer than 80 m and supported by monopile towers, with a power capacity exceeding 6 MW. The first prototype turbine features an original blade design, while the second prototype incorporates an optimized blade design, which reduces the blade mass by several hundred kilograms to lower costs, but sacrifices approximately 10 % torsional stiffness in the middle span region. The hub and nacelle systems are identical in both prototypes. However, the turbines are installed in two adjacent offshore wind farms, each with slightly different tower designs tailored to the specific local wind, seabed conditions, and water depths.

Three test cases are considered in the measurement activity:

- Case 1: First prototype turbine, with the original blade design.
- Case 2: Second prototype turbine, with the optimized blade design featuring reduced mass and lower torsional stiffness.
- Case 3: Second prototype turbine, with the optimized blade design, but with a modified controller that operates the turbine at a higher rotor speed within the wind speed range of 11–15 m/s, thus increasing the risk of blade edgewise vibrations.

4.4.1 Measurement setup

The measurement activity was conducted by Goldwind in the second half of 2019, in accordance with the international standard for mechanical load measurement of wind turbines, IEC 61400-13 [140]. Strain gauges were installed at three blade roots to measure the flapwise and edgewise moments. Their calibration was performed by positioning the blades at the left and right horizontal azimuthal angles, using information on the blade mass and the center of mass location obtained from the blade design tool. A LIDAR system was installed at the top of the nacelle to measure the instantaneous wind speed and direction. An accelerometer, located at the top of the tower, was used to measure the tower fore-aft and side-side accelerations. Additionally, air temperature, air pressure, and humidity were recorded to estimate the air density. Operational parameters, including pitch angles, electrical power, rotor speed, and controller status, were all monitored through the turbine's control system. All measurement data were collected in 10-minute segments, classified according to wind speed bins and turbulence intensity, and subsequently organized into a capture matrix. Data collected under normal power production conditions

were then used for the subsequent analysis and comparison. The total number of 10-minute samples for the three test cases was 493, 960, and 695, respectively. For further details on the mechanical load measurement of wind turbines, readers are referred to IEC 61400-13.

4.4.2 Comparison of measurement and aeroelastic damping ratios

Unfortunately, the full set of original measurement data is no longer available, and consequently, the standard deviation ratio $r_{1E/1P}$, as defined in Section 4.3.2, cannot be analyzed. As an alternative, the standard deviations of the blade root edgewise moment M_x are computed for each 10 min time series and are directly employed in the comparison. However, a slight edgewise vibration cannot be effectively captured by the standard deviation of the blade root edgewise moment M_x due to the relatively high contribution of the 1P component generated by the blade's gravitational force, which introduces a limitation in the validation study.

The average values of measured wind speed, rotor speed, and pitch angles are calculated for each wind speed bin based on the collected data. Operational tables for wind speed, rotor speed, and pitch angles are constructed for each of the three test cases. The average air density is also analyzed, with a single average value applied across the entire operating wind speed range. Linearization and modal analyses are subsequently performed based on the measured air density and the operational tables, from which the aeroelastic damping ratios for both prototype turbines are derived.

The standard deviations of the blade root edgewise moment M_x and the aeroelastic damping ratios of the rotor first edgewise backward whirling mode are plotted in Figure 4.16.

From Figure 4.16, it is observed that the standard deviations of the blade root edgewise moment M_x in Cases 1 and 2 remain relatively constant across the operating wind speed range, suggesting that the blade does not experience significant edgewise vibrations. In contrast, the scatter data in Case 3 shows a distinct divergence in the wind speed range of 12-14 m/s, indicating the occurrence of severe edgewise vibrations.

In the corresponding damping ratio plot in Figure 4.16, it is seen that the original blade design in Case 1 exhibits positive damping ratios of the rotor first edgewise backward whirling mode across the entire operating wind speed range. When the blade design is optimized to reduce mass and torsional stiffness, as in Case 2, the overall aeroelastic damping ratios decrease for operating wind speeds below 14 m/s, reaching a minimum value of -0.0007 at a wind speed of 13 m/s. When the rotor speed is increased in the wind speed range of 11-15 m/s, as in Case 3, the aeroelastic damping ratios decrease further, resulting in significant negative damping, with the lowest damping ratio of -0.006 occurring at a wind

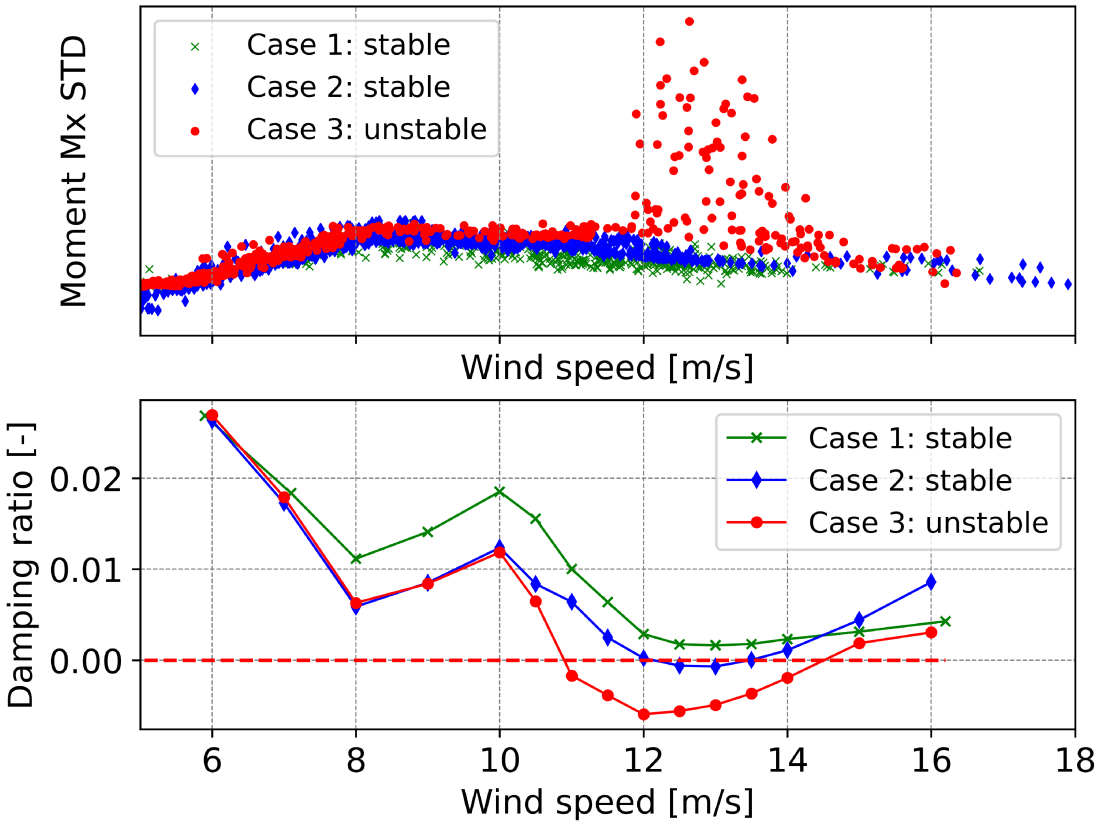

Figure 4.16: Comparison of the blade load measurement and computed aeroelastic damping ratios of the rotor first edgewise backward whirling mode. Each scatter point represents the standard deviation of the 10 min time series of the blade root edgewise moment M_x.

speed of 12 m/s.

The time series and the corresponding power spectral density (PSD) of the blade root edgewise moment M_x and the tower top side-side acceleration in the wind speed range of 12-14 m/s in Case 3 are analyzed to investigate the mechanism behind the potential blade edgewise vibrations, as shown in Figure 4.17. The blade first edgewise modal frequency f_{1E} is clearly evident in the PSD plot of the blade root edgewise moment M_x. Meanwhile, the rotor first edgewise backward and forward whirling modal frequencies, f_{1E_BW} and f_{1E_FW}, are dominant in the PSD of the tower top side-side acceleration. These PSD plots confirm that the blade experienced significant edgewise vibrations, which contributed to the divergent scatter data observed in the standard deviation plot in Figure 4.16.

Based on the comparison of the scatter plot showing the standard deviations of the blade root edgewise moment M_x and the aeroelastic damping ratios of the rotor

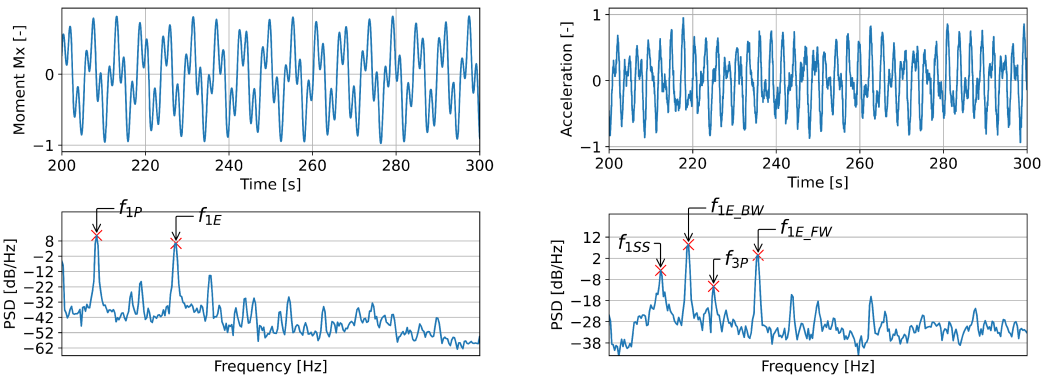

(a) Blade root edgewise moment (M_x). (b) Tower top side-side acceleration.

Figure 4.17: Time series and power spectral density (PSD) of the blade root edgewise moment (M_x) and tower top side-side acceleration selected from the wind speed range 12-14 m/s in Case 3. f_{1P}, f_{3P}: 1P, 3P rotor rotational frequencies; f_{1SS}: tower first side-side modal frequency; f_{1E}: blade first edgewise modal frequency observed in the blade root (rotating) frame; f_{1E_BW}, f_{1E_FW}: rotor first edgewise backward and forward whirling modal frequencies observed in the ground (fixed) frame.

first edgewise backward whirling mode for the three test cases, as illustrated in Figure 4.16, along with the analysis of the power spectral density (PSD) presented in Figure 4.17, it can be concluded that there is strong agreement between the aeroelastic stability predictions using the eigenvalue approach and the measurements on the prototype turbines.

However, in Case 2, although a slight negative damping ratio is predicted, the scatter data for the standard deviations of the blade root edgewise moment M_x do not exhibit any trend suggesting the presence of blade edgewise vibrations. This discrepancy may be due to the fact that the standard deviation of the blade root edgewise moment M_x is not sufficiently sensitive to detect minor edgewise vibrations. Alternatively, it could be that the vibration has not had sufficient time to develop, as the pitch angles change rapidly in turbulent wind conditions.

Additionally, the absence of anisotropic factors such as gravity, wind shear, wind inflow, yaw misalignment, pitch errors, and rotor mass imbalance, along with the neglect of dynamic inflow, dynamic stall effects on the rotor, and hydrodynamic effects on the supporting structure, may contribute to discrepancies between the numerical predictions and the measurements. These factors should be considered in future research to improve the accuracy of the predictions.

4.5 Concluding remarks

This chapter applies the proposed linearization and eigenvalue analysis methods to the stability analysis of multi-bladed rotor systems. The chapter is divided into two distinct topics, which are summarized separately.

4.5.1 Eigenvalues of the rotor's free rotation mode

The eigenvalues of the free rotation mode of three-bladed rotor systems are investigated. Numerical experiments are conducted on rotors of varying complexity, including a single rigid body, a rigid rotor, and a flexible rotor. The results demonstrate that the linearized DAEs in the multi-blade coordinates is suitable for the eigenvalue analysis of three-bladed rotors. The influence of the matrices $\boldsymbol{K}_g$, $\boldsymbol{K}_i$, $\boldsymbol{D}_i$, and $\boldsymbol{K}_c$ on the eigenvalues of the rotor's free rotation mode is discussed. The terms in the geometric stiffness matrix $\boldsymbol{K}_g$ due to transverse external follower forces, the tangent stiffness matrix of constraints $\boldsymbol{K}_c$ due to transverse external follower forces, and the inertial stiffness matrix $\boldsymbol{K}_i$ due to centrifugal forces exhibit a softening effect, shifting the eigenvalues toward real numbers. In contrast, the terms of the geometric stiffness matrix $\boldsymbol{K}_g$ due to centrifugal forces and the tangent stiffness matrix of constraints $\boldsymbol{K}_c$ due to centrifugal forces exhibit a stiffening effect, moving the eigenvalues toward pure imaginary numbers.

For effective controller design, aiming to achieve zero eigenvalues in the free rotation mode, it is generally necessary to omit the geometric stiffness matrix $\boldsymbol{K}_g$, the inertial stiffness matrix $\boldsymbol{K}_i$, and the tangent stiffness matrix of constraints $\boldsymbol{K}_c$ from the linearized DAEs. However, the inertial damping matrix $\boldsymbol{D}_i$ can still be included. The parameter sweep analysis shows that zero eigenvalues may be attainable at a specific rotational speed, even when all four matrices—$\boldsymbol{K}_g$, $\boldsymbol{K}_i$, $\boldsymbol{D}_i$, and $\boldsymbol{K}_c$—are considered. External follower forces acting on the blades tend to shift the eigenvalues toward real values, which negatively impacts the stability of the rotor's free rotation mode.

Future research should explore a rigorous corotational formulation for beam finite elements, as well as the development of a finite element model based on the Geometrically Exact Beam (GEB) theory. It would be particularly valuable to identify the conditions under which zero eigenvalues can be achieved when all geometric nonlinear terms, including $\boldsymbol{K}_g$, $\boldsymbol{K}_i$, and $\boldsymbol{K}_c$, are taken into account.

4.5.2 Verification and validation of stability analysis of wind turbines

A step-by-step verification and validation of the proposed aeroelastic stability assessment using the eigenvalue approach is performed.

Due to the significant bending-twist coupling in blade structures, the aeroelastic states in the deformed equilibrium configuration are crucial for accurate eigenvalue analysis and stability assessment of wind turbines. To this end, the modal frequencies of an isolated blade in its initial configuration, along with the blade deflections and aerodynamic information—including axial and tangential inductions, angle of attack, and aerodynamic forces—in the deformed equilibrium configuration are compared against the commercial tool Bladed, using the open-source IEA 15 MW reference wind turbine model. Excellent agreement is achieved between the present method and Bladed. Subsequently, the linearization and eigenvalue analysis of the IEA 15 MW reference wind turbine model is performed, and the Campbell diagram is presented. An analysis of the resonance risk and damping levels is subsequently carried out.

A virtual numerical experiment is then performed based on an intermediate-version wind turbine model provided by Goldwind. The standard deviation ratio of the component of the blade first edgewise mode to that of the 1P rotor rotational frequency, denoted as $r_{\mathrm{1E/1P}}$, is derived from time-domain nonlinear dynamic simulations and proposed as a measure to quantify the blade edgewise vibration level. The blade torsional stiffness is uniformly scaled along the spanwise to generate a series of wind turbine models. Time-domain dynamic simulations and modal analyses are conducted, and the standard deviation ratios $r_{\mathrm{1E/1P}}$ and the aeroelastic damping ratios of the rotor first edgewise backward whirling mode are compared across the operating wind speed range. The most critical wind speeds for blade edgewise vibration, identified from both time-domain simulations and modal analyses, deviate by 1 to 2 m/s. A strong correlation is observed between the standard deviation ratios $r_{\mathrm{1E/1P}}$ and the damping ratios ζ_{1E} of the rotor first edgewise backward whirling mode.

Finally, the aeroelastic stability predictions are validated against experimental data from two offshore prototype wind turbines provided by Goldwind. The unstable wind speed range, as observed from the standard deviations of the blade root edgewise moment, closely matches with the region of negative damping for the rotor first edgewise backward whirling mode. This validation demonstrates the applicability of the proposed aeroelastic stability assessment method in engineering practice. Potential sources of error in the present method are also discussed to guide future research directions.

Chapter 5

Modal reduction

Flexible multibody systems often involve complex structures where the flexibility cannot be ignored in order to ensure accurate dynamic simulations. Finite element methods can be directly applied to discretize flexible structures, capturing elastic deformations during large motions. However, when dealing with complex structural topologies, such as the lattice tower of an offshore wind turbine, this discretization may result in an excessive number of elements, leading to prohibitive computational costs. To address this challenge, modal reduction presents a viable approach to reduce the scale of the dynamics problem and significantly enhance computational efficiency.

In this chapter, we develop a modal reduction procedure based on the corotational concept. First, the system matrices of the subsystem are recovered from the original full-state system. A novel modal reduction transformation, which incorporates algebraic constraints, is then applied to reduce the number of DOFs using the modal acceleration method. The gross motion of the subsystem is decomposed into rigid-body motion and superimposed elastic deformation, both described in a floating frame of reference. Two projection matrices are derived to facilitate this motion decomposition. Subsequently, the tangent stiffness matrix and geometric stiffness matrix are formulated for the reduced subsystem. The inertial terms, including the mass, damping, and stiffness matrices, are analytically derived, along with the quadratic velocity term, which is crucial for accurately simulating rotating structures. External forces are also reduced accordingly, with a static correction mode introduced to capture the influence of external forces acting on the reduced internal nodes. Additionally, a scheme for updating the floating frame of reference based on Tisserand's criterion is presented. Finally, several numerical experiments are conducted to demonstrate the accuracy and effectiveness of the developed modal reduction procedure.

5.1 Introduction

For complex flexible structures undergoing large motion in the three dimensional space, the finite element technique is widely employed to discretize the continuum in the field of flexible multibody system dynamics. If the elastic deformation is small and approximately linear, the modal reduction method can be employed to significantly reduce the number of DOFs, thus enhance the computational performance while maintaining a reasonable accuracy.

The modal reduction method for flexible multibody systems has received extensive attention in the past. Here, we highlight a few key studies. Wu and Haug [287] proposed the multi-substructure technique to enhance the ability to capture geometric nonlinearity. Cardona and Géradin [51, 49] described the finite rotation in the Lie group and developed a corotational formulation for the modal reduction method, discussing some variants of mass discretization. Later, Cardona [50] extended the formulation to update the position and orientation of the floating frame as the weighted average of the incremental quantities of a selected set of element nodes, resulting in better computational accuracy. Cardona also emphasized the importance of the tangent pseudodamping matrix for improving convergence. Bauchau and Rodriguez [13] addressed five critical issues in the implementation of the modal reduction procedure based on the floating frame concept. They employed Herting's transformation as the component mode synthesis technique to provide maximum flexibility in the choice of the modal basis, and applied in the analysis of a coupled rotor-fuselage system [14].

In the FFRF, the nodal displacement field is defined relative to the floating frame of reference of the component. This formulation allows for the direct application of the modal reduction procedure [237]. However the generalized coordinates of boundary nodes among different flexible components are not consistent since the reference frames are not identical, when applying mechanical joints to build the connections between two components in the system, more effort is required to spend on the algebraic constraint formulation [287]. To this end, the absolute interface coordinates are proposed to ease the setup of constraints [75]. Meanwhile, the implementation of geometric stiffness matrix is recommended, as it can facilitate convergence in case of high external loads and/or large deformations [236]. The reference conditions used in the FFRF are of crucial importance to eliminate the redundant rigid-body motion of the flexible components relative to the floating frame of reference [46]. Zwölfer and Gerstmayr [301, 302, 303] developed a modal reduction approach for solid finite elements that calculates invariants without the cumbersome inertia shape integrals and without a lumped mass approximation. Géradin and Rixen [90, 89] proposed a two-field formulation in which the position and orientation, along with the resulting velocity field, are treated separately. This approach has been successfully applied in the dynamic analysis of high-speed rotating systems [91].

Sonneville at al. [251] proposed a linearized version of Tisserand's criterion [66] to determine the configuration of the floating frame of reference, which minimizes the elastic kinetic energy. Consequently, the gross displacement field of the flexible component is projected onto the rigid-body motion and elastic deformation measures, which are orthogonal to each other. The motion tensor is employed to parameterize the rigid-body motion [108], ensuring that the deformation measures are both objective and tensorial[1]. Numerical experiments have demonstrated that the proposed formulation, within the framework of the motion formalism, accurately captures geometrical nonlinearities.

The elastic deformation can be described in the local basis of a moving frame that accompanies the flexible component. Performing modal reduction in this local basis is intuitive, as demonstrated in the aforementioned studies. Alternatively, it is also possible to apply modal reduction in the inertial frame at the system level. A modal reduction method based on successive local linearizations at various deformed configurations for the ANCF has been developed [257, 266]. However, the frequent eigenvalue analysis and extensive matrix manipulations required by this approach may result in prohibitive computational costs. The global mode method may exhibit slow convergence and low accuracy if the modal basis is not appropriately chosen [44, 45].

In a multibody system, when a mechanical device is installed on a flexible structure, it could be possible to model it as a rigid body and attach to adjacent element nodes using fixed links. For beam elements used to discretize structures with large diameters, for instance, the tripod support structure of offshore wind turbines [148], it is preferable not to extend the beam element at 'T'-shaped welding points, as this could reduce structural stiffness and increase mass. Instead, fixed links are recommended to establish the connections, ensuring a more uniform overall flexibility of the structure. A very stiff spring or beam element could be used to replace the fixed link, thereby eliminating the algebraic constraints in the equations of motion. However, this approach makes the problem become stiff, potentially leading to numerical issues. In such scenarios, the modal reduction procedure for constrained flexible multibody systems is essential.

Cammarata et al. [47] introduced an interface reduction technique for rigid and interpolation multipoint constraints used in the FFRF. Both the rigid and interpolation multipoint constraints are eliminated via expressing the coordinates of the dependent node set with the coordinate of an independent virtual node, which is a formulation of minimal coordinate set [185], and hence no reaction forces in the multipoint constraints can be recovered directly. Furthermore, applying

[1] 'Objective' refers to quantities that remain invariant under rigid body motions of the reference frame, while 'tensorial' describes quantities that maintain consistency regardless of the chosen reference frame.

the interface reduction technique to the constraints between internal nodes is not straightforward.

Li et al. [166] developed a model reduction method via spectral submanifolds for constrained mechanical systems which involve periodic small-amplitude responses. However, this method does not address constrained flexible multibody systems that undergo large overall rigid-body motions with superimposed elastic deformations. Model order reduction for DAEs has been researched extensively within the context of control theory [27], though these approaches are not modal-based methods.

In this chapter, a modal reduction procedure based on the concept of the corotational formulation is developed. The mass, stiffness and constraint matrices of the subsystem are recovered in a local reference frame F. Subsequently, a modal reduction transformation using the mode acceleration method, which is extended here to the case of subsystems with constraints, is applied in the local reference frame. The generalized coordinates of the boundary nodes are retained unchanged to facilitate the setup of algebraic constraints with other system components. A projection method to decompose the gross motion into rigid-body motion and elastic deformations is developed. The tangent stiffness matrix and the inertial terms of the reduced subsystem are derived. A Newton–Raphson iteration scheme is proposed to update the configuration of the floating frame of reference F. In the end, several numerical examples are provided to demonstrate the applicability of the modal reduction method.

5.2 Kinematics

5.2.1 Positions, rotations and velocities

Assume a beam-like corotational subsystem moving in the three dimensional space, as schemed in Fig. 5.1. A floating frame F is attached in the subsystem and brings the shadow configuration from the initial position to the current. In this section we mark with the overline all quantities that are expressed in the local basis, i.e. in the F basis.

The motion of the subsystem can be decomposed to two components: the overall rigid-body motion represented by the movement of the floating frame of reference F, and the local elastic deformation with respect to the floating frame F.

In the initial configuration, the relative position vector of node N resolved in the initial floating frame F_0 is $\boldsymbol{u}_0 = \boldsymbol{R}_{F_0}^T (\boldsymbol{r}_0 - \boldsymbol{r}_{F_0})$[2], which is constant. The position vector of node N can be expressed as $\boldsymbol{r} = \boldsymbol{r}_F + \boldsymbol{R}_F (\boldsymbol{u}_0 + \overline{\boldsymbol{u}})$, where $\overline{\boldsymbol{u}}$ is the elastic

[2]In this chapter, the subscript '0' indicates that the quantity is evaluated in the initial configuration.

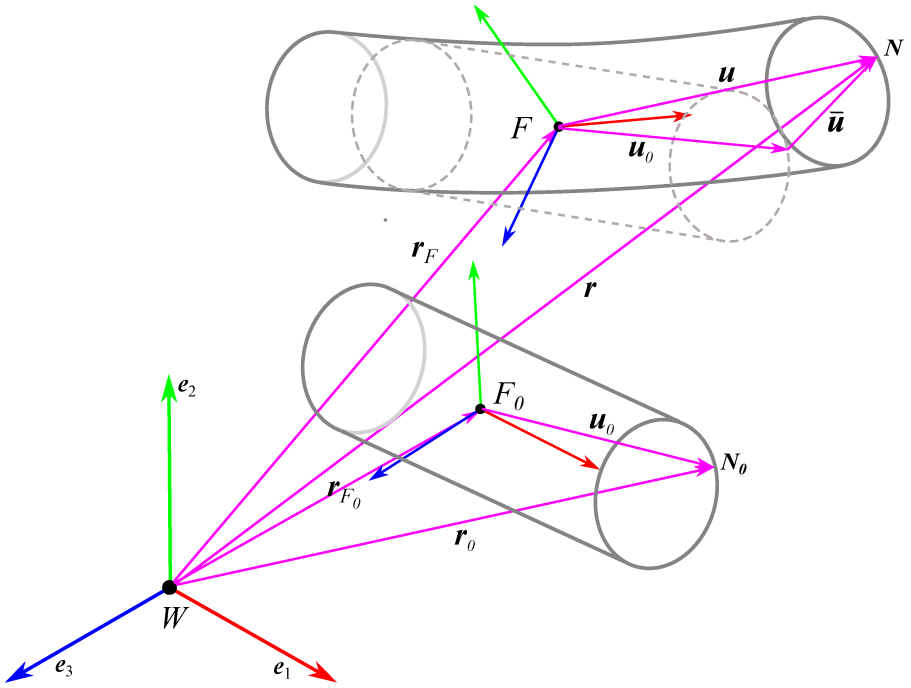

Figure 5.1: A beam-like corotational subsystem is bent and stretched. A generic node N goes from $\boldsymbol{r}_0$ to $\boldsymbol{r}$, while the floating frame of reference goes from F_0 to F. The so called shadow configuration is shown with dotted line.

deformation. The variation of the position is

$$\delta\boldsymbol{r} = \delta\boldsymbol{r}_F - \boldsymbol{R}_F\widetilde{(\boldsymbol{u}_0 + \overline{\boldsymbol{u}})}\delta\boldsymbol{\theta}_{l_F} + \boldsymbol{R}_F\delta\overline{\boldsymbol{u}} \tag{5.1}$$

The virtual rotation vector of node N in the local basis can be expressed as

$$\delta\boldsymbol{\theta}_l = \boldsymbol{R}_N^T\boldsymbol{R}_F\delta\boldsymbol{\theta}_{l_F} + \overline{\delta\boldsymbol{\theta}}_l \tag{5.2}$$

where $\boldsymbol{R}_N$ is the rotation tensor of node N.

$\overline{\delta\boldsymbol{\theta}}_l$ is the relative virtual rotation vector of node N with respect to the floating frame F but expressed in the local basis of node N; in contrast, $\delta\overline{\boldsymbol{u}}$ is the relative elastic deformation of node N with respect to the floating frame F and expressed in the floating frame F.

The translational velocity of node N can be expressed as

$$\dot{\boldsymbol{r}} = \dot{\boldsymbol{r}}_F - \boldsymbol{R}_F\widetilde{(\boldsymbol{u}_0 + \overline{\boldsymbol{u}})}\boldsymbol{\omega}_{l_F} + \boldsymbol{R}_F\dot{\overline{\boldsymbol{u}}} \tag{5.3}$$

where $\dot{\overline{\boldsymbol{u}}}$ is the elastic deformation velocity.

The relative rotational velocity $\overline{\boldsymbol{\omega}}_l$ of node N with respect to the floating frame F but expressed in the local basis of node N is given as

$$\overline{\boldsymbol{\omega}}_l = \boldsymbol{\omega}_l - \boldsymbol{R}_N^T\boldsymbol{R}_F\boldsymbol{\omega}_{l_F} \tag{5.4}$$

It can be proved that $\delta\overline{\boldsymbol{\omega}}_l = \dot{\overline{\delta\boldsymbol{\theta}}}_l + \widetilde{\overline{\boldsymbol{\omega}}}_l\overline{\delta\boldsymbol{\theta}}_l$ is also valid.

5.2.2 Coordinate transformation between inertial frame and local frame

The generalized coordinates of the subsystem $\boldsymbol{q} \in \mathbb{R}^n$ are partitioned into boundary and internal coordinates as $\boldsymbol{q} = \left[\boldsymbol{q}_B^T, \boldsymbol{q}_I^T\right]^T$. Figure 5.2 illustrates an example of this coordinate partitioning for a helicopter mesh. The boundary coordinates $\boldsymbol{q}_B \in \mathbb{R}^{n_B}$ are retained in the modal reduction procedure to ease the connection setup with other components in the system. The internal coordinates $\boldsymbol{q}_I \in \mathbb{R}^{n_I}$ will be reduced to the generalized modal coordinates $\boldsymbol{\eta} \in \mathbb{R}^{n_\eta}$.

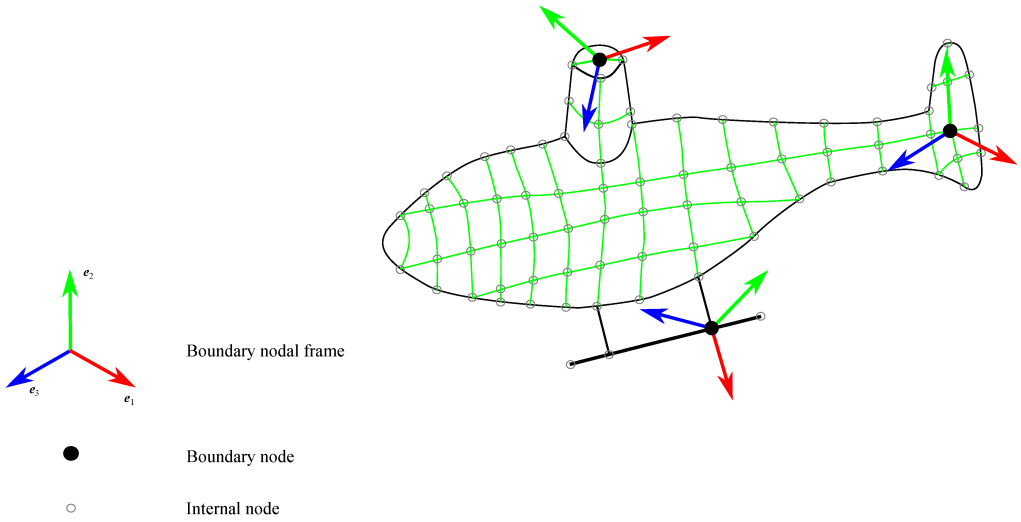

Figure 5.2: The partition of generalized coordinates of boundary and internal nodes for a helicopter mesh.

The mixed basis is employed in the full-state system, which says the translational coordinates are expressed in the absolute inertial frame, and the rotational coordinates in the local frame,

$$\delta\boldsymbol{q}_B = \begin{pmatrix} \delta\boldsymbol{r}_B \\ \delta\boldsymbol{\theta}_{l_B} \end{pmatrix}, \quad \delta\boldsymbol{q}_I = \begin{pmatrix} \delta\boldsymbol{r}_I \\ \delta\boldsymbol{\theta}_{l_I} \end{pmatrix}, \quad \delta\boldsymbol{q} = \begin{pmatrix} \delta\boldsymbol{q}_B \\ \delta\boldsymbol{q}_I \end{pmatrix} \tag{5.5}$$

The relative coordinates of boundary and internal nodes are introduced, respectively, as

$$\delta\overline{\boldsymbol{q}}_B = \begin{pmatrix} \delta\overline{\boldsymbol{u}}_B \\ \delta\overline{\boldsymbol{\theta}}_{l_B} \end{pmatrix}, \quad \delta\overline{\boldsymbol{q}}_I = \begin{pmatrix} \delta\overline{\boldsymbol{u}}_I \\ \delta\overline{\boldsymbol{\theta}}_{l_I} \end{pmatrix}, \quad \delta\overline{\boldsymbol{q}} = \begin{pmatrix} \delta\overline{\boldsymbol{q}}_B \\ \delta\overline{\boldsymbol{q}}_I \end{pmatrix} \tag{5.6}$$

Introducing the notation of the coordinate of the floating frame F

$$\delta\boldsymbol{q}_F = \begin{pmatrix} \delta\boldsymbol{r}_F \\ \delta\boldsymbol{\theta}_{l_F} \end{pmatrix} \tag{5.7}$$

and remembering the coordinate relations (5.1), (5.2), the coordinate transformation between (5.5) and (5.6) can be expressed in the compact form as

$$\delta \boldsymbol{q}_B = \boldsymbol{U}_B \delta \boldsymbol{q}_F + \boldsymbol{L}_B \delta \overline{\boldsymbol{q}}_B \tag{5.8a}$$

$$\delta \boldsymbol{q}_I = \boldsymbol{U}_I \delta \boldsymbol{q}_F + \boldsymbol{L}_I \delta \overline{\boldsymbol{q}}_I \tag{5.8b}$$

$$\delta \boldsymbol{q} = \boldsymbol{U} \delta \boldsymbol{q}_F + \boldsymbol{L} \delta \overline{\boldsymbol{q}} \tag{5.8c}$$

where

$$\boldsymbol{U} = \mathrm{vert}\left\{ \begin{bmatrix} \boldsymbol{I} & -\boldsymbol{R}_F(\widetilde{\boldsymbol{u}_0 + \overline{\boldsymbol{u}}}) \\ \boldsymbol{0} & \boldsymbol{R}_N^T \boldsymbol{R}_F \end{bmatrix} \right\}, \quad \boldsymbol{L} = \mathrm{diag}\left\{ \begin{bmatrix} \boldsymbol{R}_F & \boldsymbol{0} \\ \boldsymbol{0} & \boldsymbol{I} \end{bmatrix} \right\} \tag{5.9}$$

$\boldsymbol{U}_B$, $\boldsymbol{U}_I$, $\boldsymbol{L}_B$, $\boldsymbol{L}_I$ are the corresponding sliced sub-matrices for boundary and internal nodes.

$\boldsymbol{U}$ is the six rigid-body modes of the full-state subsystem associated with the original coordinates (5.5). The rigid-body modes $\boldsymbol{U}$ are dependent on the configuration of the subsystem and its floating frame F. Equation (5.8c) indicates that the motion of the subsystem can be decomposed to two components: the overall rigid-body motion represented by the movement of the floating frame of reference F — $\boldsymbol{U}\delta\boldsymbol{q}_F$, and the local elastic deformation with respect to the floating frame F — $\boldsymbol{L}\delta\overline{\boldsymbol{q}}$.

The corotational transformation matrix $\boldsymbol{L}$ has the following property

$$\boldsymbol{L}\boldsymbol{L}^T = \boldsymbol{L}^T\boldsymbol{L} = \boldsymbol{I} \tag{5.10}$$

Thanks to the similarity of variation and derivative, the velocity transformation can be expressed in the similar compact form as

$$\dot{\boldsymbol{q}}_B = \boldsymbol{U}_B \dot{\boldsymbol{q}}_F + \boldsymbol{L}_B \dot{\overline{\boldsymbol{q}}}_B \tag{5.11a}$$

$$\dot{\boldsymbol{q}}_I = \boldsymbol{U}_I \dot{\boldsymbol{q}}_F + \boldsymbol{L}_I \dot{\overline{\boldsymbol{q}}}_I \tag{5.11b}$$

$$\dot{\boldsymbol{q}} = \boldsymbol{U} \dot{\boldsymbol{q}}_F + \boldsymbol{L} \dot{\overline{\boldsymbol{q}}} \tag{5.11c}$$

where the notations of velocities are introduced as

$$\dot{\boldsymbol{q}}_B = \begin{pmatrix} \dot{\boldsymbol{r}}_B \\ \boldsymbol{\omega}_{l_B} \end{pmatrix}, \quad \dot{\boldsymbol{q}}_I = \begin{pmatrix} \dot{\boldsymbol{r}}_I \\ \boldsymbol{\omega}_{l_I} \end{pmatrix}, \quad \dot{\boldsymbol{q}} = \begin{pmatrix} \dot{\boldsymbol{q}}_B \\ \dot{\boldsymbol{q}}_I \end{pmatrix} \tag{5.12a}$$

$$\dot{\overline{\boldsymbol{q}}}_B = \begin{pmatrix} \dot{\overline{\boldsymbol{u}}}_B \\ \overline{\boldsymbol{\omega}}_{l_B} \end{pmatrix}, \quad \dot{\overline{\boldsymbol{q}}}_I = \begin{pmatrix} \dot{\overline{\boldsymbol{u}}}_I \\ \overline{\boldsymbol{\omega}}_{l_I} \end{pmatrix}, \quad \dot{\overline{\boldsymbol{q}}} = \begin{pmatrix} \dot{\overline{\boldsymbol{q}}}_B \\ \dot{\overline{\boldsymbol{q}}}_I \end{pmatrix} \tag{5.12b}$$

5.3 Local system matrices

In the modal reduction procedure for a subsystem undergoing large rotation, the configuration of the subsystem could experience significant changes due to the overall rigid-body motion, leading to vast differences of the tangent mass and stiffness

matrices in various configurations. To guarantee the applicability of the modal basis in the deformed configurations, we perform the modal reduction transformation in the local basis of the floating frame of reference F in this work. This could be straightforward to do in the FFRF [237], but more attention should be paid in the CRF [80, 262], the GEBT [250, 261] and the ANCF [239, 202] since in the latter three cases the inertial frame is usually chosen as the reference frame in general.

The local mass and stiffness matrices can be setup using third-party finite element packages, and then imported into the multibody dynamics simulation tool. In this case, the inertial frame in the finite element package is initialized as the reference frame of the modal element in the multibody tool. Alternatively, the local mass and stiffness matrices can be recovered from the original tangent mass and stiffness matrices associated with the coordinates (5.5) in the multibody tool, respectively. The constraint Jacobian matrix can also be tackled for constrained subsystems.

5.3.1 Local stiffness matrix

The original tangent stiffness matrix $\boldsymbol{K}$ of the subsystem associated with the coordinates (5.5), for example derived from CRF and GEBT in the multibody dynamics simulation tool, can be partitioned into four blocks according to the boundary and internal nodes

$$\boldsymbol{K} = \begin{bmatrix} \boldsymbol{K}_{BB} & \boldsymbol{K}_{BI} \\ \boldsymbol{K}_{IB} & \boldsymbol{K}_{II} \end{bmatrix} \tag{5.13}$$

Remembering (5.8c), the virtual work done by the elastic forces is evaluated as

$$\begin{aligned} \delta\mathcal{W}_{\mathrm{E}} &= \delta\boldsymbol{q}^T \boldsymbol{K} \Delta\boldsymbol{q} \\ &= \begin{pmatrix} \delta\boldsymbol{q}_F^T & \delta\overline{\boldsymbol{q}}^T \end{pmatrix} \begin{bmatrix} \boldsymbol{K}_{FF} & \boldsymbol{K}_{FB} & \boldsymbol{K}_{FI} \\ \boldsymbol{K}_{FB}^T & \boldsymbol{L}_B^T \boldsymbol{K}_{BB} \boldsymbol{L}_B & \boldsymbol{L}_B^T \boldsymbol{K}_{BI} \boldsymbol{L}_I \\ \boldsymbol{K}_{FI}^T & \boldsymbol{L}_I^T \boldsymbol{K}_{IB} \boldsymbol{L}_B & \boldsymbol{L}_I^T \boldsymbol{K}_{II} \boldsymbol{L}_I \end{bmatrix} \begin{pmatrix} \Delta\boldsymbol{q}_F \\ \Delta\overline{\boldsymbol{q}} \end{pmatrix} \end{aligned} \tag{5.14}$$

where

$$\boldsymbol{K}_{FF} = \boldsymbol{U}_B^T \boldsymbol{K}_{BB} \boldsymbol{U}_B + \boldsymbol{U}_I^T \boldsymbol{K}_{IB} \boldsymbol{U}_B + \boldsymbol{U}_B^T \boldsymbol{K}_{BI} \boldsymbol{U}_I + \boldsymbol{U}_I^T \boldsymbol{K}_{II} \boldsymbol{U}_I \tag{5.15a}$$

$$\boldsymbol{K}_{FB} = \boldsymbol{U}_B^T \boldsymbol{K}_{BB} \boldsymbol{L}_B + \boldsymbol{U}_I^T \boldsymbol{K}_{IB} \boldsymbol{L}_B \tag{5.15b}$$

$$\boldsymbol{K}_{FI} = \boldsymbol{U}_B^T \boldsymbol{K}_{BI} \boldsymbol{L}_I + \boldsymbol{U}_I^T \boldsymbol{K}_{II} \boldsymbol{L}_I \tag{5.15c}$$

The bottom-right four blocks of the centered matrix in (5.14) which are associated with the generalized coordinate $\delta\overline{\boldsymbol{q}}$, represent the stiffness property with respect to the reference frame F. Therefore, they constitute the exact local stiffness matrix

$$\boldsymbol{K}_{\mathrm{loc}} = \begin{bmatrix} \boldsymbol{L}_B^T \boldsymbol{K}_{BB} \boldsymbol{L}_B & \boldsymbol{L}_B^T \boldsymbol{K}_{BI} \boldsymbol{L}_I \\ \boldsymbol{L}_I^T \boldsymbol{K}_{IB} \boldsymbol{L}_B & \boldsymbol{L}_I^T \boldsymbol{K}_{II} \boldsymbol{L}_I \end{bmatrix} = \boldsymbol{L}^T \boldsymbol{K} \boldsymbol{L} \tag{5.16}$$

Exploiting the property of $\boldsymbol{L}$ in (5.10), one has

$$\boldsymbol{K} = \boldsymbol{L}\boldsymbol{K}_{\mathrm{loc}}\boldsymbol{L}^T \tag{5.17}$$

5.3.2 Local mass matrix

The original tangent mass matrix of the subsystem can be partitioned as

$$\boldsymbol{M} = \begin{bmatrix} \boldsymbol{M}_{BB} & \boldsymbol{M}_{BI} \\ \boldsymbol{M}_{IB} & \boldsymbol{M}_{II} \end{bmatrix} \tag{5.18}$$

Remembering (5.11c), the kinetic energy of the subsystem is evaluated as

$$\begin{aligned} \mathcal{W}_{\mathrm{K}} &= \dot{\boldsymbol{q}}^T \boldsymbol{M} \dot{\boldsymbol{q}} \\ &= \begin{pmatrix} \dot{\boldsymbol{q}}_F^T & \dot{\bar{\boldsymbol{q}}}^T \end{pmatrix} \begin{bmatrix} \boldsymbol{M}_{FF} & \boldsymbol{M}_{FB} & \boldsymbol{M}_{FI} \\ \boldsymbol{M}_{FB}^T & \boldsymbol{L}_B^T \boldsymbol{M}_{BB} \boldsymbol{L}_B & \boldsymbol{L}_B^T \boldsymbol{M}_{BI} \boldsymbol{L}_I \\ \boldsymbol{M}_{FI}^T & \boldsymbol{L}_I^T \boldsymbol{M}_{IB} \boldsymbol{L}_B & \boldsymbol{L}_I^T \boldsymbol{M}_{II} \boldsymbol{L}_I \end{bmatrix} \begin{pmatrix} \dot{\boldsymbol{q}}_F \\ \dot{\bar{\boldsymbol{q}}} \end{pmatrix} \end{aligned} \tag{5.19}$$

where

$$\boldsymbol{M}_{FF} = \boldsymbol{U}_B^T \boldsymbol{M}_{BB} \boldsymbol{U}_B + \boldsymbol{U}_I^T \boldsymbol{M}_{IB} \boldsymbol{U}_B + \boldsymbol{U}_B^T \boldsymbol{M}_{BI} \boldsymbol{U}_I + \boldsymbol{U}_I^T \boldsymbol{M}_{II} \boldsymbol{U}_I \tag{5.20a}$$

$$\boldsymbol{M}_{FB} = \boldsymbol{U}_B^T \boldsymbol{M}_{BB} \boldsymbol{L}_B + \boldsymbol{U}_I^T \boldsymbol{M}_{IB} \boldsymbol{L}_B \tag{5.20b}$$

$$\boldsymbol{M}_{FI} = \boldsymbol{U}_B^T \boldsymbol{M}_{BI} \boldsymbol{L}_I + \boldsymbol{U}_I^T \boldsymbol{M}_{II} \boldsymbol{L}_I \tag{5.20c}$$

The local mass matrix of the subsystem in the floating frame F can be extracted from the bottom-right four blocks of the centered matrix as

$$\boldsymbol{M}_{\mathrm{loc}} = \begin{bmatrix} \boldsymbol{L}_B^T \boldsymbol{M}_{BB} \boldsymbol{L}_B & \boldsymbol{L}_B^T \boldsymbol{M}_{BI} \boldsymbol{L}_I \\ \boldsymbol{L}_I^T \boldsymbol{M}_{IB} \boldsymbol{L}_B & \boldsymbol{L}_I^T \boldsymbol{M}_{II} \boldsymbol{L}_I \end{bmatrix} = \boldsymbol{L}^T \boldsymbol{M} \boldsymbol{L} \tag{5.21}$$

Here the lumped mass assumption is not employed, and hence the recovery algorithm in (5.21) is also applicable for the consistent mass matrix.

Exploiting the property of $\boldsymbol{L}$ in (5.10), one has

$$\boldsymbol{M} = \boldsymbol{L}\boldsymbol{M}_{\mathrm{loc}}\boldsymbol{L}^T \tag{5.22}$$

5.3.3 Local constraint Jacobian matrix

A constraint Jacobian matrix could be present in constrained subsystems. Similar as the mass and stiffness matrices, we also need to recover the constraint Jacobian matrix expressed in the local basis of the floating frame F.

Because the DOFs of rigid-body motions experience significant geometrical nonlinearity which is not compatible with the employed small deformation assumption,

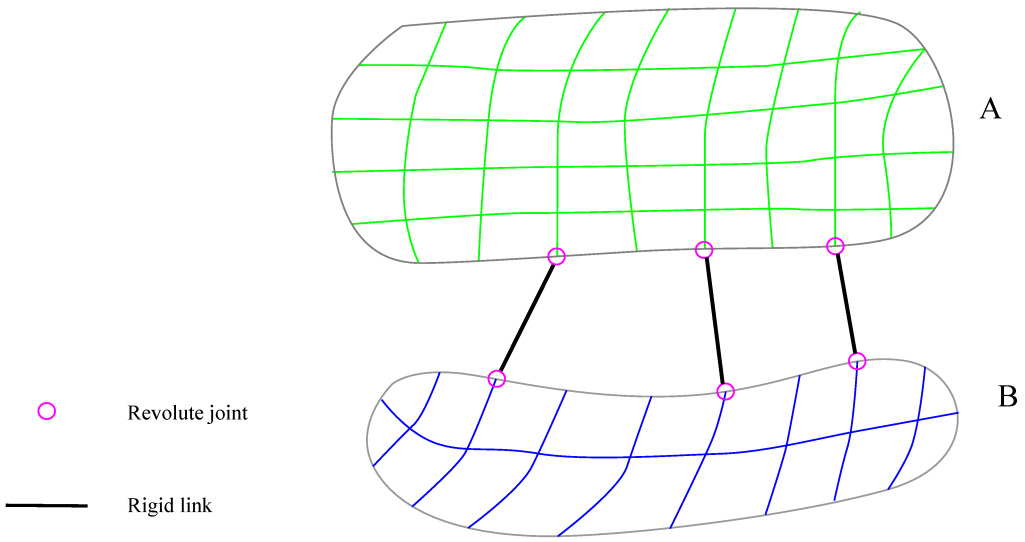

Figure 5.3: A constrained subsystem including a link mechanism, which eliminates the large rigid-body motion between two flexible parts.

it is assumed that in the modal reduction procedure only small relative displacements and rotations are expected within the constrained subsystem. This is typically the case when fixed joints are present, or when the DOFs corresponding to large rigid-body motions are eliminated through specific spatial configurations, such as the link mechanism shown in Figure 5.3.

The original constraint Jacobian matrix of the constrained subsystem can be partitioned into two blocks in the column wise according to the boundary and internal nodes as

$$\boldsymbol{C}_{\boldsymbol{q}} = \begin{bmatrix} \boldsymbol{C}_{\boldsymbol{q}_{IB}} & \boldsymbol{C}_{\boldsymbol{q}_{II}} \end{bmatrix} \tag{5.23}$$

where $\boldsymbol{C}_{\boldsymbol{q}_{IB}}$ is the fixed constraints connecting boundary nodes with internal nodes, and $\boldsymbol{C}_{\boldsymbol{q}_{II}}$ constrains two sets of internal nodes. The corresponding Lagrange Multipliers $\boldsymbol{\gamma}_I$ are tackled as generalized internal DOFs of the subsystem, which will be reduced. The links to connect two sets of boundary nodes are retained in the modal reduction procedure, and should not be collected into (5.23).

Since the constraints and their Jacobian matrices are already expressed in a local frame attached at the second node or rigid-body of the link, as described in Section 2.5, no further transformation for the Lagrange multipliers $\boldsymbol{\gamma}_I$ is required.

Remembering (5.8c), the virtual work done by the reaction forces of constraints is

$$\begin{aligned} \delta \mathcal{W}_\lambda &= \delta \boldsymbol{q}^T \boldsymbol{C}_{\boldsymbol{q}}{}^T \boldsymbol{\gamma}_I \\ &= \begin{pmatrix} \delta \boldsymbol{q}_F^T & \delta \overline{\boldsymbol{q}}^T \end{pmatrix} \begin{bmatrix} \boldsymbol{C}_{\boldsymbol{q}_{IF}} & \boldsymbol{C}_{\boldsymbol{q}_{IB}} \boldsymbol{L}_B & \boldsymbol{C}_{\boldsymbol{q}_{II}} \boldsymbol{L}_I \end{bmatrix}^T \boldsymbol{\gamma}_I \end{aligned} \tag{5.24}$$

where

$$\boldsymbol{C}_{\boldsymbol{q}IF} = \boldsymbol{C}_{\boldsymbol{q}IB}\boldsymbol{U}_B + \boldsymbol{C}_{\boldsymbol{q}II}\boldsymbol{U}_I \tag{5.25}$$

The local constraint Jacobian matrix of the constrained subsystem in the floating frame F can be extracted from the right two blocks of the centered matrix as

$$\boldsymbol{C}_{\boldsymbol{q}\mathrm{loc}} = \begin{bmatrix}\boldsymbol{C}_{\boldsymbol{q}IB}\boldsymbol{L}_B & \boldsymbol{C}_{\boldsymbol{q}II}\boldsymbol{L}_I\end{bmatrix} = \boldsymbol{C}_{\boldsymbol{q}}\boldsymbol{L} \tag{5.26}$$

Exploiting the property of $\boldsymbol{L}$ in (5.10), one has

$$\boldsymbol{C}_{\boldsymbol{q}} = \boldsymbol{C}_{\boldsymbol{q}\mathrm{loc}}\boldsymbol{L}^T \tag{5.27}$$

5.4 Modal reduction for a subsystem with constraints

In this work, the modal reduction is carried out in the initial configuration. If external forces are imposed on the subsystem in the initial configuration, the internal stress in the finite elements and the internal reaction forces of links will present in the equilibrium configuration, leading to nonzero material stiffness matrix $\boldsymbol{K}_m$, nonzero geometric stiffness matrix $\boldsymbol{K}_g$, and nonzero tangent stiffness matrix of constraints $\boldsymbol{K}_c$. If some mass particles are rotating about a central axis, the inertial stiffness matrix $\boldsymbol{K}_I$ appears. The eigenvalues and eigenvectors of the GEP with nonzero $\boldsymbol{K}_g$, $\boldsymbol{K}_c$ and $\boldsymbol{K}_I$ are complex numbers [207], which will significantly complicate the modal coordinate transformation. To simplify the problem, we assume there are no internal stress, no internal reaction forces and no rotational speed in the initial configuration. As a consequence, $\boldsymbol{K}_g$, $\boldsymbol{K}_c$ and $\boldsymbol{K}_I$ vanish, and hence only the material stiffness matrix $\boldsymbol{K}_m$ presents in (5.13).

Introduce the augmented local mass matrix $\boldsymbol{M}_{C_{\mathrm{loc}}}$ and the augmented local stiffness matrix $\boldsymbol{K}_{C_{\mathrm{loc}}}$ as

$$\boldsymbol{M}_{C_{\mathrm{loc}}} = \begin{bmatrix}\boldsymbol{M}_{BB_{\mathrm{loc}}} & \boldsymbol{M}_{BI_{\mathrm{loc}}} & \boldsymbol{0}\\ \boldsymbol{M}_{IB_{\mathrm{loc}}} & \boldsymbol{M}_{II_{\mathrm{loc}}} & \boldsymbol{0}\\ \boldsymbol{0} & \boldsymbol{0} & \boldsymbol{0}\end{bmatrix}, \quad \boldsymbol{K}_{C_{\mathrm{loc}}} = \begin{bmatrix}\boldsymbol{K}_{BB_{\mathrm{loc}}} & \boldsymbol{K}_{BI_{\mathrm{loc}}} & \boldsymbol{C}_{\boldsymbol{q}IB_{\mathrm{loc}}}^T\\ \boldsymbol{K}_{IB_{\mathrm{loc}}} & \boldsymbol{K}_{II_{\mathrm{loc}}} & \boldsymbol{C}_{\boldsymbol{q}II_{\mathrm{loc}}}^T\\ \boldsymbol{C}_{\boldsymbol{q}IB_{\mathrm{loc}}} & \boldsymbol{C}_{\boldsymbol{q}II_{\mathrm{loc}}} & \boldsymbol{0}\end{bmatrix} \tag{5.28}$$

where $\boldsymbol{M}_{\mathrm{loc}}$, $\boldsymbol{K}_{\mathrm{loc}}$, $\boldsymbol{C}_{\boldsymbol{q}\mathrm{loc}}$ are partitioned into sub-blocks according to boundary and internal nodes, similar as in (5.13), (5.18) and (5.23).

The sub-block matrices are

$$\boldsymbol{M}_{BB_{\text{loc}}} = \boldsymbol{L}_B^T \boldsymbol{M}_{BB} \boldsymbol{L}_B, \quad \boldsymbol{M}_{BI_{\text{loc}}} = \boldsymbol{L}_B^T \boldsymbol{M}_{BI} \boldsymbol{L}_I \tag{5.29a}$$

$$\boldsymbol{M}_{IB_{\text{loc}}} = \boldsymbol{L}_I^T \boldsymbol{M}_{IB} \boldsymbol{L}_B, \quad \boldsymbol{M}_{II_{\text{loc}}} = \boldsymbol{L}_I^T \boldsymbol{M}_{II} \boldsymbol{L}_I \tag{5.29b}$$

$$\boldsymbol{K}_{BB_{\text{loc}}} = \boldsymbol{L}_B^T \boldsymbol{K}_{BB} \boldsymbol{L}_B, \quad \boldsymbol{K}_{BI_{\text{loc}}} = \boldsymbol{L}_B^T \boldsymbol{K}_{BI} \boldsymbol{L}_I \tag{5.29c}$$

$$\boldsymbol{K}_{IB_{\text{loc}}} = \boldsymbol{L}_I^T \boldsymbol{K}_{IB} \boldsymbol{L}_B, \quad \boldsymbol{K}_{II_{\text{loc}}} = \boldsymbol{L}_I^T \boldsymbol{K}_{II} \boldsymbol{L}_I \tag{5.29d}$$

$$\boldsymbol{C}_{\boldsymbol{q}IB_{\text{loc}}} = \boldsymbol{C}_{\boldsymbol{q}IB} \boldsymbol{L}_B, \quad \boldsymbol{C}_{\boldsymbol{q}II_{\text{loc}}} = \boldsymbol{C}_{\boldsymbol{q}II} \boldsymbol{L}_I \tag{5.29e}$$

Ignoring the damping matrix $\boldsymbol{D}$ first, the equations of motion of the constrained subsystem can be expressed in the local basis of the floating frame F as

$$\begin{bmatrix} \boldsymbol{M}_{BB_{\text{loc}}} & \boldsymbol{M}_{BI_{\text{loc}}} & \boldsymbol{0} \\ \boldsymbol{M}_{IB_{\text{loc}}} & \boldsymbol{M}_{II_{\text{loc}}} & \boldsymbol{0} \\ \boldsymbol{0} & \boldsymbol{0} & \boldsymbol{0} \end{bmatrix} \begin{pmatrix} \delta\ddot{\overline{\boldsymbol{q}}}_B \\ \delta\ddot{\overline{\boldsymbol{q}}}_I \\ \delta\ddot{\boldsymbol{\gamma}}_I \end{pmatrix} + \begin{bmatrix} \boldsymbol{K}_{BB_{\text{loc}}} & \boldsymbol{K}_{BI_{\text{loc}}} & \boldsymbol{C}_{\boldsymbol{q}IB_{\text{loc}}}^T \\ \boldsymbol{K}_{IB_{\text{loc}}} & \boldsymbol{K}_{II_{\text{loc}}} & \boldsymbol{C}_{\boldsymbol{q}II_{\text{loc}}}^T \\ \boldsymbol{C}_{\boldsymbol{q}IB_{\text{loc}}} & \boldsymbol{C}_{\boldsymbol{q}II_{\text{loc}}} & \boldsymbol{0} \end{bmatrix} \begin{pmatrix} \delta\overline{\boldsymbol{q}}_B \\ \delta\overline{\boldsymbol{q}}_I \\ \delta\boldsymbol{\gamma}_I \end{pmatrix} = \begin{pmatrix} \overline{\boldsymbol{f}}_B \\ \overline{\boldsymbol{f}}_I \\ \boldsymbol{0} \end{pmatrix} \tag{5.30}$$

where $\overline{\boldsymbol{f}}_B \in \mathbb{R}^{n_B}$ and $\overline{\boldsymbol{f}}_I \in \mathbb{R}^{n_I}$ are the external forces imposed on boundary and internal nodes, respectively, and both are expressed in the local basis of the floating frame F.

The constrained subsystem described in (5.30) does not involve any constraints with other components in the system, thus six rigid-body modes exist in its modal result.

The eigenvectors of the full constrained subsystem can be computed by solving the GEP [178]:

$$-\boldsymbol{K}_{C_{\text{loc}}} \hat{\boldsymbol{\Phi}}_i = \lambda_i \boldsymbol{M}_{C_{\text{loc}}} \hat{\boldsymbol{\Phi}}_i \tag{5.31}$$

The natural frequency can be recovered from the eigenvalue as $\omega_i = \sqrt{-\lambda_i}$. The eigenvector can be partitioned as $\hat{\boldsymbol{\Phi}}_i = \left[\boldsymbol{\Phi}_i^T, \boldsymbol{\xi}_i^T\right]^T$, where $\boldsymbol{\xi}_i$ is the piecewise corresponding to the Lagrange multipliers of constraints $\boldsymbol{\gamma}_I$. We retain only the first n_η modes to make the modal shape matrix $\boldsymbol{\Phi} \in \mathbb{R}^{n \times n_\eta}$, which is then partitioned as $\boldsymbol{\Phi} = \left[\boldsymbol{\Phi}_B^T, \boldsymbol{\Phi}_I^T\right]^T$ according to the boundary and internal nodes. In general, $n_\eta \ll n$, leading to reduce the problem size significantly.

The constrained subsystem described in (5.30) does not involve any constraints connecting the subsystem with outer components in the system, thus six rigid-body modes exist in its modal result, leading to an important property

$$\boldsymbol{K}_{C_{\text{loc}}} \boldsymbol{U}_{C_{\text{loc}}} = \boldsymbol{0} \tag{5.32}$$

where $\boldsymbol{U}_{C_{\text{loc}}}$ is the augmented local rigid-body mode matrix expressed as

$$\boldsymbol{U}_{\text{loc}} = \text{vert}\left\{ \begin{bmatrix} \boldsymbol{I} & -\widetilde{(\boldsymbol{u}_0 + \overline{\boldsymbol{u}})} \\ \boldsymbol{0} & \boldsymbol{R}_N^T \boldsymbol{R}_F \end{bmatrix} \right\}, \quad \boldsymbol{U}_{C_{\text{loc}}} = \begin{bmatrix} \boldsymbol{U}_{\text{loc}} \\ \boldsymbol{0}_{m \times 6} \end{bmatrix} \tag{5.33}$$

$\boldsymbol{U}_{\text{loc}}$ is the rigid-body modes in the local basis of the floating frame F, and can be partitioned into two components $\boldsymbol{U}_{B_{\text{loc}}}$, $\boldsymbol{U}_{I_{\text{loc}}}$ for the boundary and internal nodes, respectively.

It might be worth noting that if $\boldsymbol{K}_g$, $\boldsymbol{K}_c$, $\boldsymbol{K}_I$ present in $\boldsymbol{K}_{C_{\text{loc}}}$ in the initial configuration, the eigenvalues μ_i corresponding to the rigid-body modes $\boldsymbol{U}_{C_{\text{loc}}}$ might be nonzero [207], then by remembering (5.31), the equation (5.32) is not valid anymore.

The dynamic response of the augmented elastic displacement field can be expressed as a linear combination of the retained modes

$$\left[\delta\overline{\boldsymbol{q}}_B^T, \delta\overline{\boldsymbol{q}}_I^T, \delta\boldsymbol{\gamma}_I^T\right]^T \approx \left[\boldsymbol{\Phi}_B^T, \boldsymbol{\Phi}_I^T, \boldsymbol{\xi}^T\right]^T \delta\boldsymbol{\eta}_{\text{pos}} \tag{5.34}$$

In the mode acceleration method, the generalized acceleration of the augmented elastic deformation can be expressed with the generalized modal coordinate $\delta\boldsymbol{\eta}_d$ approximately as [67]:

$$\left[\delta\ddot{\overline{\boldsymbol{q}}}_B^T, \delta\ddot{\overline{\boldsymbol{q}}}_I^T, \delta\ddot{\boldsymbol{\gamma}}_I^T\right]^T \approx \left[\boldsymbol{\Phi}_B^T, \boldsymbol{\Phi}_I^T, \boldsymbol{\xi}^T\right]^T \delta\boldsymbol{\eta}_d \tag{5.35}$$

where $\delta\boldsymbol{\eta}_d = \boldsymbol{\Omega}^2\delta\boldsymbol{\eta}_{\text{pos}}$ is the scaled modal coordinate representing the acceleration level. $\boldsymbol{\Omega}$ is a diagonal matrix composed of the selected natural frequencies ω_i.

For ease of notation, we introduce the augmented internal stiffness matrices

$$\boldsymbol{K}_{IBC_{\text{loc}}} = \begin{bmatrix}\boldsymbol{K}_{IB_{\text{loc}}} \\ \boldsymbol{C}_{\boldsymbol{q}IB_{\text{loc}}}\end{bmatrix}, \quad \boldsymbol{K}_{IIC_{\text{loc}}} = \begin{bmatrix}\boldsymbol{K}_{II_{\text{loc}}} & \boldsymbol{C}_{\boldsymbol{q}II_{\text{loc}}}^T \\ \boldsymbol{C}_{\boldsymbol{q}II_{\text{loc}}} & \boldsymbol{0}\end{bmatrix} \tag{5.36}$$

and the augmented local rigid-body mode matrix for the internal nodes and internal constraints

$$\boldsymbol{U}_{IC_{\text{loc}}} = \begin{bmatrix}\boldsymbol{U}_{I_{\text{loc}}} \\ \boldsymbol{0}_{m\times 6}\end{bmatrix} \tag{5.37}$$

Making use of (5.32), one obtains the equation

$$\boldsymbol{K}_{IBC_{\text{loc}}}\boldsymbol{U}_{B_{\text{loc}}} + \boldsymbol{K}_{IIC_{\text{loc}}}\boldsymbol{U}_{IC_{\text{loc}}} = \boldsymbol{0} \tag{5.38}$$

Substituting (5.35) into (5.30), and using the notations (5.36), the internal generalized coordinates can be expressed as

$$\begin{aligned}\begin{pmatrix}\delta\overline{\boldsymbol{q}}_I \\ \delta\boldsymbol{\gamma}_I\end{pmatrix} = &- \boldsymbol{K}_{IIC_{\text{loc}}}^{-1}\boldsymbol{K}_{IBC_{\text{loc}}}\delta\overline{\boldsymbol{q}}_B - \boldsymbol{K}_{IIC_{\text{loc}}}^{-1}\begin{bmatrix}\boldsymbol{M}_{IB_{\text{loc}}}\boldsymbol{\Phi}_B + \boldsymbol{M}_{II_{\text{loc}}}\boldsymbol{\Phi}_I \\ \boldsymbol{0}\end{bmatrix}\delta\boldsymbol{\eta}_d \\ &+ \boldsymbol{K}_{IIC_{\text{loc}}}^{-1}\begin{pmatrix}\overline{\boldsymbol{f}}_I \\ \boldsymbol{0}\end{pmatrix}\end{aligned} \tag{5.39}$$

We define the augmented static modes

$$\boldsymbol{\Psi}_{s_C} = \begin{bmatrix} \boldsymbol{\Psi}_{s_I} \\ \boldsymbol{\Psi}_{s_\gamma} \end{bmatrix} = -\boldsymbol{K}_{IIC_{\mathrm{loc}}}^{-1} \boldsymbol{K}_{IBC_{\mathrm{loc}}} \in \mathbb{R}^{n_I \times n_B} \tag{5.40}$$

and the augmented dynamic modes

$$\boldsymbol{\Psi}_{d_C} = \begin{bmatrix} \boldsymbol{\Psi}_{d_I} \\ \boldsymbol{\Psi}_{d_\gamma} \end{bmatrix} = -\boldsymbol{K}_{IIC_{\mathrm{loc}}}^{-1} \begin{bmatrix} \boldsymbol{M}_{IB_{\mathrm{loc}}} \boldsymbol{\Phi}_B + \boldsymbol{M}_{II_{\mathrm{loc}}} \boldsymbol{\Phi}_I \\ \mathbf{0} \end{bmatrix} \in \mathbb{R}^{n_I \times n_\eta} \tag{5.41}$$

To ensure a proper recovery of internal stress and reaction forces from the reduced subsystem, the modal truncation augmentation method is necessary to be supplemented in the mode acceleration method when external forces are imposed on the internal nodes [67, 226]. To this end, we introduce the augmented static correction mode to compensate the contribution of the absent higher-order modes to the quasi-static response under the external forces $\overline{\boldsymbol{f}}_I$

$$\boldsymbol{\Psi}_{r_C} = \begin{bmatrix} \boldsymbol{\Psi}_{r_I} \\ \boldsymbol{\Psi}_{r_\gamma} \end{bmatrix} = \boldsymbol{K}_{IIC_{\mathrm{loc}}}^{-1} \begin{pmatrix} \overline{\boldsymbol{f}}_I \\ \mathbf{0} \end{pmatrix} \in \mathbb{R}^{n_I \times 1} \tag{5.42}$$

If the forces distributed on the internal nodes $\overline{\boldsymbol{f}}_I$ are split into more sets and then the augmented static correction modes $\boldsymbol{\Psi}_{r_C}$ are constructed correspondingly, a better numerical accuracy can be achieved at the cost of lower computational performance. Alternatively, higher order static correction modes can be involved to drastically decrease the residual forces and obtain accuracy boost [226, 227, 165], but the complexity of matrix manipulation has also increased substantially, leading to a significant decline in computational performance. At the end, we simply implement the algorithm (5.42) as a compromise between numerical accuracy and computational performance.

It is worth noting that $\boldsymbol{\Psi}_{d_\gamma} \neq \mathbf{0}$, $\boldsymbol{\Psi}_{r_\gamma} \neq \mathbf{0}$ in (5.41), (5.42), respectively.

The columns in the augmented static modes $\boldsymbol{\Psi}_{s_C}$ can be interpreted as the static displacements of internal nodes and the static reaction forces of internal constraints when a unit displacement is applied on every single DOF of boundary nodes. Employing the equation (5.38), the augmented static modes $\boldsymbol{\Psi}_{s_C}$ also build the relation between the rigid-body modes of boundary and internal nodes as

$$\boldsymbol{\Psi}_{s_C} \boldsymbol{L}_B^T \boldsymbol{U}_B = \begin{bmatrix} \boldsymbol{L}_I^T \boldsymbol{U}_I \\ \mathbf{0}_{m \times 6} \end{bmatrix} \tag{5.43}$$

We remark that the computations of $\boldsymbol{\Psi}_{s_C}$, $\boldsymbol{\Psi}_{d_C}$ and $\boldsymbol{\Psi}_{r_C}$ require the inverse $\boldsymbol{K}_{IIC_{\mathrm{loc}}}^{-1}$, however there is no need to compute the inverse, that would destroy sparsity, because it is enough to perform a QR factorization of $\boldsymbol{K}_{IIC_{\mathrm{loc}}}$ once, and use such factorization n_B times to compute the n_B columns of $\boldsymbol{\Psi}_{s_C}$, as well as use it n_η times to compute the n_η columns of $\boldsymbol{\Psi}_{d_C}$, and use it another time to compute $\boldsymbol{\Psi}_{r_C}$.

This amounts to solving $n_B + n_\eta + 1$ linear systems in the preprocessing stage, but with a single QR factorization, hence this does not lead to excessive computational overhead.

Employing the definition of the augmented static modes in (5.40), we can discover the properties

$$\boldsymbol{K}_{II_{\text{loc}}}\boldsymbol{\Psi}_{s_I} + \boldsymbol{C}_{\boldsymbol{q}II_{\text{loc}}}^T\boldsymbol{\Psi}_{s_\gamma} + \boldsymbol{K}_{IB_{\text{loc}}} = \boldsymbol{0} \tag{5.44a}$$

$$\boldsymbol{C}_{\boldsymbol{q}II_{\text{loc}}}\boldsymbol{\Psi}_{s_I} + \boldsymbol{C}_{\boldsymbol{q}IB_{\text{loc}}} = \boldsymbol{0} \tag{5.44b}$$

Employing the definition of the augmented dynamic modes in (5.41), we can discover the properties

$$\boldsymbol{K}_{II_{\text{loc}}}\boldsymbol{\Psi}_{d_I} + \boldsymbol{C}_{\boldsymbol{q}II_{\text{loc}}}^T\boldsymbol{\Psi}_{d_\gamma} + \boldsymbol{M}_{IB_{\text{loc}}}\boldsymbol{\Phi}_{\boldsymbol{B}} + \boldsymbol{M}_{II_{\text{loc}}}\boldsymbol{\Phi}_{\boldsymbol{I}} = \boldsymbol{0} \tag{5.45a}$$

$$\boldsymbol{C}_{\boldsymbol{q}II_{\text{loc}}}\boldsymbol{\Psi}_{d_I} = \boldsymbol{0} \tag{5.45b}$$

Employing the definition of the augmented static correction mode in (5.42), we can discover the properties

$$\boldsymbol{K}_{II_{\text{loc}}}\boldsymbol{\Psi}_{r_I} + \boldsymbol{C}_{\boldsymbol{q}II_{\text{loc}}}^T\boldsymbol{\Psi}_{r_\gamma} = \overline{\boldsymbol{f}}_I \tag{5.46a}$$

$$\boldsymbol{C}_{\boldsymbol{q}II_{\text{loc}}}\boldsymbol{\Psi}_{r_I} = \boldsymbol{0} \tag{5.46b}$$

The internal Lagrange multipliers $\boldsymbol{\gamma}_I$ vanish in the modal reduction procedure. If one wants to retrieve the reaction forces from the reduced subsystem, the internal Lagrange multipliers $\boldsymbol{\gamma}_I$ can be recovered via

$$\delta\boldsymbol{\gamma}_I = \boldsymbol{\Psi}_{s_\gamma}\delta\overline{\boldsymbol{q}}_B + \boldsymbol{\Psi}_{d_\gamma}\delta\boldsymbol{\eta}_d + \boldsymbol{\Psi}_{r_\gamma}\delta\boldsymbol{\eta}_r \tag{5.47}$$

where $\delta\boldsymbol{\eta}_r$ is the generalized coordinate of the static correction mode.

The local elastic displacement of the inertial nodes can be recovered via

$$\delta\overline{\boldsymbol{q}}_I = \boldsymbol{\Psi}_{s_I}\delta\overline{\boldsymbol{q}}_B + \boldsymbol{\Psi}_{d_I}\delta\boldsymbol{\eta}_d + \boldsymbol{\Psi}_{r_I}\delta\boldsymbol{\eta}_r \tag{5.48}$$

Introducing the notation of the modal reduction transformation matrix

$$\boldsymbol{\Psi}_C = \begin{bmatrix} \boldsymbol{I} & \boldsymbol{0} & \boldsymbol{0} \\ \boldsymbol{\Psi}_{s_I} & \boldsymbol{\Psi}_{d_I} & \boldsymbol{\Psi}_{r_I} \\ \boldsymbol{\Psi}_{s_\gamma} & \boldsymbol{\Psi}_{d_\gamma} & \boldsymbol{\Psi}_{r_\gamma} \end{bmatrix} \tag{5.49}$$

the physical coordinates can be transformed to the local generalized coordinates of the reduced subsystem as

$$\left[\delta\overline{\boldsymbol{q}}_B^T, \delta\overline{\boldsymbol{q}}_I^T, \delta\boldsymbol{\gamma}_I^T\right]^T = \boldsymbol{\Psi}_C\left[\delta\overline{\boldsymbol{q}}_B^T, \delta\boldsymbol{\eta}_d^T, \delta\boldsymbol{\eta}_r^T\right]^T \tag{5.50}$$

Remembering the properties (5.44a),(5.44b),(5.45b),(5.46b), the reduced mass matrix can be evaluated as

$$\overline{\boldsymbol{M}} = \boldsymbol{\Psi}_C^T \boldsymbol{M}_{C_{\text{loc}}} \boldsymbol{\Psi}_C = \begin{bmatrix} \overline{\boldsymbol{M}}_{BB} & \overline{\boldsymbol{M}}_{Bd} & \overline{\boldsymbol{M}}_{Br} \\ \overline{\boldsymbol{M}}_{Bd}^T & \overline{\boldsymbol{M}}_{dd} & \overline{\boldsymbol{M}}_{dr} \\ \overline{\boldsymbol{M}}_{Br}^T & \overline{\boldsymbol{M}}_{dr}^T & \overline{\boldsymbol{M}}_{rr} \end{bmatrix} \tag{5.51}$$

where

$$\overline{\boldsymbol{M}}_{BB} = \boldsymbol{M}_{BB_{\text{loc}}} + \boldsymbol{M}_{BI_{\text{loc}}} \boldsymbol{\Psi}_{s_I} + \boldsymbol{\Psi}_{s_I}^T \boldsymbol{M}_{IB_{\text{loc}}} + \boldsymbol{\Psi}_{s_I}^T \boldsymbol{M}_{II_{\text{loc}}} \boldsymbol{\Psi}_{s_I} \tag{5.52a}$$

$$\overline{\boldsymbol{M}}_{Bd} = \left(\boldsymbol{M}_{BI_{\text{loc}}} + \boldsymbol{\Psi}_{s_I}^T \boldsymbol{M}_{II_{\text{loc}}} \right) \boldsymbol{\Psi}_{d_I} \tag{5.52b}$$

$$\overline{\boldsymbol{M}}_{Br} = \left(\boldsymbol{M}_{BI_{\text{loc}}} + \boldsymbol{\Psi}_{s_I}^T \boldsymbol{M}_{II_{\text{loc}}} \right) \boldsymbol{\Psi}_{r_I} \tag{5.52c}$$

$$\overline{\boldsymbol{M}}_{dd} = \boldsymbol{\Psi}_{d_I}^T \boldsymbol{M}_{II_{\text{loc}}} \boldsymbol{\Psi}_{d_I} \tag{5.52d}$$

$$\overline{\boldsymbol{M}}_{dr} = \boldsymbol{\Psi}_{d_I}^T \boldsymbol{M}_{II_{\text{loc}}} \boldsymbol{\Psi}_{r_I} \tag{5.52e}$$

$$\overline{\boldsymbol{M}}_{rr} = \boldsymbol{\Psi}_{r_I}^T \boldsymbol{M}_{II_{\text{loc}}} \boldsymbol{\Psi}_{r_I} \tag{5.52f}$$

and the reduced stiffness matrix can be evaluated as

$$\overline{\boldsymbol{K}} = \boldsymbol{\Psi}_C^T \boldsymbol{K}_{C_{\text{loc}}} \boldsymbol{\Psi}_C = \begin{bmatrix} \overline{\boldsymbol{K}}_{BB} & \boldsymbol{0} & \boldsymbol{0} \\ \boldsymbol{0} & \overline{\boldsymbol{K}}_{dd} & \overline{\boldsymbol{K}}_{dr} \\ \boldsymbol{0} & \overline{\boldsymbol{K}}_{dr}^T & \overline{\boldsymbol{K}}_{rr} \end{bmatrix} \tag{5.53}$$

where

$$\overline{\boldsymbol{K}}_{BB} = \boldsymbol{K}_{BB_{\text{loc}}} + \boldsymbol{K}_{BI_{\text{loc}}} \boldsymbol{\Psi}_{s_I} + \boldsymbol{\Psi}_{s_I}^T \boldsymbol{K}_{IB_{\text{loc}}} + \boldsymbol{\Psi}_{s_I}^T \boldsymbol{K}_{II_{\text{loc}}} \boldsymbol{\Psi}_{s_I} \tag{5.54a}$$

$$\overline{\boldsymbol{K}}_{dd} = \boldsymbol{\Psi}_{d_I}^T \boldsymbol{K}_{II_{\text{loc}}} \boldsymbol{\Psi}_{d_I} \tag{5.54b}$$

$$\overline{\boldsymbol{K}}_{dr} = \boldsymbol{\Psi}_{d_I}^T \boldsymbol{K}_{II_{\text{loc}}} \boldsymbol{\Psi}_{r_I} \tag{5.54c}$$

$$\overline{\boldsymbol{K}}_{rr} = \boldsymbol{\Psi}_{r_I}^T \boldsymbol{K}_{II_{\text{loc}}} \boldsymbol{\Psi}_{r_I} \tag{5.54d}$$

In this work, both $\overline{\boldsymbol{M}}$ and $\overline{\boldsymbol{K}}$ are evaluated in the initial configuration and then keep constant in the time integration. The augmented static correction mode $\boldsymbol{\Psi}_{r_C}$ in (5.42) is dependent on the imposed forces $\overline{\boldsymbol{f}}_I$, thus needs to be recomputed when the load pattern of $\overline{\boldsymbol{f}}_I$ is changed. We observe that only $\overline{\boldsymbol{M}}_{Br}$,$\overline{\boldsymbol{M}}_{dr}$,$\overline{\boldsymbol{M}}_{rr}$,$\overline{\boldsymbol{K}}_{dr}$,$\overline{\boldsymbol{K}}_{rr}$ are required to update correspondingly. Since the QR factorization of $\boldsymbol{K}_{IIC_{\text{loc}}}$ can be reused in the update of $\boldsymbol{\Psi}_{r_C}$, and $\overline{\boldsymbol{M}}_{Br}$, $\overline{\boldsymbol{M}}_{dr}$, $\overline{\boldsymbol{M}}_{rr}$, $\overline{\boldsymbol{K}}_{dr}$, $\overline{\boldsymbol{K}}_{rr}$ have only one column, the computational overhead is limited.

Both $\overline{\boldsymbol{M}}$ and $\overline{\boldsymbol{K}}$ are symmetric. We do not have the reduced constraint Jacobian matrix $\overline{\boldsymbol{C_q}}$ after the modal reduction.

5.5 Motion decomposition

In the section, a projection method to decompose the gross motion of the subsystem is introduced.

5.5.1 Constraint equation

Recalling (5.8c), the displacement in the inertial frame $\delta\boldsymbol{q}$ is decomposed to two components: the local displacement $\delta\overline{\boldsymbol{q}}$, plus the rigid-body motion represented by the configuration of the floating frame $\delta\boldsymbol{q}_F$. The unknown variables in the right-hand side of (5.8c) exceed those in the left-hand side by six, indicating the presence of six redundant variables. A constraint equation can be imposed to eliminate the redundant variables [251]

$$\boldsymbol{U}^T\boldsymbol{M}\left(\boldsymbol{L}\delta\overline{\boldsymbol{q}}\right)=\boldsymbol{0}_6 \tag{5.55}$$

which is expressed in the inertial frame.

Introducing the transformation matrix for the floating frame F

$$\boldsymbol{L}_F=\begin{bmatrix}\boldsymbol{R}_F & \boldsymbol{0}\\ \boldsymbol{0} & \boldsymbol{I}\end{bmatrix}\in\mathbb{R}^{6\times 6} \tag{5.56}$$

and remembering the relation of mass matrices between the inertial and local basis (5.21), the constraint equation (5.55) can be transformed to $\boldsymbol{L}_F\boldsymbol{U}_{\text{loc}}^T\boldsymbol{M}_{\text{loc}}\delta\overline{\boldsymbol{q}}=\boldsymbol{0}$, and further simplified by left multiplying $\boldsymbol{L}_F^T$ as

$$\boldsymbol{U}_{\text{loc}}^T\boldsymbol{M}_{\text{loc}}\delta\overline{\boldsymbol{q}}=\boldsymbol{0} \tag{5.57}$$

In this work, the modal reduction procedure is performed in the initial configuration in the preprocessing stage. In the subsequent dynamics simulation, the modal basis will not update in general, thus the reduction transformation matrix $\boldsymbol{\Psi}_{s_C}$, $\boldsymbol{\Psi}_{d_C}$ are constant. The rigid-body modes $\boldsymbol{U}_{\text{loc}}$ provide a reference to extract the deformation measures. If the reference $\boldsymbol{U}_{\text{loc}}$ is changed according to the deformed configuration, the deformation measures at two adjacent time steps might be not consistent, resulting in potential impulse or numerical divergence in the solution. Thus, the rigid-body modes $\boldsymbol{U}_{\text{loc},0}$ in the initial configuration is used in the constraint equation (5.57) to guarantee consistent deformation measures. Based on the small deformation assumption, the local mass matrix $\boldsymbol{M}_{\text{loc}}$ in the deformed configuration does not change significantly relative to the one in the initial configuration $\boldsymbol{M}_{\text{loc},0}$, thus we can assume that $\boldsymbol{M}_{\text{loc}}\approx\boldsymbol{M}_{\text{loc},0}$. The constraint equation (5.57) is then recast as

$$\boldsymbol{U}_{\text{loc},0}^T\boldsymbol{M}_{\text{loc},0}\delta\overline{\boldsymbol{q}}=\boldsymbol{0} \tag{5.58}$$

Recalling (5.8a), and introducing the local rigid-body modes of boundary nodes $\boldsymbol{U}_{B_{\text{loc},0}}$ via slicing from $\boldsymbol{U}_{\text{loc},0}$, the local elastic deformation of boundary nodes can be recast as

$$\delta\overline{\boldsymbol{q}}_B=\boldsymbol{L}_B^T\delta\boldsymbol{q}_B-\boldsymbol{U}_{B_{\text{loc},0}}\boldsymbol{L}_F^T\delta\boldsymbol{q}_F \tag{5.59}$$

For ease of notation, we introduce below notations:

- The generalized coordinate of the reduced subsystem: $\delta \boldsymbol{q}_{\text{mod}} = \left[\delta \boldsymbol{q}_B^T, \delta \boldsymbol{\eta}_d^T, \delta \boldsymbol{\eta}_r^T\right]^T$.
- The generalized elastic deformation in the local basis of the floating frame F: $\delta \overline{\boldsymbol{e}}_{\text{loc}} = \left[\delta \overline{\boldsymbol{q}}_B^T, \delta \boldsymbol{\eta}_d^T, \delta \boldsymbol{\eta}_r^T\right]^T$.
- The corotated displacement of the reduced subsystem in the local basis of the floating frame F: $\delta \overline{\boldsymbol{u}}_{\text{loc}} = \boldsymbol{L}_W^T \delta \boldsymbol{q}_{\text{mod}}$ where $\boldsymbol{L}_W = \text{diag}\left[\boldsymbol{L}_B, \boldsymbol{I}_{n_\eta+1}\right]$.
- The corotated displacement of the floating frame F in its local basis: $\delta \overline{\boldsymbol{u}}_F = \boldsymbol{L}_F^T \delta \boldsymbol{q}_F$.

Remembering (5.59), we obtain the motion decomposition for the reduced subsystem

$$\delta \overline{\boldsymbol{e}}_{\text{loc}} = \delta \overline{\boldsymbol{u}}_{\text{loc}} - \overline{\boldsymbol{U}}_{\text{loc},0} \delta \overline{\boldsymbol{u}}_F \tag{5.60}$$

where

$$\overline{\boldsymbol{U}}_{\text{loc},0} = \begin{bmatrix} \boldsymbol{U}_{B_{\text{loc},0}} \\ \boldsymbol{0}_{(n_\eta+1)\times 6} \end{bmatrix} \tag{5.61}$$

is the rigid-body mode of the reduced subsystem in the initial configuration. $\overline{\boldsymbol{U}}_{\text{loc},0} \delta \overline{\boldsymbol{u}}_F$ represents the displacement field of the rigid-body motion.

There is an interesting equality between the rigid-body modes of the full and reduced subsystem in the initial configuration

$$\boldsymbol{\Psi}_C \overline{\boldsymbol{U}}_{\text{loc},0} = \begin{bmatrix} \boldsymbol{L}_{B,0}^T \boldsymbol{U}_{B,0} \boldsymbol{P}_{F,0} \\ \boldsymbol{\Psi}_{s_C} \boldsymbol{L}_{B,0}^T \boldsymbol{U}_{B,0} \boldsymbol{P}_{F,0} \end{bmatrix} = \boldsymbol{U}_{\text{loc},0} \tag{5.62}$$

where the second row is derived using the equation (5.43).

Remembering (5.51) and (5.62) , the constraint equation (5.58) can be resolved on the reduced generalized elastic deformation as

$$\delta \boldsymbol{c}_F = \overline{\boldsymbol{U}}_{\text{loc},0}^T \overline{\boldsymbol{M}} \delta \overline{\boldsymbol{e}}_{\text{loc}} = \boldsymbol{0}_6 \tag{5.63}$$

5.5.2 Projection matrices

Substituting (5.60) into the constraint equation (5.63), yields

$$\overline{\boldsymbol{U}}_{\text{loc},0}^T \overline{\boldsymbol{M}} \left(\delta \overline{\boldsymbol{u}}_{\text{loc}} - \overline{\boldsymbol{U}}_{\text{loc},0} \delta \overline{\boldsymbol{u}}_F \right) = \boldsymbol{0} \tag{5.64}$$

The corotated displacement of the floating frame F can be resolved as

$$\delta \overline{\boldsymbol{u}}_F = \left[\left(\overline{\boldsymbol{U}}_{\text{loc},0}^T \overline{\boldsymbol{M}} \overline{\boldsymbol{U}}_{\text{loc},0} \right)^{-1} \overline{\boldsymbol{U}}_{\text{loc},0}^T \overline{\boldsymbol{M}} \right] \delta \overline{\boldsymbol{u}}_{\text{loc}} = \boldsymbol{Q} \delta \overline{\boldsymbol{u}}_{\text{loc}} \tag{5.65}$$

where

$$\boldsymbol{Q} = \left(\overline{\boldsymbol{U}}_{\mathrm{loc},0}^{T}\overline{\boldsymbol{M}\boldsymbol{U}}_{\mathrm{loc},0}\right)^{-1}\overline{\boldsymbol{U}}_{\mathrm{loc},0}^{T}\overline{\boldsymbol{M}} \tag{5.66}$$

The displacement of the floating frame F can be resolved as

$$\delta\boldsymbol{q}_F = \boldsymbol{L}_F\delta\overline{\boldsymbol{u}}_F = \boldsymbol{L}_F\boldsymbol{Q}\boldsymbol{L}_W^{T}\delta\boldsymbol{q}_{\mathrm{mod}} \tag{5.67}$$

The displacement field contributed by the rigid-body motion of the reduced subsystem expressed in the local basis of the floating frame F is

$$\overline{\boldsymbol{U}}_{\mathrm{loc},0}\delta\overline{\boldsymbol{u}}_F = \begin{bmatrix} & \overline{\boldsymbol{U}}_{\mathrm{loc},0}\boldsymbol{Q}\end{bmatrix}\delta\overline{\boldsymbol{u}}_{\mathrm{loc}} = \overline{\boldsymbol{P}}_{\parallel}\boldsymbol{L}_W^{T}\delta\boldsymbol{q}_{\mathrm{mod}} \tag{5.68}$$

where the parallel projection matrix is

$$\overline{\boldsymbol{P}}_{\parallel} = \overline{\boldsymbol{U}}_{\mathrm{loc},0}\boldsymbol{Q} \tag{5.69}$$

The generalized elastic deformation of the reduced subsystem expressed in the local basis of the floating frame F is

$$\delta\overline{\boldsymbol{e}}_{\mathrm{loc}} = \left[\boldsymbol{I} - \overline{\boldsymbol{U}}_{\mathrm{loc},0}\boldsymbol{Q}\right]\delta\overline{\boldsymbol{u}}_{\mathrm{loc}} = \overline{\boldsymbol{P}}_{\perp}\boldsymbol{L}_W^{T}\delta\boldsymbol{q}_{\mathrm{mod}} \tag{5.70}$$

where the perpendicular projection matrix is

$$\overline{\boldsymbol{P}}_{\perp} = \boldsymbol{I} - \overline{\boldsymbol{U}}_{\mathrm{loc},0}\boldsymbol{Q} \tag{5.71}$$

The two projection matrices $\overline{\boldsymbol{P}}_{\parallel}$, $\overline{\boldsymbol{P}}_{\perp}$ provide a convenient way to decompose the displacement field of the reduced subsystem $\delta\boldsymbol{q}_{\mathrm{mod}}$ into rigid-body motion and elastic deformations. The deformation measures are independent of the motion of the floating frame F, and hence are objective [251].

Since the rigid-body mode $\overline{\boldsymbol{U}}_{\mathrm{loc},0}$ is evaluated in the initial configuration and does not change in the time integration, the three matrices $\boldsymbol{Q}$, $\overline{\boldsymbol{P}}_{\parallel}$, $\overline{\boldsymbol{P}}_{\perp}$ are constant, providing great advantages in terms of computational efficiency.

5.5.3 Update of internal nodes

If one is interested, it is also possible to recover the internal displacement, the internal nodal forces and moments in the postprocessing stage.

Recalling the equation (5.8b) and remembering (5.8a),(5.43),(5.48), the corotated displacement of internal nodes can be evaluated as

$$\begin{aligned}
\boldsymbol{L}_I^{T}\delta\boldsymbol{q}_I &= \boldsymbol{L}_I^{T}\boldsymbol{U}_I\delta\boldsymbol{q}_F + \delta\overline{\boldsymbol{q}}_I \\
&= \boldsymbol{L}_I^{T}\boldsymbol{U}_I\delta\boldsymbol{q}_F + \left(\boldsymbol{\Psi}_{s_I}\delta\overline{\boldsymbol{q}}_B + \boldsymbol{\Psi}_{d_I}\delta\boldsymbol{\eta}_d + \boldsymbol{\Psi}_{r_I}\delta\boldsymbol{\eta}_r\right) \\
&= \boldsymbol{L}_I^{T}\boldsymbol{U}_I\delta\boldsymbol{q}_F + \boldsymbol{\Psi}_{s_I}\left(\boldsymbol{L}_B^{T}\delta\boldsymbol{q}_B - \boldsymbol{L}_B^{T}\boldsymbol{U}_B\delta\boldsymbol{q}_F\right) + \boldsymbol{\Psi}_{d_I}\delta\boldsymbol{\eta}_d + \boldsymbol{\Psi}_{r_I}\delta\boldsymbol{\eta}_r \\
&= \boldsymbol{\Psi}_{s_I}\boldsymbol{L}_B^{T}\delta\boldsymbol{q}_B + \boldsymbol{\Psi}_{d_I}\delta\boldsymbol{\eta}_d + \boldsymbol{\Psi}_{r_I}\delta\boldsymbol{\eta}_r - \left(\boldsymbol{\Psi}_{s_I}\boldsymbol{L}_B^{T}\boldsymbol{U}_B - \boldsymbol{L}_I^{T}\boldsymbol{U}_I\right)\delta\boldsymbol{q}_F \\
&= \boldsymbol{\Psi}_{s_I}\boldsymbol{L}_B^{T}\delta\boldsymbol{q}_B + \boldsymbol{\Psi}_{d_I}\delta\boldsymbol{\eta}_d + \boldsymbol{\Psi}_{r_I}\delta\boldsymbol{\eta}_r
\end{aligned} \tag{5.72}$$

Recalling (5.47) and remembering (5.8a), the variation of the inertial Lagrange Multipliers can be evaluated as

$$\begin{aligned}\delta\boldsymbol{\gamma}_I &= \boldsymbol{\Psi}_{s_\gamma}\left(\boldsymbol{L}_B^T\delta\boldsymbol{q}_B - \boldsymbol{L}_B^T\boldsymbol{U}_B\delta\boldsymbol{q}_F\right) + \boldsymbol{\Psi}_{d_\gamma}\delta\boldsymbol{\eta}_d + \boldsymbol{\Psi}_{r_\gamma}\delta\boldsymbol{\eta}_r \\ &= \boldsymbol{\Psi}_{s_\gamma}\boldsymbol{L}_B^T\delta\boldsymbol{q}_B + \boldsymbol{\Psi}_{d_\gamma}\delta\boldsymbol{\eta}_d + \boldsymbol{\Psi}_{r_\gamma}\delta\boldsymbol{\eta}_r \end{aligned} \tag{5.73}$$

where the property $\boldsymbol{\Psi}_{s_\gamma}\boldsymbol{L}_B^T\boldsymbol{U}_B = \boldsymbol{0}$ derived from the second row of (5.43) is used.

Employing (5.72),(5.73), one obtains the coordinate transformation for the boundary nodes, internal nodes, and internal Lagrange Multipliers as

$$\delta\boldsymbol{q}_C = \boldsymbol{L}_C\boldsymbol{\Psi}_C\boldsymbol{L}_W^T\delta\boldsymbol{q}_{\text{mod}} \tag{5.74}$$

where $\delta\boldsymbol{q}_C = \left[\delta\boldsymbol{q}_B^T, \delta\boldsymbol{q}_I^T, \delta\boldsymbol{\gamma}_I^T\right]^T$ is the augmented coordinates of the full subsystem, $\boldsymbol{L}_C = \text{diag}\left[\boldsymbol{L}, \boldsymbol{I}_{m\times m}\right]$ is the augmented corotational transformation matrix for the full subsystem.

5.6 Tangent stiffness matrix

The virtual work done by the elastic forces of the full subsystem is evaluated as

$$\delta\mathcal{W}_{\text{E}} = \delta\boldsymbol{q}_C^T\begin{bmatrix}\boldsymbol{K} & \boldsymbol{C_q}^T \\ \boldsymbol{C_q} & \boldsymbol{0}\end{bmatrix}\Delta\boldsymbol{q}_C \tag{5.75}$$

Substituting the motion decomposition (5.8c) into (5.75), and employing the similar property expressed in the inertial frame as in (5.32), together with transformation relations (5.16),(5.26), one obtains the expression in the local basis of the floating frame F

$$\begin{aligned}\delta\mathcal{W}_{\text{E}} &= \left[\delta\boldsymbol{q}_F^T\boldsymbol{U}^T + \delta\overline{\boldsymbol{q}}^T\boldsymbol{L}^T, \delta\boldsymbol{\gamma}_I^T\right]\begin{bmatrix}\boldsymbol{K} & \boldsymbol{C_q}^T \\ \boldsymbol{C_q} & \boldsymbol{0}\end{bmatrix}\begin{bmatrix}\boldsymbol{U}\Delta\boldsymbol{q}_F + \boldsymbol{L}\Delta\overline{\boldsymbol{q}} \\ \Delta\boldsymbol{\gamma}_I\end{bmatrix} \\ &= \left[\delta\overline{\boldsymbol{q}}^T, \delta\boldsymbol{\gamma}_I^T\right]\boldsymbol{K}_{C_{\text{loc}}}\begin{bmatrix}\Delta\overline{\boldsymbol{q}} \\ \Delta\boldsymbol{\gamma}_I\end{bmatrix}\end{aligned} \tag{5.76}$$

Substituting the modal reduction transformations (5.50),(5.53) into (5.76), and remembering (5.70), one obtains

$$\delta\mathcal{W}_{\text{E}} = \delta\boldsymbol{q}_{\text{mod}}^T\boldsymbol{L}_W\overline{\boldsymbol{P}}_\perp^T\overline{\boldsymbol{K}\boldsymbol{P}}_\perp\boldsymbol{L}_W^T\Delta\boldsymbol{q}_{\text{mod}} \tag{5.77}$$

The internal forces of the reduced subsystem associated with the generalized coordinates $\delta\boldsymbol{q}_{\text{mod}}$ is

$$\boldsymbol{f}_{\text{int}} = \boldsymbol{L}_W\overline{\boldsymbol{P}}_\perp^T\overline{\boldsymbol{K}\boldsymbol{P}}_\perp\boldsymbol{L}_W^T\Delta\boldsymbol{q}_{\text{mod}} = \boldsymbol{L}_W\overline{\boldsymbol{P}}_\perp^T\overline{\boldsymbol{K}}\Delta\overline{\boldsymbol{e}}_{\text{loc}} \tag{5.78}$$

which is required for the computation of the residual forces in the time integrator.

The discretized generalized elastic deformation is $\Delta \boldsymbol{q}_{\mathrm{mod}} = \overline{\boldsymbol{P}}_{\perp} \boldsymbol{L}_W^T \Delta \boldsymbol{q}_{\mathrm{mod}}$. To guarantee a proper convergence, it can be computed in the code implementation as

$$\Delta \overline{\boldsymbol{e}}_{\mathrm{loc}} = \begin{pmatrix} \Delta \overline{\boldsymbol{q}}_B \\ \Delta \boldsymbol{\eta}_d \\ \Delta \boldsymbol{\eta}_r \end{pmatrix} = \begin{pmatrix} \mathrm{vert} \begin{pmatrix} \boldsymbol{R}_F^T (\boldsymbol{r}_B - \boldsymbol{r}_F) - \boldsymbol{R}_{F0}^T (\boldsymbol{r}_{B_0} - \boldsymbol{r}_{F0}) \\ \mathrm{qaxial}(\log(\boldsymbol{\rho}_{B_0}^* \boldsymbol{\rho}_{F_0} \boldsymbol{\rho}_F^* \boldsymbol{\rho}_B)) \end{pmatrix} \\ \Delta \boldsymbol{\eta}_d \\ \Delta \boldsymbol{\eta}_r \end{pmatrix} \tag{5.79}$$

Linearizing $\boldsymbol{f}_{\mathrm{int}}$ with respect to the generalized coordinate $\delta \boldsymbol{q}_{\mathrm{mod}}$ results in the tangent stiffness matrix $\overline{\boldsymbol{K}}_{\mathrm{mod}}$, which is composed of two components: the material stiffness matrix $\overline{\boldsymbol{K}}_{m_{\mathrm{mod}}}$ and geometric stiffness matrix $\overline{\boldsymbol{K}}_{g_{\mathrm{mod}}}$.

$$\overline{\boldsymbol{K}}_{\mathrm{mod}} = \overline{\boldsymbol{K}}_{m_{\mathrm{mod}}} + \overline{\boldsymbol{K}}_{g_{\mathrm{mod}}} \tag{5.80a}$$

$$\overline{\boldsymbol{K}}_{m_{\mathrm{mod}}} = \boldsymbol{L}_W \overline{\boldsymbol{P}}_{\perp}^T \overline{\boldsymbol{K}\boldsymbol{P}}_{\perp} \boldsymbol{L}_W^T \tag{5.80b}$$

$$\overline{\boldsymbol{K}}_{g_{\mathrm{mod}}} = -\boldsymbol{L}_W \boldsymbol{V}_{f1} \boldsymbol{L}_F \boldsymbol{Q} \boldsymbol{L}_W^T + \boldsymbol{L}_W \overline{\boldsymbol{P}}_{\perp}^T \overline{\boldsymbol{K}\boldsymbol{P}}_{\perp} \boldsymbol{V}_{f2} \boldsymbol{L}_F \boldsymbol{Q} \boldsymbol{L}_W^T \tag{5.80c}$$

where

$$\boldsymbol{V}_{f1} = \begin{bmatrix} \mathrm{vert} \begin{bmatrix} \boldsymbol{0} & \left(\overline{\boldsymbol{P}}_{\perp}^T \widetilde{\overline{\boldsymbol{K}} \Delta \overline{\boldsymbol{e}}_{\mathrm{loc}}} \right)_{\boldsymbol{r}_B} \\ \boldsymbol{0} & \boldsymbol{0} \end{bmatrix} \\ \boldsymbol{0} \end{bmatrix}, \quad \boldsymbol{V}_{f2} = \begin{bmatrix} \mathrm{vert} \begin{bmatrix} \boldsymbol{0} & (\widetilde{\boldsymbol{R}_F^T \Delta \boldsymbol{r}_B}) \\ \boldsymbol{0} & \boldsymbol{0} \end{bmatrix} \\ \boldsymbol{0} \end{bmatrix} \tag{5.81}$$

The geometric stiffness matrix $\overline{\boldsymbol{K}}_{g_{\mathrm{mod}}}$ can benefit the numerical convergence in the Newton-Raphson iterations, especially when the subsystem experiences large deflections, and hence it is recommended to involve $\overline{\boldsymbol{K}}_{g_{\mathrm{mod}}}$ in the numerical computations.

5.7 Inertial terms

The kinetic energy of the full subsystem can be evaluated as

$$\mathcal{W}_{\mathrm{K}} = \dot{\boldsymbol{q}}_C^T \begin{bmatrix} \boldsymbol{M} & \boldsymbol{0} \\ \boldsymbol{0} & \boldsymbol{0} \end{bmatrix} \dot{\boldsymbol{q}}_C \tag{5.82}$$

Thanks to the similarity of variation and time derivative, we can obtain the relation $\dot{\boldsymbol{q}}_C = \boldsymbol{L}_C \boldsymbol{\Psi}_C \boldsymbol{L}_W^T \dot{\boldsymbol{q}}_{\mathrm{mod}}$ by referencing (5.74). Remembering the matrix transformations (5.21),(5.51), one obtains

$$\mathcal{W}_{\mathrm{K}} = \frac{1}{2} \dot{\boldsymbol{q}}_{\mathrm{mod}}^T \boldsymbol{L}_W \overline{\boldsymbol{M}} \boldsymbol{L}_W^T \dot{\boldsymbol{q}}_{\mathrm{mod}} = \frac{1}{2} \dot{\boldsymbol{u}}_{\mathrm{loc}}^T \overline{\boldsymbol{M}} \dot{\boldsymbol{u}}_{\mathrm{loc}} \tag{5.83}$$

where the reduced corotated velocity is

$$\dot{\overline{\boldsymbol{u}}}_{\mathrm{loc}} = \boldsymbol{L}_W^T \dot{\boldsymbol{q}}_{\mathrm{mod}} \tag{5.84}$$

The variation of the kinetic energy is

$$\delta \mathcal{W}_{\mathrm{K}} = \delta \dot{\overline{\boldsymbol{u}}}_{\mathrm{loc}}^T \overline{\boldsymbol{M}} \dot{\overline{\boldsymbol{u}}}_{\mathrm{loc}} \tag{5.85}$$

5.7.1 Nonlinear expressions

Remembering the equation $\delta\boldsymbol{\omega}_{l_B} = \delta\dot{\boldsymbol{\theta}}_{l_B} + \widetilde{\boldsymbol{\omega}}_{l_B}\delta\boldsymbol{\theta}_{l_B}$ and (5.67), the variation of the reduced corotated velocity can be evaluated as

$$\delta \dot{\overline{\boldsymbol{u}}}_{\mathrm{loc}} = \boldsymbol{L}_W^T \delta \dot{\boldsymbol{q}}_{\mathrm{mod}}^{\Diamond} + \left(\boldsymbol{O}_B + \boldsymbol{V}\boldsymbol{L}_F\boldsymbol{Q}\boldsymbol{L}_W^T \right) \delta \boldsymbol{q}_{\mathrm{mod}} \tag{5.86}$$

where

$$\boldsymbol{O}_B = \begin{bmatrix} \mathrm{diag} \begin{bmatrix} \boldsymbol{0} & \boldsymbol{0} \\ \boldsymbol{0} & \widetilde{\boldsymbol{\omega}}_{l_B} \end{bmatrix} & \\ & \boldsymbol{0} \end{bmatrix}, \quad \boldsymbol{V} = \begin{bmatrix} \mathrm{vert} \begin{bmatrix} \boldsymbol{0} & \widetilde{\boldsymbol{R}_F^T \dot{\boldsymbol{r}}_B} \\ \boldsymbol{0} & \boldsymbol{0} \end{bmatrix} \\ \boldsymbol{0} \end{bmatrix} \tag{5.87}$$

and an intermediate generalized coordinate $\delta\dot{\boldsymbol{q}}_{\mathrm{mod}}^{\Diamond}$ in introduced. We recall the definition of the other two generalized coordinates $\delta\boldsymbol{q}_{\mathrm{mod}}, \delta\dot{\boldsymbol{q}}_{\mathrm{mod}}$ to ease the discussion here.

$$\delta \dot{\boldsymbol{q}}_{\mathrm{mod}}^{\Diamond} = \begin{pmatrix} \delta\dot{\boldsymbol{r}}_B \\ \delta\dot{\boldsymbol{\theta}}_{l_B} \\ \delta\dot{\boldsymbol{\eta}}_d \\ \delta\dot{\boldsymbol{\eta}}_r \end{pmatrix}, \quad \delta \dot{\boldsymbol{q}}_{\mathrm{mod}} = \begin{pmatrix} \delta\dot{\boldsymbol{r}}_B \\ \delta\boldsymbol{\omega}_{l_B} \\ \delta\dot{\boldsymbol{\eta}}_d \\ \delta\dot{\boldsymbol{\eta}}_r \end{pmatrix}, \quad \delta \boldsymbol{q}_{\mathrm{mod}} = \begin{pmatrix} \delta\boldsymbol{r}_B \\ \delta\boldsymbol{\theta}_{l_B} \\ \delta\boldsymbol{\eta}_d \\ \delta\boldsymbol{\eta}_r \end{pmatrix} \tag{5.88}$$

It is worth noting that $\delta\dot{\boldsymbol{q}}_{\mathrm{mod}}^{\Diamond}$ is the first time derivative of $\delta\boldsymbol{q}_{\mathrm{mod}}$, but $\delta\dot{\boldsymbol{q}}_{\mathrm{mod}}$ is not, as shown in below

$$\delta \dot{\boldsymbol{q}}_{\mathrm{mod}}^{\Diamond} = \frac{\mathrm{d}}{\mathrm{d}t}\delta\boldsymbol{q}_{\mathrm{mod}}, \quad \delta \dot{\boldsymbol{q}}_{\mathrm{mod}} \neq \frac{\mathrm{d}}{\mathrm{d}t}\delta\boldsymbol{q}_{\mathrm{mod}} \tag{5.89}$$

The difference of $\delta\dot{\boldsymbol{q}}_{\mathrm{mod}}$ and $\delta\dot{\boldsymbol{q}}_{\mathrm{mod}}^{\Diamond}$ brings the geometric nonlinear term $\boldsymbol{O}_B$. The term $\boldsymbol{V}$ stems from the variation $\delta\boldsymbol{R}_F$ due to the rotation of the floating frame F.

Substituting (5.86) into (5.85), the variation of the kinetic energy can be expressed as

$$\delta \mathcal{W}_{\mathrm{K}} = \delta \dot{\boldsymbol{q}}_{\mathrm{mod}}^{\Diamond T} \boldsymbol{L}_W \overline{\boldsymbol{M}} \dot{\overline{\boldsymbol{u}}}_{\mathrm{loc}} + \delta \boldsymbol{q}_{\mathrm{mod}}^T \left(\boldsymbol{O}_B^T + \boldsymbol{L}_W \boldsymbol{Q}^T \boldsymbol{L}_F^T \boldsymbol{V}^T \right) \overline{\boldsymbol{M}} \dot{\overline{\boldsymbol{u}}}_{\mathrm{loc}} \tag{5.90}$$

According to the Hamilton principle, integrating (5.90) between two arbitrary time instants yields

$$\int_{t_i}^{t_f} \delta\mathcal{W}_{\mathrm{K}}\mathrm{d}t = -\int_{t_i}^{t_f} \delta\boldsymbol{q}_{\mathrm{mod}}^T \left(\boldsymbol{L}_W\overline{\boldsymbol{M}}\ddot{\overline{\boldsymbol{u}}}_{\mathrm{loc}} + \left(\boldsymbol{L}_W\boldsymbol{O}_F - \boldsymbol{O}_B^T - \boldsymbol{L}_W\boldsymbol{Q}^T\boldsymbol{L}_F^T\boldsymbol{V}^T\right)\overline{\boldsymbol{M}}\dot{\overline{\boldsymbol{u}}}_{\mathrm{loc}}\right)\mathrm{d}t + \left[\delta\boldsymbol{q}_{\mathrm{mod}}^T\boldsymbol{L}_W\overline{\boldsymbol{M}}\dot{\overline{\boldsymbol{u}}}_{\mathrm{loc}}\right]_{t_i}^{t_f} \tag{5.91}$$

where

$$\boldsymbol{O}_F = \begin{bmatrix} \mathrm{diag}\begin{bmatrix} \widetilde{\boldsymbol{\omega}}_{l_F} & \boldsymbol{0} \\ \boldsymbol{0} & \boldsymbol{0} \end{bmatrix} & \\ & \boldsymbol{0} \end{bmatrix} \tag{5.92}$$

The last term $\left[\delta\boldsymbol{q}_{\mathrm{mod}}^T\boldsymbol{L}_W\overline{\boldsymbol{M}}\dot{\overline{\boldsymbol{u}}}_{\mathrm{loc}}\right]_{t_i}^{t_f}$ determines the boundary conditions at time t_i and t_f.

The variation of the kinetic energy is equal to the virtual work of the inertial force

$$\delta\mathcal{W}_{\mathrm{K}} = -\delta\boldsymbol{q}_{\mathrm{mod}}^T\boldsymbol{f}_{\mathrm{iner}} \tag{5.93}$$

By comparing (5.91) and (5.93), the inertial force of the reduced subsystem are obtained

$$\boldsymbol{f}_{\mathrm{iner}} = \boldsymbol{L}_W\overline{\boldsymbol{M}}\ddot{\overline{\boldsymbol{u}}}_{\mathrm{loc}} + \left(\boldsymbol{L}_W\boldsymbol{O}_F - \boldsymbol{O}_B^T - \boldsymbol{L}_W\boldsymbol{Q}^T\boldsymbol{L}_F^T\boldsymbol{V}^T\right)\overline{\boldsymbol{M}}\dot{\overline{\boldsymbol{u}}}_{\mathrm{loc}} \tag{5.94}$$

where the reduced corotated acceleration is

$$\ddot{\overline{\boldsymbol{u}}}_{\mathrm{loc}} = \boldsymbol{L}_W^T\ddot{\boldsymbol{q}}_{\mathrm{mod}} + \boldsymbol{V}\boldsymbol{L}_F\boldsymbol{Q}\boldsymbol{L}_W^T\dot{\boldsymbol{q}}_{\mathrm{mod}} \tag{5.95}$$

Substituting (5.84), (5.95) into (5.94), and employing the property $-\boldsymbol{O}_B^T = \boldsymbol{O}_B = \boldsymbol{L}_W\boldsymbol{O}_B$, the inertial force in (5.94) can be recast as

$$\boldsymbol{f}_{\mathrm{iner}} = \boldsymbol{L}_W\overline{\boldsymbol{M}}\boldsymbol{L}_W^T\ddot{\boldsymbol{q}}_{\mathrm{mod}} + \boldsymbol{f}_{\mathrm{quad}} \tag{5.96}$$

where $\boldsymbol{f}_{\mathrm{quad}}$ is the quadratic velocity term of the reduced subsystem

$$\boldsymbol{f}_{\mathrm{quad}} = \Big(\boldsymbol{L}_W\left(\boldsymbol{O}_F + \boldsymbol{O}_B\right)\overline{\boldsymbol{M}}\boldsymbol{L}_W^T + \left(\boldsymbol{L}_W\overline{\boldsymbol{M}}\boldsymbol{V}\boldsymbol{L}_F\boldsymbol{Q}\boldsymbol{L}_W^T - \boldsymbol{L}_W\boldsymbol{Q}^T\boldsymbol{L}_F^T\boldsymbol{V}^T\overline{\boldsymbol{M}}\boldsymbol{L}_W^T\right)\Big)\dot{\boldsymbol{q}}_{\mathrm{mod}} \tag{5.97}$$

Linearizing the inertial force $\boldsymbol{f}_{\mathrm{iner}}$ in (5.96) with respect to $\delta\ddot{\boldsymbol{q}}_{\mathrm{mod}}$, $\delta\dot{\boldsymbol{q}}_{\mathrm{mod}}$, $\delta\boldsymbol{q}_{\mathrm{mod}}$, respectively, yields

$$\delta\boldsymbol{f}_{\mathrm{iner}} = \overline{\boldsymbol{M}}_{\mathrm{mod}}\delta\ddot{\boldsymbol{q}}_{\mathrm{mod}} + \overline{\boldsymbol{D}}_{I_{\mathrm{mod}}}\delta\dot{\boldsymbol{q}}_{\mathrm{mod}} + \overline{\boldsymbol{K}}_{I_{\mathrm{mod}}}\delta\boldsymbol{q}_{\mathrm{mod}} \tag{5.98}$$

where the inertial mass matrix is

$$\overline{\boldsymbol{M}}_{\mathrm{mod}} = \boldsymbol{L}_W \overline{\boldsymbol{M}} \boldsymbol{L}_W^T \tag{5.99}$$

and the inertial damping matrix is

$$\begin{aligned}\overline{\boldsymbol{D}}_{I_{\mathrm{mod}}} = &\boldsymbol{L}_W \left(\boldsymbol{O}_F \overline{\boldsymbol{M}} - \overline{\boldsymbol{M}} \boldsymbol{O}_F \right) \boldsymbol{L}_W^T + \boldsymbol{L}_W \left(\overline{\boldsymbol{M}} \boldsymbol{V} \boldsymbol{L}_F \boldsymbol{Q} - \boldsymbol{Q}^T \boldsymbol{L}_F^T \boldsymbol{V}^T \overline{\boldsymbol{M}} \right) \boldsymbol{L}_W^T \\ &+ \boldsymbol{L}_W \left(\boldsymbol{Q}^T \boldsymbol{L}_F^T \boldsymbol{V}_M^T - \boldsymbol{V}_M \boldsymbol{L}_F \boldsymbol{Q} \right) \boldsymbol{L}_W^T - \boldsymbol{O}_M + \boldsymbol{O}_B \overline{\boldsymbol{M}} \boldsymbol{L}_W^T \end{aligned} \tag{5.100}$$

where

$$\boldsymbol{O}_M = \begin{bmatrix} \mathrm{diag} \begin{bmatrix} \boldsymbol{0} & \boldsymbol{0} \\ \boldsymbol{0} & \widetilde{\left(\overline{\boldsymbol{M}} \dot{\overline{\boldsymbol{u}}}_{\mathrm{loc}} \right)_{\boldsymbol{\theta}_B}} \end{bmatrix} & \\ & \boldsymbol{0} \end{bmatrix}, \boldsymbol{V}_M = \begin{bmatrix} \mathrm{vert} \begin{bmatrix} \boldsymbol{0} & \widetilde{\left(\overline{\boldsymbol{M}} \dot{\overline{\boldsymbol{u}}}_{\mathrm{loc}} \right)_{\boldsymbol{r}_B}} \\ \boldsymbol{0} & \boldsymbol{0} \end{bmatrix} \\ \boldsymbol{0} \end{bmatrix} \tag{5.101}$$

The expression of the inertial stiffness matrix $\overline{\boldsymbol{K}}_{I_{\mathrm{mod}}}$ is excessively complex. Since $\overline{\boldsymbol{K}}_{I_{\mathrm{mod}}}$ is negligible in most cases, we do not report the analytical expression here.

5.7.2 Linear expressions

In the derivations of Section 5.7.1, we have considered two equations: $\delta\boldsymbol{\omega}_{l_B} = \delta\dot{\boldsymbol{\theta}}_{l_B} + \widetilde{\boldsymbol{\omega}}_{l_B} \delta\boldsymbol{\theta}_{l_B}$ and $\delta\boldsymbol{q}_F = \boldsymbol{L}_F \boldsymbol{Q} \boldsymbol{L}_W^T \delta\boldsymbol{q}_{\mathrm{mod}}$.

In the first equation, $\widetilde{\boldsymbol{\omega}}_{l_B} \delta\boldsymbol{\theta}_{l_B}$ is a geometrical nonlinear term due to the rotation of boundary nodes. As discussed in Section 2.3.1, because the angular velocity $\boldsymbol{\omega}_{l_B}$ can not be integrated, in case of infinitesimal increment of rotation in the local basis, we can make a first order linear assumption $\delta\boldsymbol{\omega}_{l_B} = \delta\dot{\boldsymbol{\theta}}_{l_B}$ to become compatible with the modal analysis. In the end, we obtain $\delta\dot{\boldsymbol{q}}_{\mathrm{mod}} = \dfrac{\mathrm{d}}{\mathrm{d}t} \delta\boldsymbol{q}_{\mathrm{mod}}$.

The second equation $\delta\boldsymbol{q}_F = \boldsymbol{L}_F \boldsymbol{Q} \boldsymbol{L}_W^T \delta\boldsymbol{q}_{\mathrm{mod}}$ is also a geometrical nonlinear term, which represents the interaction between the increments of the floating frame F and the generalized coordinate of the reduced subsystem. In the incremental update scheme, the floating frame F is assumed to be frozen in the previous converged configuration, thus we can neglect the increment of the floating frame F by removing $\delta\boldsymbol{q}_F$ in the derivations.

Based on above two linear assumptions, the variation of $\dot{\overline{\boldsymbol{u}}}_{\mathrm{loc}}$ in (5.86) can be simplified as

$$\delta\dot{\overline{\boldsymbol{u}}}_{\mathrm{loc}} = \boldsymbol{L}_W^T \delta\dot{\boldsymbol{q}}_{\mathrm{mod}} \tag{5.102}$$

and the reduced corotated acceleration in (5.95) is simplified as

$$\ddot{\overline{\boldsymbol{u}}}_{\mathrm{loc}} = \boldsymbol{L}_W^T \ddot{\boldsymbol{q}}_{\mathrm{mod}} \tag{5.103}$$

when the geometrical nonlinear term $\dot{\boldsymbol{R}}_F$ is neglected.

The variation of the kinetic energy in (5.85) can be simplified and further derived as

$$\begin{aligned}\delta\mathcal{W}_{\mathrm{K}} &= \delta\dot{\boldsymbol{q}}_{\mathrm{mod}}^T \boldsymbol{L}_W \overline{\boldsymbol{M}} \boldsymbol{L}_W^T \dot{\boldsymbol{q}}_{\mathrm{mod}} \\ &= \frac{\mathrm{d}}{\mathrm{d}t}\left(\delta\boldsymbol{q}_{\mathrm{mod}}^T \boldsymbol{L}_W \overline{\boldsymbol{M}} \boldsymbol{L}_W^T \dot{\boldsymbol{q}}_{\mathrm{mod}}\right) - \delta\boldsymbol{q}_{\mathrm{mod}}^T \left(\boldsymbol{L}_W \boldsymbol{O}_F \overline{\boldsymbol{M}} \boldsymbol{L}_W^T \dot{\boldsymbol{q}}_{\mathrm{mod}} + \boldsymbol{L}_W \overline{\boldsymbol{M}} \boldsymbol{L}_W^T \ddot{\boldsymbol{q}}_{\mathrm{mod}}\right)\end{aligned} \tag{5.104}$$

Integrating (5.104) between two arbitrary time instants, yields

$$\begin{aligned}\int_{t_i}^{t_f} \delta\mathcal{W}_{\mathrm{K}}\mathrm{d}t = &- \int_{t_i}^{t_f} \delta\boldsymbol{q}_{\mathrm{mod}}^T \left(\boldsymbol{L}_W \boldsymbol{O}_F \overline{\boldsymbol{M}} \boldsymbol{L}_W^T \dot{\boldsymbol{q}}_{\mathrm{mod}} + \boldsymbol{L}_W \overline{\boldsymbol{M}} \boldsymbol{L}_W^T \ddot{\boldsymbol{q}}_{\mathrm{mod}}\right) \mathrm{d}t \\ &+ \left[\delta\boldsymbol{q}_{\mathrm{mod}}^T \boldsymbol{L}_W \overline{\boldsymbol{M}} \boldsymbol{L}_W^T \dot{\boldsymbol{q}}_{\mathrm{mod}}\right]_{t_i}^{t_f}\end{aligned} \tag{5.105}$$

By comparing (5.105) and (5.93), the inertial force of the reduced subsystem can be derived as

$$\boldsymbol{f}_{\mathrm{iner}} = \boldsymbol{L}_W \overline{\boldsymbol{M}} \boldsymbol{L}_W^T \ddot{\boldsymbol{q}}_{\mathrm{mod}} + \boldsymbol{f}_{\mathrm{quad}} \tag{5.106}$$

where the quadratic velocity term of the reduced subsystem is

$$\boldsymbol{f}_{\mathrm{quad}} = \boldsymbol{L}_W \boldsymbol{O}_F \overline{\boldsymbol{M}} \boldsymbol{L}_W^T \dot{\boldsymbol{q}}_{\mathrm{mod}} \tag{5.107}$$

Linearizing the inertial force $\boldsymbol{f}_{\mathrm{iner}}$ in (5.106) with respect to $\delta\ddot{\boldsymbol{q}}_{\mathrm{mod}}$, $\delta\dot{\boldsymbol{q}}_{\mathrm{mod}}$, $\delta\boldsymbol{q}_{\mathrm{mod}}$, respectively, yields the inertial mass, damping and stiffness matrices as below

$$\overline{\boldsymbol{M}}_{\mathrm{mod}} = \boldsymbol{L}_W \overline{\boldsymbol{M}} \boldsymbol{L}_W^T \tag{5.108a}$$

$$\overline{\boldsymbol{D}}_{I_{\mathrm{mod}}} = \boldsymbol{L}_W \boldsymbol{O}_F \overline{\boldsymbol{M}} \boldsymbol{L}_W^T \tag{5.108b}$$

$$\overline{\boldsymbol{K}}_{I_{\mathrm{mod}}} = \boldsymbol{0} \tag{5.108c}$$

5.7.3 Practical choice

The expressions in (5.96), (5.97), (5.99), (5.100) are similar as those in [104], but we experienced that the dynamics simulation of the rotating beam benchmark [287] is exceptionally unstable. To remedy the issue of numerical instability, the expressions in (5.106), (5.107), (5.108a), (5.108b), (5.108c) are implemented to gain better numerical robustness. A possible explanation is that, the modal reduction transformation is a thoroughly linear method, thus only valid for the infinitesimal change around the equilibrium configuration, that is the so-called small deformation assumption. The geometrical nonlinear terms introduced by the finite rotation are not compatible with the small deformation assumption, resulting in additional challenges in Newton-Raphson iterations. In contrast, the linear model of the inertial force in (5.106) is more consistent with the small deformation assumption, and hence applicable in the numerical analysis of the modal superelement.

5.8 Reduced external forces

The external forces imposed on the subsystem needs to be reduced accordingly.

Remembering the coordinate transformation (5.74), the virtual work done by the external forces can be evaluated as

$$\delta\mathcal{W}_{\mathrm{f}} = \delta\boldsymbol{q}_C^T \begin{pmatrix} \boldsymbol{f}_B \\ \boldsymbol{f}_I \\ \boldsymbol{0} \end{pmatrix} = \delta\boldsymbol{q}_{\mathrm{mod}}^T \boldsymbol{L}_W \boldsymbol{\Psi}_C^T \boldsymbol{L}_C^T \begin{pmatrix} \boldsymbol{f}_B \\ \boldsymbol{f}_I \\ \boldsymbol{0} \end{pmatrix} \tag{5.109}$$

where $\boldsymbol{f}_B$, $\boldsymbol{f}_I$ are the external forces imposed on the boundary and internal nodes, respectively, expressed in the mixed basis of the inertial frame.

The generalized external forces applied on the reduced subsystem is extracted as

$$\overline{\boldsymbol{f}}_{\mathrm{mod}} = \boldsymbol{L}_W \boldsymbol{\Psi}_C^T \boldsymbol{L}_C^T \begin{pmatrix} \boldsymbol{f}_B \\ \boldsymbol{f}_I \\ \boldsymbol{0} \end{pmatrix} = \begin{pmatrix} \boldsymbol{f}_B + \boldsymbol{L}_B \boldsymbol{\Psi}_{s_I}^T \overline{\boldsymbol{f}}_I \\ \boldsymbol{\Psi}_{d_I}^T \overline{\boldsymbol{f}}_I \\ \boldsymbol{\Psi}_{r_I}^T \overline{\boldsymbol{f}}_I \end{pmatrix} \tag{5.110}$$

where $\overline{\boldsymbol{f}}_I = \boldsymbol{L}_I^T \boldsymbol{f}_I$ is the external forces on the internal nodes expressed in the local basis of the floating frame F.

5.8.1 Gravitational forces

The gravitational forces of the subsystem are not negligible in vast applications. The gravitational forces can be evaluated from the multiplication of the mass matrix of the full subsystem and the gravitational acceleration vector, as follows

$$\begin{pmatrix} \boldsymbol{f}_{g_B} \\ \boldsymbol{f}_{g_I} \end{pmatrix} = \boldsymbol{M}\boldsymbol{g} = \boldsymbol{L}\boldsymbol{M}_{\mathrm{loc}}\boldsymbol{L}^T\boldsymbol{g} \tag{5.111}$$

where the gravitational acceleration vector is

$$\boldsymbol{g} = \begin{pmatrix} g_x & g_y & g_z & 0 & 0 & 0, & \dots \end{pmatrix}^T \in \mathbb{R}^{n_B+n_I} \tag{5.112}$$

The gravitational forces in the local basis of the floating frame F are thus

$$\begin{pmatrix} \overline{\boldsymbol{f}}_{g_B} \\ \overline{\boldsymbol{f}}_{g_I} \end{pmatrix} = \boldsymbol{M}_{\mathrm{loc}}\boldsymbol{L}^T\boldsymbol{g} \approx \boldsymbol{M}_{\mathrm{loc},0}\boldsymbol{L}^T\boldsymbol{g} \tag{5.113}$$

where $\boldsymbol{M}_{\mathrm{loc}} \approx \boldsymbol{M}_{\mathrm{loc},0}$ based on the small deformation assumption. $\boldsymbol{M}_{\mathrm{loc},0}$ is evaluated in the initial configuration and remains constant.

Gravitational forces can be classified as a type of external force, therefore, they can be reduced using Equation (5.110).

5.9 Update the floating frame of reference

As an intuitive choice, the floating frame of reference F can be attached to one of the boundary nodes [13]. However, selecting different boundary nodes results in varying outcomes [104], making it unclear which choice is optimal. It can also be placed at the mass center and aligned with the principal axis of inertia [197]. Alternatively, the position and orientation can be updated as the weighted average of the corresponding quantities of the boundary nodes [50, 104], resulting in slightly better accuracy than attaching to a single boundary node.

Tisserand's criterion [66, 90, 251] can be employed to uniquely determine the position and orientation of the floating frame of reference F. This criterion minimizes the relative kinetic energy of the subsystem, making it more objective than the aforementioned arbitrary choices, and is thus considered a preferred method in this work.

The configuration of the floating frame of reference F can be solved from the constraint equation (5.63). Since the constraint equation (5.63) is an implicit quadratic function of the position and orientation of the floating frame F, it is not possible to obtain an analytical closed-form expression of the configuration of the floating frame F. To this end, one can seek for the Newton-Raphson iteration to find out the solution of F, where the Jacobian matrix of the constraint equation with respect to the coordinate of the floating frame F is required for the iteration.

The variation of the generalized local elastic deformation can be evaluated according to its conceptual definition

$$\delta\overline{\boldsymbol{e}}_{\mathrm{loc}} = \begin{pmatrix} \mathrm{vert}\begin{pmatrix} \boldsymbol{R}_F^T\delta\boldsymbol{r}_B - \boldsymbol{R}_F^T\delta\boldsymbol{r}_F + [\boldsymbol{R}_F^T\widetilde{(\boldsymbol{r}_B - \boldsymbol{r}_F)}]\delta\boldsymbol{\theta}_{l_F} \\ \delta\boldsymbol{\theta}_{l_B} - \boldsymbol{R}_B^T\boldsymbol{R}_F\delta\boldsymbol{\theta}_{l_F} \end{pmatrix} \\ \delta\boldsymbol{\eta}_d \\ \delta\boldsymbol{\eta}_r \end{pmatrix} \tag{5.114}$$

Since the previous configuration of the reduced subsystem is assumed to be frozen in the incremental update scheme, the variations of the generalized coordinates of boundary nodes ($\delta\boldsymbol{r}_B$, $\delta\boldsymbol{\theta}_{l_B}$) and internal modes ($\delta\boldsymbol{\eta}_d$, $\delta\boldsymbol{\eta}_r$) vanish. The variation in (5.114) can be simplified as

$$\delta\overline{\boldsymbol{e}}_{\mathrm{loc}} = \begin{pmatrix} \mathrm{vert}\begin{pmatrix} -\boldsymbol{R}_F^T\delta\boldsymbol{r}_F + [\boldsymbol{R}_F^T\widetilde{(\boldsymbol{r}_B - \boldsymbol{r}_F)}])]\delta\boldsymbol{\theta}_{l_F} \\ -\boldsymbol{R}_B^T\boldsymbol{R}_F\delta\boldsymbol{\theta}_{l_F} \end{pmatrix} \\ \boldsymbol{0}_{n_\eta+1} \end{pmatrix} = -\overline{\boldsymbol{U}}_{\mathrm{loc}}\boldsymbol{L}_F^T\delta\boldsymbol{q}_F \tag{5.115}$$

Substituting (5.115) into (5.63), the Jacobian matrix of the constraint equation with respect to the coordinate of the floating frame F can be solved as

$$\boldsymbol{J}_F = \frac{\partial\boldsymbol{c}_F}{\partial\boldsymbol{q}_F} = -\overline{\boldsymbol{U}}_{\mathrm{loc},0}^T\overline{\boldsymbol{M}\boldsymbol{U}}_{\mathrm{loc}}\boldsymbol{L}_F^T \tag{5.116}$$

It is worth noting that the rigid-body mode $\overline{\boldsymbol{U}}_{\text{loc}}$ in (5.116) depends on the deformed configuration of the reduced subsystem, in detail, depends on the coordinates of boundary nodes.

Thanks to the similarity of variation and time derivative, the velocity of the floating frame F can be evaluated simply as $\dot{\boldsymbol{q}}_F = \boldsymbol{L}_F \boldsymbol{Q} \boldsymbol{L}_W^T \dot{\boldsymbol{q}}_{\text{mod}}$ by referencing (5.67).

5.10 Numerical experiments

In the context of the mode acceleration method, a set of deflection patterns are selected as modal shape vectors to approximate the actual deflection of the subsystem in its dynamic response. This method provides maximum flexibility in computing the utilized modal shapes and supports various boundary conditions. For example, it accommodates the fixed-fixed boundary conditions used in the Craig-Bampton reduction, the free-free boundary conditions used in the Herting reduction, or the fixed-free boundary conditions specified by end users. If the boundary conditions used in the computation of the modal shapes are not consistent with the actual boundary conditions of the subsystem within the overall system, numerical accuracy and convergence may be compromised [46]. However, to maintain clear and unified APIs in a general-purpose multibody system dynamics analysis software, we use free-free boundary conditions as an arbitrary choice. In all numerical experiments, we select the lower-order modal shapes without specific consideration of their directions.

In all numerical experiments, the gravitational forces are not considered.

The HHT integrator introduced in Section 2.8 and the static equilibrium solver presented in Section 2.9 are employed to perform the time marching dynamics simulation and the static equilibrium analysis, respectively. They work in conjunction with the Eigen:PardisoLU linear solver [102], which utilizes the sparse direct LU factorization based on the Intel® oneAPI Math Kernel Library (MKL) PARDISO package. The results from the corotational Timoshenko beam element models, as introduced in Section 2.7.2, are considered as the reference to assess the accuracy of the modal reduction method.

5.10.1 Rotating beam

The rotating beam benchmark developed by Wu and Haug [287] has been widely used to verify the various proposed modal synthesis methods [51, 251, 90] due to the simulation challenges posed by the geometric nonlinearities resulting from significant rotational acceleration.

As illustrated in Figure 5.4, a cantilever beam of length $L = 8\,\text{m}$ is connected to the ground via a revolute joint and is driven to rotate by a rheonomic constraint,

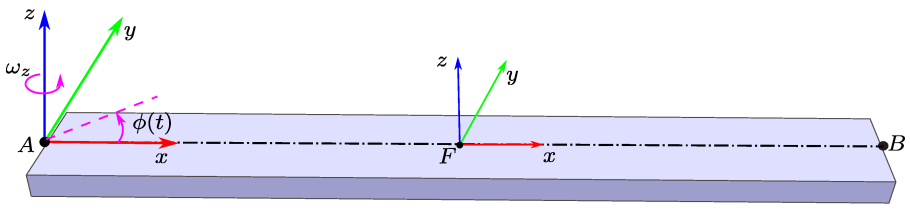

Figure 5.4: A rotating beam driven by a rheonomic constraint.

which specifies the root rotational angle $\phi(t)$ according to the following function:

$$\phi(t) = \omega_z T_s \begin{cases} \frac{1}{2}\tau^2 + \frac{1}{(2\pi)^2}\left(\cos(2\pi\tau - 1)\right) & \text{for} \quad \tau < 1 \\ \tau - \frac{1}{2} & \text{for} \quad \tau \geq 1 \end{cases} \tag{5.117}$$

where $T_s = 15\,\text{s}$, $\omega_z = 4\,\text{rad/s}$ and $\tau = t/T_s$.

As shown in Figure 5.5, the angular velocity prescribed by the rheonomic constraint increases to 4 rad/s over 15 s, after which it remains constant. The angular acceleration reaches its peak at 7.5 s before gradually decreasing.

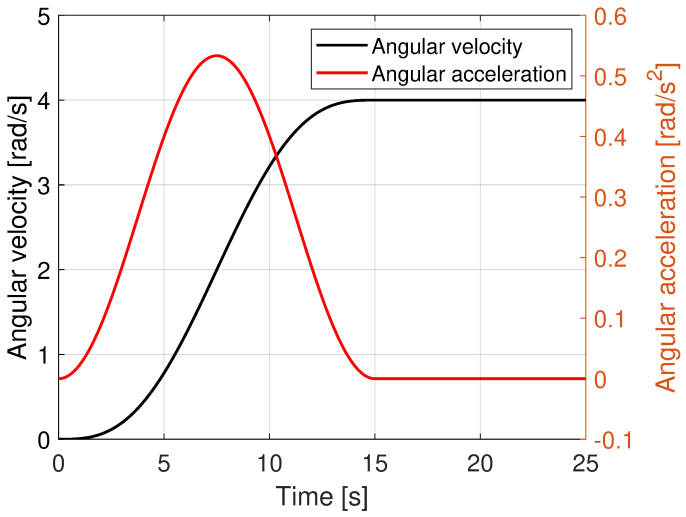

Figure 5.5: The angular velocity and angular acceleration of the rotating beam.

The beam is discretized into 10 beam elements with the cross–sectional properties detailed in Table 5.1. The dynamics simulation is is carried out over a duration of 25 s with a constant time step of 0.002 s. A single modal superelement with two boundary nodes located at the two endpoints A and B is employed to model the rotating beam. The first 20 modal shapes, including the six rigid-body modes, are selected as the modal basis for the modal reduction transformation.

The transverse deflection and the axial stretch of the beam's tip node B with respect to the root node A are illustrated in Figure 5.6a and 5.6b, respectively. In

Table 5.1: Cross-sectional properties of the rotating beam.

Property	Symbol	Value	Unit
Mass per unit length	ν	0.2019	kg/m
Mass moment of inertia about y axis	J_{yy}	6.637×10^{-8}	kg m
Mass moment of inertia about z axis	J_{zz}	2.273×10^{-5}	kg m
Polar mass moment of inertia	J_{xx}	2.279×10^{-5}	kg m
Axial stiffness	EA	5.032×10^{6}	N
Bending stiffness about y axis	EI_{yy}	1.654	N m^2
Bending stiffness about z axis	EI_{zz}	566.4	N m^2
Torsional stiffness	GI_p	216.8	N m^2
Shear stiffness along y axis	GA_y^s	1.633×10^{6}	N
Shear stiffness along z axis	GA_z^s	1.633×10^{6}	N

the modal results, the transverse deflection reaches its maximum value of 0.546 m at 6.85 s before gradually decreasing towards zero. After 15 s, the beam begins to oscillate, with the amplitude of oscillation diminishing over time due to structural damping.

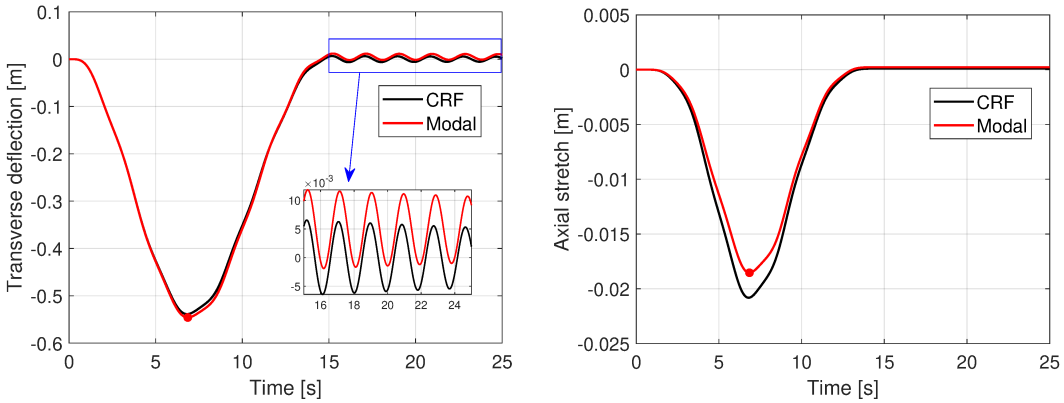

(a) Transverse deflection. (b) Axial stretch.

Figure 5.6: Elastic deflections of the rotating beam. 'CRF': Reference solution from the corotational Timoshenko beam element model; 'Modal': Results from the modal reduction method.

By extending the dynamics simulation duration to 100 s, the oscillation frequency can be determined via FFT analysis. The peak oscillation frequency identified from both the CRF and modal results is 0.5294 Hz. The damping ratios, derived through envelope analysis and logarithmic decrement fitting, are 0.00657 and 0.00566 for the CRF and modal methods, respectively. The modal reduction method exhibits a lower damping ratio compared to the full-state corotational

model.

As shown in Figure 5.6a, during the small-amplitude oscillation phase, a consistent deviation of 0.0049 m is observed in the transverse deflection in the modal results. This suggests that the inertial and elastic forces within the modal superelement do not achieve an ideal equilibrium, likely due to inaccuracies in the computation of inertial terms. However, considering the beam's length of 8 m, this transverse deviation represents only 0.06 %, which is negligible for most engineering applications.

As shown in Figure 5.6b, the maximum axial shortening reported by the modal method is 0.019 m, which is slightly less than the maximum value of 0.021 m obtained from the CRF. The modal reduction method captures the axial shortening effect due to transverse deflection with acceptable accuracy. This is a beneficial side effect of the synchronous update of the floating frame of reference F at the end of each time step.

A summary of the comparison between the modal and CRF results is provided in Table 5.2.

Table 5.2: Summary of the comparison between CRF and modal method results for the rotating beam benchmark.

	CRF	Modal	Unit
Maximum transverse deflection	0.539	0.546	m
Maximum axial shortening	0.021	0.019	m
Mean deviation of transverse deflection	0.0000	0.0049	m
Oscillation frequency	0.5294	0.5294	Hz
Damping ratio	0.00657	0.00566	–

The deformed configuration at the moment of maximum transverse deflection is illustrated in Figure 5.7, along with the shadow configuration to indicate the elastic deformation field resolved in the reference frame F.

5.10.2 Flexible slider-crank mechanism

Wu and Tiso [286] proposed a flexible slider-crank mechanism, depicted in Figure 5.8, to verify their modal derivatives approach. The system comprises a crank, a connecting rod and a slider which are assembled by three revolute joints located at point O, B and C, respectively. The slider is attached to the ground by a prismatic joint and hence is constrained to move horizontally. The lengths of the crank and connecting rod are 10 m and 20 m, respectively.

Both the crank and the connecting rod are made of aluminum and have a rectangular cross-section measuring 0.4 m × 0.4 m. Their cross-sectional properties are detailed in Table 5.3.

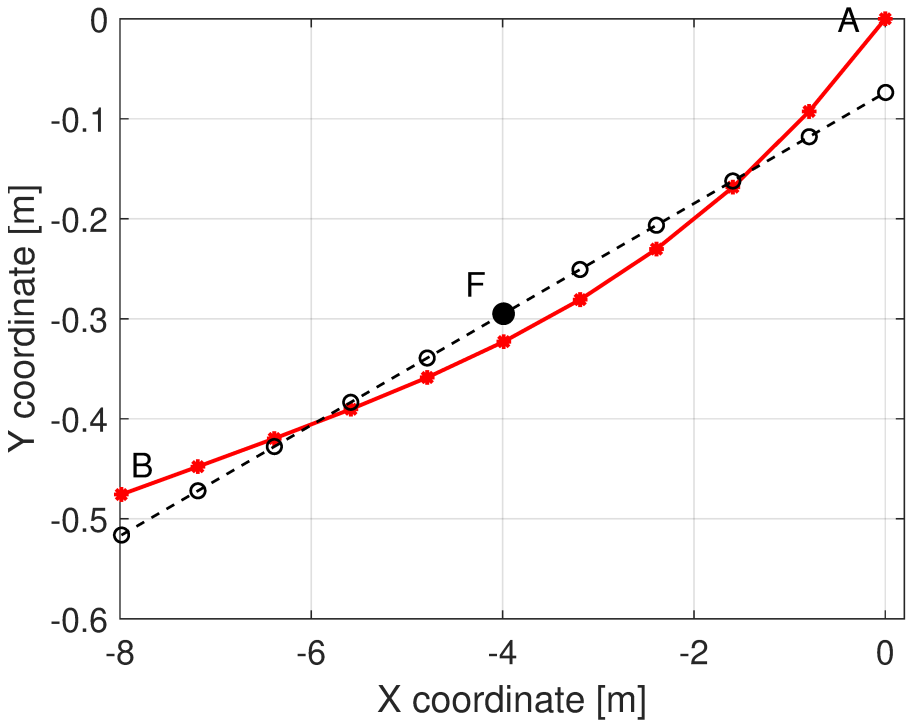

Figure 5.7: The deformed configuration, along with the shadow configuration, is shown at the moment of maximum transverse deflection ($t = 6.85\,\mathrm{s}$). Deformed configuration: red solid line with '*'; Shadow configuration: black dashed line with 'o'.

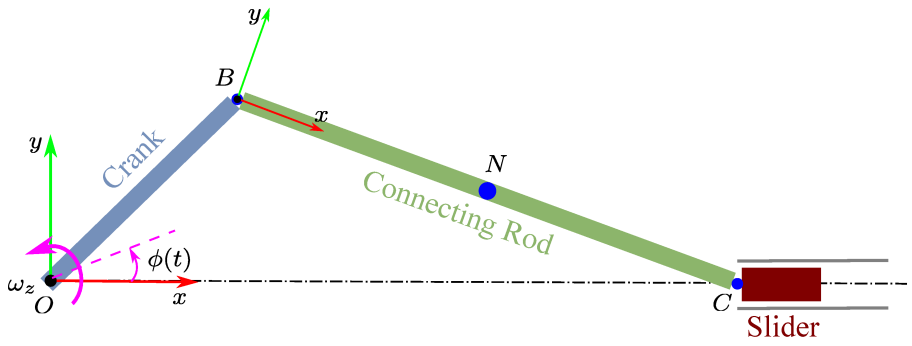

Figure 5.8: A flexible slider-crank mechanism driven by a rheonomic constraint.

In the initial configuration, the crank, connecting rod, and slider are aligned horizontally. A rheonomic constraint at the revolute joint O drives the rotational angle of the crank's root node according to the function $\phi(t) = 3\pi t^2/50$ during the first 5 s. Once the crank reaches 270° at $t = 5\,\mathrm{s}$, the rheonomic constraint holds the angle constant, locking the mechanism. This sudden locking induces significant oscillations. The dynamics simulation is conducted for 10 s with a constant time

Table 5.3: Cross-sectional properties of the crank and connecting rod.

Property	Symbol	Value	Unit
Mass per unit length	ν	432	kg/m
Mass moment of inertia about y,z axis	J_{yy},J_{zz}	5.76	kg m
Polar mass moment of inertia	J_{xx}	11.52	kg m
Axial stiffness	EA	1.12×10^{10}	N
Bending stiffness about y,z axis	EI_{yy},EI_{zz}	1.4933×10^{8}	N m^2
Torsional stiffness	GI_p	1.1399×10^{8}	N m^2
Shear stiffness along y,z axis	GA_y^s,GA_z^s	3.634×10^{9}	N

step size of 0.001 s.

The crank is discretized into 10 beam elements and then reduced to a single modal superelement with two boundary nodes at its two endpoints. Considering the significant geometric nonlinearity in the dynamics process, the connecting rod is divided into several segments. Each segment is discretized into 10 beam elements, reduced to a modal superelement with two boundary nodes at its endpoints, and connected by fixed joints. The transverse deflection and axial stretch of the midpoint of the connecting rod are measured relative to the left endpoint B and resolved in the local frame $Bxyz$.

Five simulations are conducted for a comprehensive comparison. The reference solution is computed using a full-state corotational Timoshenko beam element model, with both the crank and the connecting rod discretized into 10 beam elements. The other four solutions utilize a single modal superelement for the crank and 1, 2, 3, or 4 modal superelements for the connecting rod, respectively. The first five seconds of the simulation are uneventful and are therefore not reported here. The results for the subsequent five seconds are presented in Figures 5.9a and 5.9b.

It can be observed from Figures 5.9a and 5.9b that, as the number of modal superelements used for the connecting rod increases, the solution approaches the reference solution obtained from the CRF model. When three superelements are used, the numerical solution stabilizes and does not change significantly with further increases in the number of superelements. It is noteworthy that using only a single modal superelement for the connecting rod results in an axial stretch with an opposite direction compared to the reference solution. A multi-segment approach is necessary to effectively capture the axial shortening effect.

5.10.3 Curved beam

Bathe and Bolourchi [9] described a cantilevered beam spanning from the origin A to the endpoint B along the arc of a circle centered at point O, as illustrated

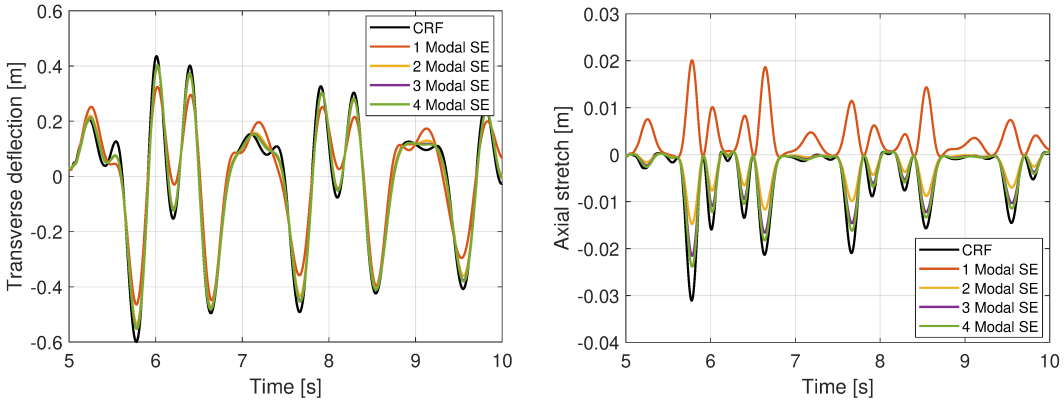

(a) Transverse deflection. (b) Axial stretch.

Figure 5.9: Elastic deformation measures at the midpoint N of the connecting rod, resolved in the local frame $Bxyz$. 'CRF': Reference solution from the corotational Timoshenko beam element model; 'i Modal SE': Solution using i modal superelements for the connecting rod, where $i = 1,2,3,4$.

in Figure 5.10. The beam has an arc radius of 100 in and subtends an angle of 45 °. The curved beam is fixed to the ground at point A and is subjected to a concentrated force of $P = 600\,\text{lb}$ applied at point B. Notably, the direction of the applied force remains constant as the beam deflects.

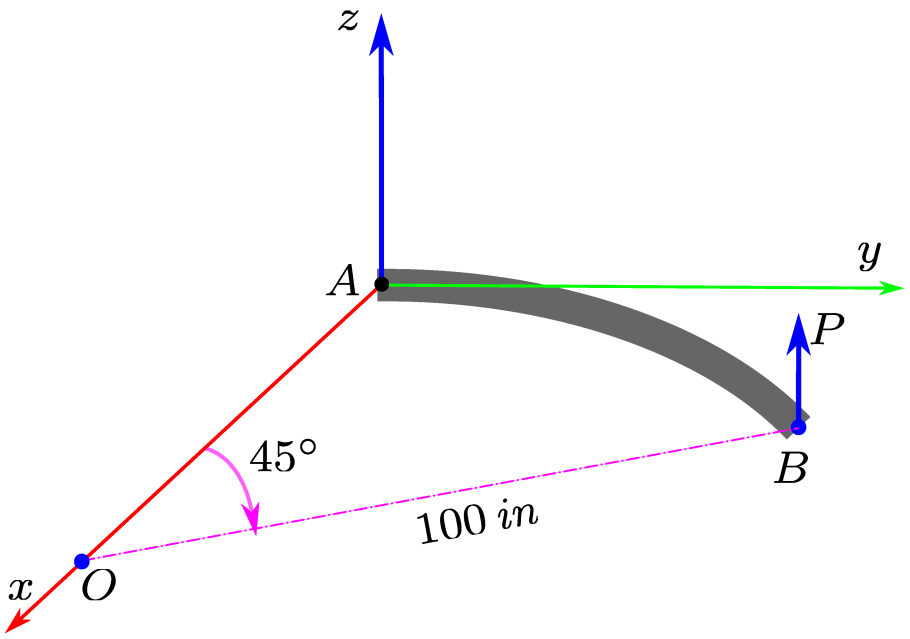

Figure 5.10: A 45 ° curved beam under a concentrated force P at the tip.

The cross-sectional properties are detailed in Table 5.4. The mass and inertia properties are irrelevant in the static equilibrium analysis, and therefore not reported here. The bending-stretch coupling stiffness terms $k_{u\theta}$,$k_{u\psi}$ are included in this benchmark, which necessitate the use of the FPM stiffness matrix. Consequently, the shape functions must be updated, and the element stiffness matrix is integrated using Gauss quadrature [26].

Table 5.4: Cross-sectional properties of the curved beam.

Property	Symbol	Value	Unit
Axial stiffness	EA	1.0×10^7	lb
Bending stiffness about y,z axis	EI_{yy},EI_{zz}	8.333×10^5	$\text{lb} \cdot \text{in}^2$
Torsional stiffness	GI_p	7.03×10^5	$\text{lb} \cdot \text{in}^2$
Shear stiffness along y,z axis	GA_y^s,GA_z^s	4.167×10^6	lb
Bending-stretch coupling stiffness	$k_{u\theta}$,$k_{u\psi}$	-8.333×10^3	$\text{lb} \cdot \text{in}$

A static equilibrium analysis is conducted to analyze the deflection of the curved beam. Due to the significant geometric nonlinearity present in this benchmark, a minimum of four modal superelements is necessary to achieve converged and reasonable results. The reference solution is computed from the CRF model, which utilizes 20 FPM Timoshenko beam elements. In the modal reduction models, each segment is represented by 10 beam elements, with the first 20 modal shapes serving as the modal basis. The displacement field of the curved beam in the static equilibrium configuration, as solved by the multi-segment modal reduction models, is compared to the reference solution, as illustrated in Figures 5.11.

As observed in Figure 5.11, the displacements along the y- and z-directions exhibit good agreement between the modal reduction and CRF methods. The displacement along the x-direction obtained from the modal reduction method converges toward the CRF result as the number of modal superelements increases. It is important to note that the geometric stiffness matrix of the modal superelement, as defined in (5.80c), is crucial for achieving convergence in this static equilibrium analysis. Without this term, convergence becomes challenging.

The tip displacements are detailed in Table 5.5.

5.10.4 Rotating beam linked with a rigid-body

The proposed modal reduction method is extended to accommodate systems with internal constraints. To validate this extension and assess its accuracy, a rigid-body is attached at the midpoint of the rotating beam via a fixed joint, building upon the benchmark described in Section 5.10.1. This extended model is depicted in Figure 5.12.

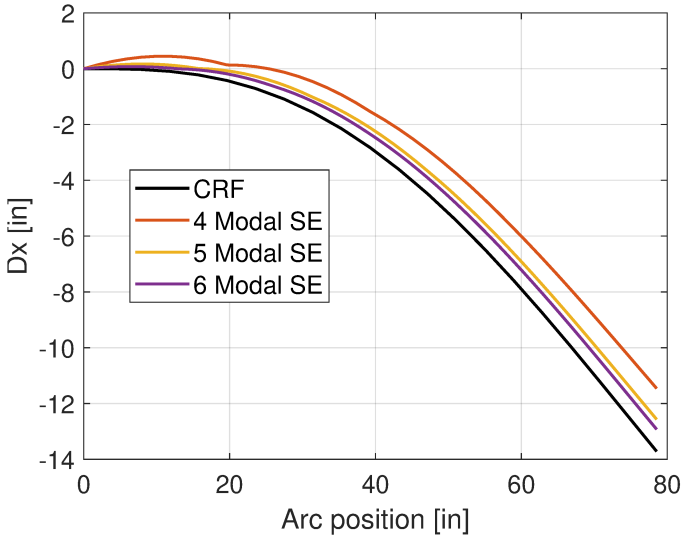

(a) Displacement along x.

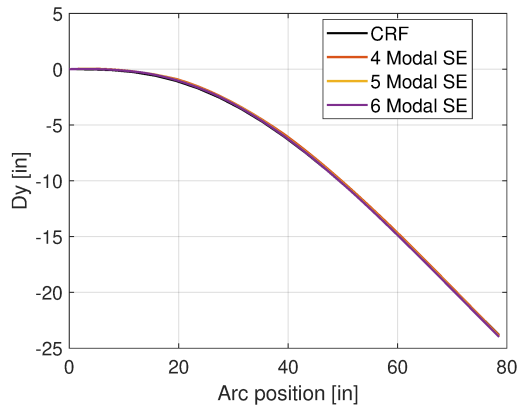

(b) Displacement along y.

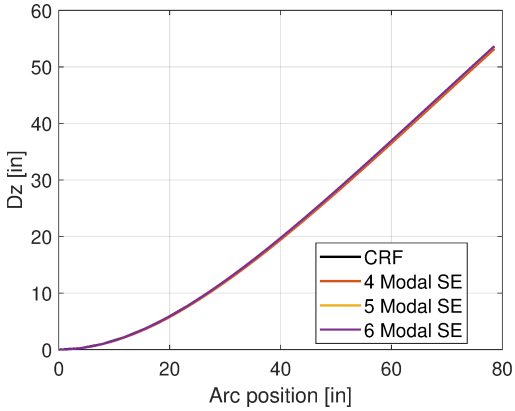

(c) Displacement along z.

Figure 5.11: The displacement field of the curved beam along x,y and z directions. The horizontal axes in the plots represent the arc position of each beam node, starting from point A. 'CRF': Reference solution from the corotational Timoshenko beam element model; 'i Modal SE': Solution using i modal superelements for the connecting rod, where $i = 4,5,6$.

The bending stiffness out of the plane of rotation, EI_{yy}, is increased to match the in-plane stiffness, such that $EI_{yy} = EI_{zz} = 566.4\,\mathrm{N\,m^2}$, ensuring proper convergence of the dynamics simulation. All other parameters of the beam elements remain consistent with those presented in Table 5.1. The driving function $\phi(t)$ for the rotational angle at the beam root follows the expression given in (5.117). A concentrated follower force, expressed as a quadratic function of the angular velocity $P(t) = 0.2\omega_z^2\,\mathrm{N}$, is applied at the beam's midpoint $L_{AC} = 4\,\mathrm{m}$ in the local y direction. The rigid body is positioned $d = 0.018\,\mathrm{m}$ away from the midpoint C

Table 5.5: The tip displacements of the curved beam.

Models	Disp. x [in]	Disp. y [in]	Disp. z [in]
CRF	−13.712	−23.817	53.613
4 Modal SE	−11.459	−23.848	53.155
5 Modal SE	−12.568	−23.929	53.548
6 Modal SE	−12.925	−23.974	53.645

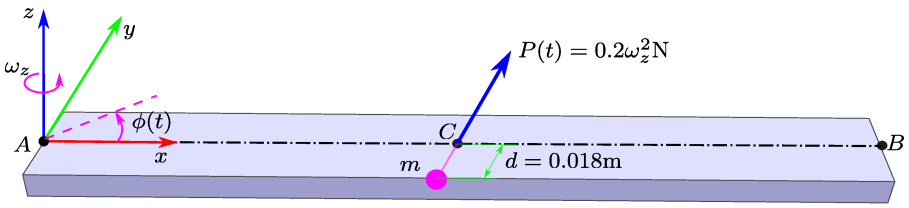

Figure 5.12: A rotating beam linked with a rigid-body and driven by a rheonomic constraint.

along the negative y axis and is connected to the middle node via a fixed joint. The rigid body has a mass of 0.008 kg and moments of inertia about the x,y and z axes of 0.001 kg $\cdot$ m^2 each.

The dynamic simulation is conducted over a duration of 25 s with a constant time step size of 0.002 s. The transverse and axial displacements of the attached rigid-body, relative to the reference frame at the root node A, are presented in Figures 5.13a and 5.13b, respectively.

Figure 5.13a shows that the maximum transverse displacement aligns well between the CRF and modal methods. However, a consistent shift in the mean value of the transverse displacement during the small-amplitude oscillation period is observed after 15 s. A more pronounced discrepancy in the axial displacement is seen in Figure 5.13b, similar to the behavior observed in Figure 5.6b.

The reaction forces and moments at the fixed joint between the attached rigid body and the middle node are presented in Figure 5.14. The reaction force F_x and reaction moment M_z show strong agreement between the CRF and modal methods. However, the reaction force F_y exhibits a different behavior. During the ramp-up phase of F_y, the two methods align well, but a discrepancy emerges as the force decreases, with the modal method resulting in a smaller amplitude compared to the CRF.

The discrepancy in the reaction force F_y observed in Figure 5.14b can be explained using Figure 5.15. During the final small-amplitude oscillation period, the primary source of the reaction forces and moments at the fixed joint is the centrifugal force F_{cent} acting on the rigid-body. If the intersection angle between the centrifugal force F_{cent} and the tangent direction of the beam's reference line at the

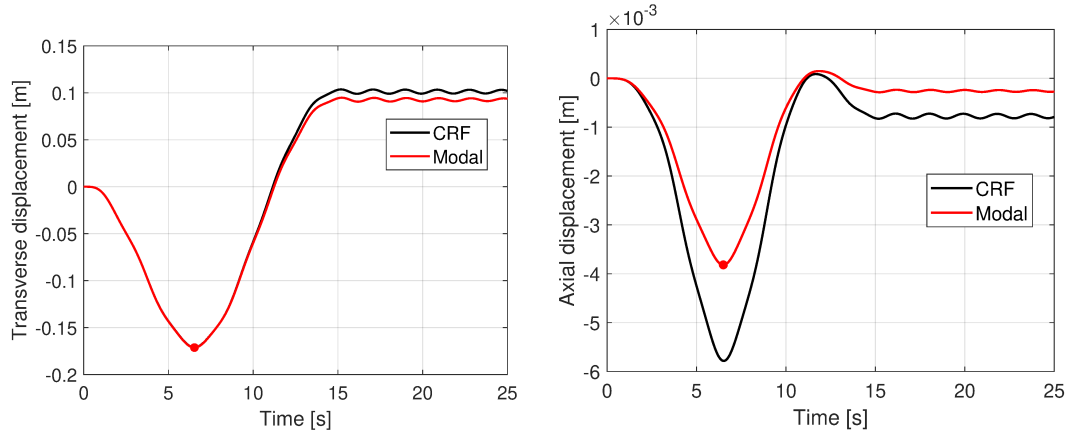

(a) Transverse displacement. (b) Axial displacement.

Figure 5.13: The displacements of the attached rigid-body relative to the root node A. 'CRF': Reference solution from the full-state model; 'Modal': Results from the modal reduction method.

middle node is ψ, the reaction forces can be expressed as $F_x = F_{\text{cent}} \cos(\psi)$ and $F_y = -F_{\text{cent}} \sin(\psi)$.

The intersection angle ψ consists of two components: an initial value ψ_0 determined by the geometry in the initial configuration, and a small angle $\Delta\psi$ introduced by the elastic deformation. In the modal reduction procedure, the modal reduction transformation matrix (5.49) is computed based on the initial configuration and remains fixed throughout the dynamics simulation. Consequently, the small angle $\Delta\psi$ is not accounted for in the modal reduction method. Since $\Delta\psi$ arises from geometric nonlinearity in the deformed configuration, it cannot be accurately captured by the modal reduction approach. If $\Delta\psi$ is sufficiently small, the effects of geometric nonlinearity diminish, leading to better agreement in the reaction force F_y between the methods.

A virtual experiment was conducted to increase the stiffness properties, thereby reducing the elastic deformation and resulting in a smaller $\Delta\psi$. As illustrated in Figure 5.16, increasing the beam's stiffness properties leads to a closer alignment of the reaction force F_y between the CRF and modal methods. However, a persistent deviation remains even with an extremely stiff beam. The cause of this constant deviation deserves additional investigation in future developments in this research, because it could be an inherent limitation of the proposed modal method.

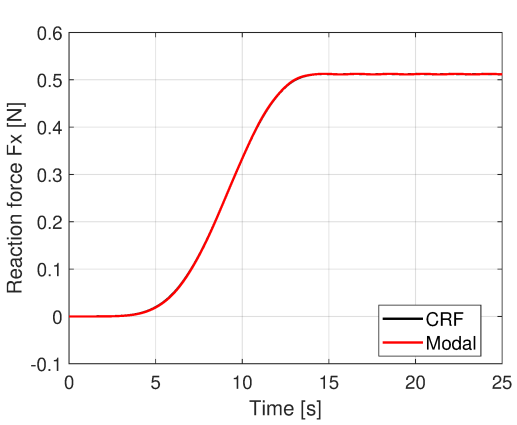

(a) Reaction force F_x.

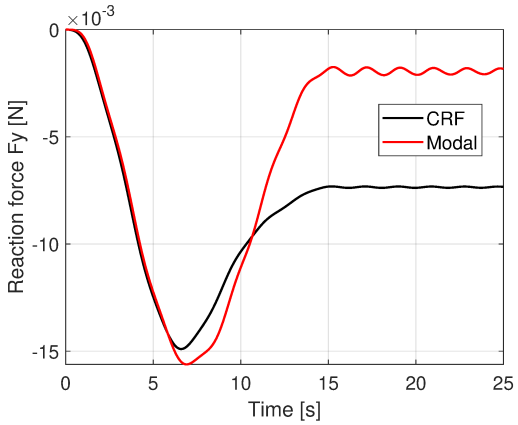

(b) Reaction force F_y.

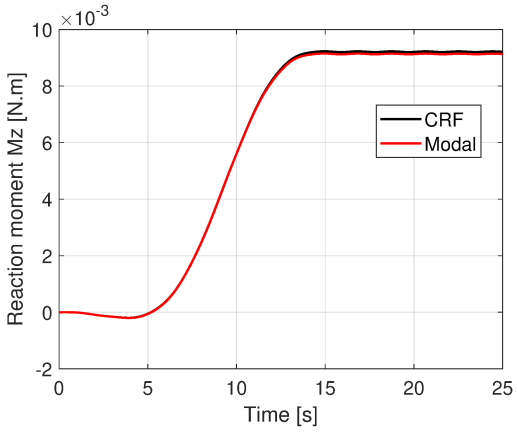

(c) Reaction moment M_z.

Figure 5.14: The reaction forces and moments at the fixed joint between the attached rigid-body and the middle node. 'CRF': Reference solution from the full-state model; 'Modal': Results from the modal reduction method.

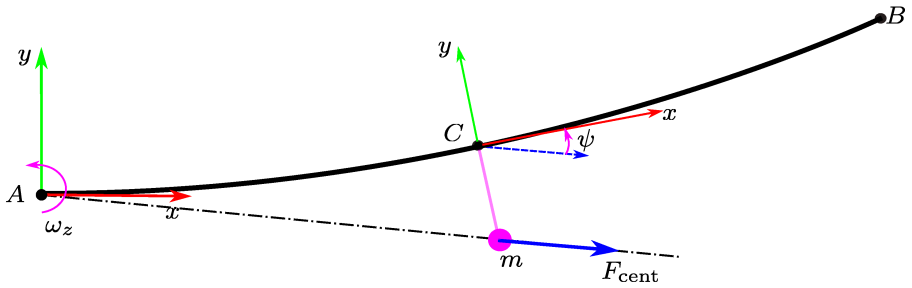

Figure 5.15: A scheme for interpreting the reaction forces and moments at the fixed joint.

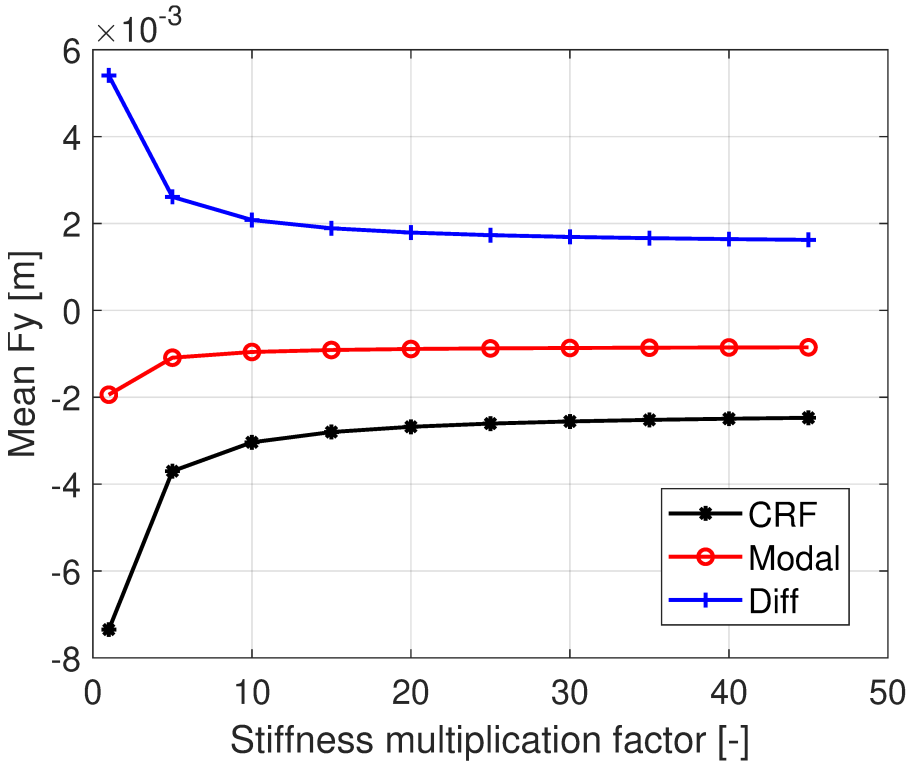

Figure 5.16: Sensitivity analysis of the mean value of the reaction force F_y during the small-amplitude oscillation period after 15 s.

Chapter 6

Final remarks

6.1 Conclusions

This thesis investigates the linearization and modal problems in multibody system dynamics, with a particular emphasis on the aeroelastic stability assessment of modern wind turbines.

The key findings and primary contributions of this research are summarized as follows:

Static equilibrium solver accommodating rheonomic constraints

An efficient static equilibrium solver that accommodates rheonomic constraints is developed. The inertial and damping forces are transferred to the right-hand side of the equations of motion, transforming the problem into a traditional static analysis formulation, which is then solved using the Newton-Raphson iterative method. During the iteration process, the generalized velocities, generalized accelerations, and the resulting inertial and damping forces, along with any external forces (e.g., aerodynamic forces), are explicitly updated in accordance with the rheonomic constraints. The proposed solver has been successfully applied to determine the quasi-static equilibrium configurations of operating wind turbines, regardless of the damping level, including systems with negative damping.

Krylov-Schur eigenvalue solver

A sparsity-preserving Krylov-Schur eigenvalue solver is implemented to address the eigenvalue problem in large-scale multibody dynamic systems. The shift-and-invert technique is employed to facilitate the extraction of eigenvalues clustered around specified values. A simple yet effective preconditioning strategy is applied by scaling the Jacobian matrix of constraints to mitigate ill-conditioning. The proposed

eigenvalue solver has been successfully applied in the stability analysis of wind turbines and in the modal reduction process for generating modal superelements. It is demonstrated that the solver can effectively handle arbitrary rigid body modes and arbitrary algebraic constraints.

Tangent stiffness matrix of constraints

Based on quaternion parametrization for finite rotations, a general formulation of holonomic constraint equations and their corresponding Jacobian matrix is derived. This formulation is initially developed for a fixed joint, but it can be readily extended to a series of derived free-motion joints by suppressing specific rows in the constraint equations and the Jacobian matrix. Subsequently, a consistent and unified analytical expression for the tangent stiffness matrix of constraints is derived. The tangent stiffness matrix of constraints consists of two components: $\boldsymbol{K}_c = \boldsymbol{K}_c^{(M)} + \boldsymbol{K}_c^{(P)}$, where the block patterns of $\boldsymbol{K}_c^{(M)}$ and $\boldsymbol{K}_c^{(P)}$ are symmetric; however, in general, neither of them is symmetric nor skew-symmetric. A numerical analysis of an anchor chain illustrates the critical role of the tangent stiffness matrix of constraints in ensuring the proper convergence of static equilibrium analysis and in achieving accurate eigenvalue results for multibody systems featuring free-motion joints under stressed equilibrium conditions.

Linearization and modal analysis framework for wind turbines

A linearization and modal analysis framework for multi-bladed wind turbines is developed. Auxiliary reference frames, corresponding to the blade azimuthal positions, are introduced at the rotor center. Auxiliary coordinates, defined with respect to these reference frames, are established for the blade element nodes. By neglecting unsteady aerodynamic effects, the aerodynamic forces are linearized in the quasi-static equilibrium configuration using numerical differentiation. Analytical linearization is performed for the inertial, elastic, and viscous terms in the blade structural dynamics, modeled using the corotational formulation, as well as for the Jacobian matrix and tangent stiffness matrix of the algebraic constraints in the rotor. All aerodynamic, inertial, elastic, viscous, and algebraic terms are then transformed into the auxiliary coordinates to ensure isotropy from a mathematical perspective. Subsequently, the sub-blocks corresponding to the hub center are rotated back into consistent coordinates to facilitate the assembly of the system matrices. The system tangent stiffness matrix consists of the material stiffness matrix $\boldsymbol{K}_m$, the geometric stiffness matrix $\boldsymbol{K}_g$, the aerodynamic stiffness matrix $\boldsymbol{K}_a$, the inertial stiffness matrix $\boldsymbol{K}_i$, and the tangent stiffness matrix of constraints $\boldsymbol{K}_c$, while the system tangent damping matrix includes the material damping matrix $\boldsymbol{D}_m$, the aerodynamic damping matrix $\boldsymbol{D}_a$, and the inertial damping matrix $\boldsymbol{D}_i$.

Finally, the multi-blade coordinate (MBC) transformation is applied to both generalized coordinates and Lagrange multipliers, resulting in a linear time-invariant (LTI) system suitable for eigenvalue analysis. A comprehensive interpretation of the modal dynamics of wind turbines is also presented.

Eigenvalues of a rotor's free rotation mode

The eigenvalues corresponding to the free rotation mode of three-bladed rotor systems are investigated. Numerical experiments are conducted on rotors of varying complexity, including a single rigid body, a rigid rotor, and a flexible rotor. It is shown that the eigenvalues associated with the rotor's free rotation mode are not necessarily zero. The results demonstrate that the developed linearization and modal analysis framework is well-suited for eigenvalue analysis of the free rotation modes in three-bladed rotors.

The influence of the matrices $\boldsymbol{K}_g$, $\boldsymbol{K}_i$, $\boldsymbol{D}_i$, and $\boldsymbol{K}_c$ on the eigenvalues of the rotor's free rotation mode is also discussed. Specifically, the terms in the geometric stiffness matrix $\boldsymbol{K}_g$ due to transverse external follower forces, the tangent stiffness matrix of constraints $\boldsymbol{K}_c$ due to transverse external follower forces, and the inertial stiffness matrix $\boldsymbol{K}_i$ due to centrifugal forces exhibit a softening effect, shifting the eigenvalues toward real numbers. In contrast, the terms in the geometric stiffness matrix $\boldsymbol{K}_g$ and the tangent stiffness matrix of constraints $\boldsymbol{K}_c$ due to centrifugal forces exhibit a stiffening effect, driving the eigenvalues toward pure imaginary numbers.

Aeroelastic stability analysis of wind turbines

Aeroelastic stability analysis of wind turbines in normal operational conditions is performed using the developed linearization and modal analysis framework. A comprehensive verification and validation procedure is also proposed.

The standard deviation ratio of the filtered component of the blade first edgewise mode to that of the 1P rotor rotational frequency, in the time series of the blade root edgewise moment, denoted as $r_{\mathrm{1E/1P}}$, is introduced as a measure to quantify the blade edgewise vibration level. A virtual numerical experiment is conducted using an intermediate-version commercial wind turbine model. The blade torsional stiffness is uniformly scaled along the spanwise to generate a series of wind turbine models. Time-domain dynamic simulations and modal analyses are performed on these models. The standard deviation ratios $r_{\mathrm{1E/1P}}$ and the aeroelastic damping ratios ζ_{1E} of the rotor first edgewise backward whirling mode are compared across the operating wind speed range. A strong correlation between $r_{\mathrm{1E/1P}}$ and ζ_{1E} is observed from the numerical experiments.

Subsequently, the aeroelastic stability predictions are validated against experimental measurements from two offshore prototype wind turbines. The unstable

wind speed range, as observed from the standard deviations of the blade root edgewise moment, closely aligns with the region of negative damping for the rotor first edgewise backward whirling mode.

The verification and validation analysis demonstrates the applicability of the proposed aeroelastic stability assessment method for wind turbines in engineering practice.

Modal reduction

A modal reduction procedure based on the corotational concept is developed within the context of multibody system dynamics.

A modal coordinate transformation is employed for subsystems comprising rigid bodies, finite elements, and algebraic constraints in the initial configuration. The mode acceleration method is utilized in the transformation, offering great flexibility in the selection of boundary conditions and effectively avoiding over-constraints. The gross motion of the elastic subsystem is decomposed into rigid-body motion, represented by a floating frame of reference, and elastic deformations, expressed in the local basis of this floating frame. The local elastic deflections are comprised of three components: the response of static modes, the response of dynamic modes, and the response of a static correction mode.

Constraint equations are imposed by enforcing the orthogonality of the rigid-body modes and elastic deflections in the metric of the mass matrix, resolved in the local basis of the floating frame of reference. Two projection matrices are derived to facilitate the motion decomposition. Subsequently, the tangent stiffness matrix and the geometric stiffness matrix are formulated for the reduced subsystem. The inertial terms, including the mass, damping, and stiffness matrices, are analytically derived, along with the quadratic velocity term, which is essential for accurately simulating rotating structures. External forces are also reduced accordingly, with a static correction mode introduced to account for the influence of external forces acting on the reduced internal nodes. The inclusion of the static correction mode is crucial for improving the accuracy of the recovery of internal stresses and internal constraint reaction forces. A scheme for updating the configuration of the floating frame of reference based on Tisserand's criterion is also proposed.

Numerical experiments are conducted using academic examples. In cases of large deflections experienced by the subsystems, a multi-segment strategy is recommended to capture geometric nonlinearities. It is found that the geometric stiffness matrix is beneficial for improving numerical convergence in the static equilibrium analysis. The results from various numerical examples demonstrate the accuracy and effectiveness of the developed modal reduction procedure.

6.2 Recommendations for future research

Several research directions are identified that may contribute to the advancement of the linearization and modal analysis framework for modern wind turbines:

1. The incorporation of linearized unsteady aerodynamic effects, such as dynamic wake and dynamic stall models, into the present framework could enhance the accuracy of aeroelastic stability predictions for wind turbines [119, 118, 120, 40, 41]. These effects should therefore be considered for implementation in future research.

2. An advanced GEBT-based tapered beam element that incorporates warping and Wagner effects, supports arbitrary cross-sections, accommodates inhomogeneous anisotropic material properties, and is capable of handling initially curved and twisted configurations would be valuable for enhancing the accuracy of long slender blade modeling in wind turbines. Verification against high-fidelity shell element models, as well as validation using measurements from test rigs and operational wind turbines, is also recommended [38].

3. The eigenvalues of the rotor's free rotation mode, along with the modal dynamics of wind turbines, can be evaluated using the advanced GEBT-based blade modeling and compared with the results obtained from the current corotational Timoshenko beam element.

4. By employing linearization based on generalized coordinates that incorporate the virtual rotation vector and its derivatives $\delta\boldsymbol{\theta}_l$, $\delta\dot{\boldsymbol{\theta}}_l$, $\delta\ddot{\boldsymbol{\theta}}_l$ for rotations, along with the advanced GEBT-based blade modeling, a more rigorous framework for linearization and modal analysis of multi-bladed rotor systems is anticipated. It would be particularly valuable to identify the conditions under which zero eigenvalues can occur for the rotor's free rotation mode, when all geometric nonlinear terms, including $\boldsymbol{K}_g$, $\boldsymbol{K}_i$, and $\boldsymbol{K}_c$, are considered.

5. More complete verification and validation of the aeroelastic stability analysis for wind turbines should be prioritized in future research. A code-to-code comparison between the present method and other established tools, such as Bladed and HAWCStab2, is recommended. Significant discrepancies in the absolute values of aeroelastic damping ratios, particularly for the less-damped edgewise modes, are expected between these tools. It is suggested that the verification process begin with a simple rotor model, such as a rotating rotor with straight blades in a vacuum (neglecting aerodynamics), and gradually increase the complexity of the numerical models in subsequent stages.

6. The developed modal reduction method can be applied to blade modeling for wind turbines, providing an alternative linearization and modal analysis

framework that aligns more closely with tools such as Bladed [2] and HAWC-Stab2 [117, 110]. The modal dynamics, evaluated using both the modal reduction method and the corotational formulation—and potentially a GEBT-based model—can be compared to gain further insights into the discrepancies in aeroelastic damping ratios for the less-damped edgewise modes across these tools.

7. It is beneficial to account for the flexibility, particularly in bending directions, in the load transmission path from the hub to the tower top within simulation models. Additionally, hydrodynamic effects should be incorporated into the linearization and modal analysis of the full offshore wind turbine system. The modeling parameters should be carefully examined and updated based on detailed finite element analysis, component testing in the factory, and modal testing in the field under idling conditions, to ensure the accuracy of the numerical model for subsequent code-to-measurement validation under operating conditions.

8. Experimental validation of the aeroelastic stability assessment can be enhanced by collecting additional measurement data at various rotor speeds within the less stable wind speed range. The critical rotor speed associated with the rotor edgewise backward whirling mode can be identified through experimental measurements and used to validate the corresponding numerical predictions.

9. Operational modal analysis (OMA) [204, 37, 224, 271, 72] can be utilized to identify the modal parameters of wind turbines in both simulation and field measurement environments. The results from OMA can serve as an additional reference for code-to-code verification and code-to-measurement validation in the aeroelastic stability analysis of wind turbines.

Appendix A

Mathematics

A.1 Projection matrix of quaternions

By introducing a projection matrix $\boldsymbol{P}(\boldsymbol{\rho}) \in \mathbb{R}^{3\times 3}$ equal to the bottom three rows of the matrix $\frac{1}{2}\boldsymbol{F}(\boldsymbol{\rho}^*)_{\oplus}{}^T$ (see (2.27b))

$$\boldsymbol{P}(\boldsymbol{\rho}) = \frac{1}{2}\left(s\boldsymbol{I}_{3\times 3} + \widetilde{\boldsymbol{v}}\right) \tag{A.1}$$

the imaginary vectorial part of (2.36a) can be written as

$$\mathrm{Im}\left(\delta\boldsymbol{\rho}\right) = \boldsymbol{P}(\boldsymbol{\rho})\,\delta\boldsymbol{\theta}_l \tag{A.2}$$

The projection matrix $\boldsymbol{P}(\boldsymbol{\rho})$ of a unit quaternion $\boldsymbol{\rho}$ holds important properties as follows

$$\boldsymbol{P}(\boldsymbol{\rho})^T = \boldsymbol{P}(\boldsymbol{\rho}^*) \tag{A.3a}$$

$$\boldsymbol{P}(\boldsymbol{\rho}) = \boldsymbol{P}(\boldsymbol{\rho})^T\boldsymbol{R}(\boldsymbol{\rho}) \tag{A.3b}$$

$$\boldsymbol{P}(\boldsymbol{\rho}) = \boldsymbol{R}(\boldsymbol{\rho})^T\boldsymbol{P}(\boldsymbol{\rho})\,\boldsymbol{R}(\boldsymbol{\rho}) \tag{A.3c}$$

$$\boldsymbol{P}(\boldsymbol{\rho})^{-1} = \frac{1}{s}\left(\boldsymbol{R}(\boldsymbol{\rho})^T + \boldsymbol{I}_{3\times 3}\right) \tag{A.3d}$$

When the rotational angle represented by $\boldsymbol{\rho}$ is equal to $\pm\pi$, the scalar part $s = 0$, resulting in a singular projection matrix $\boldsymbol{P}(\boldsymbol{\rho})$.

For the quaternion $\boldsymbol{\rho}_{F_1(F_2)}$ representing the relative rotation of the driven frame F_1 with respect to the main frame F_2, remembering (A.3b), and expanding the relative rotation $\boldsymbol{R}\left(\boldsymbol{\rho}_{F_1(F_2)}\right) = \boldsymbol{R}_{F_2}^T\boldsymbol{R}_{F_1}$, one obtains

$$\boldsymbol{P}\left(\boldsymbol{\rho}_{F_1(F_2)}\right)^T\boldsymbol{R}_{F_2}^T = \boldsymbol{P}\left(\boldsymbol{\rho}_{F_1(F_2)}\right)\boldsymbol{R}_{F_1}^T \tag{A.4}$$

For an arbitrary unit quaternion $\boldsymbol{\rho} = (s, \boldsymbol{v})$, its variation can be denoted as

$$\delta\boldsymbol{\rho} = (\delta s, \delta\boldsymbol{v}) \tag{A.5}$$

Recalling the equality (2.35a), and remembering the multiplication formula (2.22b), the variation of a quaternion can be derived as

$$\delta\boldsymbol{\rho} = \frac{1}{2}(s, \boldsymbol{v})(0, \delta\boldsymbol{\theta}_l) = \frac{1}{2}(-\boldsymbol{v}\cdot\delta\boldsymbol{\theta}_l, s\delta\boldsymbol{\theta}_l + \boldsymbol{v}\times\delta\boldsymbol{\theta}_l) \tag{A.6}$$

Comparing (A.5) and (A.6), the scalar and vectorial parts of the variations should be identical respectively, leading to

$$\delta s = -\frac{1}{2}\boldsymbol{v}\cdot\delta\boldsymbol{\theta}_l \tag{A.7}$$

$$\delta\boldsymbol{v} = \frac{1}{2}(s\delta\boldsymbol{\theta}_l + \boldsymbol{v}\times\delta\boldsymbol{\theta}_l) \tag{A.8}$$

Remembering the definition of the projection matrix (A.1), after substituting (A.7) and (A.8), and employing the properties (2.1b), (2.1d), the variation of the projection matrix $\boldsymbol{P}(\boldsymbol{\rho})$ can be derived as

$$\delta\boldsymbol{P}(\boldsymbol{\rho}) = \frac{1}{4}\left(-(\boldsymbol{v}\cdot\delta\boldsymbol{\theta}_l)\boldsymbol{I}_{3\times3} + (s\boldsymbol{I}_{3\times3} + \widetilde{\boldsymbol{v}})\widetilde{\delta\boldsymbol{\theta}}_l - \widetilde{\delta\boldsymbol{\theta}}_l\widetilde{\boldsymbol{v}}\right) \tag{A.9}$$

Its multiplication with Lagrange multipliers $\boldsymbol{\gamma}_m$ can be further expressed as

$$\delta\boldsymbol{P}(\boldsymbol{\rho})\boldsymbol{\gamma}_m = \left(-\frac{1}{4}\boldsymbol{\gamma}_m\boldsymbol{v}^T - \frac{1}{4}\widetilde{\boldsymbol{\gamma}_m}(s\boldsymbol{I}_{3\times3} + \widetilde{\boldsymbol{v}})\right)\delta\boldsymbol{\theta}_l \tag{A.10}$$

where the equality $(\boldsymbol{a}\cdot\boldsymbol{b})\boldsymbol{c} = \left(\boldsymbol{c}\boldsymbol{a}^T\right)\boldsymbol{b}, \forall\boldsymbol{a},\boldsymbol{b},\boldsymbol{c}\in\mathbb{R}^3$ is used in conjunction with the properties (2.1a) and (2.1c).

By introducing another auxiliary matrix $\boldsymbol{G}(\boldsymbol{\rho},\boldsymbol{\gamma}_m)\in\mathbb{R}^{3\times3}$

$$\boldsymbol{G}(\boldsymbol{\rho},\boldsymbol{\gamma}_m) = -\frac{1}{4}\boldsymbol{\gamma}_m\boldsymbol{v}^T - \frac{1}{4}\widetilde{\boldsymbol{\gamma}_m}(s\boldsymbol{I}_{3\times3} + \widetilde{\boldsymbol{v}}) \tag{A.11}$$

one obtains an equality in a compact form

$$\delta\boldsymbol{P}(\boldsymbol{\rho})\boldsymbol{\gamma}_m = \boldsymbol{G}(\boldsymbol{\rho},\boldsymbol{\gamma}_m)\delta\boldsymbol{\theta}_l \tag{A.12}$$

A.2 Gauss-Legendre quadrature

The computation of the mass, stiffness, and damping matrices for a Timoshenko beam element requires integration along the element length. The integrand functions involve the product of the shape functions with the constitutive mass matrix,

as well as the product of the strain-displacement matrices with the constitutive stiffness matrix. When the constitutive matrices are fully populated, performing these integrations analytically becomes highly complex and cumbersome.

To address this challenge, the Gauss-Legendre quadrature method can be employed to perform the numerical integrations. This method approximates the integral over the interval $[-1, 1]$ as a weighted sum of polynomial terms, thereby simplifying the integration process.

$$\int_{-1}^{1} f(x)dx \approx \sum_{i=1}^{n_G} w_i f(x_i) \tag{A.13}$$

where $x_i, i = 1,2,\cdots, n_G$ are the Gauss-Legendre quadrature points, and w_i are the corresponding weights.

Gauss-Legendre quadrature points are also called sampling points, as the function values sampled at these points are used in the weighted summation to approximate the integral. An n_G-point Gauss-Legendre quadrature scheme can exactly compute the integral of a polynomial up to degree $2n_G-1$. If the integrand function $f(x)$ is not a polynomial, or is a polynomial of degree higher than $2n_G - 1$, the weighted summation provides an approximation of the integral. In such cases, increasing the number of sampling points can enhance the accuracy of the numerical approximation.

The Gauss-Legendre quadrature points and their corresponding weights for low-order integration schemes over the interval $[-1, 1]$ are presented in Table A.1.

To approximate an integral over the interval $[a, b]$, the Gauss-Legendre quadrature method can be applied using the following expression

$$\int_{a}^{b} f(x)dx \approx \frac{b-a}{2} \sum_{i=1}^{n_G} w_i f\left(\frac{b-a}{2}\xi_i + \frac{a+b}{2}\right) \tag{A.14}$$

where $\xi_i = \dfrac{2x_i - a - b}{b-a} \in [-1,1]$ represents the normalized sampling points for the integral over $[-1,1]$, and w_i denotes the corresponding weights.

Table A.1: Gauss-Legendre quadrature points and weights for low-order integration schemes.

Number of points, n_G	Sampling points, x_i		Weights, w_i	
1	0		2	
2	$\pm\frac{1}{\sqrt{3}}$	± 0.57735	1	
3	0		$\frac{8}{9}$	0.888889
	$\pm\sqrt{\frac{3}{5}}$	± 0.774597	$\frac{5}{9}$	0.555556
4	$\pm\sqrt{\frac{3}{7}-\frac{2}{7}\sqrt{\frac{6}{5}}}$	± 0.339981	$\frac{18+\sqrt{30}}{36}$	0.652145
	$\pm\sqrt{\frac{3}{7}+\frac{2}{7}\sqrt{\frac{6}{5}}}$	± 0.861136	$\frac{18-\sqrt{30}}{36}$	0.347855
5	0		$\frac{128}{225}$	0.568889
	$\pm\frac{1}{3}\sqrt{5-2\sqrt{\frac{10}{7}}}$	± 0.538469	$\frac{322+13\sqrt{70}}{900}$	0.478629
	$\pm\frac{1}{3}\sqrt{5+2\sqrt{\frac{10}{7}}}$	± 0.90618	$\frac{322-13\sqrt{70}}{900}$	0.236927

Bibliography

[1] *Modeling Slope Discontinuity of Large Size Wind-Turbine Blade Using Absolute Nodal Coordinate Formulation*, volume Volume 6: 1st Biennial International Conference on Dynamics for Design; 14th International Conference on Advanced Vehicle Technologies of *International Design Engineering Technical Conferences and Computers and Information in Engineering Conference*, 08 2012.

[2] *Bladed Theory Manual, Version 4.11*. DNV GL, 2020.

[3] H. Aagaard Madsen, J. Thirstrup Petersen, A. Björck, H. Ganander, D. Winkelaar, A. Brand, A. Bruining, M. Graham, P. Enevoldsen, and S. Øye. *Prediction of dynamic loads and induced vibrations in stall STALLVIB. Final report*. Risø National Laboratory, 1998.

[4] Sheldon Andrews, Marek Teichmann, and Paul Kry. Geometric stiffness for real-time constrained multibody dynamics. *Computer Graphics Forum*, 36:235–246, 05 2017.

[5] ANSYS Inc. *ANSYS Mechanical APDL 2023*. Canonsburg, PA, USA, 2023.

[6] Rafael Avilés, Goizalde Ajuria, Vicente Gómez-Garay, and Santiago Navalpotro. Comparison among nonlinear optimization methods for the static equilibrium analysis of multibody systems with rigid and elastic elements. *Mechanism and Machine Theory*, 35(8):1151–1168, 2000.

[7] Balakumar Balachandran and Edward B. Magrab. *Vibrations*. Cambridge University Press, 2018.

[8] Galih Bangga, Marina Carrion, William Collier, and Steven Parkinson. Technical modeling challenges for large idling wind turbines. *Journal of Physics: Conference Series*, 2626(1):012026, oct 2023.

[9] Klaus-Jürgen Bathe and Saïd Bolourchi. Large displacement analysis of three-dimensional beam structures. *International Journal for Numerical Methods in Engineering*, 14(7):961–986, 1979.

[10] Jean-Marc Battini and Costin Pacoste. Co-rotational beam elements with warping effects in instability problems. *Computer Methods in Applied Mechanics and Engineering*, 191(17):1755–1789, 2002.

[11] O.A. Bauchau. *Flexible Multibody Dynamics*. Solid mechanics and its applications. Springer, 2010.

[12] Olivier Bauchau and Yuri Nikishkov. An implicit floquet analysis for rotorcraft stability evaluation. *Journal of The American Helicopter Society - J AMER HELICOPTER SOC*, 46, 07 2001.

[13] Olivier Bauchau and Jesus Rodriguez. Formulation of modal-based elements in nonlinear, flexible multibody dynamics. *International Journal for Multiscale Computational Engineering*, 1:161–180, 01 2003.

[14] Olivier Bauchau, Jesus Rodriguez, and Shyi-Yaung Chen. Coupled rotor-fuselage analysis with finite motions using component mode synthesis. *Journal of The American Helicopter Society*, 49, 04 2004.

[15] Olivier Bauchau and Jielong Wang. Efficient and robust approaches to the stability analysis of large multibody systems. *Journal of Computational and Nonlinear Dynamics - J COMPUT NONLINEAR DYN*, 3, 01 2008.

[16] Olivier A. Bauchau. *DYMORE User's Manual*. Georgia Institute of Technology, 2006.

[17] Olivier A. Bauchau, Alexander Epple, and Carlo L. Bottasso. Scaling of Constraints and Augmented Lagrangian Formulations in Multibody Dynamics Simulations. *Journal of Computational and Nonlinear Dynamics*, 4(2):021007, 03 2009.

[18] Olivier A. Bauchau, Shilei Han, Aki Mikkola, and Marko K. Matikainen. Comparison of the absolute nodal coordinate and geometrically exact formulations for beams. *Multibody System Dynamics*, 32(1):67–85, Jun 2014.

[19] Olivier A. Bauchau and André Laulusa. Review of Contemporary Approaches for Constraint Enforcement in Multibody Systems. *Journal of Computational and Nonlinear Dynamics*, 3(1):011005, 11 2007.

[20] Olivier A. Bauchau and Valentin Sonneville. The Motion Formalism for Flexible Multibody Systems. *Journal of Computational and Nonlinear Dynamics*, 17(3):030801, 01 2022.

[21] Olivier A. Bauchau and Lorenzo Trainelli. The vectorial parameterization of rotation. *Nonlinear Dynamics*, 32(1):71–92, Apr 2003.

[22] J. Baumgarte. Stabilization of constraints and integrals of motion in dynamical systems. *Computer Methods in Applied Mechanics and Engineering*, 1(1):1–16, 1972.

[23] Eduardo Bayo, Javier Garcia De Jalon, and Miguel Angel Serna. A modified lagrangian formulation for the dynamic analysis of constrained mechanical systems. *Computer Methods in Applied Mechanics and Engineering*, 71(2):183–195, 1988.

[24] AH Bayoumy, AA Nada, and SM Megahed. Methods of modeling slope discontinuities in large size wind turbine blades using absolute nodal coordinate formulation. *Proceedings of the Institution of Mechanical Engineers, Part K: Journal of Multi-body Dynamics*, 228(3):314–329, 2014.

[25] Ahmed H. Bayoumy, Ayman A. Nada, and Said M. Megahed. A Continuum Based Three-Dimensional Modeling of Wind Turbine Blades. *Journal of Computational and Nonlinear Dynamics*, 8(3):031004, 10 2012.

[26] Abdelaziz Bazoune and Yehia Khulief. Shape functions of three-dimensional timoshenko beam element. *Journal of Sound and Vibration*, 259:473–480, 01 2003.

[27] Peter Benner and Tatjana Stykel. *Model Order Reduction for Differential-Algebraic Equations: A Survey*, pages 107–160. Springer International Publishing, Cham, 2017.

[28] M. Berzeri and A.A. Shabana. Study of the centrifugal stiffening effect using the finite element absolute nodal coordinate formulation. *Multibody System Dynamics*, 7:357–387, 2002.

[29] Gunjit Bir. *Multi-Blade Coordinate Transformation and its Application to Wind Turbine Analysis*.

[30] Gunjit Bir and Jason Jonkman. Aeroelastic instabilities of large offshore and onshore wind turbines. *Journal of Physics: Conference Series*, 75(1):012069, jul 2007.

[31] Gunjit Bir and Karl Stol. *Modal analysis of a teetered-rotor wind turbine using the Floquet approach*. 2000.

[32] José Pedro Albergaria Amaral Blasques. *User's Manual for BECAS: A cross section analysis tool for anisotropic and inhomogeneous beam sections of arbitrary geometry*. Number 1785(EN) in Denmark. Forskningscenter Risoe. Risoe-R. Risø DTU – National Laboratory for Sustainable Energy, 2012.

[33] Marco Borri, Lorenzo Trainelli, and Alessandro Croce. The embedded projection method: A general index reduction procedure for constrained system dynamics. *Computer Methods in Applied Mechanics and Engineering*, 195(50):6974–6992, 2006. Multibody Dynamics Analysis.

[34] Pietro Bortolotti, Mayank Chetan, Emmanuel Branlard, Jason Jonkman, Andy Platt, Derek Slaughter, and Jennifer Rinker. Wind turbine aeroelastic stability in OpenFAST. *Journal of Physics: Conference Series*, 2767(2):022018, jun 2024.

[35] Carlo L. Bottasso, Olivier A. Bauchau, and Alberto Cardona. Time-step-size-independent conditioning and sensitivity to perturbations in the numerical solution of index three differential algebraic equations. *SIAM Journal on Scientific Computing*, 29(1):397–414, 2007.

[36] Carlo L. Bottasso, Daniel Dopico, and Lorenzo Trainelli. On the optimal scaling of index three DAEs in multibody dynamics. *Multibody System Dynamics*, 19(1):3–20, Feb 2008.

[37] C.L. Bottasso and S. Cacciola. Model-independent periodic stability analysis of wind turbines. *Wind Energy*, 18(5):865–887, 2015.

[38] C.L. Bottasso, S. Cacciola, and A. Croce. Estimation of blade structural properties from experimental data. *Wind Energy*, 16(4):501–518, 2013.

[39] C.L. Bottasso and A. Croce. Cp-Lambda User's Manual. Technical report, Dipartimento di Scienze e Tecnologie Aerospaziali, Politecnico di Milano, Milano, Italy, 2006-2015.

[40] E Branlard, B Jonkman, G R Pirrung, K Dixon, and J Jonkman. Dynamic inflow and unsteady aerodynamics models for modal and stability analyses in OpenFAST. *Journal of Physics: Conference Series*, 2265(3):032044, may 2022.

[41] E. Branlard, J. Jonkman, J. H. Porter, G. Vijayakumar, B. Jonkman, M. Singh, E. Mayda, and K. Dixon. A generalized wind turbine cross section as a reduced-order model to gain insights in blade aeroelastic challenges. *Journal of Physics: Conference Series*, 2767(2):022005, jun 2024.

[42] Emmanuel Simon Pierre Branlard. Flexible multibody dynamics using joint coordinates and the Rayleigh-Ritz approximation: The general framework behind and beyond Flex. *Wind Energy*, 22(7):877–893, 2019.

[43] T. Burton, N. Jenkins, D. Sharpe, and E. Bossanyi. *Wind Energy Handbook*. Wiley, 2011.

[44] Alessandro Cammarata. Global modes for the reduction of flexible multibody systems. *Multibody System Dynamics*, 53(1):59–83, Sep 2021.

[45] Alessandro Cammarata and Pietro Davide Maddío. A system-based reduction method for spatial deformable multibody systems using global flexible modes. *Journal of Sound and Vibration*, 504:116118, 2021.

[46] Alessandro Cammarata and Carmine Maria Pappalardo. On the use of component mode synthesis methods for the model reduction of flexible multibody systems within the floating frame of reference formulation. *Mechanical Systems and Signal Processing*, 142:106745, 2020.

[47] Alessandro Cammarata, Rosario Sinatra, and Pietro Davide Maddìo. Interface reduction in flexible multibody systems using the floating frame of reference formulation. *Journal of Sound and Vibration*, 523:116720, 2022.

[48] Eduardo M.B. Campello and Leonardo B. Lago. Effect of higher order constitutive terms on the elastic buckling of thin-walled rods. *Thin-Walled Structures*, 77:8–16, 2014.

[49] A. Cardona and M. Géradin. A superelement formulation for mechanism analysis. *Computer Methods in Applied Mechanics and Engineering*, 100(1):1–29, 1992.

[50] Alberto Cardona. Superelements modelling in flexible multibody dynamics. *Multibody System Dynamics*, 4(2):245–266, Aug 2000.

[51] Alberto Cardona and Michel Geradin. Modelling of superelements in mechanism analysis. *International Journal for Numerical Methods in Engineering*, 32(8):1565–1593, 1991.

[52] Marina Carrio and William Collier. Description of Bladed model of IEA 15 MW turbine. Technical Report Rev. 1, DNV Digital Solutions, 02 2022.

[53] Bei Chen, Zili Zhang, Xugang Hua, Søren R.K. Nielsen, and Biswajit Basu. Enhancement of flutter stability in wind turbines with a new type of passive damper of torsional rotation of blades. *Journal of Wind Engineering and Industrial Aerodynamics*, 173:171–179, 2018.

[54] M. Chetan, S. Yao, and D. T. Griffith. Flutter behavior of highly flexible blades for two- and three-bladed wind turbines. *Wind Energy Science*, 7(4):1731–1751, 2022.

[55] W. Collier, D. Ors, T. Barlas, F. Zahle, P. Bortolotti, D. Marten, C. S. L. Jensen, E. Branlard, D. Zalkind, and K. Lønbæk. Aeroelastic code comparison using the IEA 22MW reference turbine. In *The Science of Making*

Torque from Wind (TORQUE 2024): Modeling and simulation technology, number 5 in Journal of Physics: Conference Series, United Kingdom, 2024. IOP Publishing. The Science of Making Torque from Wind (TORQUE 2024), TORQUE 2024 ; Conference date: 29-05-2024 Through 31-05-2024.

[56] Matt Copeman. Vestas is readying New York for offshore wind and moves forward conditional agreement for the Empire Wind 1 project. https://www.vestas.com/en/media/company-news/2024/vestas-is-readying-new-york-for-offshore-wind-and-moves-c3941164, March 2024.

[57] P J Couturier, L Mailly, D Molitor, and Q Wang. On the importance of the beam reference line. *Journal of Physics: Conference Series*, 1618(5):052054, sep 2020.

[58] P J Couturier and P F Skjoldan. Implementation of an advanced beam model in BHawC. *Journal of Physics: Conference Series*, 1037(6):062015, jun 2018.

[59] Curran Crawford. Re-examining the precepts of the blade element momentum theory for coning rotors. *Wind Energy*, 9(5):457–478, 2006.

[60] M. A. Crisfield, U. Galvanetto, and G. Jelenić. Dynamics of 3-D co-rotational beams. *Computational Mechanics*, 20(6):507–519, Nov 1997.

[61] M.A. Crisfield. A consistent co-rotational formulation for non-linear, three-dimensional, beam-elements. *Computer Methods in Applied Mechanics and Engineering*, 81(2):131–150, 1990.

[62] M.A. Crisfield and G.F. Moita. A unified co-rotational framework for solids, shells and beams. *International Journal of Solids and Structures*, 33(20):2969–2992, 1996.

[63] Alessandro Croce, Riccardo Riva, Ainara Irisarri Ruiz, Helge A. Madsen, Vasilis Riziotis, and Feike Savenije. Comparison of models with respect to stability analysis. Technical Report D4.1, ver 6, Polytechnic University of Milan, 03 2015. WP4 Deliverable D4.1 Report in AVATAR project.

[64] Federica Cutroneo. Development of a numerical method for the modal analysis of constrained multibody systems. Thesis, University of Parma, 2021.

[65] D. A. Danielson and D. H. Hodges. A Beam Theory for Large Global Rotation, Moderate Local Rotation, and Small Strain. *Journal of Applied Mechanics*, 55(1):179–184, 03 1988.

[66] B.Fraeijs De Veubeke. The dynamics of flexible bodies. *International Journal of Engineering Science*, 14(10):895–913, 1976.

[67] J.M. Dickens, J.M. Nakagawa, and M.J. Wittbrodt. A critique of mode acceleration and modal truncation augmentation methods for modal response analysis. *Computers & Structures*, 62(6):985–998, 1997.

[68] Xiong Ding. Krylov schur algorithm in matlab. https://github.com/dingxiong/KrylovSchur.

[69] DNV-GL Garrad Hassan. Bladed software. https://www.dnv.com/services/wind-turbine-design-software-bladed-3775. Accessed: 2024-06-20.

[70] DTU Wind Energy. HAWCStab2. https://www.hawcstab2.vindenergi.dtu.dk/. Accessed: 2024-06-20.

[71] Adnan Durakovic. First Siemens Gamesa 14.7 MW turbine stands at Moray West offshore wind farm. https://www.offshorewind.biz/2024/04/22/first-siemens-gamesa-14-7-mw-turbine-stands-at-moray-west-offshore-wind-farm/, April 2024.

[72] K. L. Ebbehøj, P. J. Couturier, L. M. Sørensen, and J. J. Thomsen. Experimental validation of a short-term damping estimation method for wind turbines in nonstationary operating conditions. *Wind Energy Science*, 9(4):1005–1024, 2024.

[73] Edda Eich-Soellner and Claus Führer. *Numerical methods in multibody dynamics*, volume 45. Springer, 1998.

[74] H. El-Absy and A.A. Shabana. Geometric stiffness and stability of rigid body modes. *Journal of Sound and Vibration*, 207(4):465–496, 1997.

[75] Marcel Ellenbroek and Jurnan Schilder. On the use of absolute interface coordinates in the floating frame of reference formulation for flexible multibody dynamics. *Multibody System Dynamics*, 43(3):193–208, Jul 2018.

[76] European Commission and Directorate-General for Communication. *The European Climate Law*. Publications Office, 2020.

[77] Celso Jaco Faccio Júnior, Ana Carolina Pegoraro Cardozo, Valdemar Monteiro Júnior, and Alfredo Gay Neto. Modeling wind turbine blades by geometrically-exact beam and shell elements: A comparative approach. *Engineering Structures*, 180:357–378, 2019.

[78] Dogger Bank Wind Farm. World's largest offshore wind farm produces power for the first time. https://doggerbank.com/construction/worlds-largest-offshore-wind-farm-produces-power-for-the-first-time/, October 2023.

[79] Touraj Farsadi and Altan Kayran. Classical flutter analysis of composite wind turbine blades including compressibility. *Wind Energy*, 24(1):69–91, 2021.

[80] C.A. Felippa and B. Haugen. A unified formulation of small-strain corotational finite elements: I. theory. *Computer Methods in Applied Mechanics and Engineering*, 194(21):2285–2335, 2005. Computational Methods for Shells.

[81] Oliver Filsoof, Morten Hansen, Anders Yde, Peter Bøttcher, and Xuping Zhang. A novel methodology for analyzing modal dynamics of multi-rotor wind turbines. *Journal of Sound and Vibration*, 493:115810, 02 2021.

[82] Erik Kaspar Fritz, Carlos Ferreira, and Koen Boorsma. An efficient blade sweep correction model for blade element momentum theory. *Wind Energy*, 25(12):1977–1994, 2022.

[83] C. Führer and B. J. Leimkuhler. Numerical solution of differential-algebraic equations for constrained mechanical motion. *Numerische Mathematik*, 59(1):55–69, Dec 1991.

[84] Evan Gaertner, Jennifer Rinker, Latha Sethuraman, Frederik Zahle, Benjamin Anderson, Garrett Barter, Nikhar Abbas, Fanzhong Meng, Pietro Bortolotti, Witold Skrzypinski, George Scott, Roland Feil, Henrik Bredmose, Katherine Dykes, Matt Sheilds, Christopher Allen, and Anthony Viselli. Definition of the IEA 15-megawatt offshore reference wind turbine. Technical report, International Energy Agency, 2020.

[85] Jaydeep L. Gaikwad, Bhaskar Dasgupta, and Ujwal Joshi. Static equilibrium analysis of compliant mechanical systems using relative coordinates and loop closure equations. *Mechanism and Machine Theory*, 39(5):501–517, 2004.

[86] C.W. Gear, B. Leimkuhler, and G.K. Gupta. Automatic integration of Euler-Lagrange equations with constraints. *Journal of Computational and Applied Mathematics*, 12-13:77–90, 1985.

[87] G. Genta. *Dynamics of Rotating Systems*. Mechanical Engineering Series. Springer New York, 2007.

[88] Giancarlo Genta and Mario Silvagni. On Centrifugal Softening in Finite Element Method Rotordynamics. *Journal of Applied Mechanics*, 81(1), 08 2013. 011001.

[89] Michel Géradin. Dynamics of a flexible body: a two-field formulation. *Multibody System Dynamics*, 54(1):1–29, Jan 2022.

[90] Michel Géradin and Daniel J. Rixen. A fresh look at the dynamics of a flexible body application to substructuring for flexible multibody dynamics. *International Journal for Numerical Methods in Engineering*, 122(14):3525–3582, 2021.

[91] Michel Géradin and Valentin Sonneville. A two-field approach to multibody dynamics of rotating flexible bodies. *Multibody System Dynamics*, 60(3):375–415, Mar 2024.

[92] Johannes Gerstmayr and Ahmed A. Shabana. Efficient integration of the elastic forces and thin three-dimensional beam elements in the absolute nodal coordinate formulation. In *Proceedings of the Multibody Dynamics 2005 ECCOMAS Thematic Conference*, 2005.

[93] Johannes Gerstmayr, Hiroyuki Sugiyama, and Aki Mikkola. Review on the Absolute Nodal Coordinate Formulation for Large Deformation Analysis of Multibody Systems. *Journal of Computational and Nonlinear Dynamics*, 8(3):031016, 03 2013.

[94] H. Glauert and Great Britain. Aeronautical Research Committee. *The Analysis of Experimental Results in the Windmill Brake and Vortex Ring States of an Airscrew*. ARC/R & M-1026. H.M. Stationery Office, 1926.

[95] Francisco González, Pierangelo Masarati, Javier Cuadrado, and Miguel A. Naya. Assessment of linearization approaches for multibody dynamics formulations. *Journal of Computational and Nonlinear Dynamics*, 12(4), 2017.

[96] Mehmet Ozan Gözcü. *Wind turbine blade large deflections: A non-intrusive method for blade nonlinear reduced order models*. PhD thesis, Technical University of Denmark, Denmark, 2020.

[97] O. Gözcü and D. R. Verelst. The effects of blade structural model fidelity on wind turbine load analysis and computation time. *Wind Energy Science*, 5(2):503–517, 2020.

[98] D Todd Griffith and Mayank Chetan. Assessment of flutter prediction and trends in the design of large-scale wind turbine rotor blades. *Journal of Physics: Conference Series*, 1037(4):042008, jun 2018.

[99] C. Grinderslev, F. Houtin-Mongrolle, N. Nørmark Sørensen, G. Raimund Pirrung, P. Jacobs, A. Ahmed, and B. Duboc. Forced-motion simulations of vortex-induced vibrations of wind turbine blades – a study of sensitivities. *Wind Energy Science*, 8(10):1625–1638, 2023.

[100] C. Grinderslev, N. Nørmark Sørensen, G. Raimund Pirrung, and S. González Horcas. Multiple limit cycle amplitudes in high-fidelity predictions of standstill wind turbine blade vibrations. *Wind Energy Science*, 7(6):2201–2213, 2022.

[101] Marc Guadayol Roig. *Application of Model Predictive Control to Wind Turbines*. Doctoral thesis, ETH Zürich, Zürich, 2017.

[102] Gaël Guennebaud, Benoît Jacob, et al. Eigen v3. http://eigen.tuxfamily.org, 2010.

[103] GWEC. Global wind report 2024. Technical report, Global Wind Energy Council, 2024.

[104] Michel Géradin and Alberto Cardona. *Flexible Multibody Dynamics: A Finite Element Approach*, volume 4. John Wiley & Sons, 01 2001.

[105] O Hach, H Verdonck, J D Polman, C Balzani, S Müller, J Rieke, and H Hennings. Wind turbine stability: Comparison of state-of-the-art aeroelastic simulation tools. *Journal of Physics: Conference Series*, 1618(5):052048, sep 2020.

[106] H. Haddadpour, R. D. Firouz-Abadi, and M. M. Fotouhi. Equilibrium analysis of multibody dynamic systems using genetic algorithm in comparison with constrained and unconstrained optimization techniques. *Structural and Multidisciplinary Optimization*, 36(4):381–391, Oct 2008.

[107] Seon M. Han, Haym Benaroya, and Timothy Wei. Dynamics of transversely vibrating beams using four engineering theories. *Journal of Sound and Vibration*, 225(5):935–988, 1999.

[108] Shilei Han and Olivier A. Bauchau. Manipulation of motion via dual entities. *Nonlinear Dynamics*, 85(1):509–524, Jul 2016.

[109] Shilei Han and Olivier A. Bauchau. Spectral formulation for geometrically exact beams: A motion-interpolation-based approach. *AIAA Journal*, 57(10):4278–4290, 2019.

[110] M. Hansen, L. Henriksen, C. Tibaldi, L. Bergami, D. Verelst, G. Pirrung, and R. Riva. HAWCStab2 user manual. Technical report, Technical University of Denmark, 2018.

[111] M. H. Hansen. Vibrations of a three-bladed wind turbine rotor due to classical flutter. volume ASME 2002 Wind Energy Symposium of *Wind Energy Symposium*, pages 256–266, 01 2002.

[112] M. H. Hansen. Improved modal dynamics of wind turbines to avoid stall-induced vibrations. *Wind Energy*, 6(2):179–195, 2003.

[113] M. H. Hansen. Modal dynamics of structures with bladed isotropic rotors and its complexity for two-bladed rotors. *Wind Energy Science*, 1(2):271–296, 2016.

[114] M.H. Hansen. *Anisotropic damping of Timoshenko beam elements*. Number 1267(EN) in Denmark. Forskningscenter Risoe. Risoe-R. 2001.

[115] M.H. Hansen and T. Buhl. *Design guidelines for passive instability suppression - Task-11 report*. Number 1575(EN) in Denmark. Forskningscenter Risoe. Risoe-R. 2006.

[116] M.O.L. Hansen, J.N. Sørensen, S. Voutsinas, N. Sørensen, and H.Aa. Madsen. State of the art in wind turbine aerodynamics and aeroelasticity. *Progress in Aerospace Sciences*, 42(4):285–330, 2006.

[117] Morten Hansen. Stability analysis of three-bladed turbines using an eigenvalue approach. In *42nd AIAA Aerospace Sciences Meeting and Exhibit*, 01 2004.

[118] Morten Hansen. Aeroelastic instability problems for wind turbines. *Wind Energy*, 10:551 – 577, 11 2007.

[119] Morten Hansen, Mac Gaunaa, and Helge Madsen. A Beddoes–Leishman type dynamic stall model in state-space and indicial formulations. 01 2004.

[120] Morten Hartvig Hansen. *Aeroelastic Properties of Backward Swept Blades*. 01 2011.

[121] Khazar Hayat and Sung Kyu Ha. Flutter performance of large-scale wind turbine blade with shallow-angled skins. *Composite Structures*, 132:575–583, 2015.

[122] Joachim C. Heinz, Niels N. Sørensen, Frederik Zahle, and Witold Skrzypiński. Vortex-induced vibrations on a modern wind turbine blade. *Wind Energy*, 19(11):2041–2051, 2016.

[123] Vicente Hernandez, Jose E. Roman, and Vicente Vidal. SLEPc: A scalable and flexible toolkit for the solution of eigenvalue problems. *ACM Transactions on Mathematical Software*, 31(3):351–362, September 2005.

[124] Michael A. Heroux, Roscoe A. Bartlett, Vicki E. Howle, Robert J. Hoekstra, Jonathan J. Hu, Tamara G. Kolda, Richard B. Lehoucq, Kevin R. Long, Roger P. Pawlowski, Eric T. Phipps, Andrew G. Salinger, Heidi K.

Thornquist, Ray S. Tuminaro, James M. Willenbring, Alan Williams, and Kendall S. Stanley. An overview of the Trilinos project. *ACM Transactions on Mathematical Software*, 31(3):397–423, September 2005.

[125] D. H. Hodges and W. Yu. A rigorous, engineer-friendly approach for modelling realistic, composite rotor blades. *Wind Energy*, 10(2):179–193, 2007.

[126] Dewey H. Hodges. A mixed variational formulation based on exact intrinsic equations for dynamics of moving beams. *International Journal of Solids and Structures*, 26(11):1253–1273, 1990.

[127] Dewey H. Hodges. Geometrically exact, intrinsic theory for dynamics of curved and twisted anisotropic beams. *AIAA Journal*, 41(6):1131–1137, 2003.

[128] Dewey H Hodges. *Nonlinear composite beam theory*. American Institute of Aeronautics and Astronautics, 2006.

[129] Dewey H. Hodges and G. Alvin Pierce. *Introduction to Structural Dynamics and Aeroelasticity*. Cambridge University Press, August 2011.

[130] J.G. Holierhoek, J.B. de Vaal, A.H. van Zuijlen, and H. Bijl. Comparing different dynamic stall models. *Wind Energy*, 16(1):139–158, 2013.

[131] D. Holm. *Geometric Mechanics-Part II: Rotating, Translating and Rolling*. World Scientific, 2011.

[132] S. G. Horcas, T. Barlas, F. Zahle, and N. N. Sørensen. Vortex induced vibrations of wind turbine blades: Influence of the tip geometry. *Physics of Fluids*, 32(6):065104, 06 2020.

[133] S. G. Horcas, N. N. Sørensen, F. Zahle, G. R. Pirrung, and T. Barlas. Vibrations of wind turbine blades in standstill: Mapping the influence of the inflow angles. *Physics of Fluids*, 34(5):054105, 05 2022.

[134] Sergio González Horcas, Mads Madsen, Niels N. Sørensen, and Frederik Zahle. *Suppressing Vortex Induced Vibrations of Wind Turbine Blades with Flaps*, pages 11–24. Springer Tracts in Mechanical Engineering (STME). Springer, 2019.

[135] Lokanna Hoskoti, Shakti S. Gupta, and Mahesh M. Sucheendran. Modeling of geometrical stiffening in a rotating blade–A review. *Journal of Sound and Vibration*, 548:117526, 2023.

[136] Jiasheng Huang, Kai Wang, Jiabo Tang, Jialu Xu, and Hanwen Song. An experimental study of the centrifugal hardening effect on rotating cantilever beams. *Mechanical Systems and Signal Processing*, 165:108291, 2022.

[137] Stephanos Theodossiades Hyeongmin Moon, Haeseong Cho and Taeseong Kim. Development of an anisotropic co-rotational beam model including variable cross-section. *Mechanics of Advanced Materials and Structures*, 30(3):423–436, 2023.

[138] Stephanos Theodossiades Hyeongmin Moon, Haeseong Cho and Taeseong Kim. Development of three-dimensional co-rotational beam model for nonlinear dynamic analysis of highly flexible slender composite blades. *Mechanics of Advanced Materials and Structures*, 30(10):1943–1954, 2023.

[139] Wind energy generation systems - Part 1: Design requirements. Standard, International Electrotechnical Commision, 02 2019. IEC 61400-1, 8th February 2019, Edition 4.0.

[140] Wind turbine generator systems - Part 13: Measurement of mechanical loads. Standard, International Electrotechnical Commision, 12 2015. IEC 61400-13, 21st December 2015, Edition 1.0.

[141] Wind energy generation systems - Part 3-1: Design requirements for fixed offshore wind turbines. Standard, International Electrotechnical Commision, 04 2019. IEC 61400-3-1, 5th April 2019, Edition 1.0.

[142] Wind energy generation systems - Part 3-2: Design requirements for floating offshore wind turbines. Standard, International Electrotechnical Commision, 04 2019. IEC TS 61400-3-2, 5th April 2019, Edition 1.0.

[143] The MathWorks Inc. Symbolic Toolbox version: 9.4 (R2022b), 2022.

[144] G. Jelenić and M. A. Crisfield. Interpolation of rotational variables in nonlinear dynamics of 3D beams. *International Journal for Numerical Methods in Engineering*, 43(7):1193–1222, 1998.

[145] G. Jelenić and M.A. Crisfield. Geometrically exact 3D beam theory: implementation of a strain-invariant finite element for statics and dynamics. *Computer Methods in Applied Mechanics and Engineering*, 171(1):141–171, 1999.

[146] Mohui Jin, Xianmin Zhang, and Benliang Zhu. A numerical method for static analysis of pseudo-rigid-body model of compliant mechanisms. *Proceedings of the Institution of Mechanical Engineers, Part C: Journal of Mechanical Engineering Science*, 228(17):3170–3177, 2014.

[147] Nicholas A. Johnson. Verification and validation of the geometrically exact beam theory with legendre spectral finite elements for wind turbine blade analysis, a, 2014.

[148] J. Jonkman and W. Musial. Offshore code comparison collaboration (OC3) for IEA Wind task 23 offshore wind technology and deployment. Technical Report NREL/TP-5000-48191, National Renewable Energy Laboratory, 12 2010.

[149] J M Jonkman and B J Jonkman. Fast modularization framework for wind turbine simulation: full-system linearization. *Journal of Physics: Conference Series*, 753(8):082010, sep 2016.

[150] Jason Jonkman, Alan Wright, Greg Hayman, and Amy Robertson. Full-system linearization for floating offshore wind turbines in OpenFAST. In *Proceedings of 1st International Offshore Wind Technical Conference*, number NREL/CP-5000-71865, 11 2018.

[151] Bjarne S. Kallesøe and Knud A. Kragh. Field validation of the stability limit of a multi MW turbine. *Journal of Physics: Conference Series*, 753(4):042005, 09 2016.

[152] J. W. Kamman and R. L. Huston. Dynamics of Constrained Multibody Systems. *Journal of Applied Mechanics*, 51(4):899–903, 12 1984.

[153] C L Kelley and J Paquette. Investigation of flutter for large, highly flexible wind turbine blades. *Journal of Physics: Conference Series*, 1618(5):052078, sep 2020.

[154] Taeseong Kim, Anders M. Hansen, and Kim Branner. Development of an anisotropic beam finite element for composite wind turbine blades in multi-body system. *Renewable Energy*, 59:172–183, 2013.

[155] Steen Krenk and Philippe J. Couturier. Equilibrium-based nonhomogeneous anisotropic beam element. *AIAA Journal*, 55(8):2773–2782, 2017.

[156] Likith Krishnappa, Aljoscha Sander, and Klaus-Dieter Thoben. Aerodynamic devices to reduce/suppress vortex induced vibrations on a wind turbine tower: A review. *Journal of Physics: Conference Series*, 2265(3):032053, may 2022.

[157] Torben J. Larsen, Helge Aagaard Madsen, and K. Thomsen. Investigation of stability effects of an offshore wind turbine. The new aeroelastic code HAWC2. *Windtech International*, 2(March):33–35, 2006.

[158] Torben J. Larsen and Anders Melchior Hansen. *How 2 HAWC2, the user's manual*. Number 1597(ver. 3-1)(EN) in Denmark. Forskningscenter Risoe. Risoe-R. Risø National Laboratory, 2007.

[159] André Laulusa and Olivier A. Bauchau. Review of Classical Approaches for Constraint Enforcement in Multibody Systems. *Journal of Computational and Nonlinear Dynamics*, 3(1):011004, 11 2007.

[160] Giovanni Legnani, Irene Fassi, Alessandro Tasora, and Dario Fusai. A practical algorithm for smooth interpolation between different angular positions. *Mechanism and Machine Theory*, 162:104341, August 2021.

[161] R. B. Lehoucq and D. C. Sorensen. Deflation Techniques for an Implicitly Restarted Arnoldi Iteration. *SIAM Journal on Matrix Analysis and Applications*, 17(4):789–821, October 1996.

[162] Remco Leine, Giuseppe Capobianco, Perry Bartelt, Marc Christen, and Andrin Caviezel. Stability of rigid body motion through an extended intermediate axis theorem: application to rockfall simulation. *Multibody System Dynamics*, 52, 08 2021.

[163] A. Li, G. R. Pirrung, M. Gaunaa, H. A. Madsen, and S. G. Horcas. A computationally efficient engineering aerodynamic model for swept wind turbine blades. *Wind Energy Science*, 7(1):129–160, 2022.

[164] Bei Li, De Tian, Xiaoxuan Wu, Huiwen Meng, and Yi Su. The impact of bend–twist coupling on structural characteristics and flutter limit of ultralong flexible wind turbine composite blades. *Energies*, 16(15), 2023.

[165] Li Li and Yujin Hu. Generalized mode acceleration and modal truncation augmentation methods for the harmonic response analysis of nonviscously damped systems. *Mechanical Systems and Signal Processing*, 52-53:46–59, 2015.

[166] Mingwu Li, Shobhit Jain, and George Haller. Model reduction for constrained mechanical systems via spectral submanifolds. *Nonlinear Dynamics*, 111(10):8881–8911, May 2023.

[167] Pengfei Li, Florentina M. Gantoi, and Ahmed A. Shabana. Higher order representation of the beam cross section deformation in large displacement finite element analysis. *Journal of Sound and Vibration*, 330(26):6495–6508, 2011.

[168] Don W. Lobitz. Aeroelastic stability predictions for a MW-sized blade. *Wind Energy*, 7(3):211–224, 2004.

[169] Don W. Lobitz. Parameter sensitivities affecting the flutter speed of a MW-sized blade. *Journal of Solar Energy Engineering*, 127(4):538–543, 07 2005.

[170] Aitziber Lopez, Iñigo Puente, and Hodei Aizpurua. Experimental and analytical studies on the rotational stiffness of joints for single-layer structures. *Engineering Structures*, 33(3):731–737, 2011.

[171] J. Loubeyres, J.-L. Pfister, F. Blondel, and N. Guy. Stall flutter instabilities on the iea-15 reference wind turbine in idling conditions: code-to-code comparisons and physical analyses. *Journal of Physics: Conference Series*, 2265(3):032019, may 2022.

[172] Yunhua Luo. An efficient 3D timoshenko beam element with consistant shape functions. *Advances in Applied Mechanics*, 1:95–106, 10 2008.

[173] Per Lötstedt and Linda Petzold. Numerical solution of nonlinear differential equations with algebraic constraints I: Convergence results for backward differentiation formulas. *Mathematics of Computation*, 46(174):491–516, 1986.

[174] Xinwen Ma, Xianghua Peng, Jingwei Sun, Yan Chen, and Zhihong Huang. A comprehensive investigation of linear and nonlinear beam models on flexible wind turbine blade load calculations. *Journal of Marine Science and Engineering*, 12(4), 2024.

[175] Miles Macklin, Kenny Erleben, Matthias Müller, Nuttapong Chentanez, Stefan Jeschke, and Viktor Makoviychuk. Non-smooth newton methods for deformable multi-body dynamics. *ACM Trans. Graph.*, 38(5), oct 2019.

[176] H. A. Madsen, T. J. Larsen, G. R. Pirrung, A. Li, and F. Zahle. Implementation of the blade element momentum model on a polar grid and its aeroelastic load impact. *Wind Energy Science*, 5(1):1–27, 2020.

[177] Helge Aa. Madsen, Christian Bak, Mads Døssing, Robert Mikkelsen, and Stig Øye. Validation and modification of the blade element momentum theory based on comparisons with actuator disc simulations. *Wind Energy*, 13(4):373–389, 2010.

[178] Dario Mangoni, Alessandro Tasora, and Chao Peng. Complex eigenvalue analysis of multibody problems via sparsity-preserving krylov–schur iterations. *Machines*, 11(2), 2023.

[179] D. I. Manolas, V. A. Riziotis, and S. G. Voutsinas. Assessing the Importance of Geometric Nonlinear Effects in the Prediction of Wind Turbine Blade Loads. *Journal of Computational and Nonlinear Dynamics*, 10(4):041008, 07 2015.

[180] Dimitris I. Manolas, Panagiotis K. Chaviaropoulos, and Vasilis A. Riziotis. Assessment of vortex induced vibrations on wind turbines. *Journal of Physics: Conference Series*, 2257(1):012011, apr 2022.

[181] David Manta and Rodrigo Gonçalves. A geometrically exact kirchhoff beam model including torsion warping. *Computers & Structures*, 177:192–203, 2016.

[182] David Marten. *QBlade: A Modern Tool for the Aeroelastic Simulation of Wind Turbines*. PhD thesis, Technical University of Berlin, 10 2020.

[183] P Masarati. Constraint stabilization of mechanical systems in ordinary differential equations form. *Proceedings of the Institution of Mechanical Engineers, Part K: Journal of Multi-body Dynamics*, 225(1):12–33, 2011.

[184] Pierangelo Masarati. Adding kinematic constraints to purely differential dynamics. *Computational Mechanics*, 47(2):187–203, Feb 2011.

[185] Pierangelo Masarati, M. Jihad Ummul Quro, and Andrea Zanoni. Projection continuation for minimal coordinate set formulation and singularity detection of redundantly constrained system dynamics. *Multibody System Dynamics*, Sep 2023.

[186] Adnan Memija. Mingyang's 20 MW offshore wind turbine stands complete. https://www.offshorewind.biz/2024/08/29/mingyangs-20-mw-offshore-wind-turbine-stands-complete/, August 2024.

[187] Jiyuan Men, Gang Ma, Qingwei Ma, Xing Zheng, and Hanbing Sun. Aeroelastic instability analysis of floating offshore and onshore wind turbines under extreme conditions. *Ocean Engineering*, 296:117014, 2024.

[188] B.P. Minaker. The tangent stiffness matrix in rigid multibody vehicle dynamics. *Mathematical and Computer Modelling of Dynamical Systems*, 21(3):288–310, 2014.

[189] Bruce Minaker. The tangent stiffness matrix of a constant velocity joint. In *2021 CCToMM Mechanisms, Machines, and Mechatronics (M^3) Symposium*, 2021.

[190] Marco Morandini, Maria Chierichetti, and Paolo Mantegazza. Characteristic behavior of prismatic anisotropic beam via generalized eigenvectors. *International Journal of Solids and Structures*, 47(10):1327–1337, 2010.

[191] Karin Nachbagauer, Peter Gruber, and Johannes Gerstmayr. Structural and Continuum Mechanics Approaches for a 3D Shear Deformable ANCF Beam Finite Element: Application to Static and Linearized Dynamic Examples. *Journal of Computational and Nonlinear Dynamics*, 8(2):021004, 07 2012.

[192] Ayman Nada. Efficient modeling of continuum blades using ancf curved shell elements. In *11th World Congress on Computational Mechanics (WCCM XI)*, 07 2014.

[193] Ayman Nada and Mona Bayoumi. Development of a constraint stabilization method of multibody systems based on fuzzy logic control. *Multibody System Dynamics*, 61(2):233–265, Jun 2024.

[194] National Renewable Energy Laboratory. OpenFAST. https://www.nrel.gov/wind/nwtc/openfast.html. Accessed: 2024-06-20.

[195] Dan Negrut and Jose Ortiz. A practical approach for the linearization of the constrained multibody dynamics equations. *Journal of Computational and Nonlinear Dynamics*, 1, 03 2006.

[196] Dan Negrut, Rajiv Rampalli, Gisli Ottarsson, and Anthony Sajdak. On the Use of the HHT Method in the Context of Index 3 Differential Algebraic Equations of Multibody Dynamics. In *International Design Engineering Technical Conferences and Computers and Information in Engineering Conference*, volume Volume 6: 5th International Conference on Multibody Systems, Nonlinear Dynamics, and Control, Parts A, B, and C, pages 207–218, 09 2005.

[197] Parviz E. Nikravesh and Yi-shih Lin. Use of principal axes as the floating reference frame for a moving deformable body. *Multibody System Dynamics*, 13(2):211–231, Mar 2005.

[198] Andrew Ning, Gregory Hayman, Rick Damiani, and Jason Jonkman. Development and validation of a new blade element momentum skewed-wake model within aerodyn. 01 2015.

[199] S. Andrew Ning. A simple solution method for the blade element momentum equations with guaranteed convergence. *Wind Energy*, 17(9):1327–1345, 2014.

[200] P. Noever-Castelos, D. Melcher, and C. Balzani. Model updating of a wind turbine blade finite element timoshenko beam model with invertible neural networks. *Wind Energy Science*, 7(2):623–645, 2022.

[201] B. Nour-Omid and C.C. Rankin. Finite rotation analysis and consistent linearization using projectors. *Computer Methods in Applied Mechanics and Engineering*, 93(3):353–384, 1991.

[202] Keisuke Otsuka, Kanjuro Makihara, and Hiroyuki Sugiyama. Recent Advances in the Absolute Nodal Coordinate Formulation: Literature Review From 2012 to 2020. *Journal of Computational and Nonlinear Dynamics*, 17(8):080803, 04 2022.

[203] Brian Christopher Owens, Daniel Griffith, Brian Ray Resor, and John E. Hurtado. Impact of modeling approach on flutter predictions for very large wind turbine blade designs. Number Report Number: SAND2013-4114C,

United States, May 2013. Research Org.: Sandia National Lab. (SNL-NM), Albuquerque, NM (United States). Sponsor Org.: USDOE National Nuclear Security Administration (NNSA).

[204] Muammer Ozbek and Daniel J. Rixen. Operational modal analysis of a 2.5MW wind turbine using optical measurement techniques and strain gauges. *Wind Energy*, 16(3):367–381, 2013.

[205] Anthoula N. Panteli, Dimitris I. Manolas, Vasilis A. Riziotis, and Konstantinos V. Spiliopoulos. Comparative study of two geometrically non-linear beam approaches for the coupled wind turbine system. *Journal of Wind Engineering and Industrial Aerodynamics*, 231:105231, 2022.

[206] Carmine M. Pappalardo, Antonio Lettieri, and Domenico Guida. Stability analysis of rigid multibody mechanical systems with holonomic and nonholonomic constraints. *Archive of Applied Mechanics*, 90(9):1961–2005, September 2020.

[207] Chao Peng and Alessandro Tasora. Eigenvalues of the free rotation mode of the multi-bladed rotor. In Fulei Chu and Zhaoye Qin, editors, *Proceedings of the 11th IFToMM International Conference on Rotordynamics*, pages 495–514, Cham, 2024. Springer International Publishing.

[208] Chao Peng, Alessandro Tasora, Dario Fusai, and Dario Mangoni. A unified analytical expression of the tangent stiffness matrix of holonomic constraints. *Computer Methods in Applied Mechanics and Engineering*, 419:116667, 2024.

[209] Chao Peng, Alessandro Tasora, and Pin Lyu. A method for the analysis of the aeroelastic stability of slender wind turbines and its validation. In Walter Lacarbonara, editor, *Advances in Nonlinear Dynamics, Volume I*, pages 631–641, Cham, 2024. Springer Nature Switzerland.

[210] C.P. Pesce, A.L.C. Fujarra, A.N. Simos, and E.A. Tannuri. Analytical and closed form solutions for deep water riser-like eigenvalue problem, 05 1999. ISOPE-I-99-154.

[211] Linda Petzold and Per Lötstedt. Numerical solution of nonlinear differential equations with algebraic constraints II: Practical implications. *SIAM Journal on Scientific and Statistical Computing*, 7(3):720–733, 1986.

[212] Georg R Pirrung, Helge Aa Madsen, and Taeseong Kim. The influence of trailed vorticity on flutter speed estimations. *Journal of Physics: Conference Series*, 524(1):012048, jun 2014.

[213] Georg Raimund Pirrung, Christian Grinderslev, Niels Nørmark Sørensen, and Riccardo Riva. Vortex-induced vibrations of wind turbines: From single blade to full rotor simulations. *Renewable Energy*, 226:120381, 2024.

[214] Gregory Politakis, Wouter Haans, and Gerard van Bussel. *Suppression of Classical Flutter Using a 'Smart Blade'*. 2008.

[215] Evangelos Politis, P.K. Chaviaropoulos, V. Riziotis, S. Voutsinas, and I Romero-Sanz. Stability analysis of parked wind turbine blades. volume 1, 01 2009.

[216] J.S. Przemieniecki. *Theory of Matrix Structural Analysis*. Dover Civil and Mechanical Engineering. Dover, 1985.

[217] Yixuan Qiu. Spectra. https://github.com/yixuan/spectra, 2024.

[218] C.C. Rankin and B. Nour-Omid. The use of projectors to improve finite element performance. *Computers & Structures*, 30(1):257–267, 1988.

[219] E. Reissner. On one-dimensional large-displacement finite-strain beam theory. *Studies in Applied Mathematics*, 52(2):87–95, 1973.

[220] Brian Resor, B.C. Owens, and D. Griffith. Aeroelastic instability of very large wind turbine blades. *European Wind Energy Conference and Exhibition 2012, EWEC 2012*, 2:998–1003, 01 2012.

[221] Jennifer Rinker, Evan Gaertner, Frederik Zahle, Witold Skrzypiński, Nikhar Abbas, Henrik Bredmose, Garrett Barter, and Katherine Dykes. Comparison of loads from HAWC2 and OpenFAST for the IEA Wind 15 MW Reference Wind Turbine. *Journal of Physics: Conference Series*, 1618(5):052052, sep 2020.

[222] Matteo Ripepi and Pierangelo Masarati. Reduced order models using generalized eigenanalysis. *Proceedings of the Institution of Mechanical Engineers, Part K: Journal of Multi-body Dynamics*, 225:52–65, 03 2011.

[223] R Riva, S Cacciola, and C L Bottasso. A MIMO periodic ARX identification algorithm for the Floquet stability analysis of wind turbines. *Journal of Physics: Conference Series*, 753(4):042015, sep 2016.

[224] R. Riva, S. Cacciola, and C. L. Bottasso. Periodic stability analysis of wind turbines operating in turbulent wind conditions. *Wind Energy Science*, 1(2):177–203, 2016.

[225] Riccardo Riva. *Stability analysis of wind turbines through system identification techniques*. PhD thesis, Politecnico di Milano, 01 2018.

[226] Daniel Rixen. Generalized mode acceleration methods and modal truncation augmentation. In *Structures, Structural Dynamics and Material Conference and Exhibit, 42st AIAA/ASME/ASCE/AHS/ASC*, 2001.

[227] Daniel Rixen. High order static correction modes for component mode synthesis. In *Fifth World Congress on Computational Mechanics, WCCM V*, 07 2002.

[228] V. Riziotis, S. Voutsinas, Evangelos Politis, and P.K. Chaviaropoulos. Stability analysis of parked wind turbine blades using a vortex model. 06 2010.

[229] V. A. Riziotis, S. G. Voutsinas, E. S. Politis, and P. K Chaviaropoulos. Aeroelastic stability of wind turbines: the problem, the methods and the issues. *Wind Energy*, 7(4):373–392, 2004.

[230] Marcos Antonio Campos Rodrigues, Rodrigo Bird Burgos, and Luiz Fernando Martha. A unified approach to the timoshenko geometric stiffness matrix considering higher-order terms in the strain tensor. *Latin American Journal of Solids and Structures*, 16(4):e185, 2019.

[231] Ignacio Romero. A comparison of finite elements for nonlinear beams: the absolute nodal coordinate and geometrically exact formulations. *Multibody System Dynamics*, 20(1):51–68, Aug 2008.

[232] Ignacio Romero and Juan J. Arribas. A simple method to impose rotations and concentrated moments on anc beams. *Multibody System Dynamics*, 21(4):307–323, May 2009.

[233] Jili Rong, Zhipei Wu, Cheng Liu, and Olivier Brüls. Geometrically exact thin-walled beam including warping formulated on the special euclidean group se(3). *Computer Methods in Applied Mechanics and Engineering*, 369:113062, 2020.

[234] Rune Rubak and Jørgen Thirstrup Petersen. Monopile as part of aeroelastic wind turbine simulation code. In *Proceedings of Copenhagen Offshore Wind*, 01 2005.

[235] Aditya Sabale and K.V. Nagendra Gopal. Nonlinear aeroelastic response of wind turbines using simo-vu-quoc rods. *Applied Mathematical Modelling*, 65:696–716, 2019.

[236] Jurnan Schilder, Koen Dwarshuis, Marcel Ellenbroek, and André de Boer. The tangent stiffness matrix for an absolute interface coordinates floating frame of reference formulation. *Multibody System Dynamics*, 47(3):243–263, Nov 2019.

[237] A. A. Shabana. *Dynamics of Multibody Systems*. Cambridge University Press, Cambridge, England, fourth edition, 2013.

[238] Ahmed A. Shabana. An overview of the ancf approach, justifications for its use, implementation issues, and future research directions. *Multibody System Dynamics*, 58(3):433–477, Aug 2023.

[239] Ahmed A. Shabana and Refaat Y. Yakoub. Three Dimensional Absolute Nodal Coordinate Formulation for Beam Elements: Theory . *Journal of Mechanical Design*, 123(4):606–613, 05 2000.

[240] Lina Shang, Pinqi Xia, Junhao Zhang, and Changliang Lin. Geometrically exact aeroelastic stability analysis of helicopter composite rotor blades in forward flight. *Aerospace Science and Technology*, 144:108818, 2024.

[241] Matt Shields, Philipp Beiter, Jake Nunemaker, Aubryn Cooperman, and Patrick Duffy. Impacts of turbine and plant upsizing on the levelized cost of energy for offshore wind. *Applied Energy*, 298:117189, 2021.

[242] J.C. Simo. A finite strain beam formulation. the three-dimensional dynamic problem. part i. *Computer Methods in Applied Mechanics and Engineering*, 49(1):55–70, 1985.

[243] J.C. Simo and L. Vu-Quoc. A three-dimensional finite-strain rod model. part ii: Computational aspects. *Computer Methods in Applied Mechanics and Engineering*, 58(1):79–116, 1986.

[244] J.C. Simo and L. Vu-Quoc. A geometrically-exact rod model incorporating shear and torsion-warping deformation. *International Journal of Solids and Structures*, 27(3):371–393, 1991.

[245] Peter Skjoldan. Modal dynamics of wind turbines with anisotropic rotors. In *47th AIAA Aerospace Sciences Meeting including the New Horizons Forum and Aerospace Exposition*, Orlando, Florida, 01 2009.

[246] Peter Skjoldan. *Aeroelastic modal dynamics of wind turbines including anisotropic effects*. PhD thesis, Technical University of Denmark, 03 2011.

[247] Peter Skjoldan and Morten Hansen. On the similarity of the Coleman and Lyapunov-Floquet transformation for modal analysis of blade rotor structures. *Journal of Sound and Vibration*, 327:424–439, 11 2009.

[248] Peter Skjoldan and Morten Hansen. Implicit Floquet analysis of wind turbines using tangent matrices of a nonlinear aeroelastic code. *Wind Energy*, 15:275 – 287, 03 2012.

[249] Peter Skjoldan and Morten Hansen. Effects of extreme wind shear on aeroelastic modal damping of wind turbines. *Wind Energy*, 16:401–415, 04 2013.

[250] V. Sonneville, A. Cardona, and O. Brüls. Geometrically exact beam finite element formulated on the special euclidean group se(3). *Computer Methods in Applied Mechanics and Engineering*, 268:451–474, 2014.

[251] Valentin Sonneville, Matteo Scapolan, Minghe Shan, and Olivier Bauchau. Modal reduction procedures for flexible multibody dynamics. *Multibody System Dynamics*, 51:1–42, 04 2021.

[252] Alexander Stäblein and Morten Hartvig Hansen. Timoshenko beam element with anisotropic cross-sectional properties. In *Proceedings of the VII European Congress on Computational Methods in Applied Sciences and Engineering*. European Community on Computational Methods in Applied Sciences, 2016. ECCOMAS Congress 2016 : VII European Congress on Computational Methods in Applied Sciences and Engineering ; Conference date: 05-06-2016 Through 10-06-2016.

[253] M Stettner, M J Reijerkerk, A Lünenschloß, V Riziotis, A Croce, L Sartori, R Riva, and J M Peeringa. Stall-induced vibrations of the AVATAR rotor blade. *Journal of Physics: Conference Series*, 753(4):042019, sep 2016.

[254] G. W. Stewart. A krylov–schur algorithm for large eigenproblems. *SIAM Journal on Matrix Analysis and Applications*, 23(3):601–614, 2002.

[255] Alexander R. Stäblein, Morten H. Hansen, and Georg Pirrung. Fundamental aeroelastic properties of a bend–twist coupled blade section. *Journal of Fluids and Structures*, 68:72–89, 2017.

[256] H Sugiyama and Y Suda. A curved beam element in the analysis of flexible multi-body systems using the absolute nodal coordinates. *Proceedings of the Institution of Mechanical Engineers, Part K: Journal of Multi-body Dynamics*, 221(2):219–231, 2007.

[257] Yixuan Tang, Haiyan Hu, and Qiang Tian. Model order reduction based on successively local linearizations for flexible multibody dynamics. *International Journal for Numerical Methods in Engineering*, 118(3):159–180, 2019.

[258] Yixuan Tang, Marko K. Matikainen, and Aki Mikkola. The improvements of new absolute nodal coordinate formulation based continuum beam elements in convergence, accuracy and efficiency. *European Journal of Mechanics - A/Solids*, 105:105252, 2024.

[259] A. Tasora and M. Anitescu. A matrix-free cone complementarity approach for solving large-scale, nonsmooth, rigid body dynamics. *Computer Methods in Applied Mechanics and Engineering*, 200(5-8):439 – 453, 2011.

[260] A. Tasora, R. Serban, H. Mazhar, A. Pazouki, D. Melanz, J. Fleischmann, M. Taylor, H. Sugiyama, and D. Negrut. Chrono: An open source multi-physics dynamics engine. pages 19–49. Springer, 2016.

[261] Alessandro Tasora, Simone Benatti, Dario Mangoni, and Rinaldo Garziera. A geometrically exact isogeometric beam for large displacements and contacts. *Computer Methods in Applied Mechanics and Engineering*, 358:112635, 2020.

[262] Alessandro Tasora and Pierangelo Masarati. Analysis of rotating systems using general-purpose multibody dynamics. In Paolo Pennacchi, editor, *Proceedings of the 9th IFToMM International Conference on Rotor Dynamics*, pages 1689–1701, Cham, 2015. Springer International Publishing.

[263] Alessandro Tasora and Pierangelo Masarati. Analysis of rotating systems using general-purpose multibody dynamics. In Paolo Pennacchi, editor, *Proceedings of the 9th IFToMM International Conference on Rotor Dynamics*, pages 1689–1701, Cham, 2015. Springer International Publishing.

[264] Alessandro Tasora and Paolo Righettini. Application of quaternion algebra to the efficient computation of jacobians for holonomic-rheonomic constraints. In *Advances in Computational Multibody Dynamics*. IDMEC/IST, Lisbon, Portugal, 1999.

[265] Olivier Thomas, Aurélien Sénéchal, and J-F Deü. Hardening/softening behavior and reduced order modeling of nonlinear vibrations of rotating cantilever beams. *Nonlinear dynamics*, 86:1293–1318, 2016.

[266] Qinglong Tian, Peng Lan, and Zuqing Yu. Model-Order Reduction of Flexible Multibody Dynamics Via Free-Interface Component Mode Synthesis Method. *Journal of Computational and Nonlinear Dynamics*, 15(10):101008, 08 2020.

[267] C. Tibaldi, T. Kim, T. J. Larsen, F. Rasmussen, R. de Rocca Serra, and F. Sanz. An investigation on wind turbine resonant vibrations. *Wind Energy*, 19(5):847–859, 2016.

[268] Antonio Torres, Javier Gil, Aitor Plaza, and Jokin Aginaga. 4P operational harmonic and blade vibration in wind turbines: A real case study of an active yaw system and a concrete tower. *Renewable Energy*, 227:120503, 2024.

[269] Maxime Tournier, Matthieu Nesme, Benjamin Gilles, and Francois Faure. Stable constrained dynamics. *ACM Transactions on Graphics*, 34, 07 2015.

[270] Sri Tudjono, Han Lie, Dinh Nguyen, Shota Kiryu, and Buntara Gan. Exact shape functions for timoshenko beam element. *IOSR Journal of Computer Engineering*, 19:12–20, 05 2017.

[271] A. A. W. van Vondelen, S. T. Navalkar, A. Iliopoulos, D. C. van der Hoek, and J.-W. van Wingerden. Damping identification of offshore wind turbines using operational modal analysis: a review. *Wind Energy Science*, 7(1):161–184, 2022.

[272] P. Veers, C. L. Bottasso, L. Manuel, J. Naughton, L. Pao, J. Paquette, A. Robertson, M. Robinson, S. Ananthan, T. Barlas, A. Bianchini, H. Bredmose, S. G. Horcas, J. Keller, H. A. Madsen, J. Manwell, P. Moriarty, S. Nolet, and J. Rinker. Grand challenges in the design, manufacture, and operation of future wind turbine systems. *Wind Energy Science*, 8(7):1071–1131, 2023.

[273] H. Verdonck, O. Hach, J. D. Polman, O. Schramm, C. Balzani, S. Müller, and J. Rieke. Uncertainty quantification of structural blade parameters for the aeroelastic damping of wind turbines: a code-to-code comparison. *Wind Energy Science*, 9(8):1747–1763, 2024.

[274] Hendrik Verdonck and Oliver Hach. Hierarchical sensitivity study on the aeroelastic stability of the IEA 15 MW reference wind turbine. *Journal of Physics: Conference Series*, 2767(2):022036, jun 2024.

[275] GE Vernova. GE's Haliade-X 14.7 MW-220 turbine obtains full DNV type certificate. https://www.gevernova.com/news/press-releases/ge-haliade-x-14-7mw-220-turbine-obtains-full-dnv-type-certificate, December 2022.

[276] S. VimalKumar, D. De Tavernier, D. von Terzi, M. Belloli, and A. Viré. Force-partitioning analysis of vortex-induced vibrations of wind turbine tower sections. *Wind Energy Science*, 9(10):1967–1983, 2024.

[277] A. Viré, A. Derksen, M. Folkersma, and K. Sarwar. Two-dimensional numerical simulations of vortex-induced vibrations for a cylinder in conditions representative of wind turbine towers. *Wind Energy Science*, 5(2):793–806, 2020.

[278] Dillon M. Volk, Bjarne S. Kallesøe, Scott Johnson, Georg R. Pirrung, Riccardo Riva, and Félix Barnaud. Large wind turbine edge instability field validation. *Journal of Physics: Conference Series*, 1618(5):052014, 09 2020.

[279] Gang Wang, Zhaohui Qi, and Jinshuai Xu. A high-precision co-rotational formulation of 3D beam elements for dynamic analysis of flexible multibody systems. *Computer Methods in Applied Mechanics and Engineering*, 360:112701, 2020.

[280] K. Wang, V. A. Riziotis, and S. G. Voutsinas. Aeroelastic stability of idling wind turbines. *Wind Energy Science*, 2(2):415–437, 2017.

[281] Kai Wang, Vasilis A. Riziotis, and Spyros G. Voutsinas. Aeroelastic stability of idling wind turbines. *Journal of Physics: Conference Series*, 753(4):042008, sep 2016.

[282] Lin Wang, Xiongwei Liu, Nathalie Renevier, Matthew Stables, and George M. Hall. Nonlinear aeroelastic modelling for wind turbine blades based on blade element momentum theory and geometrically exact beam theory. *Energy*, 76:487–501, 2014.

[283] Qi Wang, Michael A. Sprague, Jason Jonkman, Nick Johnson, and Bonnie Jonkman. Beamdyn: a high-fidelity wind turbine blade solver in the fast modular framework. *Wind Energy*, 20(8):1439–1462, 2017.

[284] Qi Wang, Michael A. Sprague, and Jason M. Jonkman. *Nonlinear Legendre Spectral Finite Elements for Wind Turbine Blade Dynamics*. 01 2014.

[285] WindEurope. Wind energy in Europe: 2023 Statistics and the outlook for 2024-2030. Technical report, WindEurope, 2024.

[286] Long Wu and Paolo Tiso. Nonlinear model order reduction for flexible multibody dynamics: a modal derivatives approach. *Multibody System Dynamics*, 36(4):405–425, 2016.

[287] Shih-Chin Wu and Edward J. Haug. Geometric non-linear substructuring for dynamics of flexible mechanical systems. *International Journal for Numerical Methods in Engineering*, 26(10):2211–2226, 1988.

[288] Xinhua. GLOBALink | 26MW offshore wind turbine rolls off production line in SE China's Fujian. https://english.news.cn/20241013/1eb5541f05754c889ea5ed2f7a71e926/c.html, October 2024.

[289] Haidong Yu, Chunzhang Zhao, and Hui Zheng. A higher-order variable cross-section viscoelastic beam element via ancf for kinematic and dynamic analyses of two-link flexible manipulators. *International Journal of Applied Mechanics*, 09(08):1750116, 2017.

[290] Wenbin Yu. VABS manual for users. 02 2013.

[291] Wenbin Yu, Dewey H. Hodges, and Jimmy C. Ho. Variational asymptotic beam sectional analysis – An updated version. *International Journal of Engineering Science*, 59:40–64, 2012. The Special Issue in honor of VICTOR L. BERDICHEVSKY.

[292] Frederik Zahle, Athanasios Barlas, Kenneth Lønbæk, Pietro Bortolotti, Daniel Zalkind, Lu Wang, Casper Labuschagne, Latha Sethuraman, and Garrett Barter. *Definition of the IEA Wind 22-Megawatt Offshore Reference Wind Turbine*. Technical University of Denmark, 2024. DTU Wind Energy Report E-0243 IEA Wind TCP Task 55.

[293] Pinting Zhang and Shuhong Huang. Review of aeroelasticity for wind turbine: Current status, research focus and future perspectives. *Frontiers in Energy*, 5(4):419–434, Dec 2011.

[294] Yimin Zhang, Bangcun Wen, and Suhuan Chen. Eigenvalue problem of constrained flexible multibody systems. *Mechanics Research Communications*, 24(1):11–16, January 1997.

[295] Zili Zhang, Bei Chen, and Søren R.K. Nielsen. Coupled-mode flutter of wind turbines and its suppression using torsional viscous damper. *Procedia Engineering*, 199:3254–3259, 2017. X International Conference on Structural Dynamics, EURODYN 2017.

[296] Guowei Zhao, Jianming Du, and Zhigang Wu. A geometric softening phenomenon of a rotating cantilever beam. *Archive of Applied Mechanics*, 87:1049–1059, 2017.

[297] Ping Zhou, Andrea Zanoni, and Pierangelo Masarati. Projection continuation for minimal coordinate set dynamics of constrained systems. In *Proceedings of ECCOMAS Thematic Conference on Multibody Dynamics*, pages 184–196, Budapest, Hungary, 01 2021.

[298] Ping Zhou, Andrea Zanoni, and Pierangelo Masarati. A projection continuation approach for minimal coordinate set constrained dynamics. *Multibody System Dynamics*, 57(3):237–257, Apr 2023.

[299] Xiandong Zhou, Kefu Huang, and Zheng Li. Effects of bend-twist coupling on flutter limits of composite wind turbine blades. *Composite Structures*, 192:317–326, 2018.

[300] Wenguo Zhu and Marco Morandini. Multiphysics cross-section analysis of smart beams. *Mechanics of Advanced Materials and Structures*, 28(22):2281–2298, 2021.

[301] Andreas Zwölfer and Johannes Gerstmayr. A concise nodal-based derivation of the floating frame of reference formulation for displacement-based solid finite elements. *Multibody System Dynamics*, 49(3):291–313, Jul 2020.

[302] Andreas Zwölfer and Johannes Gerstmayr. The nodal-based floating frame of reference formulation with modal reduction. *Acta Mechanica*, 232(3):835–851, Mar 2021.

[303] Andreas Zwölfer and Johannes Gerstmayr. A unified framework for corotational flexible multibody system dynamics formulations. *Journal of Structural Dynamics*, pages 51–81, 06 2023.

[304] Stig Øye. *FLEX 5 User Manual*. Technical University of Denmark, 1999.

Acknowledgments

During my research, I have received invaluable support from various professionals, organizations, colleagues, friends, and family.

First, I would like to express my sincere gratitude to my PhD supervisor, Prof. Alessandro Tasora, for his unwavering support, guidance, and encouragement throughout my doctoral journey. He provided the opportunity to embark on this PhD, offering essential guidance on complex mathematical derivations and code implementations. More importantly, his insightful feedback and support during challenging moments—such as when I faced discrepancies between my results and those from widely-used tools, or when I encountered the counterintuitive results of nonzero eigenvalues for a rotor's free rotation mode—were crucial in helping me overcome uncertainties and successfully navigate the research process. His expertise and continuous mentorship have been pivotal to the completion of this thesis.

I would also like to extend my deep appreciation to Prof. Morten H. Hansen. My interest in the modal dynamics of wind turbines was ignited by a training course he led at Southern Denmark University in the summer of 2018. Since then, his extensive knowledge and insightful discussions on wind turbine aeroelasticity have been a constant source of inspiration and guidance throughout my research.

I am grateful for the financial support from the PON REACT-EU program under PON DM 1061/2021, which has been essential for the completion of this research.

Special thanks to Goldwind for hosting me abroad, providing financial support, simulation and measurement data, computational resources, and testing environments—all critical to the success of my research.

I would like to thank my colleagues and lab mates, particularly Dr. Dario Mangoni and Dr. Dario Fusai, for their collaboration, insightful discussions, and unwavering support, both professionally and personally, throughout the PhD program.

Lastly, my heartfelt gratitude goes to my family for their constant emotional and practical support throughout this journey.

Chao Peng
December 2024

UNIONE EUROPEA
Fondo Sociale Europeo
Ministero dell'Università e della Ricerca
PON RICERCA E INNOVAZIONE 2014 - 2020
REACT EU
UNIVERSITÀ DI PARMA

La borsa di dottorato è stata cofinanziata con risorse del
Programma Operativo Nazionale Ricerca e Innovazione 2014-2020, risorse FSE REACT-EU
Azione IV.4 “Dottorati e contratti di ricerca su tematiche dell’innovazione”
e Azione IV.5 “Dottorati su tematiche Green”